

**METAL OXIDES FOR ENVIRONMENTAL
FRIENDLY APPLICATIONS**

A Thesis submitted to Goa University for the Award of the Degree of

DOCTOR OF PHILOSOPHY

in

CHEMISTRY

By

RAJASHRI SUBHASH KARMALI

Research Guide

Mrs Vrinda Borker

546.3

KAR/met

Research Co-Guide

Prof. A. V. Salker

Goa University

Taleigao Goa

2012

T-575

STATEMENT

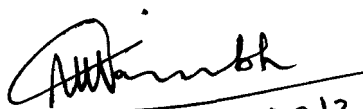
I hereby declare that the matter embodied in this thesis entitled, “*Metal oxides for environmental friendly applications*” is the result of the investigations carried out by me in the Department of Chemistry, Goa University, Goa, India, under the supervision of Mrs Vrinda Borker.

In keeping with the general practice of reporting scientific observations, due acknowledgement has been made wherever the work described is based on the findings of other investigators.

Date:

Place: Taleigao Plateau

**EXAMINED
BY**



29.10.2012
(Dr. A.K. Nikumbh)
(External Referee)



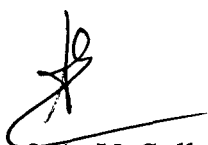
Rajashri Subhash Karmali
(candidate)

CERTIFICATE

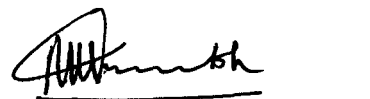
This is to certify that the work entitled, "*Metal oxides for environmental friendly applications*" presented in this thesis has been carried out by Ms Rajashri Subhash Karmali under my supervision and the same has not been submitted elsewhere for the award of a degree.



Mrs Vrinda Borker
Research Guide



Prof. A. V. Salker
Research Co-Guide



29.10.2012
External Examiner
Dr. A.K. Nikumbh)

Date:

ACKNOWLEDGEMENT

I extend my sincere gratitude and appreciation to many people who have made this dream of pursuing research possible. First and foremost, I would like to express my sincere thanks to my research guide, Mrs. V. P. Borker for being my inspiration. I thank her for valuable guidance, persistent and enthusiastic support, constant motivation provided to me at every stage of my research.

My gratitude goes to our collaborator and my former co-guide, Prof. K. S. Rane, for his dedicated help, encouragement, constant support and valuable guidance throughout my Ph.D. His diligent passion and enthusiasm are my source of inspiration and always motivate me to work proficiently and smartly throughout my life.

I would like to acknowledge my co-guide, Prof. A. V. Salker of Chemistry Department, Goa University, for his valuable guidance.

I thank the present H.O.D, Chemistry Department, Prof. A.V. Salker and also the former H.O.D., Prof. J. B. Fernandes and Prof. S. P. Kamat for extending necessary facilities.

I also acknowledge my subject expert Dr. Kaustubh Priolkar, for his expert opinion and suggestions during the FRC meetings.

My sincere thanks to all the teachers of Chemistry Department, Goa University for helping and motivating me in all possible way.

My heartfelt thanks to Prof. Julio Fernandes and Prof. B. R. Srinivasan for their motivation and advice.

I appreciate and acknowledge the help given by Librarian and all the library staff of Goa university.

I acknowledge UGC-DAE, CSR for granting financial support through major research project and Vasant Rao Dempo Educational and Research Foundation for financial assistance during the research work.

My genuine gratitude towards our research group - Dr. P.Y. Sawant, Dr. Rathan, Sifali, Manisha, Sneha, Rita, Savita.

I convey my cordial thanks to Sifali, Manisha and Rita for their exceptional help.

I also thank all the research scholars, Lactina, Puzy, Srikant, Santosh, Siddhali, Satish, Rohan, Kiran, Umesh, Prachi, Sonia, Priyanka, Hari, Sandesh, Prakash, Chinmay and Kashinath for their kind cooperation and friendship.

I am grateful to the non-teaching staff of Chemistry Department, Goa University for their co-operation and help.

My special thanks to two Principals of Dhempe College, Dr S. V. Deshpande and Dr. Y. Modassir as well as two H.O.Ds of Chemistry Dept, Dr.Lina Talwadker, Dr.Udai Naik. My gratitude goes to all the teaching staff of Chemistry Dept of Dhempe College. My special thanks to the Librarian and Non-teaching of Dhempe College for all the help given.

My thanks are also due to Dr. A.K.Tyagi, BARC, Mumbai, Dr. S. K. Deshpande, UGC-DAE,CSR, Dr. R. Mishra, BARC, Mumbai., Dr. S.R. Dharwadkar, Institute of Science, Mumbai. Dr. Cora Lind, University of Toledo, Dr. C. G. Naik, NIO, Goa, Dr. C. S. Gopinath, NCL, pune , Dr. G. Nayak- Marine Science Dept, Goa University, Prof. Sarkar, IIT Kanpur, Dr Thamban Meloth, Dr. Rahul Mohan – NCAOR, Goa.

My honest thanks to Ms Amruta Bartakke, Ms Lina, Mr. Girish Prabhu, Mr. Vijay Khedekar, Ms Sahina Gazi, Ms Reshma Raut Desai and Ms Nimali Prabhu.

Finally, on a more personal level, I would like to thank my parents and brother for their unconditional love and support through the years. I am very grateful for what they have gone through to provide me with this opportunity of receiving an advanced education. I genuinely thank my fiancé and in-laws for their unconditional love and support during the final stages of Ph.D. Thesis.

And I am very much grateful to almighty god who bestowed upon me the blessing of accomplishing this work.

Contents

Chapter 1	Introduction and Review of Literature
1.1	Introduction.....01
1.2	Background.....02
1.3	Pollutants and their sources.....03
1.4	Literature Survey.....08
	a. Pyrochlore system for Nuclear Waste disposal.....08
	b. Zinc oxide system.....17
	(i) Degradation of Dyes.....21
	(ii)Antibacterial Properties.....23
	(iii)Abatement of NOx.....24
	c. Iron ore Tailing.....25
	d. Synthetic methods for oxides.....28
1.5	Aims and Objectives.....32
1.6	Methodology.....34
1.7	Organisation of the Thesis.....35
Chapter 2	Pyrochlore System for Nuclear Waste Disposal
2.1	Introduction36
2.2	Methods of preparation of Materials.....37
2.2.1	Ceramic method.....37
2.2.2	Green Methods of synthesis of metal oxides.....38
2.2.2.1	Precursor method synthesis of $\text{Nd}_2\text{Zr}_2\text{O}_7/\text{Gd}_2\text{Zr}_2\text{O}_7/\text{Gd}_2\text{ZrCeO}_7$...38
2.2.2.1a	Oxalate Method.....39
	b Hydrazinated oxalate.....39
2.2.2.2	Sol-gel Method.....40
	(i) Synthesis of $\text{Nd}_2\text{Zr}_x\text{Ti}_{2-x}\text{O}_7$ ($x = 2.0, 1.8, 1.6, 1.4, 1.2$ and 1.0).....40
	(ii) Synthesis of $\text{Nd}_{2-y}\text{Sr}_y\text{Zr}_2\text{O}_7$ ($x = 1.8, 1.0, 0.05$).....41
2.3	Characterization techniques..... 41

2.3.1 Chemical analysis.....	41
2.3.1.1 Estimation of Hydrazine.....	41
2.3.1.2 Estimation of Oxalate.....	42
2.3.2 Instrumental Analysis.....	42
2.3.2.1 Fourier Transform Infrared (FTIR) Spectroscopy.....	42
2.3.2.2 Thermal analysis.....	43
2.3.2.3 X-ray diffraction (XRD).....	45
2.3.2.4 High Temperature X-ray diffraction (XRD).....	46
2.3.2.5 UV-Visible Diffuse Reflectance spectroscopy (DRS).....	47
2.3.2.6 Scanning Electron Microscopy (SEM).....	48
2.3.2.7 X-ray Photoelectron Spectroscopy (XPS).....	49
2.3.2.8 Electron Spin Resonance (ESR).....	49
2.3.2.9 Density Measurement.....	50
2.3.2.10 A. C. Conductivity: Impedance Measurements.....	51
2.3.2.11 Leaching Studies.....	52
2.4 Results and Discussions.....	53
2.4.1 $\text{Nd}_2\text{Zr}_2\text{O}_7 / \text{Gd}_2\text{Zr}_2\text{O}_7 / \text{Gd}_2\text{ZrCeO}_7$	53
2.4.1.1 Characterization of oxalate and hydrazinated oxalate precursors....	53
2.4.1.1.1 Chemical analysis and formula fixation of oxalate and hydrazinated oxalate precursors.....	53
2.4.1.1.2 FTIR analysis of oxalate and hydrazinated oxalate precursors ...	54
2.4.1.1.3 Thermal analysis of oxalate and hydrazinated oxalate precursors.	55
2.4.1.2 Characterization of oxides.....	57
2.4.1.2.1 Phase identification of the thermal products of oxalate and hydrazinated oxalate precursors by XRD.....	57
2.4.1.2.2 High temperature XRD of $\text{Gd}_2\text{Zr}_2\text{O}_7$ (hydrazinated oxalate).....	59
2.4.2 $\text{Nd}_2\text{Zr}_x\text{Ti}_{2-x}\text{O}_7$ ($x = 2.0, 1.8, 1.6, 1.4, 1.2$ and 1.0).....	60
2.4.2.1 Characterization of citrate gel precursor.....	60
2.4.2.1.1 FTIR analysis of citrate gel precursor.....	60
2.4.2.1.2 Thermal analysis of citrate gel precursor.....	61
2.4.2.2 Characterization of oxides, $\text{Nd}_2\text{Zr}_x\text{Ti}_{2-x}\text{O}_7$	63
2.4.2.2.1 Phase identification of oxides, $\text{Nd}_2\text{Zr}_x\text{Ti}_{2-x}\text{O}_7$ prepared by citrate gel and ceramic method.....	63

2.4.2.2.2 Density measurements of oxides, $\text{Nd}_2\text{Zr}_x\text{Ti}_{2-x}\text{O}_7$ prepared by citrate gel and ceramic method.....	68
2.4.2.2.3 Microstructure (SEM) of $\text{Nd}_2\text{Zr}_x\text{Ti}_{2-x}\text{O}_7$	68
2.4.2.2.4 Diffuse Reflectance and Absorbance spectra of $\text{Nd}_2\text{Zr}_x\text{Ti}_{2-x}\text{O}_7$	70
2.4.2.2.5 Conductivity studies.....	73
2.4.3 $\text{Nd}_{2-y}\text{Sr}_y\text{Zr}_2\text{O}_7$ ($y = 1.8, 1.0, 0.05$).....	84
2.4.3.1 Phase identification of oxides, $\text{Nd}_{2-y}\text{Sr}_y\text{Zr}_2\text{O}_7$ ($y = 1.8, 1.0, 0.05$)....	84
2.4.3.2 Diffuse Reflectance and Absorbance of $\text{Nd}_{2-y}\text{Sr}_y\text{Zr}_2\text{O}_7(0.05)$	84
2.4.3.3 Leaching studies on $\text{Nd}_{2-y}\text{Sr}_y\text{Zr}_2\text{O}_7$ ($x = 0.05$).....	85

Chapter 3 ZnO System :Photomineralization of organic compounds

Antibacterial Action and Photodegradation of NOx

3.1 Introduction.....	89
3.2 Methods of preparation of Materials.....	90
3.2.1 Oxalate method.....	91
3.2.2 Hydrazinated oxalate (equilibration).....	91
(i) ZnO.....	91
(ii) Aluminium doped ZnO.....	91
3.2.3 Hydrazinated oxalate (solution).....	92
(a)ZnO.....	92
(b) Aluminium doped ZnO.....	92
3.2.4 Spray pyrolysis synthesis of zinc oxide.....	92
3.3 Characterization techniques.....	94
3.3.1 Chemical analysis.....	94
3.3.1.1 Estimation of Hydrazine.....	94
3.3.1.2 Estimation of Zinc.....	94
3.3.2 Instrumental Analysis.....	94
3.3.2.1 Fourier Transform Infrared (FTIR) Spectroscopy.....	94
3.3.2.2 Thermal analysis.....	94
3.3.2.3 X-ray Diffraction (XRD).....	94

3.3.2.4 Density Measurements.....	95
3.3.2.5 UV-Visible Diffuse Reflectance spectroscopy (DRS).....	95
3.3.2.6 Scanning Electron Microscopy (SEM).....	95
3.3.2.7 BET Surface Area Measurements.....	95
3.3.2.8 Energy Dispersive X-ray Spectroscopy (EDS).....	96
3.3.2.9 X-ray Photoelectron Spectroscopy (XPS).....	97
3.4 Photocatalytic applications.....	97
3.4.1 Dye Degradations.....	97
3.4.1.1 Methylene Blue (MB) dye degradation.....	97
a. UV-Visible Absorbance.....	97
b. Chemical Oxygen Demand (COD).....	98
c. Electro Spray Ionisation –Mass Spectrometry(ESI-MS).....	98
d. Sulphate and Nitrate.....	98
3.4.1.2 Industrial effluent degradation.....	99
a. UV-Visible Absorbance.....	99
b. Chemical Oxygen Demand (COD).....	100
3.4.2 Antibacterial studies.....	100
3.4.2.1 Disk diffusion Assay.....	102
3.4.2.2 Minimum Bactericidal Concentration (MBC).....	102
3.4.3 Photodegradation of NO _x	103
3.4.3.1 Generation of NO _x	103
3.4.3.2 Estimation of nitrite using calibration curve.....	103
3.4.3.3 Abatement of NO _x by photocatalysts.....	104
3.4.3.4 Qualitative estimation of nitrate.....	104
3.5 Results and discussions.....	105
3.5.1 ZnO and ZnO _{1-x} N _x system.....	105
3.5.1.1 Characterization of oxalate and hydrazinated oxalate precursors...105	
3.5.1.1.1 Chemical analysis and formula fixation of oxalate and hydrazinated oxalate precursors.....	105
3.5.1.1.2 FTIR analysis of oxalate and hydrazinated oxalate precursors...105	
3.5.1.1.3 Thermal analysis of oxalate and hydrazinated oxalate precursors.107	
3.5.1.2 Characterization of oxides.....	109

3.5.1.2.1	Phase identification of ZnO and ZnO _{1-x} N _x system by XRD.....	109
3.5.1.2.2	Density studies of ZnO and ZnO _{1-x} N _x system.....	111
3.5.1.2.3	Microstructure (SEM) analysis of ZnO and ZnO _{1-x} N _x system...	111
3.5.1.2.4	BET Surface area measurements on ZnO and ZnO _{1-x} N _x system.	112
3.5.1.2.5	Diffuse Reflectance and Absorbance spectra of ZnO and ZnO _{1-x} N _x system.....	113
3.5.1.2.6	XPS studies on ZnO and ZnO _{1-x} N _x system.....	115
3.5.2	Aluminium doped ZnO system.....	117
3.5.2.1	Characterization of precursors.....	118
3.5.2.1.1	Chemical analysis and formula fixation of precursors.....	118
3.5.2.1.2	FTIR analysis of precursors.....	119
3.5.2.1.3	Thermal analysis of precursors.....	120
3.5.2.2	Characterization of oxides.....	122
3.5.2.2.1	Phase identification of the oxides by XRD.....	122
3.5.2.2.2	Microstructure analysis of the oxides by SEM.....	123
3.5.2.2.3	Diffuse Reflectance and Absorbance spectra of the oxides.....	124
3.5.2.2.4	Elemental analysis of the oxides by EDS.....	126
3.5.3	Zinc Oxide prepared by Spray pyrolysis.....	127
3.5.3.1	Microstructure analysis by SEM.....	127
3.5.3.2	Elemental analysis by EDS.....	127
3.5.3.3	IR analysis.....	128
3.5.4	Photocatalytic degradations.....	129
3.5.4.1	Photocatalytic degradation of MB on.....	129
(i)	ZnO and ZnO _{1-x} N _x	
a.	UV-Visible Absorbance.....	129
b.	COD removal capacity/ Mineralization studies.....	136
c.	Electro Spray Ionisation –Mass Spectrometry(ESI-MS).....	138
d.	Identification and separation of degradation products of MB.....	142
e.	Mechanism of photodegradation of MB.....	143
f.	Reuse of ZnO and ZnO _{1-x} N _x	146
(ii)	Al doped ZnO.....	148
3.5.4.2	Photocatalytic degradation of Industrial effluents on ZnO and ZnO _{1-x} N _x system.....	148

3.5.5 Antibacterial activity of ZnO, ZnO _{1-x} N _x and Al doped ZnO.....	152
3.5.5.1 Disk diffusion Assay.....	152
3.5.5.2 MBC.....	155
3.5.6 NO _x studies on ZnO, ZnO _{1-x} N _x and Al doped ZnO.....	157

Chapter 4 Iron oxide system for Photomineralization of organic compounds

4.1 Introduction.....	160
4.2 Characterization.....	162
4.2.1 Chemical analysis of the ore reject sample.....	162
4.2.2 Instrumental analysis.....	162
4.2.2.1 X-ray Diffraction (XRD): Phase identification.....	162
4.2.2.2 Energy Dispersive X-ray Spectroscopy(EDS).....	163
4.2.2.3 Magnetization Measurements.....	163
4.2.2.4 Scanning Electron Microscopy (SEM).....	163
4.2.2.5 UV-Visible Diffuse Reflectance spectroscopy (DRS).....	164
4.2.2.6 Fourier Transform Infrared (FTIR) Spectroscopy.....	164
4.3 Degradation of Methylene Blue (MB) Dye.....	164
4.3.1 Photocatalytic Degradation of MB.....	164
4.3.1.1 Photocatalytic Degradation of MB on iron ore rejects.....	165
4.3.1.2 Degradation of MB on iron ore rejects at alkaline and neutral pH in sunlight.....	166
4.3.1.3 Effect of dyeing chemicals and additives on MB degradation by ore rejects.....	166
4.3.2 Thermal degradation of MB.....	167
4.4 Results and Discussion.....	167
4.4.1 Characterization of ore rejects.....	167
4.4.1.1 Chemical Analysis of the ore reject sample: Presence of Fe	167
4.4.1.2 Analysis of ore rejects by XRD: Phase identification.....	168
4.4.1.3 Elemental analysis of ore rejects by EDS.....	169
4.4.1.4 Saturation Magnetization studies of ore rejects	170
4.4.1.5 Scanning Electron Microscopy of ore rejects.....	170
4.4.1.6 Diffuse Reflectance and Absorbance spectra of the ore rejects.....	170

4.4.1.7 IR analysis of ore rejects.....	172
4.4.2 Photocatalytic degradations of MB.....	173
4.4.2.1 Degradation of MB on Fe ₂ O ₃ and γ -Fe ₂ O ₃ from iron ore rejects in sunlight	173
4.4.2.2 Degradation of MB on iron ore rejects in sunlight.....	173
4.4.2.3.1 Effect of pH on degradation of MB on iron ore rejects in sunlight ..	174
4.4.2.3.2 Effect of initial concentration of dye on degradation of MB by iron ore rejects in sunlight.....	175
4.4.2.3.3 Effect of concentration of ore rejects on degradation of MB by iron ore rejects in sunlight.....	176
4.4.2.3.4 Effect of temperature on degradation of MB on iron ore rejects in sunlight.....	178
4.4.2.4 Degradation of MB on iron ore rejects at alkaline and neutral pH in sunlight.....	180
a. UV-Visible absorbance.....	180
b. Mineralization of MB.....	181
c. ESI-MS studies.....	183
d. Kinetics of photodegradation.....	184
e. Mechanism of photocatalytic degradation of MB.....	185
4.4.2.5 Effect of dyeing chemicals on MB degradation by iron ore rejects.....	187
4.4.2.5.1 Presence of NaCl along with MB dye.....	187
4.4.2.5.2 Presence of Na ₂ CO ₃ along with MB dye.....	189
4.4.2.6 Effect of additives on MB degradation by iron ore rejects	191
4.4.2.6.1 Effect of addition of K ₂ S ₂ O ₈ to MB dye.....	191
4.4.2.6.2 Effect of addition of H ₂ O ₂ to MB dye.....	192
4.4.2.7 Reuse of iron ore rejects for MB degradation.....	194
4.4.2.8 Thermal degradation of MB by iron ore rejects.....	197

Chapter 5 Summary, conclusions and Future Scope

Summary and conclusions.....	199
Future scope	203
References	204
Appendix I.....	223
Appendix II.....	236

List of Figures

1.1 Disposal of radioactive wastes.....	04
1.2 The pyrochlore structure.....	11
1.3 Contour plot of A^{+3} atomic radii against B^{+4} atomic radii.....	13
1.4 Structure of ZnO (Wurtzite).....	19
2.1 Schematic diagram of Scanning Electron Microscope.....	48
2.2 XRD patterns of Gadolinium Zirconate	58
2.3 XRD patterns of Neodymium Zirconate	58
2.4 XRD patterns of Gadolinium Cerium Zirconate.....	59
2.5 High temperature XRD of $Gd_2Zr_2O_7$ prepared by hydrazinated oxalate method.....	60
2.6 IR spectrum of the citrate gel precursor calcined at $300^\circ C$	61
2.7 DTA-TG of citrate gel precursor calcined at $300^\circ C$	62
2.8 DTA-TG of intimate mixture of ceramic powders.....	63
2.9a XRD of the pyrochlore oxides $Nd_2Zr_xTi_{2-x}O_7$ (citrate gel method).....	64
2.9b XRD of the pyrochlore oxides $Nd_2Zr_xTi_{2-x}O_7$ (ceramic method).....	65
2.10 Refinement profile of $Nd_2Zr_2O_7$ prepared by citrate gel method.....	65
2.11 Variation of lattice parameter with concentration of zirconium.....	66
2.12 SEM of (as prepared) $Nd_2Zr_{1.8}Ti_{0.2}O_7$ (citrate gel method).....	69
2.13 SEM of $Nd_2Zr_{1.8}Ti_{0.2}O_7$ (i) Citrate gel and (ii) Ceramic method.....	69
2.14 SEM of $Nd_2Zr_{1.0}Ti_{1.0}O_7$ (i) Citrate gel and (ii) Ceramic method.....	69
2.15 Variation of band gap with Ti concentration.....	71
2.16 Diffuse reflectance spectra of $Nd_2Zr_xTi_{2-x}O_7$ (citrate gel method).....	72

2.17 Absorbance spectra of $\text{Nd}_2\text{Zr}_x\text{Ti}_{2-x}\text{O}_7$ (citrate gel method).....	73
2.18 Impedance plots of a) $\text{Nd}_2\text{Zr}_2\text{O}_7$, b) $\text{Nd}_2\text{Zr}_{1.8}\text{Ti}_{0.2}\text{O}_7$ (citrate gel method).....	74
2.19 σ_{dc} of (i) ceramic and (ii) citrate gel samples.....	75
2.20 Variation of σ_{dc} with Zr content.....	77
2.21 Variation of activation energy with Zr content.....	77
2.22 Variation of σ_0 with Zr content.....	78
2.23 XPS spectra of (a) O 1S electron,(b) Nd 4d electron, (c)Zr 3d electron, (d) Ti 2p electron (citrate gel method).....	80
2.24 ESR spectra of representative pyrochlore oxides (citrate gel method)....	83
2.25 XRD patterns of $\text{Nd}_{2-y}\text{Sr}_y\text{Zr}_2\text{O}_7$ ($y = 0.05$).....	84
2.26 Diffuse Reflectance spectrum of $\text{Nd}_{2-y}\text{Sr}_y\text{Zr}_2\text{O}_7$ ($y = 0.05$).....	85
2.27 SEM of pelletized $\text{Nd}_{1.95}\text{Zr}_2\text{Sr}_{0.05}\text{O}_7$ sintered at 1000°C	87
2.28 SEM of pelletized $\text{Nd}_{1.95}\text{Zr}_2\text{Sr}_{0.05}\text{O}_7$ sintered at 1400°C	88
2. 29 Leaching of strontium from $\text{Nd}_{2-y}\text{Sr}_y\text{Zr}_2\text{O}_7$ ($y = 0.05$).....	88
3.1 Set-up for spray pyrolysis.....	93
3.2 Diagram explaining principle of EDS.....	97
3.3 UV-Visible spectrum of industrial effluent.....	100
3.4 Set-up for abatement of NO_x	104
3.5 IR spectra of the precursors decomposed at different temperatures.....	107
3.6 Thermogram of oxalate and hydrazinated oxalate precursors.....	108
3.7 XRD of ZnO from oxalate and hydrazinated oxalate precursors.....	110
3.8 XRD of ZnO from OXS at temperatures of i) 500°C and ii) 900°C	110
3.9 SEM pictures of ZnO and $\text{ZnO}_{1-x}\text{N}_x$	112
3.10 Diffuse reflectance spectra of ZnO and $\text{ZnO}_{1-x}\text{N}_x$	113
3.11 UV-Visible absorbance spectra of ZnO and $\text{ZnO}_{1-x}\text{N}_x$	114
3.12 X-ray photoelectron spectrum of N 1s electron in $\text{ZnO}_{1-x}\text{N}_x$	116
3.13 X-ray photoelectron spectrum of Zn 2p electron in $\text{ZnO}_{1-x}\text{N}_x$	117
3.14 Stepwise IR spectra of the hydrazinated oxalate precursor E1 decomposed at different temperatures.....	120
3.15 Thermograms of precursors E1 and S1.....	121
3.16 X-Ray diffraction patterns of Al doped ZnO samples.....	123
3.17 SEM of a) 0.001% Al doped ZnO (from S1) and b) 0.001% Al doped ZnO (from E1).....	124

3.18 Diffuse reflectance spectra of Al doped samples.....	125
3.19 Absorbance spectra of Al doped samples.....	126
3.20 EDS of representative samples Solution method (S1) and Equilibration method (E1).....	126
3.21 SEM image of ZnO prepared by spray pyrolysis.....	127
3.22 EDS of ZnO prepared by spray pyrolysis.....	128
3.23 FTIR of ZnO prepared by spray pyrolysis.....	128
3.24 UV-Visible spectrum of Methylene Blue Dye.....	130
3.25a. UV- Visible spectrum of MB on ZnO.....	132
b. UV- Visible spectrum of MB on ZnO _{1-x} N _x (E).....	132
c. UV- Visible spectrum of MB on ZnO _{1-x} N _x (S).....	133
3.26 UV- Visible spectrum of MB on solar degradation (photolysis).....	133
3.27 Absorbance against time plots for MB degradation.....	134
3.28 Plot of log Co/C for MB degradation by the photocatalysts.....	135
3.29 TLC of the degraded MB solution.....	143
3.30 UV-Visible spectrum of Industrial effluent.....	149
3.31 UV-Visible spectrum of Industrial effluent during degradation.....	150
3.32 Degradation of effluent using ZnO and ZnO _{1-x} N _x with time.....	150
3.33 Degradation of industrial effluent at different pH values.....	151
3.34 Disc diffusion assay of i) ZnO _{1-x} N _x ii) ZnO (spray pyrolysis).....	153
3.35 Bacteriocidal action in MacConkey broth by 1.0 mM ZnO _{1-x} N _x	157
4.1 XRD pattern of iron ore rejects.....	168
4.2 Elemental analysis of iron ore rejects.....	169
4.3 SEM of iron ore rejects at different magnifications.....	170
4.4 Diffuse reflectance spectra of iron ore rejects.....	171
4.5 Absorbance spectra of iron ore rejects.....	172
4.6 Degradation of MB at different pH in sunlight.....	174
4.7 Degradation of MB at different dye concentrations in sunlight with fixed amount (200 mg) of iron ore rejects.....	176
4.8 Degradation of MB at different concentrations of ore rejects in sunlight at 5 x 10 ⁻⁵ M of MB and alkaline pH.....	177

4.9 Degradation of MB at different temperatures in sunlight and 200 mg of ore rejects, 5×10^{-5} M (16 ppm) of MB and alkaline pH.....	179
4.10 Degradation of MB in sunlight at alkaline pH using iron ore rejects.....	181
4.11 Plot of $\ln C_0/C$ V/s time for solar degradation of MB by iron ore rejects..	185
4.12 Degradation of MB at different concentrations of NaCl.....	187
4.13 Degradation of MB (16 ppm) by iron ore rejects (200 mg) in presence of 200 mg of NaCl.....	188
4.14 Degradation of MB (16 ppm) by iron ore rejects (200mg) at different concentrations of Na_2CO_3	189
4.15 Degradation of MB (16 ppm) by iron ore rejects (200 mg) in presence of 200 mg of Na_2CO_3	190
4.16 Degradation of MB (16 ppm) by iron ore rejects (200 mg) at different concentrations of $\text{K}_2\text{S}_2\text{O}_8$	191
4.17 Degradation of MB (16 ppm) by iron ore rejects (200 mg) in presence of 200 mg of $\text{K}_2\text{S}_2\text{O}_8$	192
4.18 Degradation of MB (16 ppm) by iron ore rejects (200 mg) at different concentrations of H_2O_2	193
4.19 Degradation of MB (16 ppm) by iron ore rejects (200 mg) in presence of 0.04M H_2O_2	194
4.20 Degradation of MB on iron ore rejects in second run.....	195
4.21 Degradation of MB on iron ore rejects in third run.....	195
4.22 XRD of iron ore rejects after use for photodegradation of MB.....	196
4.23 SEM images of iron ore rejects after use for degradation of MB.....	196
4.24 Thermal degradation of MB by iron ore rejects at 60°C	198

List of Tables

1.1 Major air pollutants with their sources and ill effect on nature.....	07
1. 2 Some common applications of ZnO.....	17
2.1 Chemical analysis of oxalate and hydrazinated oxalate precursors and the proposed chemical formulae.....	53
2.2 IR absorptions of oxalate and hydrazinated oxalate precursors.....	54
2.3 DTA-TG data of the oxalate and hydrazinated oxalate precursors.....	56
2.4 IR absorptions of citrate gel precursor.....	61

2.5 Comparison of XRD data of $\text{Nd}_2\text{Zr}_2\text{O}_7$ obtained by citrate gel and ceramic method with reported data.....	66
2.6 Lattice parameter and density of $\text{Nd}_2\text{Zr}_x\text{Ti}_{2-x}\text{O}_7$	67
2.7 Densities of $\text{Nd}_2\text{Zr}_x\text{Ti}_{2-x}\text{O}_7$ prepared by citrate gel method and ceramic method.....	68
2.8 Bandgaps of $\text{Nd}_2\text{Zr}_x\text{Ti}_{2-x}\text{O}_7$ prepared by citrate gel method.....	71
2.9 variation of σ_{dc} , pre-exponential factor (σ_0) and activation energy (E) with decrease in concentration of Zr.....	76
2.10 Leaching of Sr from $\text{Nd}_{1.95}\text{Zr}_2\text{Sr}_{0.05}\text{O}_7$ lattice	86
3.1 Chemical analysis of oxalate and hydrazinated oxalate precursors and the proposed chemical formulae.....	105
3.2 IR absorptions of the oxalate and hydrazinated oxalate precursors.....	106
3.3 Thermogravimetric data of the OX, OXE and OXS precursors.....	107
3.4 Physical properties of ZnO and $\text{ZnO}_{1-x}\text{N}_x$ system.....	113
3.5 Band gap values of ZnO and $\text{ZnO}_{1-x}\text{N}_x$ system photocatalysts.....	115
3.6 Proposed formulae for the hydrazinated oxalate precursors of Al doped ZnO.....	118
3.7 IR absorptions for the oxalate and hydrazinated oxalate precursors of Al doped ZnO.....	119
3.8 Thermogravimetric data of representative precursors E1 and S1.....	122
3.9 Bandgap values of Al doped ZnO	124
3.10 EDS data of the oxides from precursors S1 and E1.....	127
3.11 Structure and absorption wavelength of Methylene Blue.....	130
3.12 Time required for decolourization of MB by ZnO and $\text{ZnO}_{1-x}\text{N}_x$	134
3.13 Percent degradation and the rate constant of MB degradation.....	135
3.14 Products of mineralization of MB on photocatalysts.....	138
3.15(a, b, c) Products of MB degradation analyzed by ESI-MS.....	140
3.16 Products of mineralization of MB during reuse on photocatalysts.....	147
3.17 Degradation of MB by aluminium doped ZnO samples.....	148
3.18 Zone of inhibitions of <i>E. coli</i> on ZnO and $\text{ZnO}_{1-x}\text{N}_x$	153
3.19 Colonies of <i>E. coli</i> on various concentrations of ZnO and $\text{ZnO}_{1-x}\text{N}_x$	156
3.20 Time taken by ZnO and doped ZnO for removal of NO_x	158

4.1 Elemental analysis of iron ore rejects.....	169
4.2 Chemical analysis of iron ore rejects.....	170
4.3 Derivative peaks from diffuse reflectance spectra of iron ore rejects...	171
4.4 IR absorptions of iron ore rejects.....	173
4.5 Products of mineralization of MB at alkaline and neutral pH.....	182
4.6 Products of solar degradation of MB on iron ore rejects analyzed by ESI-MS.....	183
4.7 COD removal and mineralization products of MB degradation on reuse.....	195
4.8 Calculated bandgaps of iron ore rejects.....	197
4.9 Products of thermal degradation of MB by iron ore rejects analyzed by ESI-MS.....	198

Abbreviations

Atomic Absorption Spectroscopy	A. A. S.
Chemical Oxygen Demand	C. O. D.
Minimum Bactericidal Concentration	M. B. C.
Methylene Blue	M B
Colony Forming Unit	C F U
N-(1- naphtha ethylene diamine) hydrochloride	NEDA

Chapter 1

Introduction and Review of Literature

1.1 Introduction

Awareness of environment has always been there with the human being ever since the existence on planet Earth. In Indian theology, Vedas emphasized that the relationship with the nature and the animals should not be that of dominion and subjugation but of mutual respect and kindness. Since these guidelines were strictly followed by the people of Indian civilization, they worshipped the elements of environment viz. earth, water and air besides no one dared to misuse or pollute them. Later, the book 'Arthashastra' written by Kautilya, as early as between 321 and 300 BC, contained provisions meant to regulate a number of aspects related to the environment. Based on it, King Ashoka made several laws for the preservation of the ecology of India. The earliest known writings of Persian scientists concerned with environment and its damage from 9th to 13th centuries, found in the article 'Arabic Treatise on Environmental Pollution up to the end of the Thirteenth Century' by Lutfallah, in Environment and History, reports the coinage of words like 'air contamination', 'water contamination', 'soil contamination', 'solid waste management' and 'environmental assessment'.

Environment is the aggregate of external conditions that influence the life of an individual or population. Environment determines the quality and survival of life and hence any disturbance in the environment disturbs the life processes of the population. Thus any unfavourable alteration of our surrounding, wholly or largely by a byproduct of man's actions, through direct or indirect effects of changes in energy patterns, radiation levels, chemical and physical constitution and abundance of organisms is referred to as environmental pollution. These changes may affect man directly or indirectly through his supplies of water and other biological products, his physical objects or possessions or his opportunities for recreation and appreciation of nature.

1.2 Background

It was the industrial revolution that gave birth to environmental pollution as we know today. The first incident of awareness about environmental pollution was as early as in 1272, when King Edward I banned the burning of sea-coal by proclamation in London after its smoke had become a problem. The word pollution however, caught the real imagination of common man after the World War II (1939-1945), due to radioactive fallout from atomic warfare and testing. This followed by a non-nuclear event, 'The Great Smog' of 1952 in London which killed at least 4000 people, prompted 'The Clean Air Act' of 1956. Later in 1956, the world witnessed death of hundreds of Japanese people due to mercury poisoning on eating polluted fish from Minamata Bay. The emergence of large number of factories and onslaught of immense quantities of coal and fossil fuels gave rise to the unprecedented air pollution and the large volume of industrial chemical discharge added to the growing load of untreated human waste. As the Industrial Revolution progressed, water sources especially rivers were made a convenient means of waste disposal (both domestic and industrial). A fire on the Cuyahoga River in Ohio, US in 1969, due to flammable material dumped in it led to the enactment of the 1972 Clean Water Act (CWA). Release of radioactivity into the atmosphere through accidents as in Three Mile Island (1979) due to partial meltdown of reactor and Chernobyl reactor explosion (1986) and the recent Fukushima disaster at Japan again terrified people. The release of lethal methyl isocyanate gas in 1984, into the air in Bhopal, India, from a Union Carbide plant also killed thousands of people immediately.

The discovery of hole in the ozone layer in 1987, by scientists led to the drafting of 'The Montréal Protocol'. The global climate change accord signed in Rio de Janeiro, Brazil, in 1992 addressed the so-called 'green-house gases', which trap heat in the

atmosphere and lead to a global warming trend. The environmental pollution has continued being a menace even in the 21st century. The problem of solid wastes has added to the existing pollutants. The 'Great East Japan Earthquake', the tsunami that followed, and the resulting Fukushima I Nuclear Power Plant disaster in March 2011 has forced people to think again on the radioactive pollution.

1.3 Pollutants and their sources

The Indian Environment Act 1986 defines a pollutant as any solid, liquid or gaseous substance present in concentrations injurious to environment. Many types of pollutants get distributed over the entire earth in short periods. Radioactive fallout from atmospheric nuclear tests conducted in any part of the world becomes detectable in other parts of the world within a few days. The accidents due to improper shielding of the nuclear power plants are reported in history [1]. The nuclear tests carried out to invent better nuclear weapons release 15 to 20% radioactive material into the stratosphere which then falls into the troposphere which is the lowest layer of earth's atmosphere; and is retained there for months to several years. The radioactive fallout settles on the leaves of plants and trees which are eaten by the grazing animals. This makes the radioactive material enter the ecosystem and the food chain. Ingestion of radioactive material can lead to cancer and genetic mutation in humans. Fallouts that do not drop on leaves accumulate over the sea and can be harmful for the sea life, which ultimately affects the humans.

Radioactive waste is a waste product containing radioactive materials. Depending upon the level of radioactivity associated, it is classified as 'low level waste', 'Intermediate level waste' and 'High level waste'. Low level and intermediate level radioactive wastes are usually confined in the repositories. High-level radioactive waste (HLW)

generally contains highly concentrated liquid solutions of nuclear fission products and extremely long lived radionuclides requiring permanent isolation from man's environment. These wastes like unburnt fuels, fission products are incorporated in borosilicate glass and then inserted in concrete and steel canisters kept in underground trenches.

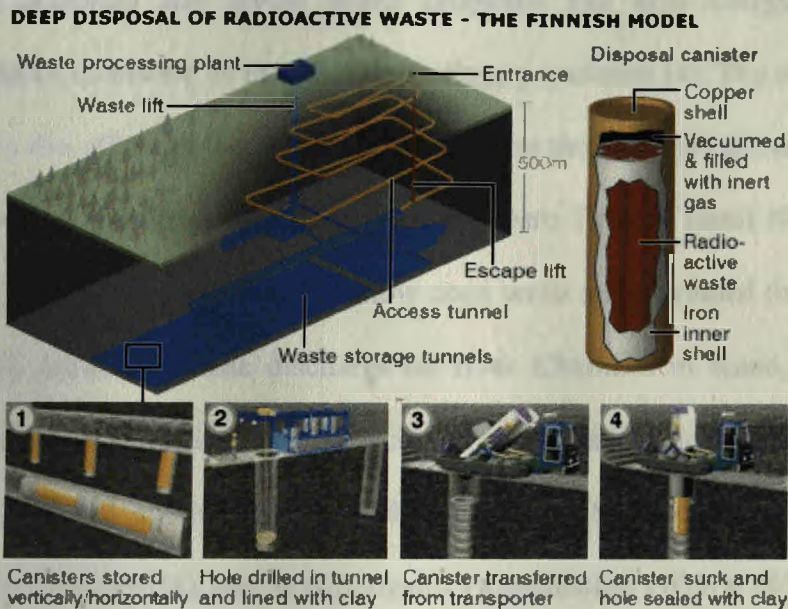


Figure 1.1 Disposal of radioactive wastes (Ref:news.bbc.co.uk)

The leaching of these radioactive nuclei into the ground water contaminates the water table. In addition to this there is a wide range of contaminated solid items like equipment, components, filters, residues, clothing and materials used for construction which also exhibit some radioactivity [2] and need proper disposal.

Water pollution may also derive its origin from several other sources including chemical pollutants from runoff of chemicals used in agriculture or debris from geological processes, but the greatest source of pollution is organic waste coming from industrial effluents. Industrial effluents are the materials generally discarded from industrial operations or derived from manufacturing processes. These effluents enter the

environment, especially in freshwater and cause contamination of drinking water. Other disposal practices such as deep well injection and improper disposal of wastes in surface impoundments also cause water contamination [3]. Sometimes the effluents are released in the rivers or on land without any pretreatment as in Tirupur, Chennai where industrial effluents from dyeing and bleaching industries released in river Noyyal basin caused water pollution and severe health problems like skin allergy, respiratory infection, gastritis, ulcers etc. in the adjoining village population [4]. The metals and the salts present in the effluents then enter the food chain through the cultivated plants or the water table e.g. industries located in Mettupalayam Taluka, Tamil Nadu disposed their effluents on land which polluted shallow open wells and increased the salt content of the soil [5]. Industrial waste discharge on river Challawa in Kano, Nigeria and Tamburawa old water treatment plant have caused an increase in heavy metal content in the river beyond the maximum permissible limit set by Food and Environment Protection Act 1985 (FEPA) and World Health Organization (WHO) [6]. In Karachi, vegetables grown on the lands irrigated with industrial effluents on both sides of the Malir River near Korangi Industrial Area and Shah Faisal Colony have caused people to suffer from gastric ailments [7].

Although chemical pollutants get diluted on entering the water bodies, they can alter the ecosystem and cause overproduction of certain forms of algae and bacteria. Once in the water, the growth of the microorganism can be exacerbated by environmental factors such as water, temperature and the chemical composition of the water. For example, runoff of fertilizers from nearby places infuse watercourse with nitrogen, potassium and phosphorous which are desirable for bacterial growth causing their proliferation. Another aspect of water pollution is the coloured effluents and mining residues released in water acting as a block for the sunlight used for photosynthesis by aquatic plants.

Entry of the ore rejects into the fields also disturbs the local ecosystems. Due to extensive mining activities by Kudremukh Iron Ore Company Limited, Karnataka the paddy yield in the nearby fields has decreased. The silt and tailings carried to the Bhadra reservoir also pose a threat to the reservoir, which is designed to last for 180 years [8]. Disposal of iron ore tailings along the shore of Tolo Harbour, Hong Kong has altered the adjacent environment. Higher metal contents are found in the tissue of the organisms like *Paphia* sp. (clam); *Scopimera intermedia* (crab); *Chaetomorpha brychagona* (green alga); *Enteromorpha crinita* (green alga); and *Neyraudia reynaudiana* (grass) due to release of metals associated with the tailings as soluble compounds [9].

Air pollution is considered to be the most dangerous of all forms of pollution as it has no boundaries and spreads through the atmosphere. It is produced by gases from factories, power stations and vehicle exhausts. Oxides of nitrogen and sulphur, Volatile Organic Compounds (VOCs), particulate matter etc. are some examples of air pollutants. Table 1.1 lists some of the major air pollutants with their source and their ill effects on plants and animals.

Nitrogen oxides are formed under high pressure and temperature conditions in the combustion engine of automobiles. A high level of NO_x in industrial regions is due to power plants and industrial boilers [10]. Catalytic converters in car exhaust systems break down heavier nitrogen gases, forming nitrogen dioxide (NO₂) - 300 times more potent than carbon dioxide as a greenhouse gas. NO₂ makes up about 7.2 % of the gases that cause global warming. Vehicles with catalytic converters produce nearly 50% lesser NO₂. The concentration of NO_x at the take-off condition of the aircrafts is as dense as a hundred thousand times of that of the air quality standard on the ground [11].

Table 1.1 Major air pollutants with their sources and ill effects.

Pollutant	Sources	Ill effects
CO	Incomplete combustion of carbonaceous matter in automobile engines	Anorexia
SO ₂	Combustion sulphur bearing fuels like coal, oil. Roasting of sulphide ores	Respiratory irritation, Necrosis of leaves in plants.
NO _x	Combustion of fuel in automobiles, combustion of coal, oil, natural gas in industrial units.	Causes respiratory diseases, fading of textiles. Destroys ozone layer.
VOCs and particulates	Incomplete combustion of fuels in automobile engines. Smelting and mining operations, Petroleum refineries.	Reduces visibility, respiratory illness, Corrosion of metals sculptures.
CFCs	Industrial units manufacturing refrigerants, solvents.	Destroys ozone layer.
Photochemical smog	Photochemical reaction between Hydrocarbons + oxides of nitrogen + soot.	Eye irritant.

Sulphur and nitrogen oxides pollute the environment in both wet and dry depositions. Dry depositions usually affect areas close to the source. Wet depositions turn the atmospheric water vapour to acid. They are carried thousands of kilometres away from the source by air currents. Sulphur dioxide and nitrogen oxides dissolve into clouds to form acids (pH=4.0) which fall back to earth as acid rain. This rain corrodes metal railings and stonework on buildings. Acid rain has become more of a problem for the Asian countries particularly Japan and China (China more so than Japan) who are seen as the culprits in emitting toxic gases into the atmosphere. There is excess SO₂ production due to motor vehicles and coal burning power stations. In the past 20 years, Japan has seen the deterioration of trees, particularly, pine and fir as a direct effect of

acid precipitations. Scientists have detected an unusual active growth of pine bugs which is induced by the acid [12].

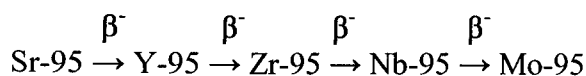
1.4 Literature survey

Environmental pollution is the collective term for deterioration of elements of environment i.e. air, water etc. as a result of man's activities. Nuclear wastes, industrial wastes, gaseous pollutants are increasing at an alarming rate and thus finding proper disposal solutions for these contaminants is the worry of the developed and developing nations.

Pyrochlore system for nuclear waste management

World is facing growing demand of energy. Nuclear energy is the safe and less polluting source if care is taken at every step and so all countries meet their energy needs using nuclear power plants. Though nuclear waste is less as compared to wastes from coal operated power plants, nuclear waste still requires safe disposal for centuries to come. The borosilicate glasses are used in confining this waste before geological disposal. However owing to devitrification and dissolution, these glasses have use for approx. 100 years in nuclear waste disposal. Crystalline materials with the pyrochlore structure having more resistance to radiation have been suggested as candidates for the immobilization of actinide species found in high-level nuclear waste (HLW) streams from the nuclear power industry and weapons decommissioning programmes. HLW includes radioactive fission products with long half-life and unspent fuel. When Uranium-235 fuel is bombarded with thermal neutrons, the nucleus undergoes fission in about 30 different modes releasing enormous energy. This energy is tapped in a nuclear power plant. The fission fragments formed have excess neutrons as compared to stable isotope and decay by beta emission till a stable nucleus is obtained. One of the fission

fragments is Strontium (Sr) which decays to stable Mo as:



The first proposed ceramic for immobilization of nuclear wastes was a polyphase titanate called Synroc, with zirconolite $\text{CaZrTi}_2\text{O}_7$ as the principal actinide host [13-15]. The resilience of these crystalline ceramics to intrinsic radiation damage and degradation by repository groundwater is likely to far exceed that of the borosilicate glasses currently employed for immobilization [16]. These pyrochlore oxides can withstand radiation and remain stable for around 30 million years [17].

The name ‘‘Pyrochlore’’ finds its origin from ‘Pyros’ meaning fire, ‘Khloros’ meaning green which is derived from the green colour obtained when pyrochlore mineral is heated. Pyrochlore Oxides are represented in general by $\text{A}_2\text{B}_2(\text{O}_1)_6(\text{O}_2)$ where, A site ions are trivalent and B site ions are tetravalent $(\text{A}^{+3})_2(\text{B}^{+4})_2(\text{O}_1)_6(\text{O}_2)$ [III, IV type] or A site ions are bivalent and B site ions are pentavalent $(\text{A}^{+2})_2(\text{B}^{+5})_2(\text{O}_1)_6(\text{O}_2)$ [II, V type]. The pyrochlore structure is a channeled structure that can be described in several different ways. The cubic pyrochlore structure belongs to the space group $\text{Fd}\bar{3}\text{m}$ that retains the FCC Lattice. In a stoichiometric pyrochlore, there are 88 atoms and 8 of the formula units of $\text{A}_2\text{B}_2(\text{O}_1)_6(\text{O}_2)$ in a full unit cell. The A cations are 8 co-ordinated and are located within scalenohedra (distorted cubes AO_8) and the smaller B cations are 6 co-ordinated and located within trigonal antiprism (distorted octahedra BO_6) [18]. There are 4 crystallographically independent atom sites (A, a rare earth ion at 16d position at $1/2 \ 1/2 \ 1/2$, B in 16c at 000, O(1) in 48f at $x \ 1/8 \ 1/8$ and O(2) in 8b at $3/8 \ 3/8 \ 3/8$). The larger A cations are co-ordinated to six O(1) atoms and two O(2) atoms forming an axially compressed scalenohedron. The smaller B cations are co-ordinated to six O (1) atoms at equal distance in trigonal antiprisms. The O (1) atoms are bonded to two A and

two B cations. The O (2) atoms are bonded only to the A cations. The ionic radius ratio of large cation to small cation and the oxygen parameter x are observed to be crucial factors in deciding the stability of the pyrochlore structure [19]. Oxygen parameter x indicates the extent to which the 48f oxygen ion is off centered, and is sensitive to the sizes and size differences between constituent A and B ions [20]. Theoretically x ranges between 0.375 and 0.4375. Ideal value of $x = 0.375$, where there is perfect cubic array of 48f oxygen ions and A cations are located in a perfect cubic 8 fold co-ordination. When x reaches the upper limit, the B cations are in perfect octahedral co-ordination. This description refers to an ideal pyrochlore. All real pyrochlore compounds exhibit some disorder [21]. In another description, the oxide pyrochlore structure is explained based on ordered anion deficient fluorite structure or alternatively in terms of BO_6 octahedra linked through all vertices. The A type of cations have distorted (6+2) co-ordination to oxygen. In this polyhedral description, one oxygen denoted by O (2) in the crystallographic description does not form a part of the BO_6 framework interacting solely with the A type of cations [22]. All the oxygen ions lie within a tetrahedron of nearest neighbour cations as is characteristic of the fluorite structure [23]. Another description of the pyrochlore structure is, it is a super structure derivative of the simple fluorite structure ($\text{BO}_2 = \text{B}_4\text{O}_8$). In the fluorite structure (BO_2), B cations occupy face centered cubic sites and O is located in the tetrahedral sites. When this oxide is doped with aliovalent cations A^{+3} , oxygen vacancies are generated to maintain charge balance. When A/B mole ratio becomes 1, one out of 8 oxygen sites get vacant. In fluorite, A and B cations are in 100% disorder and oxygen atoms are evenly distributed to all the tetrahedral sites formed by the cations [24].

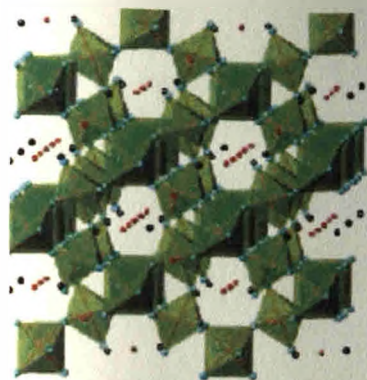


Figure 1.2 The pyrochlore structure (BO₆ octahedra shaded in green, A cations in red, black are non-framework oxygen (R.I. Walton, *Progress in crystal growth and characterization of materials*, 57(2011) 93-108.

[II, V] type Pyrochlore Oxides $A_2B_2O_7$ have remarkable physical properties like Ferroelectricity ($Cd_2Nb_2O_7$) [25], electronic and magnetic properties ($Cd_2Re_2O_7$) [26], $R_2Ir_2O_7$ ($R = Y, Sm, Eu$ and Lu) [27]. Pyrochlore oxides of [III, IV] type show exciting properties like frustrated magnetism ($R_2TM_2O_7$ where $R =$ rare earth metal and $TM =$ transition metal) [28]. Catalytic properties are shown by $Ln_2Ti_2O_7$ (where $Ln = Y, Sm, Gd$ and Tb) [29] and Calcium doped Lanthanum Zirconate [30]. Zirconate pyrochlores of rare earth metals have low thermal conductivity hence find use as thermal barrier coatings for gas turbine engine applications [31]. Pyrochlore oxides [III, IV] with Ti/Zr at the B site are used for nuclear waste disposal studies. In the present study, rare earth [III, IV] pyrochlore oxides with Nd^{+3} at the A site and Zr^{+4}/Ti^{+4} at the B site are focused. Pyrochlore oxides with zirconium and titanium at the 'B' site are also good ionic conductors besides being radiation resistant and hence find use in solid oxide fuel cells in high radiation environment [32], disposal of nuclear wastes [33], and as oxygen sensors [34]. The use of pyrochlores in radioactive waste disposal is an outcome of the intensive research done to find alternative hosts in the form of ceramic matrix for

nuclear waste forms around 1970s by Ringwood and co-workers. The ceramic matrix is chosen because of its high thermodynamic stability for a long time [35]. A material called Synroc – an advanced ceramic composed of pyrochlore phases such as titanates was the first synthetic pyrochlore developed in 1979 by late Professor Ted Ringwood, a mineralogist at the Australian National University. Pyrochlores readily accommodate radioactive actinides and are vulnerable to the effects of radioactive alpha decay which gradually destroys the crystalline structure by producing numerous atomic defects in the lattice structure. Titanate pyrochlores are of more interest for use in nuclear waste disposal because of their chemical durability and low aqueous solubility [36-37]. However titanates experience a radiation induced transition from crystalline to a periodic state due to radiation damage from the alpha decay of actinides. Recent ion beam irradiation has shown that zirconates remain crystalline as a defect fluorite structure [38]. The transformation to fluorite structure is caused by the disordering between cations and between oxygen and oxygen vacancies [36]. When radioactive atoms are put into such lattices, the radioactive emissions jostle the atoms out of their carefully ordered arrangement which makes the material unstable and thus prone to cracking, swelling or structural change, the process referred to as amorphisation. Studies indicate radiation-induced order-disorder transformation occurring in many $A_2B_2O_7$ pyrochlore structure-types through disordering of the A- and B-site cations, as well as anion vacancies. This order-disorder transformation increases the ionic conductivity [39-40]. The studies also suggest that anion disorder precedes cation disordering in the pyrochlore structure [41] and the ordered pyrochlore superstructure transforms to a cation disordered defect fluorite structure type. The cation disordering occurs by cation antisite formation [42]. In a cation antisite pyrochlore unit cell, part of the A cations occupy the B site and vice versa. i. e. swapping of the position of one

cation (A or B) for that of other takes place. Contour maps produced by plotting the various A^{+3} atomic radii against B^{+4} atomic radii, suggest that the pyrochlore oxides in which the A and B cation radii are closely similar, have low energies for cation defect formation [43]. These compounds are more tolerant to radiation.

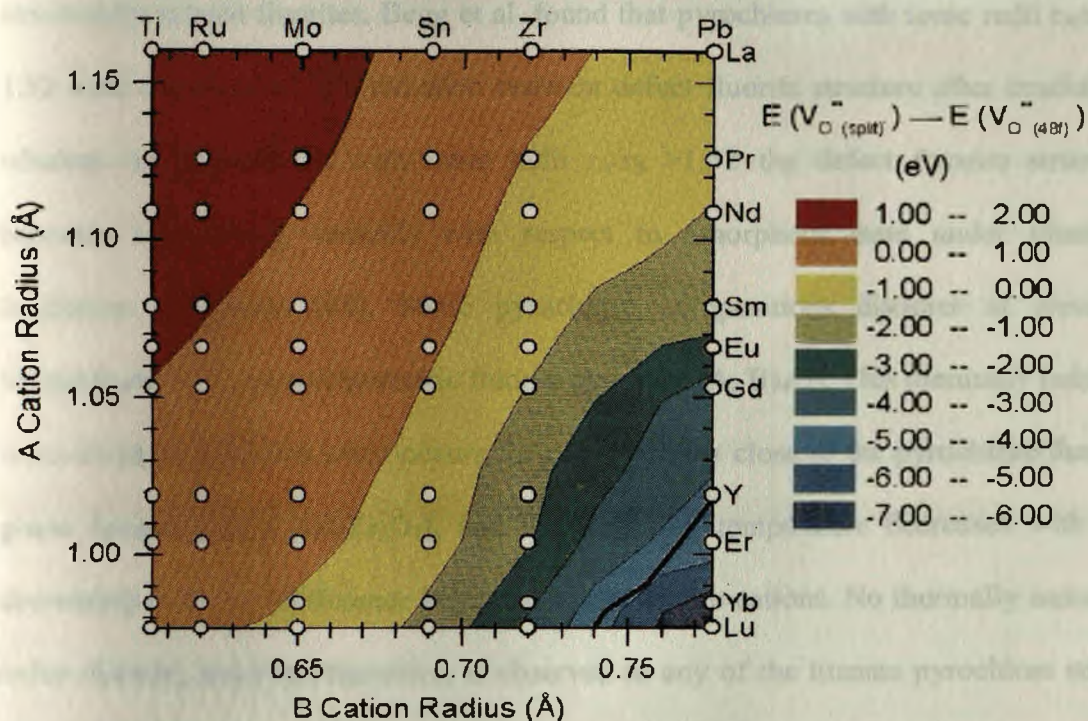


Figure 1.3 Contour plots of A^{+3} atomic radii against B^{+4} atomic radii (M. Pirzada et. Al, *Solid State Ionics* 140(2001) 201-208).

Systematic ion irradiation studies of $Ln_2B_2O_7$ (with $B = Ti, Zr$ and Sn) have indicated that the radiation response of pyrochlore compounds is highly dependent on compositional change [44]. The radiation tolerance is promoted by an increase in the Pauling cation-anion electronegativity difference [45]. Ordered pyrochlore to disordered defect fluorite transformation in $Gd_2Zr_2O_7$ takes place also on application of high pressure. At pressures still higher, a high-pressure phase having distorted defect-fluorite-structure of lower symmetry is formed which gradually transforms back to the cubic defect-fluorite structure [46].

A structural transition study of $^{241}\text{Am}_2\text{Zr}_2\text{O}_7$ from pyrochlore to defect fluorite further support the transition through oxygen frenkel and cation antisite formation and reveal that the ZrO polyhedron is stable against irradiation [47]. It was noted by some researchers that the most radiation tolerant compounds are not pyrochlores but closely structurally related fluorites. Begg et al. found that pyrochlores with ionic radii $r_A/r_B \leq 1.52$ were transformed into radiation resistant defect fluorite structure after irradiation whereas for pyrochlores with ionic radii $r_A/r_B > 1.52$ the defect fluorite structure becomes increasingly unstable with respect to amorphous state under identical irradiation conditions [48]. Some pyrochlore compositions disorder at elevated temperatures to a nonstoichiometric fluorite structure $(A, B)_4\text{O}_7$. This thermally induced order-disorder transition often occurs for compositions close to the pyrochlore/fluorite phase boundary (e.g. $\text{Gd}_2\text{Zr}_2\text{O}_7$), and the transition temperature decreases with the decreasing ionic size difference between A- and B-site cations. No thermally induced, order-disorder structural transition is observed in any of the titanate pyrochlore series due to the strong tendency for structural ordering on the A- and B-sites [49].

When Titanate pyrochlores are doped with zirconium ion at the B site, many interesting features are observed in the series $\text{Gd}_2(\text{Ti}_{2-x}\text{Zr}_x)\text{O}_7$, one of which is radiation resistance. $\text{Gd}_2\text{Ti}_2\text{O}_7$ is readily amorphisable and $\text{Gd}_2\text{Zr}_2\text{O}_7$ is extremely resistant to amorphisation. The system $\text{Gd}_2(\text{Ti}_{2-x}\text{Zr}_x)\text{O}_7$ shows increase in radiation resistance with the substitution of Zr for Ti until the end member $\text{Gd}_2\text{Zr}_2\text{O}_7$ cannot be amorphised [50]. In $\text{Gd}_2(\text{Ti}_{1-x}\text{Zr}_x)_2\text{O}_7$ solid solutions, doping 25 mol% of Ti with Zr to form $\text{Gd}_2(\text{Ti}_{1-x}\text{Zr}_x)_2\text{O}_7$ ($0.25 < x \leq 0.75$) shows disordering on the anion and cation lattices as characterized by XPS which is responsible for an increase in ionic conductivity [34]. Heremans et al. studied $\text{Y}_2(\text{Ti}_{1-x}\text{Zr}_x)_2\text{O}_7$ using neutron diffraction and found that cation and anion disordering

occurs separately which gives rise to a non-stoichiometric fluorite structure. There is resultant rise in ionic conductivity in the system with increase in Zr content [51]. In the solid solution system $Y_2(Zr_yTi_{1-y})_2O_7$, ($0 \leq y \leq 0.9$) a clear two-phase region is established. A pyrochlore-type solid solution field at ($0 \leq y \leq \sim 0.54$) and a “defect fluorite” type solid solution field at ($\sim 0.68 \leq y \leq 1$) has been found [52]. Moreno et al. studied $Dy_2(Ti_{1-y}Zr_y)_2O_7$ ($y = 0.55$ and 0.90) system and pointed out that mechanical milling synthesis introduces significant disorder in the system, which is supported by an increase in ionic conductivity [53].

Doping pyrochlore $Nd_2Zr_2O_7$ with Gd at the A site, increases the structural disorder and the conductivity increases by almost an order of magnitude over that of $Gd_2Zr_2O_7$ at 1:1 concentration at 696K [54]. The rise in conductivity in the system is an indication of the oxygen disorder prevailing in the lattice structure because the conductivity in the pyrochlore lattice arises due to intrinsic frenkel disorder. Neutron diffraction studies reveal that a typical pyrochlore like $Nd_2Zr_2O_7$ has around 5% frenkel defects in the oxide ion sub lattice at 673K [55]. Due to intrinsic frenkel disorder some oxide ions leave their lattice sites and occupy interstitial positions. The degree of ordering in the oxide ion sublattice is decided by the cation radius ratio. The ordered arrangement of the lattice provides low energy pathway for oxide ion migration. This results in a decrease in activation energy but the number of mobile ions remain small due to orderliness in the crystal lattice. A change in composition or high temperature treatments can result in cation disordering which brings about an increase in the number of frenkel defects at the oxygen sites [56]. The increase in ionic conductivity in Zr-Ti pyrochlores on increased addition of Zr is matched by a decrease in electronic conductivity associated with narrowing of the Ti 3d band. However the maximum electronic conductivity even at high Ti content is limited by the low electron mobility

[57]. The diffusion mechanism observed in pyrochlore oxides is an oxygen ion 48f vacancy hopping mechanism [23].

In the system under investigation the starting member of the series, neodymium zirconate is cubic pyrochlore whereas the end member neodymium titanate is monoclinic. There is limited solubility of $\text{Nd}_2\text{Ti}_2\text{O}_7$ in $\text{Nd}_2\text{Zr}_2\text{O}_7$. Exsolution of a monoclinic phase ($P2_1$, $Z=8$) rich in $\text{Nd}_2\text{Ti}_2\text{O}_7$ is observed at approximately $x=0.56$ in $\text{Nd}_2(\text{Zr}_{1-x}\text{Ti}_x)_2\text{O}_7$ [58]. $\text{Nd}_2\text{Zr}_2\text{O}_7$ have peculiarity in that it transforms into fluorite category defective structure on irradiation and the resulting defect fluorite structure is resistant to further amorphization[49], thus making it very suitable for nuclear waste disposal. Studies done on radiation stability of $\text{Nd}_2\text{Zr}_2\text{O}_7$ irradiated with 300 KeV Ar^+ ions at fluences ranging from 1×10^{16} to 5×10^{17} ion/cm² indicate its resistance to amorphization, however swapping of the ions is observed [59].

$\text{Nd}_2\text{Zr}_2\text{O}_7$ has been extensively studied for its low thermal conductivity. Its thermal conductivity is lower than ZrO_2 stabilized in its cubic structure and thus can be used as inert matrix for minor actinide transmutation in composite form [60-61]. Insolubility in aqueous media and resistance to radiation makes $\text{Nd}_2\text{Zr}_2\text{O}_7$ a suitable candidate in the composite form [62]. $\text{Nd}_2\text{Zr}_2\text{O}_7$ composite with MgO is replacing MOX (mixed oxides) ($\text{MOX PuO}_2/\text{UO}_2$) fuel as during reactor operation, MgO- $\text{Nd}_2\text{Zr}_2\text{O}_7$ composite (PuO_2/UO_2) fuel controls plutonium production through neutron capture [63-64]. Studies by other researchers have indicated that the uniformity in the microstructure and thermal conductivity of the MgO- $\text{Nd}_2\text{Zr}_2\text{O}_7$ composites vary with the methods of processing [65] and ball milling produces the most homogeneous and consistent microstructures in the composite materials [66]. Work on reprocessing of MgO- $\text{Nd}_2\text{Zr}_2\text{O}_7$ composites as inert matrix material has also been done by studying their

dissolution in acid solutions [67]. Transparent neodymium zirconate $\text{Nd}_2\text{Zr}_2\text{O}_7$ ceramics fabricated from nanoparticles prepared by combustion synthesis show wider absorption bands than those of Nd doped $\text{Y}_3\text{Al}_5\text{O}_{12}$ (Nd:YAG) facilitating pumping over a broader range of wavelengths in laser applications [68].

Zinc oxide system

The growing population of the world and the increased standard of living has resulted in environmental issues. Hence the need is to use environment friendly materials. One such compound is ZnO which finds applications in many environmental friendly commercial products. Zinc oxide or philosopher's wool, (ZnO) is the most important zinc compound obtained by burning zinc metal in air or by heating zinc carbonate, hydroxide or nitrate. Zinc oxide is an amphoteric oxide and dissolves in both acids and alkalies. The compound sublimes at 673K. It is almost insoluble in water. ZnO is a constituent of many important commercially available commodities. Table 1.2 below gives various applications of ZnO.

Table 1.2 Some common applications of ZnO

Industry	Uses	Reference
Preservation of plantation latex.	Reacts with the enzymes responsible for the decomposition.	Nav Bharat Metallic Oxide Industries Pvt. Limited.
Vulcanization of rubber.	Acts as an effective stabilizer of rubber compounds.	Porter, F. Zinc Handbook: Properties, Processing, and Use in Design.(1991) CRC Press.
Cosmetic industry.	Ability to absorb the ultraviolet sunburn rays.	U.S. Food and Drug Administration. Mitchnick, MA; Fairhurst, D; Pinnell, SR (1999). "Microfine zinc oxide (Z-cote) as a photostable UVA/UVB sunblock agent." Journal of the American Academy of Dermatology 40: 85–90.

Zinc Oxide paints	Provide excellent protection to steel structures. Does not get darkened with age.	Bishop and Locket, (1960) An Introduction to Chemistry Oxford at the Clarendon press 2 Ed 261-262
Paints and pigments	Acts as a binder	H. A. Gardner, Natl Paint Varnish and Lacquer Assoc. inc, circulars 443(1933), 448(1934), 464(1934), 475(1935), 526(1937), 558(1928).
Glass	Reduces the coefficient of thermal expansion, imparts high brilliance and luster and high stability against deformation under stress	
Heavy-duty pneumatic tyres	For heat conductivity as well as reinforcement since heat-buildup is critical at their higher operating speeds compared with their solid-rubber counterparts.	Nav Bharat Metallic Oxide Industries Pvt. Limited.
Cigarette filters.	Removal of selected ingredients from tobacco smoke.	Nav Bharat Metallic Oxide Industries Pvt. Limited.
The processing and packaging of food products.	Special fungi-static and chemical properties.	Nav Bharat Metallic Oxide Industries Pvt. Limited.
Varnish linings of the metal containers	Prevent formation of black sulphides which discolour the food.	Nav Bharat Metallic Oxide Industries Pvt. Limited.
Portland cement	Retardation of setting and hardening (to reduce the rate of heat evolution), improvement in whiteness and final strength.	www. Surendra Oxides Pvt. Ltd.com

Besides these applications, ZnO is an active component of electronic products like LEDs [69], field emitters [70], transistors [71], nanorod sensors [72-73].

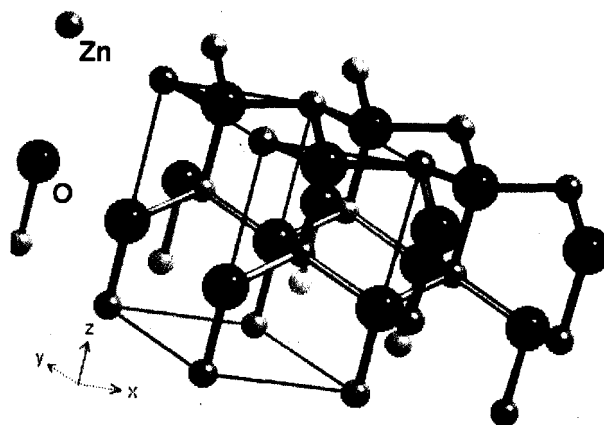
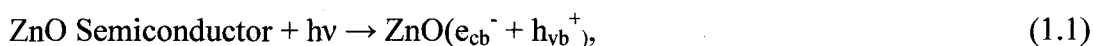


Figure1.4 Structure of ZnO(Wurtzite)[<http://vagabondguru.com/blog-mt/mt.tb.fcgi/309>].

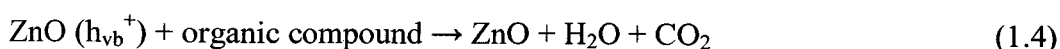
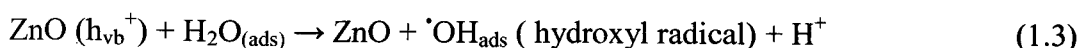
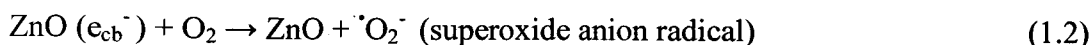
ZnO crystallizes with wurtzite structure which is formed by hexagonal close packing of anions wherein cations occupy the alternate tetrahedral voids. The typical values of lattice parameters of zinc oxide are, $a = 3.2494 \text{ \AA}$, $c = 5.2069 \text{ \AA}$, $c/a = 1.602$. On heating, the colour of ZnO changes to yellow due to the loss of oxygen from the lattice to give a non-stoichiometric phase. Such non-stoichiometric oxygen deficient zinc oxides are n-type semiconductors. ZnO with such defects can be activated by both UV and visible light. In the presence of light, electron-hole pairs are produced in the conduction band and in the valence band respectively. These electrons and holes undergo charge transfer reactions across the interface with oxygen, water or organic compounds adsorbed on ZnO surface. The reaction of hole with OH^- or water leads to the generation of reactive Hydroxyl radicals ($\cdot\text{OH}$) which are powerful oxidants [74].



Where e_{cb}^- = electrons in the conduction band (cb)

h_{vb}^+ = holes in the valence band (vb)

Then the following series of reactions are possible



These hydroxyl radicals and superoxide radicals are strong oxidising agents and degrade organic compounds to CO_2 and water [75]. It is this reaction of hydroxide radicals with organic compounds degrading them to simple products in presence of light is referred to as photocatalysis. The significant discovery of splitting of water by titania (TiO_2), under irradiation by Fujishima and Honda in the early 1970's has opened up this field of photocatalysis [76]. But the work carried out further on oxidation ability of TiO_2 under irradiation turned out to be incredible in sterilization, deodourization and decontamination of the environmental pollutants [77]. Thus focus is now on advanced oxidation processes using semiconductor oxides for oxidation of organic compounds. ZnO is a widely used semiconductor photocatalyst after TiO_2 anatase. Owing to the structure and properties of ZnO, it finds application in abatement of environmental pollutants. The greatest advantage of ZnO is that it absorbs large fraction of the solar spectrum and more light quanta than TiO_2 [78]. The efficiency of ZnO in photo degradation has been extensively investigated as a photocatalyst in degradation of organic dyes [74, 79-88], pesticides [89], phenol [90]. Most of the investigations are studied in UV light. The use of high-energy UV light is not only costly but also hazardous [91]. Also the scope of using the ideal source of energy that bountiful in the form of sunlight is limited as it has a smaller amount of UV radiations. Hence researchers are striving hard to exploit the visible light in photocatalysis by modifying

the material properties through cation or anion doping and introducing oxygen deficiency. In the process of photocatalysis, the photons with energies matching or exceeding the band-gap of a semiconductor catalyst can promote electrons jumping from valence band to the conduction band and leaving holes behind. However high rate of recombination of photogenerated electrons and holes is a major factor limiting the photocatalytic efficiency [92]. Doping zinc oxide with metals and/or non-metals also creates quasi-stable energy states within the band gap (surface defects). Increased electron trapping due to higher defect sites leads to enhancement in the photocatalytic efficiency by delaying the electron-hole pair recombination. There are reports on the enhancement of visible light absorption in ZnO by doping it with Cobalt (Co)[93], Manganese (Mn) [94], Lead (Pb) and Silver (Ag) [95], Vanadium [96], Magnesium [97], Aluminium [98], Lanthanum [99] etc. and non-metals such as Sulphur [100-101], Nitrogen [102-103], Carbon [104], Iodine [105].

Degradation of Dyes

Dyes are the major environmental pollutants and water contaminants. Various organic dyes released in the aquatic ecosystems are a source of non-aesthetic pollution, eutrophication and other perturbations in the aquatic life [74]. Reports say that 15% of the total world production of dyes is lost during dyeing process as it is not fixed on the fabric. It is released as textile effluent which eventually pollutes the ground water [106]. Among the different dyes, methylene blue (MB), a member of thiazine class of dyes is difficult to be decomposed under visible light and is usually regarded as a model dye contaminant to evaluate the activity of a photocatalyst [106]. The photodegradation of organic dyes is usually carried out using UV radiation in the range of 200nm. An enhancement in the rate of degradation is observed in presence of oxidants like H_2O_2 due to formation of very reactive hydroxyl radicals. An excess of oxidants added in the

treatment solution can interfere with the process [107]

The photocatalytic degradation of organics proceeds through a series of steps i.e.

i) Generation of charge carriers like electron and hole on the surface of the photocatalyst under sunlight illumination, ii) transfer of charge carriers to adsorbed reactants on the photocatalyst to initiate a series of bond breaking and bond forming steps. The ultimate products of the degradation are likely to be CO₂ and H₂O. Other elements like N, S are oxidized to NH₄⁺ or NO₃⁻ and SO₄⁻² respectively [108]. Many researchers have tried to predict mechanism of dye degradation based on their observations [109 -111]. The photodegradation reaction of MB is given as [112]:



The oxidative photodegradation of a dye involves several intermediates and identification of all of them becomes difficult due to very low concentrations and many of them cannot be detected because of their poor extractability in the organic medium. Gnaser et al. have proposed formation of Leuco methylene blue, sulfoxide and sulfone intermediates in degradation of MB dye on nano crystalline TiO₂ films irradiated with UV followed by investigation using mass spectrometry. A detailed degradation pathway of MB is given by Houas et al. after identification of intermediates and mineralization products CO₂ and H₂O, NH₄⁺, NO₃⁻ and SO₄⁻² in the TiO₂/UV photodegradation of MB. ZnO when used as a photocatalyst however undergoes photocorrosion through self-oxidation. ZnO powder dissolves with decrease in pH as per the reaction:



In strongly alkaline environment, ZnO can undergo dissolution according to the equation [89]:



Antibacterial properties of ZnO

Another environmental friendly use of ZnO is due to its antibacterial action. ZnO is found to strongly resist growth of micro-organisms. Antibacterial effects of ZnO powders [113], nano ZnO powders [114-115], ZnO based polymer films [116-117] are reported in literature. Fabrics with ZnO are also tested for antibacterial activity [118]. The advantage of using these inorganic oxides as anti-microbial agents is that they contain mineral elements essential to humans and exhibit strong activity even when administered in small amounts. They also show superior durability, less toxicity, greater selectivity and heat resistance. The antibacterial activity of ZnO is attributed to the generation of reactive oxygen species like hydroxyl radicals and superoxide radicals on the surface of these oxides as studied by conductometric method. The hydroxyl radicals and superoxide radicals are negatively charged particles hence remain in direct contact with the outer surface of the bacteria. These reactive oxygen species generate H_2O_2 which penetrates and kills the bacterial cell [119-120]. The hydrogen peroxide inside the cell can be activated by ferrous ion via the Fenton reaction.



The ability of bacteria such as *E. coli*, to sequester iron is reported. Iron levels on the cell surface, in the periplasmic space or inside the cell, either as iron clusters or in iron storage proteins (such as ferritin) are significant and can serve as a source of ferrous ion. As ZnO produces H_2O_2 on illumination, there is simultaneous production of hydroxide radicals in the cell via Fenton reaction [121]. The activity of ZnO is affected by its particle size [122-124]. The reason for strong antibacterial activity of ZnO with small particle size was explained by Yamamoto as follows: the contact of moisture in the medium per unit ZnO mass increases with the decrease in particle size, because of the increase of specific surface area. This results in the increased H_2O_2 generation from

its surface [125]. Some reports however indicate no effect of particle size on the toxicity of ZnO [126]. It is also commented that the antibacterial effect of ZnO may be because of abrasive surface texture of ZnO arising due to surface defects. This surface roughness contributes to mechanical damage of the cell membrane of *E. coli*. Akhavan et al. observed that ZnO with defects show excellent UV induced photocatalytic degradation of *E. coli* due to surface OH bonds [127]. ZnO may distort and damage the bacterial cell membrane resulting in leakage of intracellular contents and eventually the death of bacterial cells [128]. ZnO suspensions in the lower concentration range seem to exhibit less antimicrobial property. This might be due to Zn^{+2} ions acting as a nutrient [123]. When the level of Zn crosses the essential threshold, it inhibits bacterial enzymes including dehydrogenase and certain protective enzymes, such as thiolperoxidase, and glutathione reductase. Zn inhibition of NADH oxidase is proposed to impede the respiratory chain of *E. coli*. Additionally, loss of membrane potential is associated with inhibition by Zn ions at cytochrome c oxidase in *Rhodobacter sphaeroides* [129].

Abatement of NO_x

Industrial revolution in a country increases its Gross Domestic Product (GDP) and also pollution in the atmosphere. Laws are framed to minimize the gases responsible for greenhouse effect and global warming viz. NO_x, SO_x. Although the use of low NO_x burners and selective catalytic/non-catalytic reduction are the most popular techniques for NO_x removal, photocatalytic oxidation using metal oxides is an attractive approach to reduce them to simple environment friendly gases. Nitric oxide (NO) and nitrogen dioxide (NO₂) are collectively referred to as NO_x. Currently about one half of all NO_x emissions into the environment are due to power plants and industrial boilers. NO_x gas, the precursor to nitric and nitrous acids, causes acid rain and photochemical smog. NO_x is formed in all combustion processes from the high temperature reaction between N₂

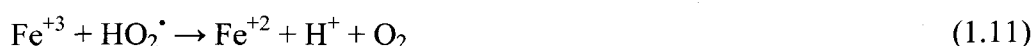
and O_2 . To date, a number of researchers have investigated the dynamics of the photocatalytic removal of nitrogen oxides. Some of the NO_x control methodology is to reduce NO_x back to N_2 [130]. Another approach is to oxidize NO to NO_2 and HNO_3 along the general direction of nitrogen fixation by using the concept of photocatalysis. Photocatalytic oxidation (PCO) of NO_x offers the advantages like (i) no extra reactants required and (ii) NO_x recycled or recovered as nitric acid, a potential raw material for fertilizers [131]. Removal of NO_x by photocatalysis using TiO_2 Degussa P25 powder [132], $TiO_{2-x}N_y$ [133] powders is reported in literature. The degradation of NO_x compounds employing commercial concrete paving stones with TiO_2 in road construction is studied theoretically [134] and it has been practically applied in the abatement of NO_x on a large scale by coating TiO_2 on roads, pavements, structures causing successful removal of oxides of nitrogen at street level to around 60% of NO in Milan, Italy. More recently, Westminster borough of London cooperated with Mitsubishi Materials Corporation to pave roads with TiO_2 - containing paving stone (NOXER), under an intensity of UV light of 12 W/m^2 , an 80% NO_x removal rate was achieved [135].

Iron ore tailings

With industrialization, there is growing demand for various metals. The ores are mined and processed to get high grade metals. Goa and Karnataka have resources rich in iron ore. The iron mine industry caters high-grade ore for the domestic steel industry requirements and also for export. The highly mechanized industry discards the low-grade ore and tailings at the mining areas that are not only creating environmental problem, but are the national wastes [136]. The low grade ore is the material remaining after beneficiation of the ore and is referred to as iron ore tailing/reject. These tailings

are stored in the tailing ponds/pits developed during mining which eventually get washed away during rains in fields and seas and alter the adjacent environment [137]. Thus the management of tailings from iron ore mines is an important issue, from the point of view not only of pollution control but also of the conservation of resources [138]. These rejects contain iron concentrations of 45% or more which can be utilized for any other purpose. And, considering deteriorating mineral resources, it is high time that one should look into the low-grade ores to add value to them. The iron ore industry is the main industry of mining in Goa. It also forms the backbone of Goan economy. In 1996-97 the total mineral ore produced in Goa was 137.37 lakh tons, of which iron ore was 136.43 lakh tons. In the recent years 2002-2007 the Goa's iron ore exports have touched almost 40 million tons per year [139]. The generated rejects are a source of aesthetic pollution, road accidents by trucks carrying the ore and silting of streams of water in nearby villages of Goa where they are dumped. Worldwide efforts to utilize these wastes in cements, glasses and construction materials [140-143] consider tailing as waste mud and the fine iron oxide present (~50%) is not used as technically important material. In our research group [144-148] modest efforts have been made to use these ore rejects to synthesize active pure iron oxides and from these ferrites to see the suitability of such iron oxide sources in ferrite industry, after chemical beneficiation. Literature reports say that ores find applications in decomposition of H_2O_2 in the aqueous medium and oxidation of dyes. De souza et al. [149] used limonite ore (natural ore of hydrated iron (III) oxides, mostly goethite $[FeOOH]$), in decomposition of H_2O_2 in aqueous medium and oxidize dyes like methylene blue using a Fenton like system combining H_2O_2 and an organic acid with the ore. Pelagite an autogenic manganese ore in deep sea bed consisting of oxides and hydroxides of manganese i.e. amorphous MnO_2 and $MnOOH$ and iron is used for degradation and

decolourization of methyl orange within 120 minutes through photocatalysis [150]. Natural manganese ore is also used as an adsorbent for degradation of phenol [151] and dyes [152]. In the literature survey, no reports are found regarding the use of tailing materials in degradation. During beneficiation the ore is processed to fine powder so no extra energy is required for this process and the rejects can be directly used for the degradation making the process cost effective. Using ore rejects for degradation of organic wastes helps in dual process, (i) removal of dye effluents, and (ii) avoiding local ecosystems getting contaminated by ore rejects. An added advantage of using ore reject for degradation of organic wastes is that, being a water pollutant it can curb the other pollutant in the water body i. e. organic effluents. Degradation of organic wastes by iron salts usually proceeds by Fenton Mechanism. The high efficiency of this process is traditionally thought to be due to the generation of hydroxyl radical ($\cdot\text{OH}$), which is of a high oxidation potential ($E^0 = 2.80 \text{ V}$) and can mineralize the organic compounds completely to water and carbon dioxide. In acidic medium, this radical mechanism can be simply described by the following equations:



The combination of Fenton reaction with UV (Ultraviolet) light, the so-called photo-Fenton reaction, enhances the efficiency of the Fenton process.



The Fenton degradation of organic compounds by iron salts have been used on various substrates like phenol [153], Rhodamine B (an acid dye of Xanthene series) [154], coking waste waters [155], effluent wastes [156-157] etc. Significance of Fenton reaction is that it continuously goes on in the eukaryotic cells. Eukaryotic cells continuously produce reactive oxygen intermediates (ROIs) as a side product of

electron transfer. The most dangerous among all ROI species is hydroxyl radical and it arises as a product of the reaction between superoxide and H_2O_2 . The reaction is catalysed by Fe^{+2}



This Fenton Reaction catalysed by iron is thus responsible for the multiplication of free radicals in the cells.

Synthetic methods for oxides

World's energy resources are dwindling and hence any synthetic process involving heat energy needs to be relooked in to newer way for conserving the same. Besides, the gases and effluents released during synthesis have to be monitored from environmental perspective. Synthetic methods used in the preparation of oxides are classified according to whether they involve solid state reactions, solutions, gel formation or vapour phase processes. Mixed metal oxides like pyrochlore oxides are traditionally synthesized by solid state methods [20, 22, 35, 158] using high-temperature reactions that often require several days of heating period because solid diffusion is the rate-limiting step in their formation by solid state route. The resulting oxides are of large grain size, extensively agglomerated with reduction in surface area due to firing at high temperature and poor chemical homogeneity with formation of multiphase powders [159]. Such methods cannot be used in synthesis of oxides to be used in applications involving small and uniform particle sizes. Alternative methods of synthesis of pyrochlore oxides at low temperatures are co-precipitation [160], hydrothermal synthesis [159,161], sol-gel process [162-164] etc. Co-precipitation is one of the oldest techniques for the preparation of oxides wherein aqueous solutions of desired cations

are mixed with precipitating agent in solution form. The main merit of this method is that the salts are homogeneously mixed in the course of precipitation. Various parameters such as pH, mixing rates, temperature and concentration need to be controlled to get the desired product. Co-precipitated metal complexes of various carboxylic acids have attracted the specific attention of many researches for a long time due to their overwhelming practical applications in science and technology. Co-precipitation by using oxalic acid and modification of the precursor using hydrazine is also reported [148,165]. High-quality ceramic powders are synthesised by the hydrothermal synthetic route which has advantages of yielding highly-crystallized powders [166] with small particle sizes. The temperatures of the reaction are also low [159]. Sol-gel process involving formation of an amorphous gel usually using citric acid, followed by calcination at relatively low temperatures is used to obtain single phase compound during the synthesis of many technologically important compounds. Rare earth doped zirconia $(\text{ZrO}_2)_{0.85}(\text{REO}_{1.5})_{0.15}$ (RE = Y, Sc) solid solutions in pure cubic fluorite structure was obtained at the temperature of 1073K [167], ternary oxide, $\text{Sn}_{0.2}\text{Zr}_{0.8}\text{TiO}_4$ was synthesized at 873K compared to conventional ceramic method at 1173K [168], $\text{La}_{0.7}\text{Sr}_{0.3}\text{MnO}_3$ was synthesized at 1073K [169], homogeneous and fine powder of $\text{Bi}_2\text{Sr}_2\text{CaCu}_2\text{O}_8$ superconductor with sharp transition temperature was obtained at 1073K [170]. Homogeneous and single phase $\text{Bi}_2\text{Ru}_2\text{O}_7$ Pyrochlore Oxide [171], $\text{La}_{1.9}\text{Ca}_{0.1}\text{Zr}_2\text{O}_{6.95}$ for catalytic use in synthesis of ammonia [172], Bismuth zinc niobate pyrochlores $\text{Bi}_{1.5}\text{ZnNb}_{1.5}\text{O}_7$ (α -BZN), and $\text{Bi}_2(\text{Zn}_{1/3}\text{Nb}_{2/3})_2\text{O}_7$ (β -BZN) phases were obtained by sol gel method at 973K [173]. By citrate gel method the required phase is obtained at relatively low calcination temperatures which improves the chemical homogeneity, nanoparticle size uniformity and crystallinity, sinterability and electrical conductivity [167] of the resulting oxides. The reaction takes place in

aqueous solution and no special atmospheres are needed [173]. Pechini gel method similar to sol gel [174] uses the metal-organic compounds in citric acid and ethylene glycol solutions. Drying the mixture followed by heating at 973K and further calcination provides oxide with a desired phase.

Simple metal oxides like ZnO are synthesized by green methods such as, microwave technique [175], porous starch (PS), citric acid-modified PS (CAPS) ZnO [176] apart from conventional routes of synthesis. Metal salts are the easily available precursors for the synthesis of metal oxides. When co-precipitation technique is followed, choice for the precipitating agents is numerous, such as carboxylic acids to precipitate out metal carboxylates, ammonia for metal hydroxide precipitation etc. On the large scale if metal salts such as metal chlorides, M_xCl_y , metal sulfates, $M_x(SO_4)_y$ and metal nitrates, $M_x(NO_3)_y$ are thermally decomposed there will be plenty of corrosive and obnoxious gases like chlorine Cl_2 , sulfur oxides SO_x and nitrogen oxides, NO_x released to the atmosphere. The environmental conscious society now has to find some way to minimize the release of such undesirable gases. At the same time synthetic process involving heat energy needs to be relooked into newer way for conserving the energy. Our research group has been always cautious of these aspects of conservation of energy and minimization of environmental pollution burden and in our pot synthesis through precipitation followed by thermal decomposition of metal oxide precursors such as carboxylates, hydroxides we have been modifying the precursors by a novel hydrazine method. Hydrazine not only acts as a fuel but also takes part as a ligand in altering the precursor composition and also thermal path resulting into thermal product at much lower temperatures as compared to the ordinary precursors. Other advantages of using hydrazinated precursors over others are i) Very low ignition temperature, ii) Autocatalytic decomposition once ignited, iii) Evolution of gases like NH_3 , H_2O , CO_2 ,

N_2 and iv) Formation of ultrafine oxide materials having large surface area [177]. Hydrazine method of synthesis had been adopted in our earlier studies in the preparation of $\gamma\text{-Fe}_2\text{O}_3$ [148], $\text{MnZnFe}_2\text{O}_4$, LaAlO_3 , $\text{La}(\text{Sr})\text{AlO}_3$, $\text{La}(\text{Sr})\text{MnO}_3$ [165]. Metal precursors modified with hydrazine are found to decompose at lower temperatures than those without such modifications [178]. Another merit of these hydrazine assisted syntheses is the introduction of nitrogen in the lattice of prepared oxides.

Synthetic strategy for $\text{ZnO}_{1-x}\text{N}_x$

It is stated in the literature that doping semiconductor oxides with metals and nonmetals helps in increasing the absorption in the visible range. Among the various heteroatoms, N is widely used dopant, because of its compatible size and electron affinity to O and the fact that it has the smallest ionization energy. The N doping either decreases the band gap by mixing of N 2p states with O 2p states on the top of the valence band or creates N induced mid-gap level. Various synthetic methods are reported for doping TiO_2 by nitrogen, one of which is hydrazine method [178]. The problem with nitrogen doping in ZnO arises due to poor nitrogen solubility in ZnO. Also the formation of Zn-O is energetically more favourable than the formation of Zn-N bonds [104].

The pot synthesis of N doped ZnO using carboxylic acids and hydrazine may lead to agglomerated sintered particles of non-uniform particle size distributions. Present day nano science and nano technology era demands materials having particles in nano-submicron to few micron sizes of uniform and narrow size distributions to get improved properties. There are several improvised techniques for synthesizing nano materials, but for the large scale manufacturing, it is the spray pyrolysis method which can still be used but with some modification by changing the process parameters. If precursors used for the spray pyrolysis are metal chlorides, sulfates or nitrates, then the corrosive and

obnoxious gases will always be there to pollute the environment. When metal nitrates are used as raw materials for metal oxide synthesis, hydrazine assisted pyrolysis becomes energy effective and environmentally friendly [179]. Hydrazine not only acts as a fuel to minimize the need of energy for pyrolysis, but it also scavenges the nitrate ions and produces environment friendly gaseous products such as nitrogen and water vapour.

1.5 Aim and Objectives

Though industrialization has created unlimited problems to the flora and fauna of this planet, one cannot live today without this industrialization, so there is need felt for sustainable development. One can certainly minimize, if not completely avoid, the environmental problems and make life of the living beings pleasant. Keeping this in mind, scientists all over the world are actively researching on a range of remedies for the environmental pollution. A chemist has much wider role to play in this arena and being a student of chemistry a thorough literature survey was made with one point agenda of finding out abatement processes to minimize the devastation of the environment. One of the environmental pollutants is nuclear waste considering the increase in number of nuclear power plants. The literature review reveals that efforts are made to replace presently used borosilicate glass matrix by pyrochlore oxide matrix to hold this waste. The aim is to confine this high level waste within the lattice to delay the environmental problem of leaching of radioactive wastes to the surroundings. Amongst the number of host lattices proposed, pyrochlore oxides of the type $A_2B_2O_7$ containing Zr and Ti at the B site and any trivalent metal ion at the A site are seen as leading candidates by various researchers. $Gd_2(Ti_{1-x}Zr_x)_2O_7$ system has been studied by various research groups. Similar system with Nd at the A site is chosen by us for study.

In the system $Gd_2(Ti_{1-x}Zr_x)_2O_7$, the starting member $Gd_2Zr_2O_7$ and the end member $Gd_2Ti_2O_7$ are pyrochlores whereas in the system $Nd_2Zr_xTi_{2-x}O_7$ chosen by us, the starting member $Nd_2Zr_2O_7$ is pyrochlore but the end member $Nd_2Ti_2O_7$ is monoclinic. The solid solution of $Nd_2Zr_2O_7$ and $Nd_2Ti_2O_7$ seems to create vacancies in the lattice. According to literature survey, vacancies in the lattice of pyrochlore oxide create disorder in the structure and increase the ionic conductivity and radiation tolerance of the oxide system. These materials thus find their use in fuel cells and disposal of radioactive wastes. These applications demand synthetic route which will yield materials of uniform and compact morphology.

The other environmental pollutants are organic dye effluents and inorganic gases like NO_x . Literature suggests use of Titanium oxide, TiO_2 and zinc oxide, ZnO as photocatalysts in abatement of these pollutants. The aim is to increase the absorbance of these photocatalysts in the visible light along with surface area so as to increase the efficiency in tackling these airborne and waterborne pollutants. ZnO has antibacterial properties and this activity is also enhanced by an increase in its surface area. So the focus is on synthetic route which gives fine oxides with large surface area and absorbance in visible region of the electromagnetic spectrum. In all the methods of synthesis of oxides, environment friendly processes are chosen. The use of hydrazine in the synthesis scavenges the obnoxious gases to convert them to simpler gases. The processes also lower the energy consumption in the synthesis. Co-precipitation, citrate gel method and use of hydrazine all help in synthesizing the oxides with better morphology and properties at lower temperatures.

As a student of chemistry from Goa, a need to find some solutions to the local environmental problems was felt. The iron ore rejects considered as environmental pollutants which create problems to poor farmers and health problems to public and are

seen as technologically important materials and utilized for betterment. Thus experiments are aimed to exploit oxides from iron ore rejects in mineralising the organics. This will serve a dual purpose of removal of organic wastes as well as disposal of ore rejects.

Keeping in mind the above aim and objectives and based on the exhaustive literature survey, eco-friendly oxides were synthesized by environment friendly methods. The oxides were used as a means of abatement of some of the environmental pollutants. The details of all the investigations carried out are presented in the current thesis.

1.6 Methodology

- i) Synthesis of oxide systems pyrochlore through citrate gel, Zinc oxide and doped ZnO by Oxalate and hydrazinated oxalate methods and ZnO by spray pyrolysis method.
- ii) Characterization of precursors through chemical analysis, Infra-red analysis, Thermal analysis etc.
- iii) X-ray diffraction of the thermal products of the precursors and phase identifications.
- iv) Study of microstructure through Scanning Electron Microscope (SEM).
- v) Examination of UV-visible reflectance spectra, electron spin resonance, X-ray photoelectron, Energy dispersive X-ray spectroscopy,
- vi) Study of conductivity of pyrochlore oxides and deriving a correlation between conductivity and disorder in the lattice.
- vii) Assessment of leaching of strontium from Sr doped pyrochlore.
- viii) Assessment of methylene blue degradation on ZnO in the sunlight and NO_x destruction on ZnO in UV-Visible region.

- ix) Assessment of Antibacterial property of ZnO against *E. coli*.
- x) Assessment of NO_x removal by Al doped ZnO in the presence of sunlight.
- xi) Assessment of methylene blue degradation on iron ore rejects in sunlight and thermally.

1.7 Organization of Thesis

The Thesis consists of five chapters organized in the following manner.

<u>Chapter 1</u>	Introduction, Review of literature, Aim and methodology
<u>Chapter 2</u>	Pyrochlore system for nuclear waste Management
<u>Chapter 3</u>	ZnO system for <ul style="list-style-type: none">i) Photo-mineralization of organic compoundsii) Antibacterial Actioniii) Photo-degradation of NO_x
<u>Chapter 4</u>	Iron oxide system for photo-mineralization of organic compounds
<u>Chapter 5</u>	Summary, conclusions and future scope
References	

Chapter 2

Pyrochlore System for Nuclear Waste Disposal

2.1 Introduction

Pyrochlore oxides of [III, IV] type are known for their applications in fuel cells, catalysis, nuclear waste management etc. They are considered as attractive candidates in nuclear waste disposal due to their ability to hold the radioactive wastes for millions of years as compared to borosilicate glass holding radionuclides for 100 years during geological disposal. In order to be used for nuclear waste disposal, the materials should have uniform and compact morphology. Thus method of synthesis of these oxides is very important. Usually these materials are prepared by high temperature methods consuming large amount of energy. This puts a burden on energy resources. In our approach of environmental friendly synthesis a soft chemical route yielding material at low temperature is chosen. This produces oxides with better morphology at low temperature.

The chapter deals with the experimental details of the investigations done on pyrochlore systems synthesized with the purpose of studying it in nuclear waste disposal. The various low temperature synthetic routes adopted viz. oxalate method, hydrazinated oxalate method; citrate gel method and also conventional ceramic method are described in this chapter. Also the analytical techniques used to analyse the precursors and their product oxides are described in the experimental section. The results and discussion section presents the data collected during characterization of precursors of pyrochlore oxides prepared by oxalate method, hydrazinated oxalate method and citrate gel method. The thermal decomposition of these leading to pyrochlore oxides is monitored by thermal analysis technique. X-ray diffraction analysis is used for phase identifications of the oxides prepared by the precursor methods. Microstructure studies of the product oxides are done using SEM. The conductivity studies are done on these oxides and the trend of the conductivity is studied by XPS and ESR. The pyrochlore

oxides are envisaged as inert fuel matrix for fission of U-235. Strontium being one of the radioactive fission products of U-235, it is thought to be studied as a material that could be confined in the pyrochlore oxide synthesized. In view of this, Sr (non-radioactive) is doped in the pyrochlore $\text{Nd}_2\text{Zr}_2\text{O}_7$ and the leaching of it from the lattice of pyrochlore oxides is investigated.

2.2 Methods of preparation of Materials

The preparation of the oxides is a chemical process and puts a lot of burden on the environment either in the form of obnoxious gases released as by-products during synthesis or high temperature requirement in the synthesis of a particular metal oxide. The conventional method of preparation of pyrochlore oxides i.e. Ceramic method involves long and laborious heating cycles of 1200-1400°C with lot of energy consumption during the process for the desired phase formation. The resulting oxides are agglomerated with reduction in their surface areas. Such method cannot be used in synthesis of oxides to be used in applications involving small and uniform particle sizes. Also considering the present-day load on energy resources and environment, there is a need to utilize green processes in the synthesis of metal oxides too.

In the current study an effort is made to synthesize these high temperature pyrochlore materials by methods involving comparatively lower temperatures. The series is also synthesized by ceramic method to understand the difference between the properties of oxides prepared by conventional and green methods. The chemicals used for the synthesis are of analytical grade (AR). Distilled water is used throughout the synthesis.

2.2.1 Ceramic method

This is the conventional and most widely used method of synthesizing pyrochlore

oxides [20, 22, 35, 158]. $Gd_2Zr_xTi_{2-x}O_7$ system investigated by many researchers show very good radiation resistance and conductivity upon doping Zr with Ti [32, 34]. To study the effect of doping Zr at the B site with Ti in $Nd_2Zr_2O_7$, we have investigated the system $Nd_2Zr_xTi_{2-x}O_7$ ($x = 2, 1.8, 1.6, 1.4, 1.2$ and 1.0). The stoichiometric amount of Nd_2O_3 , ZrO_2 and TiO_2 were mixed to obtain $Nd_2Zr_xTi_{2-x}O_7$ ($x = 2.0, 1.8, 1.6, 1.4, 1.2$ and 1.0). The mixture was ground thoroughly in an agate mortar using an organic solvent medium and the dry mass was pelletized (10mm dia. and 2-3mm thickness). The pellets were heated slowly to $500^\circ C$ in a muffle furnace for 12 hours. The cooled pellets were then crushed, ground, re-pelletized and heated slowly to $1000^\circ C$. Sintering was carried out at $1200-1400^\circ C$ for 48 hours.

2.2.2 Green Methods of synthesis of metal oxides

2.2.2.1 Precursor technique.

Precursor methods of synthesis have become promising methods for the material synthesis because of the production of crystalline materials with superior properties like low agglomeration, desired morphology and stoichiometry and controlled particle size distribution at low temperature. The phase or morphology of particles can be altered by modifying the thermal decomposition path and surrounding atmospheres of the precursors. The temperature of calcination of precursors is also much low. The precursor powders are directly precipitated from the solution by taking advantages of the complex reactions in aqueous medium. In the present investigation the metals are precipitated as oxalate and hydrazinated oxalate precursors which are then thermally decomposed to yield the desired oxides.

Precursor method synthesis of $Gd_2Zr_2O_7$ / $Nd_2Zr_2O_7$ / Gd_2ZrCeO_7

$Gd_2Zr_2O_7$ and $Nd_2Zr_2O_7$ are the materials widely studied in nuclear applications for

their radiation resistance. Though $Gd_2Zr_2O_7$ is extensively studied for nuclear applications [33], $Nd_2Zr_2O_7$ is gaining interest recently due to its use in inert matrix fuel systems [60-61]. Ceria is generally used as a surrogate material in place of plutonia for simulation of plutonia fixation in the pyrochlore structure due to the similarities in their physicochemical properties [35]. Thus our first attempt in the study is synthesis of these materials by low temperature oxalate and hydrazinated oxalate methods.

a. Oxalate Method

i) For synthesis of $Gd_2Zr_2O_7$, stoichiometric amount of gadolinium oxide was dissolved in minimum quantity of acid. To this, a solution of zirconyl oxychloride, $ZrOCl_2 \cdot 8H_2O$ in required stoichiometry was added. Ammonium oxalate solution was added dropwise to get a precipitate of gadolinium zirconium oxalate, ii) For synthesis of $Nd_2Zr_2O_7$, stoichiometric amount of neodymium oxide was dissolved in minimum quantity of acid. To this a solution of zirconyl oxychloride, $ZrOCl_2 \cdot 8H_2O$ in stoichiometric amounts was added. Ammonium oxalate solution was added dropwise to get a precipitate of neodymium zirconium oxalate. iii) For synthesis of Gd_2ZrCeO_7 , stoichiometric amount of gadolinium oxide and cerium oxide were dissolved in minimum quantity of acid. To this, a solution of zirconyl oxychloride, $ZrOCl_2 \cdot 8H_2O$ in required stoichiometry was added. Ammonium oxalate solution was added dropwise to get a precipitate of gadolinium zirconium cerium oxalate. The oxalate precipitates thus formed were preserved overnight, filtered next day followed by washing with distilled water to remove chlorides. They were then dried over $CaCl_2$ in desiccator after final wash with absolute alcohol.

b. Hydrazinated oxalate

The dry oxalate powder as prepared in a) above was spread over a Petri dish and placed in desiccator containing hydrazine hydrate, $N_2H_4 \cdot H_2O$ (99%, Merck). The hydrazine

uptake by the precursors was monitored titrimetrically using KIO_3 [180].

2.2.2.2 Sol-gel Method

Single phase $\text{Gd}_2\text{Zr}_2\text{O}_7$ and $\text{Nd}_2\text{Zr}_2\text{O}_7$ formation was confirmed by oxalate and hydrazinated oxalate route. The extension of the method to prepare solid solution, $\text{Nd}_2\text{Zr}_x\text{Ti}_{2-x}\text{O}_7$ met with difficulties. It was observed that the precipitate of zirconium oxalate formed dissolved in oxalic acid if added in excess. Hence simultaneous precipitation of all the desired constituents was inconsistent. In order to retain all the constituent elements in the reaction vessel, citrate gel route which does not involve filtration was adopted.

The technique consists of preparation of amorphous gel mixtures from solutions containing the required metal ions and organic polyfunctional acids like citric acid, tartaric acid, glycolic and lactic acid. In the present study citric acid is used for gel formation. The gel containing required metals in stoichiometry were rapidly dehydrated and decomposed at a lower temperature to give the desired oxide.

(i) Synthesis of $\text{Nd}_2\text{Zr}_x\text{Ti}_{2-x}\text{O}_7$ ($x = 1.8, 1.6, 1.4, 1.2$ and 1.0)

Gels are formed on mixing metal salts/oxides individually i.e., Nd_2O_3 , TiO_2 , $\text{ZrOCl}_2 \cdot 8\text{H}_2\text{O}$ with citric acid. These gels decompose in the muffle furnace to give the corresponding oxides with 99% yields. For the synthesis of pyrochlore oxides $\text{Nd}_2\text{Zr}_x\text{Ti}_{2-x}\text{O}_7$ ($x = 2.0, 1.8, 1.6, 1.4, 1.2$ and 1.0), the metal salts/oxides [Nd_2O_3 , TiO_2 , $\text{ZrOCl}_2 \cdot 8\text{H}_2\text{O}$ stock solution (0.298g/ml)] and citric acid (28.7g/50ml) were heated on a burner to form a pink viscous gel. The gels were then decomposed in a muffle furnace at 900°C for 6 hours.

The oxides obtained were fine, foamy and hence a binder, bee's wax (1%) was added before pelletization on a hydraulic press and slowly heated to 500°C . It was further

sintered at 1400°C for 24 hours.

(ii) Synthesis of $\text{Nd}_{2-y}\text{Sr}_y\text{Zr}_2\text{O}_7$ ($x = 1.8, 1.0, 0.05$)

Now days $\text{MgO-Nd}_2\text{Zr}_2\text{O}_7$ composites are studied to be used as inert matrix fuels [60-61] as $\text{MgO-Nd}_2\text{Zr}_2\text{O}_7$ composite (PuO_2/UO_2) fuel control plutonium production through neutron capture. Strontium is one of the radioactive (β emitter) fission products of U-235. To check whether neodymium zirconate can hold it in its matrix, it was doped with Sr (non-radioactive) as a model during synthesis.

For the synthesis of $\text{Nd}_{2-y}\text{Sr}_y\text{Zr}_2\text{O}_7$ ($x = 1.8, 1.0, 0.05$), stoichiometric amounts of Nd_2O_3 , $\text{Sr}(\text{NO}_3)_2$, $\text{ZrOCl}_2 \cdot 8\text{H}_2\text{O}$ stock solution (0.298g/ml) and citric acid (28.7g/50ml) were heated on a burner to form viscous gels. The gels were then decomposed in a muffle furnace at 900°C for 6 hours. Pelletization was done on a hydraulic press. One set of pellets was heated at 1000°C and other set was sintered at 1400°C for 24 hours.

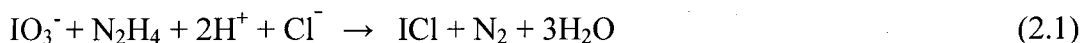
2.3. Characterization techniques

2.3.1. Chemical analysis

Chemical analysis is the basic tool available in the laboratory to characterize the samples. The oxalate and hydrazinated oxalate precursors were characterized by chemical analysis. The percentage of oxalate and hydrazine were determined by standard chemical methods [180].

2.3.1.1 Estimation of hydrazine from the precursors:

Hydrazine estimation was done under Andrew's conditions.



Thus $\text{KIO}_3 = \text{N}_2\text{H}_4$

To the known amount of sample taken in a glass stoppered bottle, 15 mL of concentrated HCl and 10 mL of double distilled water was added followed by addition of CCl_4 . Standard KIO_3 (5.350 g/L) was then added drop-wise from the burette with constant stirring and shaking the bottle until the CCl_4 layer decolourises indicating the end point of the titration.

Percentage of hydrazine in the sample was then calculated by using the relation,

$$1 \text{ mL of } 0.025 \text{ M } \text{KIO}_3 = 0.0008103 \text{ g of } \text{N}_2\text{H}_4. \quad (2.2)$$

2.3.1.2 Estimation of oxalate from the precursors:

Oxalate content was estimated by oxidation with Potassium permanganate. About 100 mg of sample was dissolved in a 25mL of 1M H_2SO_4 . The solution was warmed to 60°C and was titrated against standard 0.01M KMnO_4 till the colourless solution was changed to permanent faint pink colour. Percentage of oxalate in the sample was then calculated by using the relation,

$$1000\text{mL of } 0.01\text{M } \text{KMnO}_4 = 88\text{g of oxalate.} \quad (2.3)$$

2.3.2. Instrumental Analysis

2.3.2. 1 Fourier Transform Infrared (FTIR) Spectroscopy

Infrared spectroscopy is a valuable tool for analyzing samples. The region of infra red spectrum lies between $4000\text{-}400 \text{ cm}^{-1}$. Absorption bands in the spectrum result from energy changes arising as a consequence of molecular vibrations of the bond stretching and bending type [181]. It has been widely used for identifying the organic ligands bound to the metal ion, metal oxygen bonds as well as the adsorbed species on the catalysts surface. IR instrument can be divided into two classes namely dispersive and non dispersive. The dispersive type of instrument is similar to UV-Visible

spectrophotometer while the non dispersive type has an interferometer in the place of monochromator and the instrument is called as Fourier Transform Infra-red Spectroscopy (FTIR). The different components of FTIR are 1) Source, 2) Michelson Interferometer, 3) Sample compartment, 4) Detector. The spectrum of the sample can be interpreted by matching the corresponding group frequencies for the various functional groups present with reported data. IR spectra of the metal precursors and their decomposed products were recorded on SHIMADZU FTIR instrument, model IR Prestige –21 fitted with diffuse reflectance accessories. The instrument was calibrated using polystyrene film. The samples were mixed with spectroscopic grade KBr and ground well. IR spectra were scanned in the frequency range of 4000-500 cm^{-1} . The spectra were recorded in percent transmittance (%T) mode against wavenumber ($1/\lambda$) cm^{-1} .

2.3.2.2. Thermal analysis

Thermal analysis is a group of techniques in which a physical property of a sample is measured as a function of temperature whilst it is subjected to a controlled temperature. It is extensively used in the characterization of materials especially the precursors. The techniques include TGA, DTA, DSC, and DTG.

(i) Isothermal weight loss:

Isothermal weight loss concedes examination of weight loss. The various oxalate and hydrazinated oxalate precursors were weighed in silica crucibles. The initial weight of the crucible and samples were noted. The crucibles containing the samples were placed in a muffle furnace and the temperature was slowly raised to 900°C. The loss in weight of the complexes was measured by finding the difference in the final and initial weight of the crucibles + sample. The isothermal weight loss % was then calculated.

(ii) Thermogravimetric(TG) and differential scanning calorimetric (DSC)/**Differential Thermal analysis (DTA)**

Thermogravimetry (TG) provides quantitative analysis of weight loss with thermally induced transitions. It also provides information regarding the thermal stability of the material. The changes in physical and chemical properties of the material can be monitored as a function of temperature. Essential components of a TG analyzer are 1) Furnace, 2) Sample crucible with thermocouple, 3) Automatic recording balance, and 4) Printer/plotter. Differential Scanning Calorimetry (DSC) analysis provides the differential heat flux between the sample and reference material as a function of temperature. The different components of a DSC instrument are 1) Sample and reference container, 2) Average temperature amplifier, 3) Differential temperature amplifier, 4) Programmer. Differential Thermal analysis (DTA) is one of the oldest and simplest thermal techniques used for the study of physical and chemical transformations in materials associated with the energy changes. In DTA, the temperature difference ΔT between the sample and the thermally inert reference is measured as a function of temperature/time when both are heated simultaneously at the predetermined constant heating rate in the controlled atmosphere. Thermal techniques, TG/DSC and TG/DTA were used to characterize the metal precursors and oxides. Simultaneous TG/DSC, TG/DTA measurements were done on thermal analyzer, STA 409 PC LUXX – NETZSCH from room temperature (RT) to 1000°C using alumina crucible, with heating rate of 10 K/ min. Dry nitrogen was used as purge gas. Instrument was calibrated using Gold metal. Based on the thermal analysis, final decomposition temperature of precursors was fixed.

2.3.2.3 X-ray diffraction (XRD)

The X-ray diffraction technique is most extensively used for characterization of different crystalline solids. The position and intensities of X-rays diffracted by a crystalline solid provide a lot of information such as crystal structure, composition of the solid, particle size etc. X-rays are a form of electromagnetic radiation of very short wavelength from 0.1 to 100 Å and are produced when high speed electrons are stopped by a solid object. In a crystal different atoms and molecules are arranged in different planes in a systematic and repetitive manner. These interplanar distances are of the same order of magnitude as the wavelength of the characteristic X-rays emitted by the target. Hence the crystal planes act as a diffraction grating to the X-rays and diffraction occurs. The necessary condition for X-ray diffraction to occur is represented by Bragg's equation.

$$n \lambda = 2d \sin \theta \quad (2.4)$$

where n is an integer (1, 2, 3 etc.) called the order of reflection, θ is the glancing angle of incident X-ray beams on the crystal surface, d is the interplanar spacing and λ is the wavelength of X-rays. The phase formation of the prepared pure and doped metal oxide samples was studied by powder diffraction technique. This method uses sample in powder form. In a powdered sample, the various lattice planes are present in every possible orientation. For each set of planes, therefore at least some crystals must be oriented at the Bragg angle θ to the incident beam and thus diffraction occurs for these crystals and planes. Different components of powder diffractometer are 1) Evacuated X-ray tube (source), 2) Sample compartment, 3) Detector.

The X-ray diffraction patterns were obtained on Seifert XRD 3003 TT diffractometer using Cu K α ($\lambda = 1.5418$ Å) radiation filtered through Nickel filter in the instrument operating at $V = 40$ kV and $I = 30$ mA, Philips analytical PW1710 using Cu K α ($\lambda =$

1.5418 Å) radiation filtered through Nickel filter in the instrument operating at V = 30kV and I= 20mA, instrument Philips analytical PW3710 using Cu K α (λ = 1.5418 Å) radiation filtered through Nickel filter in the instrument operating at V = 30kV and I= 20mA and on the instrument Xpert Pro using Cu K α (λ = 1.5418 Å) radiation filtered through Nickel filter in the instrument operating at V = 45kV and I= 40mA. Instruments were standardized using SiO₂. The powders were scanned from 2 θ angle of 10 to 80°. XRD patterns were obtained as intensity of peaks against 2 θ . Crystallite phase identification was done by matching the peaks with JCPDS cards. Lattice parameter was calculated as follows.

$$d = a / \sqrt{h^2 + k^2 + l^2} \quad (2.5)$$

Where d is the interplanar spacing in Å, a is lattice parameter in Å and h k l are the miller indices for the corresponding lattice plane. X-ray density was calculated as,

$$d_x = 8M/N a^3 \quad (2.6)$$

Where M is the molecular mass, N is Avogadro no and a is the lattice parameter.

Crystallite size was calculated by Scherer formula,

$$\tau = 0.9\lambda / \beta_{\text{corr}} \cos \theta \quad (2.7)$$

Where λ is the wavelength in Å, $\beta_{\text{corr}} = \sqrt{(\beta^2 - \beta_{\text{si}}^2)}$ is the line broadening, and θ is the Bragg angle [182]. Rietveld refinements were carried out for Nd₂Zr₂O₇ prepared by citrate gel method using the standard Fd $\bar{3}$ m cubic model.

2.3.2.4 High Temperature X-ray diffraction (XRD)

High Temperature X-ray Diffraction is an extremely useful technique to study the crystallographic transformations of crystalline phases at high temperatures. The high temperature X-ray diffractometer, apart from having X-ray camera and other diffractometer attachments also contains one very low heat capacity heater capable of

providing uniform temperature to the specimen and arrangements to control the ambient temperature.

High temperature X-ray diffraction studies were carried out on $\text{Gd}_2\text{Zr}_2\text{O}_7$ obtained after decomposing hydrazinated oxalate precursor using Philips X'pert pro unit with an anton par high temperature attachment. The data was recorded at room temperature, 200 °C, 400 °C, 600 °C, 800 °C, 1000 °C and on cooling to room temperature.

2.3.2.5. (i) UV-Visible diffuse reflectance spectroscopy

UV-Visible diffuse reflectance spectroscopy (DRS) is a powerful technique which provides information regarding the band gap of the materials, especially the semiconducting metal oxides. It is a non-destructive technique that uses the interaction of light, absorption and scattering, to produce a characteristic reflectance spectrum. The diffuse reflectance spectra of dry powders were recorded using a Shimadzu UV-2450 UV-Visible Spectrometer equipped with a diffuse reflectance accessory in the wavelength range of 800–200 nm. BaSO_4 was used as a reference. The band gap energies of the oxides was calculated from the differential plots obtained from the UV-Visible reflectance spectra by using the formula,

$$\text{Band gap (Eg) in eV} = 1239.8 / \lambda_{\text{max}} \quad (2.8)$$

Where λ_{max} is the maximum wavelength of absorption obtained from differential plots of the UV-Visible reflectance spectra.

2.3.2.5. (ii) UV-Visible Absorbance spectroscopy

Absorptions in the UV-Visible region of the spectrum are dependent on the electronic structure of the compound. The reflectance data obtained above was converted to absorbance using the software Kubelka Munk to obtain the absorbance spectra.

2.3.2.6 Scanning electron microscopy

The scanning electron microscope is used to study the samples at microscopic levels. The instrument produces electron images of specimen's surface of up to $\times 1,80,000$ magnifications with resolution better than 100 \AA . The technique is used for the investigation of shape, size and surface texture. In Scanning electron microscopy (SEM), the electron beam does not pass through the specimen rather it interacts with the specimen surface and results in reflection of low energy secondary electrons from it which takes part in image formation. The SEM does not produce a true image of the specimen; instead it produces a point by point reconstruction of the specimen from the signal emitted from the specimen when illuminated by the high energy electron beam. An electron microscope consists of an electron gun chamber maintained at high vacuum and consisting of tungsten or lanthanum hexaboride filament. When high voltage is applied, the thermo-ionic emission takes place in the filament and the electrons are ejected out. The condenser lens condenses the electron beam to a small pencil of ray which falls on the specimen. The objective lens forms the first image which acts as object for the intermediate lens, and the image formed by it becomes the object for the projector lens to produce highly magnified image [183].

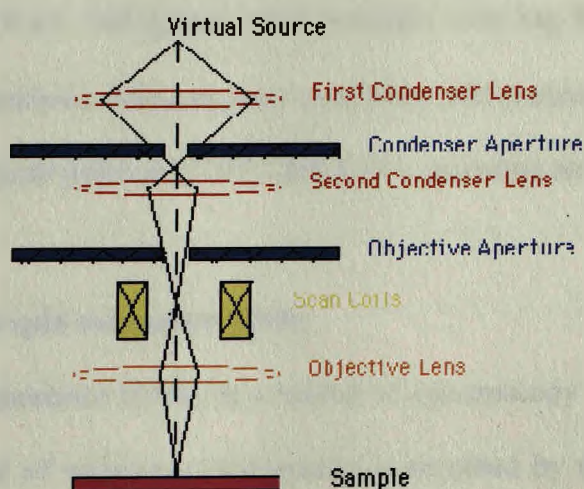


Figure 2.1 Schematic diagram of Scanning Electron Microscope

In our study, Scanning electron micrographs (SEM) were obtained on JEOL JSM – 5800. The samples were mounted on specimen stubs with double sided adhesive tapes and coated with thin layer of conducting material like gold by sputtering. The morphology of the samples was studied by SEM.

2.3.2.7 X-ray Photoelectron spectroscopy (XPS)

X-ray Photoelectron Spectroscopy (XPS) also known as ESCA (Electron Spectroscopy for Chemical Analysis) is a very important technique for determining the atomic and molecular energy levels and hence the ionization energies of atoms and molecules. When the atom or molecule is irradiated with highly energetic radiation, there is ejection of core electron. The kinetic energy E of this electron is equal to the difference in energy of the incident radiation E_i and the binding energy of the electron E_g . Measurement of E and E_g therefore provides a means of the identification of the atoms. The ionizing radiation used is X-rays and hence this technique is also known as X-ray photoelectron spectroscopy (XPS). XPS analysis was done at 298K using MgK_{α} radiation on a VG Microtech Multilab ESCA 3000 spectrometer. Measurements were carried out in vacuum. Binding energy (BE) calibration was performed with Au ($4f_{7/2}$) core level at 83.9 eV. All spectra were recorded with $Mg K_{\alpha}$. Sample surfaces were scraped before analysis. Measurement conditions and parameters were verified to get the right carbon peak position ($C 1s = 284.8$ eV), assuming an error lower than 0.2 eV.

2.3.2.8. Electron spin resonance (ESR)

Electron Spin Resonance (ESR), is a branch of spectroscopy in which electromagnetic radiation (usually of microwave frequency) is absorbed by molecules, ions, or atoms possessing electrons with unpaired spins, i.e. electronic spin $S > 0$, which is a common

feature of transition metals. The reversal of spins of these unpaired electrons in an applied magnetic field is recorded. The spectra are obtained by varying magnetic field at constant microwave frequency. The condition for absorption of resonant energy is

$$\Delta E = gB_e H \quad (2.9)$$

Where B_e is a constant, i.e. the Bohr Magneton, H is the strength of the applied magnetic field, the factor 'g' is the gyromagnetic ratio and has a value of 2.0023 for a free electron. ESR spectra are usually represented as the first derivative of the absorption. From ESR spectra information on the paramagnetic ion and its immediate environment in the host structure can be obtained.

The Electron spin resonance (ESR) spectra were recorded on Bruker BioSpin Gx, with Field sweep width 8000 G and Microwave frequency 9.425 GHz. Reference compound used is DPPH(2,2-Diphenyl-1-Picrylhydrazyl) with g value of 2.0036.

2.3.2.9 Density Measurement

Electrical properties of a material depend on the density. Density of the sintered material is an important physical parameter. Geometrical density of the sintered material was calculated by measuring the dimensions (diameter and thickness) and mass of the pellets after sintering by using the relation,

$$\text{Density} = \text{Mass} / \text{Volume} \quad (2.10)$$

Where mass is the weight of the sample pellet, volume = $\Pi r^2 h$, r is the radius of the pellet and h is the thickness both measured by using a micrometer screw gauge. Densities of the powdered samples were also found by liquid displacement method. Water was used as the liquid medium.

2.3.2.10 A. C. Conductivity: Impedance Measurements

Impedance measurement is one of the most important measurements of electrical properties. In an impedance bridge the measurements are made with a Wheatstone bridge in which the resistance R , and capacitance C , in series with each other are balanced against variable resistors and capacitors. The impedance measurements were done on 1260 solartron impedance analyzer at 100Hz to 10 MHz at several temperatures from room temperatures to 700°C on well sintered pellets of dimension 10 mm diameter and 2-3 mm thickness. The samples were placed in the sample holder which is inserted in the constant temperature zone of furnace. All the measurements were carried out in air as there is no difference in the measurements carried out in air and under vacuum [20]. In the present study, this technique is used to determine the conductivity (derived from the resistance values). The conductivity values are evaluated from the resistance values obtained from nyquist plots. Nyquist plots consist of imaginary part (Z'') of the impedance plotted against real part (Z'). The curve obtained in the nyquist plots was curve fitted to the semicircular shape. The intercept of the semicircle on real axis gives the resistance of the material. The direct current (dc) bulk resistance values from these plots were used to find dc conductivity. The long range migration of oxygen ions take place by thermally activated hopping to adjacent oxygen vacancies, which yields the dc conductivity of the form,

$$\sigma_{dc} T = \sigma_0 e^{-E/K_B T} \quad (2.11)$$

E is the activation energy for conduction, T is the Temperature, K_B is the Boltzmann constant and σ_0 is the pre-exponential factor that depends on the concentration of the mobile species. The values of activation energy were determined from the slopes of the linear fits to the σ_{dc} against temperature plots. Pre-exponential factors were calculated from the intercept of the linear fits to the σ_{dc} against temperature plots on σ_{dc} axis.

2.3.2.11. Leaching Studies

When $\text{Nd}_2\text{Zr}_2\text{O}_7$ is used in composite form with MgO as inert matrix fuel, it should not allow the unreacted fuel and fission products to leach out of it on geological disposal. Leaching studies were carried out on strontium (non-radioactive) doped neodymium zirconate, both powdered and pelletized samples. Pelletized samples were sintered at 1000°C and 1400°C before using for leaching studies. Deionised water was used as a reference liquid and a simulant of fresh type groundwater. The sample pellets were immersed in beakers carrying distilled water, one of which was maintained at 75°C and other at room temperature. The studies carried out at 75°C for the duration of 3 months are equivalent to the investigations done at room temperature for a period of three years. The powdered sample was put in distilled water kept at room temperature with continuous stirring. Loss of distilled water due to evaporation was compensated by refilling. After every 30 days an aliquot of the distilled water was withdrawn and analyzed by Atomic absorption spectroscopy (A. A. S.) for the presence of Strontium. The studies were done for 3 months.

Atomic absorption spectroscopy (A. A. S.)

When an element is introduced into a flame, a few of its atoms absorb thermal energy from the source of radiation and get excited. The excited atoms then emit the characteristic radiation of the element and return to the ground state. The intensity of the emitted radiation is directly proportional to the number of excited atoms and hence to the concentration of the element introduced in the flame. The measurement of the intensity of the emitted radiation permits quantitative estimation of the element and the determination of the wavelength of the emitted radiation helps us to identify the element. Element strontium was analyzed from the leachate by AAS on the instrument Varian AA 240 FS using N_2O -acetylene flame after proper dilution of the aliquot.

2.4 Results and discussions

2.4.1. $Gd_2Zr_2O_7$ / $Nd_2Zr_2O_7$ / Gd_2ZrCeO_7

2.4.1.1. Characterization of oxalate and hydrazinated oxalate precursors

2.4.1.1.1 Chemical analysis and formula fixation of precursors

The formula fixation of all the precursors prepared by oxalate and hydrazinated oxalate methods was done taking into account the results of chemical analysis, FTIR and total weight loss studies before decomposition to the corresponding oxides. In general, the observed (obsd) percentage (%) of total isothermal weight loss, oxalate ($C_2O_4^{2-}$) and hydrazine (N_2H_4) match well with the calculated (calcd.) values based on plausible formula in each case. The proposed chemical formulae along with the analytical data of oxalate and hydrazinated oxalate precursors for pyrochlore oxides are summarized in table 2.1.

Table 2.1 Chemical analysis of oxalate and hydrazinated oxalate precursors and the proposed chemical formulae.

Precursor	Hydrazine %		Oxalate %		Total Weight loss	
	Calcd	Obsd	Calcd	Obsd	Calcd	Obsd
$Gd_2Zr_2(C_2O_4)_7 \cdot 10H_2O$	-----	-----	47.6	46.6	52.9	52.8
$Gd_2Zr_2(C_2O_4)_7 \cdot 10N_2H_4$	22.3	27.6	43.0	43.4	57.5	59.5
$Nd_2Zr_2(C_2O_4)_7 \cdot 10H_2O$	-----	-----	48.6	49.1	54.0	55.4
$Nd_2Zr_2(C_2O_4)_7 \cdot 10N_2H_4$	22.7	22.3	43.8	42.5	58.6	56.8
$Gd_2ZrCe(C_2O_4)_7 \cdot 10H_2O$	-----	-----	45.9	45.0	51.0	50.6
$Gd_2ZrCe(C_2O_4)_7 \cdot 10N_2H_4$	21.5	20.8	41.6	42.2	55.6	54.3

2.4.1.1.2 FTIR analysis of the precursors

The infrared (IR) band positions of all the precursors have been compiled in the table 2.2. The IR bands characteristic of the coordinated oxalate groups [184-185] observed at ~ 1630 and 1320 cm^{-1} corresponding to $\nu_{as}(\text{o-c-o})$ and $\nu_s(\text{o-c-o})$, respectively suggest that there is coordination of oxalate ion with the metal ions. A broad band in the region $3600\text{-}3000 \text{ cm}^{-1}$ which is due to $\nu(\text{O-H})$ stretching is found in all complexes and is due to the presence of water. It is evident from these studies that there is formation of metal oxalate hydrates whose formulas have been fixed, as given in Table 2.1, through chemical analysis.

Table 2.2 IR absorptions of oxalate and hydrazinated oxalate precursors.

Precursor	$\nu_s(\text{o-c-o}) / \nu_{as}(\text{o-c-o}) \text{ cm}^{-1}$	$\delta(\text{o=c-o}) \text{ cm}^{-1}$	$\nu(\text{H}_2\text{O}) / \nu(\text{N-H}) \text{ cm}^{-1}$	$\nu(\text{N-N}) \text{ cm}^{-1}$	$\delta(\text{NH}_2) \text{ cm}^{-1}$
$\text{Gd}_2\text{Zr}_2(\text{C}_2\text{O}_4)_7 \cdot 10\text{H}_2\text{O}$	1320 /1630	800	3100-3500	-----	-----
$\text{Gd}_2\text{Zr}_2(\text{C}_2\text{O}_4)_7 \cdot 10\text{N}_2\text{H}_4$	1320 /1630	760	3400	960	1150
$\text{Nd}_2\text{Zr}_2(\text{C}_2\text{O}_4)_7 \cdot 10\text{H}_2\text{O}$	1320 /1630	800	3100-3500	----	----
$\text{Nd}_2\text{Zr}_2(\text{C}_2\text{O}_4)_7 \cdot 10\text{N}_2\text{H}_4$	1320 /1630	800	3400	960	1160
$\text{Gd}_2\text{ZrCe}(\text{C}_2\text{O}_4)_7 \cdot 10\text{H}_2\text{O}$	1320 /1630	800	3100-3600	-----	-----
$\text{Gd}_2\text{ZrCe}(\text{C}_2\text{O}_4)_7 \cdot 10\text{N}_2\text{H}_4$	1320 /1630	780	3400	970	1150

In case of hydrazinated oxalates, infra-red studies reveal the modification of the oxalate by hydrazine linkage to the metal by characteristic band positions due to $\nu(\text{N-N})$ peak at $960\text{-}970 \text{ cm}^{-1}$ and $\delta(\text{NH}_2)$ peak at $1150\text{-}1160 \text{ cm}^{-1}$ [186] along with the usual oxalate band positions due to $\delta(\text{o=c-o})$ and $\nu_s(\text{o-c-o})$ and $\nu_{as}(\text{o-c-o})$. The broad peaks shown by oxalates in the region $3100\text{-}3500 \text{ cm}^{-1}$ due to $\nu(\text{H}_2\text{O})$, get sharpened on hydrazination

indicating appearance of $\nu(\text{N-H})$ stretching bands. The presence of hydrazine is also supported by chemical analysis (Table 2.1).

2.4.1.1.3 Thermal analysis

Gadolinium Zirconium oxalate/ hydrazinated oxalate

$\text{Gd}_2\text{Zr}_2(\text{C}_2\text{O}_4)_7 \cdot 10\text{H}_2\text{O}$ shows (table 2.3), an endothermic loss of water at $\sim 119^\circ\text{C}$ followed by a broad exothermic peak $\sim 600^\circ\text{C}$ indicating decarboxylation and sharp exothermic process $\sim 900^\circ\text{C}$ indicating a total loss at $\sim 900^\circ\text{C}$. The hydrazine derivative of the oxalate, $\text{Gd}_2\text{Zr}_2(\text{C}_2\text{O}_4)_7 \cdot 10\text{N}_2\text{H}_4$, on the other hand, undergoes sequential exothermic processes at the temperatures 111.7, 247.1, 387.2 $^\circ\text{C}$ corresponding to dehydrazination followed by decarboxylation but the total loss, however, is found to occur at a lower temperature compared to the oxalate precursor.

Neodymium Zirconium oxalate/ hydrazinated oxalate

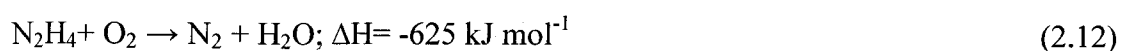
The $\text{Nd}_2\text{Zr}_2(\text{C}_2\text{O}_4)_7 \cdot 10\text{H}_2\text{O}$ decomposes stepwise showing (table 2.3), endothermic peak $\sim 156^\circ\text{C}$ corresponding to loss of water followed by a sharp endotherm at $\sim 399^\circ\text{C}$ and an endotherm at $\sim 574^\circ\text{C}$ due to decarboxylation and finally a broad exotherm at $\sim 750^\circ\text{C}$, while its hydrazinated complex, $\text{Nd}_2\text{Zr}_2(\text{C}_2\text{O}_4)_7 \cdot 10\text{N}_2\text{H}_4$ decomposes sequentially with endothermic process at $\sim 123^\circ\text{C}$ followed by a continuous linear weight loss showing a broad exothermic process $\sim 470^\circ\text{C}$ due to decarboxylation and a very sharp exotherm at $\sim 739^\circ\text{C}$. The hydrazine complex, however, shows total loss at a lower temperature than that of the oxalate complex.

Gadolinium Zirconium Cerium oxalate/ hydrazinated oxalate

$\text{Gd}_2\text{ZrCe}(\text{C}_2\text{O}_4)_7 \cdot 10\text{H}_2\text{O}$ shows (table 2.3), a small sharp endotherm at 110°C and exotherms at 350, 570, 840, 920 respectively. The hydrazinated derivative of the oxalate also undergoes exothermic reactions sequentially at the temperatures 400, 600,

750, 860 °C respectively.

Such observation of hydrazinated complex decomposing exothermically at much lower temperature compared to the oxalate complex is a general observation in many of our systems [148,165,187]. Thus it can be inferred from the thermal analysis studies that the thermal path of the oxalate precursor is altered on hydrazination and the hydrazinated complexes decompose at much lower temperatures compared to the unhydrazinated ones. Hydrazine acts as a fuel and the combustion process is sustained by the enormous energy released by the reaction of hydrazine with atmospheric oxygen, [188]



The liberated energy is then utilized by the complex enabling it to decompose easily without necessitating any more external heat energy. Based on thermal analysis complete decomposition temperature was fixed for the oxalate and its hydrazinated derivative and the precursors were decomposed to yield the corresponding oxides.

Table 2.3 DTA-TG data of the oxalate and hydrazinated oxalate complexes.

Precursor	DTA Peaks
$\text{Gd}_2\text{Zr}_2(\text{C}_2\text{O}_4)_7 \cdot 10\text{H}_2\text{O}$	119 °C (sharp endotherm), 600 °C (broad exotherm) 900 °C (sharp exotherm)
$\text{Gd}_2\text{Zr}_2(\text{C}_2\text{O}_4)_7 \cdot 10\text{N}_2\text{H}_4$	111.7 °C (sharp exotherm), 247.1 °C (small exotherm) 387.2 °C (sharp exotherm)
$\text{Nd}_2\text{Zr}_2(\text{C}_2\text{O}_4)_7 \cdot 10\text{H}_2\text{O}$	156.2 °C (endotherm), 399.4 °C (sharp endotherm) 574.1 °C (broad exotherm), 750 °C (broad exotherm)
$\text{Nd}_2\text{Zr}_2(\text{C}_2\text{O}_4)_7 \cdot 10\text{N}_2\text{H}_4$	122.8 °C (sharp endotherm), 470.1 °C (broad exotherm) 739.2 °C (sharp exotherm)
$\text{Gd}_2\text{ZrCe}(\text{C}_2\text{O}_4)_7 \cdot 10\text{H}_2\text{O}$	110 °C (small sharp endotherm), 350 °C (broad exotherm), 570 °C (sharp exotherm) 840 °C (exotherm), 920 °C (sharp exotherm)
$\text{Gd}_2\text{ZrCe}(\text{C}_2\text{O}_4)_7 \cdot 10\text{N}_2\text{H}_4$	400 °C (broad exotherm), 600 °C (sharp exotherm) 750 °C (exotherm), 860 °C (sharp exotherm)

2.4.1.2 Characterization of oxides

2.4.1.2.1 Phase identification of the thermal products of oxalate and hydrazinated oxalate precursors by XRD: $Gd_2Zr_2O_7$, $Nd_2Zr_2O_7$ and Gd_2ZrCeO_7

XRD patterns of the decomposed Gadolinium zirconate, Neodymium zirconate and Gadolinium cerium zirconate from oxalate and hydrazinated oxalate samples are compiled in the figures 2.2-2.4. The phase identification of all the final thermal products of the precursors have been done by X-ray diffraction studies and the (hkl) values has been compared with the JCPDS file no.17-0458. In general the d values calculated from the XRD patterns match well with reported d-values (table A-1, appendix) for synthesized gadolinium zirconate, neodymium zirconate and gadolinium cerium zirconate except the superstructure peaks corresponding to pyrochlore oxide. Pyrochlore structure is close to the fluorite structure and show similar interplanar spacings. Peaks at 111(14.4), 311(27.8), 331(36.8) and 511(44.2) [54] in the lattice structure of pyrochlore oxides referred to as “superstructure peaks” are not seen in XRD patterns of fluorite which serves as a distinguishing feature for both [189]. These superstructure peaks were not conspicuously observed in the crystal structure of the prepared oxides. It is reported that the intensity of these superstructure peaks decrease with increase in disorder in the pyrochlore lattice [20]. It can be clearly seen that the products obtained by the hydrazinated oxalate method show broad peaks indicating narrower particle size formation compared to the oxalate method. The crystallite sizes calculated by Scherer’s method are compiled in table A-2 in appendix.

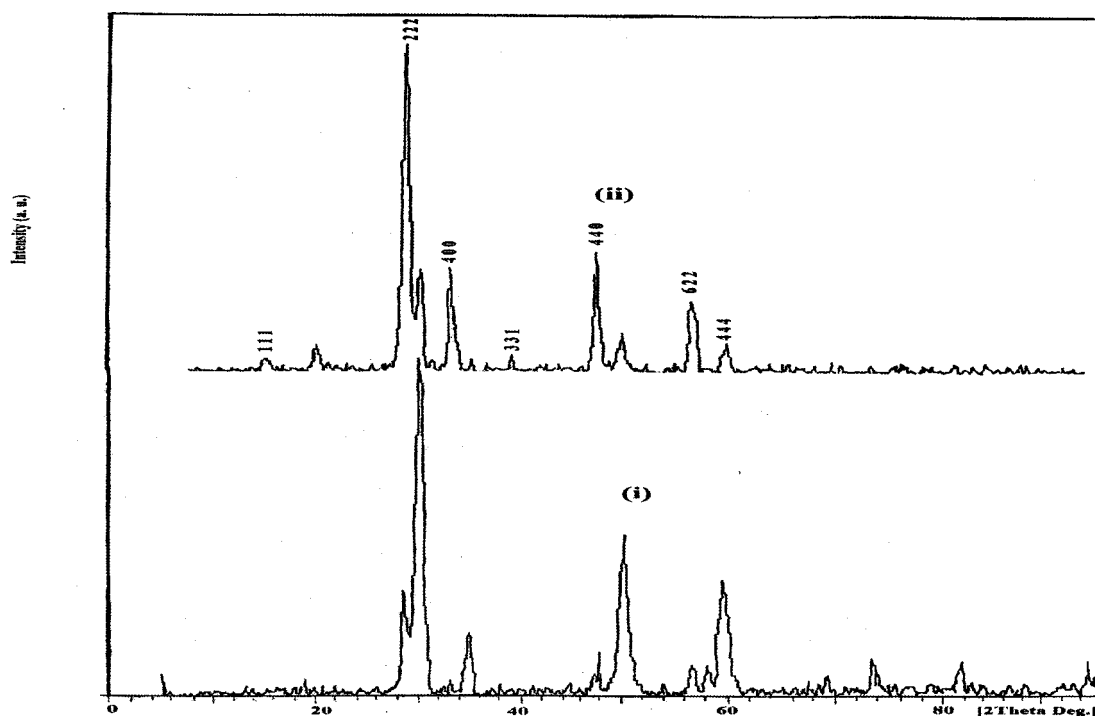


Figure 2.2 XRD patterns of Gadolinium Zirconate prepared by (i) Oxalate method and (ii) Hydrazinated oxalate method.

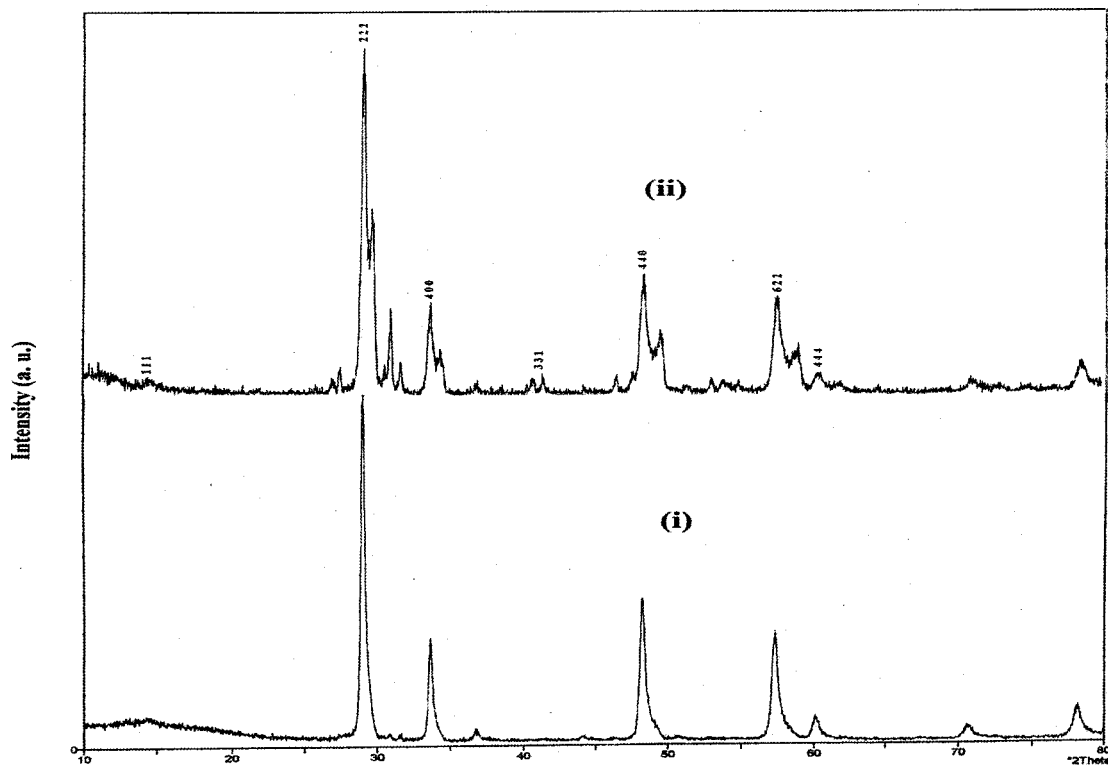


Figure 2.3 XRD patterns of Neodymium Zirconate prepared by (i) Oxalate method and (ii) Hydrazinated oxalate method.

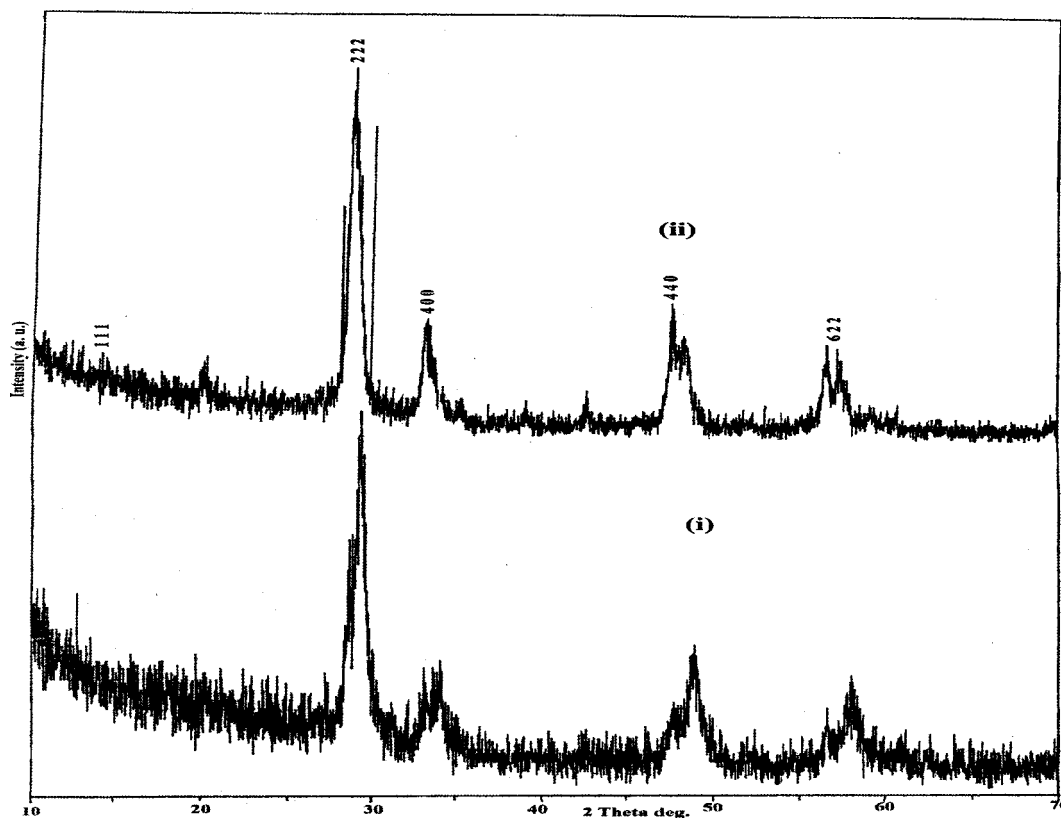


Figure 2.4 XRD patterns of Gadolinium Cerium Zirconate prepared by (i) Oxalate method and (ii) Hydrazinated oxalate method.

2.4.1.2.2 High Temperature XRD

High temperature X-ray diffraction studies were carried out on $Gd_2Zr_2O_7$ obtained after decomposing hydrazinated oxalate precursor. The study was carried out to see if there is a change in the structure of pyrochlore oxide with increase in temperature (figure 2.5). It can be seen that as the temperature is increased from 200 to 1000 °C in the steps of 200 °C, the crystallites grow as indicated by the narrowing of the XRD peaks with increase in heating temperature. Further a sample that was heated at 1000 °C and then cooled to room temperature does not show any change in the pattern suggesting no change in the crystallite structure on cooling.

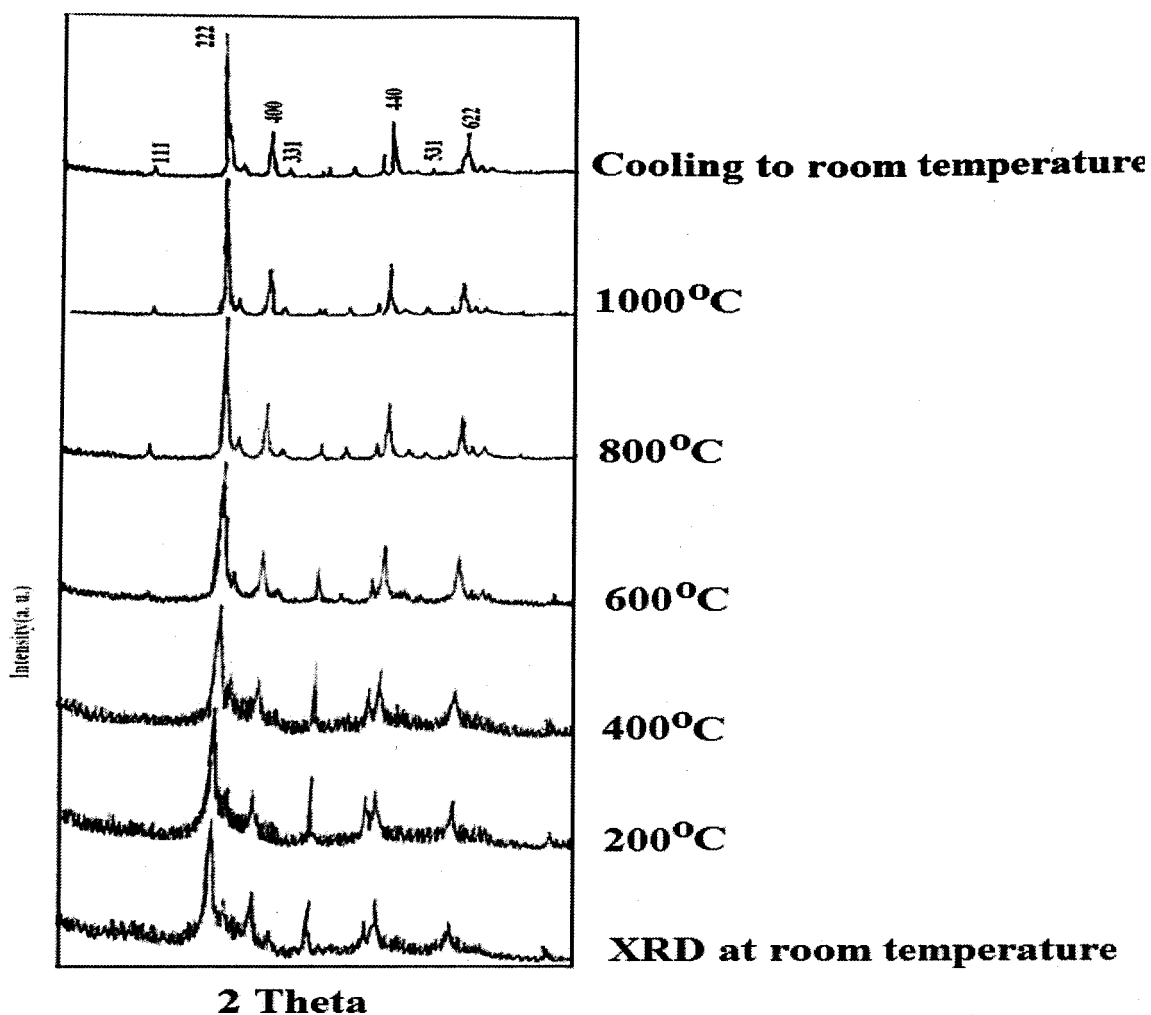


Figure 2.5 High temperature XRD of $Gd_2Zr_2O_7$ prepared by hydrazinated oxalate.

2.4.2 $Nd_2Zr_xTi_{2-x}O_7$ ($x = 2.0, 1.8, 1.6, 1.4, 1.2$ and 1.0)

2.4.2.1 Characterization of citrate gel precursors

2.4.2.1.1 FTIR analysis of citrate gel precursor

The IR spectrum of the citrate gel precursor was obtained after calcination of the gel up to 300°C to a solid powder form (figure 2.6).

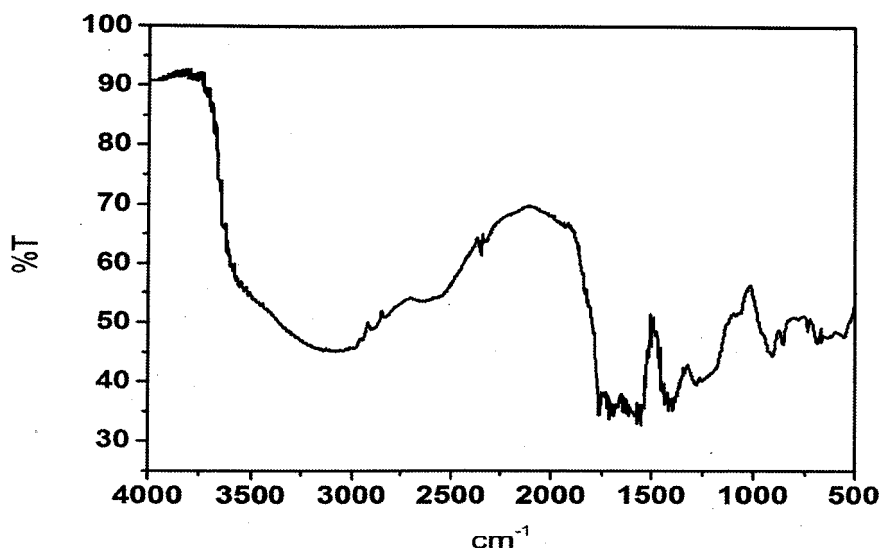


Figure 2.6 FTIR spectrum of the citrate gel precursor calcined at 300°C.

The presence of IR bands of co-ordinated citrate groups at $\sim 1408/1562$ cm^{-1} corresponding to $\nu_{\text{as}}(\text{o-c-o})$ and $\nu_{\text{s}}(\text{o-c-o})$, $\nu(\text{C-O})$ at ~ 1281 cm^{-1} and bending mode $\delta(\text{o=c-o})$ at 907 cm^{-1} suggest the co-ordination of the citrate group to the metal. Presence of a broad band for water indicates presence of water. Similar co-ordination of the citrate gel with metal ions is reported by S. Zanetti et al. in their work on pyrochlore system [173].

Table 2.4 IR absorptions of citrate gel precursor.

precursor	$\nu_{\text{s}}(\text{o-c-o}) / \nu_{\text{as}}(\text{o-c-o})$ cm^{-1}	$\delta(\text{o=c-o})$ cm^{-1}	$\nu(\text{H}_2\text{O})$ cm^{-1}	$\nu(\text{C-H})$ cm^{-1}	$\nu(\text{C-O})$ cm^{-1}	$\nu(\text{O-H})$ cm^{-1}
Citrate	1408/1562	907	3000-3500	2617	1281	1762

2.4.2.1.2 Thermal analysis of citrate gel precursor

Although precursor formula could not be fixed for citrate gel precursor, the thermal decomposition path of the precursor to give the desired pyrochlore oxide traced by

TG/DTA studies is given in figure 2.7.

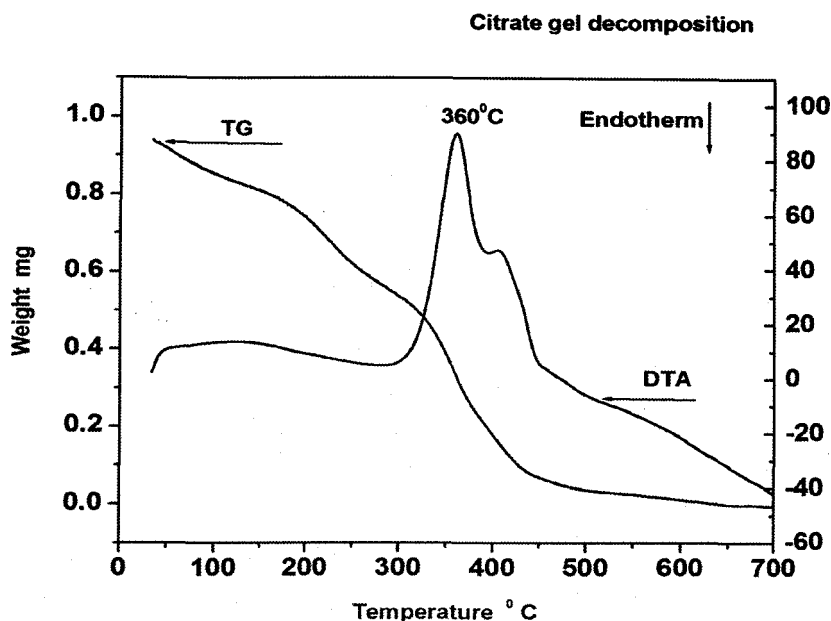


Figure 2.7 DTA-TG of citrate gel precursor calcined at 300°C.

From the DTA-TG analysis of the precursor, it is observed that in the citrate gel decomposition major weight loss is complete by 450°C. The DTA analysis indicates that the decomposition reaction of citrate precursor is exothermic and liberates energy. The exothermic peaks centered at 380°C correspond to the elimination of the organic material. A small peak centered at 450°C may be due to the crystallization of the cubic phase. Thus citrate gel synthesis produces pyrochlore oxides at lower temperature. There is strong coordination interaction between the ---COO^- groups of the citrate ion and metal ions and this effectively prevents the segregation of metal ions during the gel formation. It is reported that the bonding nature between ---COO^- groups and metal ions changes with temperature: unidentate (110–250 °C) \rightarrow bridging (300–350 °C) \rightarrow ionic (400–500 °C) [167]. Further heating the obtained residue upto 1000°C indicates small endotherm at 699, 876 and 980 °C .

Although ceramic method is a conventional route to synthesis of pyrochlore oxides, it requires input of large amount of energy. The DTA-TG of the intimately ground mixture of neodymium and zirconium oxides (figure 2.8) indicates endotherms at 291 and 384 °c.

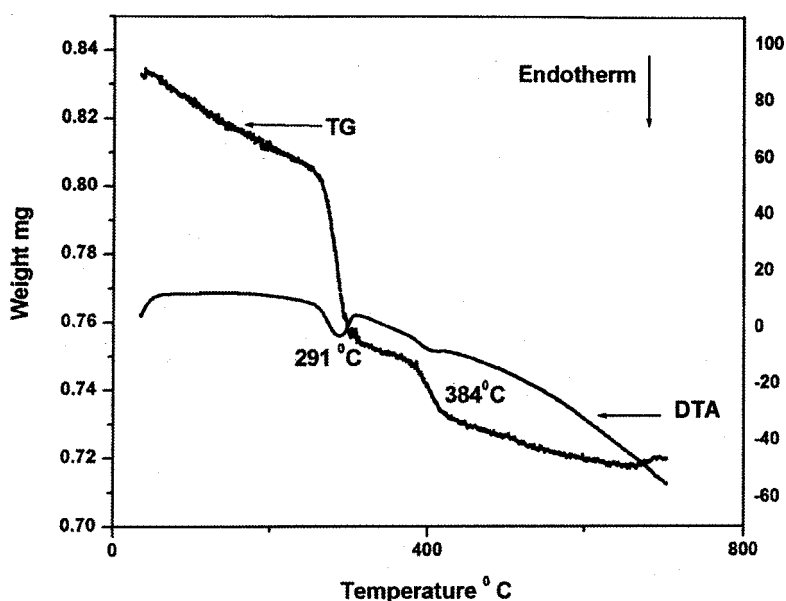


Figure 2.8 DTA-TG of intimate mixture of ceramic powders

2.4.2.2 Characterization of oxides, $\text{Nd}_2\text{Zr}_x\text{Ti}_{2-x}\text{O}_7$ ($x = 2.0, 1.8, 1.6, 1.4, 1.2$ and 1.0)

2.4.2.2.1 Phase identification of the oxides, $\text{Nd}_2\text{Zr}_x\text{Ti}_{2-x}\text{O}_7$ ($x = 2.0, 1.8, 1.6, 1.4, 1.2$ and 1.0) prepared by citrate gel and ceramic method

The X-ray diffraction patterns of green sample of $\text{Nd}_2\text{Zr}_2\text{O}_7$ and $\text{Nd}_2\text{Zr}_{1.8}\text{Ti}_{0.2}\text{O}_7$ prepared by citrate gel method show all the superstructure peaks in addition to the 100% peak (figure A-1 in appendix). The X-ray diffraction patterns of pyrochlore oxides of the series prepared by citrate gel method and sintered at 1400°C are shown in figure 2.9a. The crystalline phase formation was also observed for the products obtained by ceramic route, figure 2.9b. The d_{hkl} match well with the reported values in JCPDS file 17-0458.

The comparison of X-ray diffraction data of $\text{Nd}_2\text{Zr}_2\text{O}_7$ prepared by citrate gel method and ceramic method with reported data is tabulated in table 2.5. The calculated d values for other compositions of the series are compiled in table A-4 and A-5 respectively for ceramic method and citrate gel method samples. Rietveld refinement is done on $\text{Nd}_2\text{Zr}_2\text{O}_7$ prepared by citrate gel method. The profile is as given in figure 2.10.

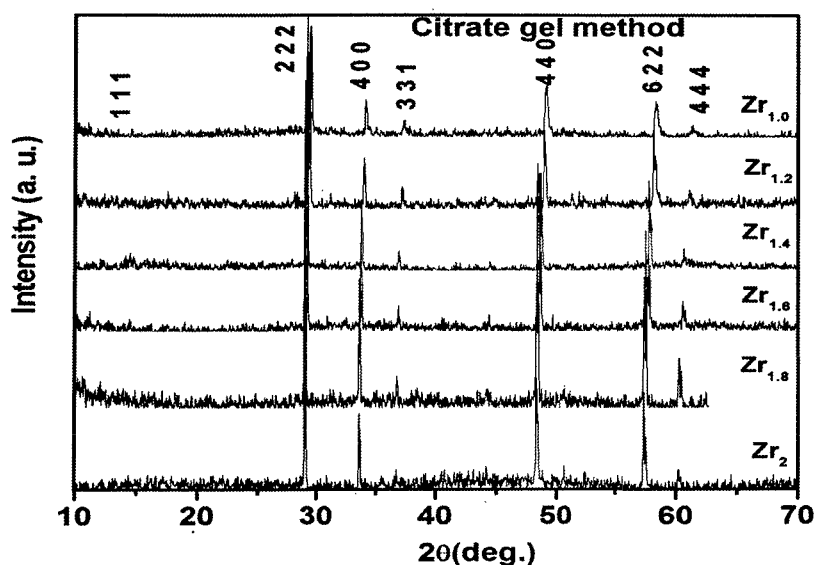


Figure 2.9a XRD patterns of the pyrochlore oxides $\text{Nd}_2\text{Zr}_x\text{Ti}_{2-x}\text{O}_7$ ($x = 2.0, 1.8, 1.6, 1.4, 1.2$ and 1.0) prepared by citrate gel method.

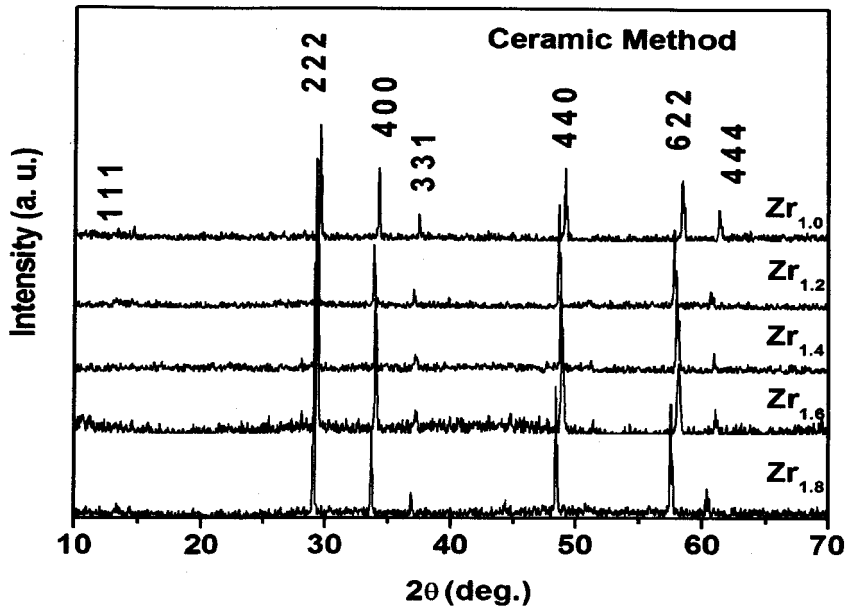


Figure 2.9b XRD patterns of the pyrochlore oxides $\text{Nd}_2\text{Zr}_x\text{Ti}_{2-x}\text{O}_7$ ($x = 1.8, 1.6, 1.4, 1.2$ and 1.0) prepared by ceramic method.

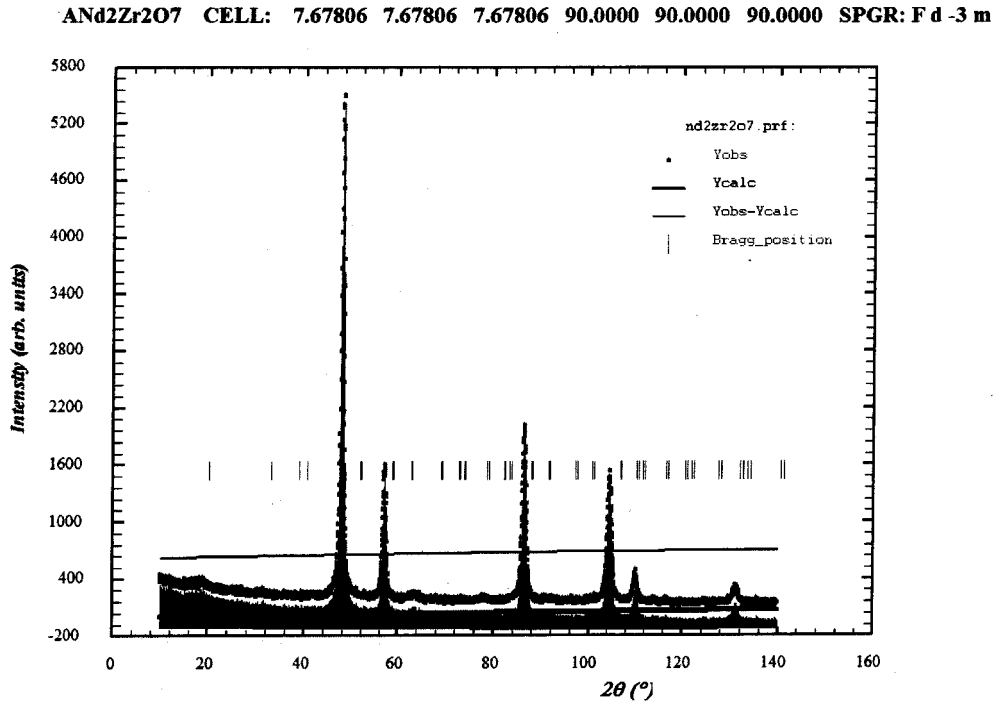


Figure 2.10 Refinement profile of $\text{Nd}_2\text{Zr}_2\text{O}_7$ prepared by citrate gel method

Table 2.5 Comparison of X-ray data of $\text{Nd}_2\text{Zr}_2\text{O}_7$ obtained by citrate gel method and ceramic method with reported data.

XRD Data of $\text{Nd}_2\text{Zr}_2\text{O}_7$ Roth.J.Res.Natl.Bur.Stand(U.S)56,17(1956)			XRD Data of $\text{Nd}_2\text{Zr}_2\text{O}_7$ Citrate gel method		XRD Data of $\text{Nd}_2\text{Zr}_2\text{O}_7$ Ceramic method	
2 θ	I/I ₀	hkl	2 θ	I/I ₀	2 θ	I/I ₀
14.413	6	111	14.420	2	14.255	1.4
29.061	100	222	29.020	100	28.940	100
33.664	50	400	33.640	32	33.545	29.9
36.803	8	331	36.886	3	36.670	4.3
44.230	6	511	44.260	7	44.050	2.6
48.318	70	440	48.314	47	48.145	42.1
57.359	65	222	57.356	41	57.165	40.1
60.151	16	444	60.216	4	59.658	9.8

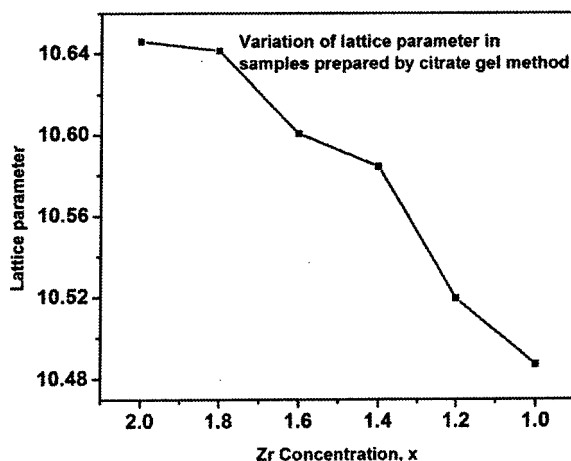


Figure 2.11 Variation lattice parameter with concentration of zirconium ion.

There is a linear decrease in the lattice parameter of the samples prepared by citrate gel

method with substitution of Zr by Ti. This is in accordance with Vegard's law for solid solutions [58]. The difference in ionic radii of Zirconium ion ($Zr^{+4} = 0.72 \text{ \AA}$) and Titanium ion ($Ti^{+4} = 0.605 \text{ \AA}$) are reflected in the decrease in lattice contraction on substitution of Zr by Ti. This lattice contraction upon substitution of Zr by Ti in neodymium zirconate corroborates the incorporation of Ti in the lattice. Similar trend is observed in the X-ray density (calculated from equation 2.6). The X-ray density decreases upon substitution of Zr by Ti. The reason for decrease in density may be due to vacancies created in the lattice on substitution of Zr by Ti.

The reported value of lattice parameter for $Nd_2Zr_2O_7$ is 10.648 [190]. Crystallite sizes calculated by using Scherer's formula suggest formation of nano sized oxides of 30-40 nm when prepared by citrate gel method. The crystallite size increases to 100-200 nm on sintering at higher temperatures. Samples prepared by ceramic method show a crystallite size of 100-200 nm = 1-2 μm (table A-5, appendix).

Table 2.6 Lattice parameter and density of $Nd_2Zr_xTi_{2-x}O_7$ ($x = 2.0, 1.8, 1.6, 1.4, 1.2$ and 1.0)

Ceramic method			Citrate gel method		
Sample	Lattice parameter 'a' (\AA)	Density (g/cm^3)	Sample	Lattice parameter 'a' (\AA)	Density (g/cm^3)
$Nd_2Zr_2O_7$	10.6821	6.3521	$Nd_2Zr_2O_7$	10.6459	6.4171
$Nd_2Zr_{1.8}Ti_{0.2}O_7$	10.6295	6.3509	$Nd_2Zr_{1.8}Ti_{0.2}O_7$	10.6414	6.3296
$Nd_2Zr_{1.6}Ti_{0.4}O_7$	10.5356	6.4242	$Nd_2Zr_{1.6}Ti_{0.4}O_7$	10.6006	6.3063
$Nd_2Zr_{1.4}Ti_{0.6}O_7$	10.5554	6.2897	$Nd_2Zr_{1.4}Ti_{0.6}O_7$	10.5843	6.2383
$Nd_2Zr_{1.2}Ti_{0.8}O_7$	10.5882	6.1344	$Nd_2Zr_{1.2}Ti_{0.8}O_7$	10.5192	6.2559
$Nd_2Zr_{1.0}Ti_{1.0}O_7$	10.5435	6.1144	$Nd_2Zr_{1.0}Ti_{1.0}O_7$	10.4869	6.2140

2.4.2.2.2 Density measurements of $\text{Nd}_2\text{Zr}_x\text{Ti}_{2-x}\text{O}_7$ ($x = 2.0, 1.8, 1.6, 1.4, 1.2$ and 1.0) prepared by citrate gel and ceramic method

Densities calculated by liquid displacement for powdered samples prepared by citrate gel method does not show a particular trend (Table 2.7), however a decrease in density within the series may be attributed to the presence of voids in the pyrochlore lattice. On sintering, the oxides prepared by citrate gel method achieve 90% of the theoretical density (calculated by using XRD data, Table 2.6) whereas oxides synthesized by ceramic method shows only 70% of the theoretical density. This supports the fact that samples synthesized by citrate gel method are dense.

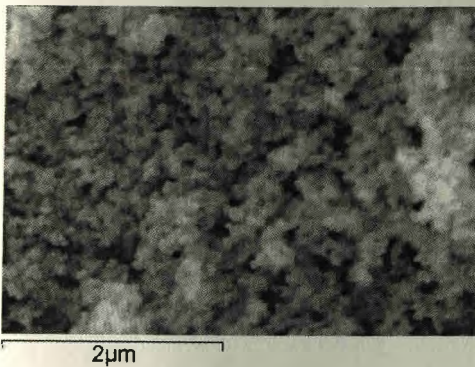
Table 2.7 Densities of $\text{Nd}_2\text{Zr}_x\text{Ti}_{2-x}\text{O}_7$ prepared by citrate gel method and ceramic method.

Sample	Citrate gel method		Ceramic method Density on sintering(g/cm^3)
	Pycnometric density (g/cm^3) (powdered sample)	Density on sintering(g/cm^3)	
$\text{Nd}_2\text{Zr}_2\text{O}_7$	3.73	6.31	4.43
$\text{Nd}_2\text{Zr}_{1.8}\text{Ti}_{0.2}\text{O}_7$	3.45	6.17	4.03
$\text{Nd}_2\text{Zr}_{1.6}\text{Ti}_{0.4}\text{O}_7$	4.49	6.25	3.60
$\text{Nd}_2\text{Zr}_{1.4}\text{Ti}_{0.6}\text{O}_7$	3.94	5.97	4.03
$\text{Nd}_2\text{Zr}_{1.2}\text{Ti}_{0.8}\text{O}_7$	4.56	5.44	3.82
$\text{Nd}_2\text{Zr}_{1.0}\text{Ti}_{1.0}\text{O}_7$	4.84	5.69	4.46

2.4.2.2.3 Microstructure (SEM) of $\text{Nd}_2\text{Zr}_x\text{Ti}_{2-x}\text{O}_7$ ($x = 2.0, 1.8, 1.6, 1.4, 1.2$ and 1.0) prepared by citrate gel and ceramic method

The SEM pictures of powders prepared by citrate gel method show uniform fine particles of 30-40 nm (figure 2.12). Representative micrographs of two compositions

(prepared by citrate gel and ceramic method), $\text{Nd}_2\text{Zr}_{1.8}\text{Ti}_{0.2}\text{O}_7$ and $\text{Nd}_2\text{Zr}_{1.0}\text{Ti}_{1.0}\text{O}_7$ are shown in the Figure 2.13-2.14. Micrographs of remaining compositions are compiled in figures A-2 (citrate gel method) and A-3 (ceramic method).



2.12 SEM of (as prepared) $\text{Nd}_2\text{Zr}_{1.8}\text{Ti}_{0.2}\text{O}_7$, citrate gel method(X30000)

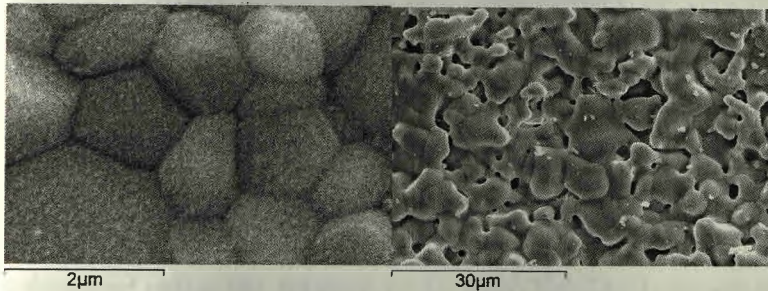


Figure 2.13 SEM of $\text{Nd}_2\text{Zr}_{1.8}\text{Ti}_{0.2}\text{O}_7$ (i) Citrate gel method and (ii) Ceramic method

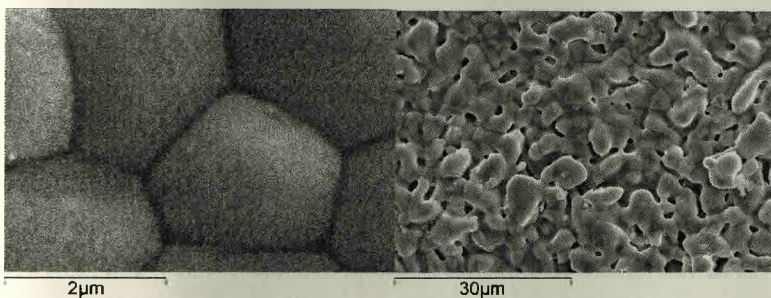


Figure 2.14 SEM of $\text{Nd}_2\text{Zr}_{1.0}\text{Ti}_{1.0}\text{O}_7$ (i) Citrate gel method and (ii) Ceramic method

These have very good sinterability and pack compactly on sintering. Zanetti et al. reported similar morphology of the oxides prepared by gel method [173]. The crystallites grow to $\sim 200\text{nm}$ on sintering thus forming dense pyrochlores. In the samples prepared by ceramic method there is no regularity in particle size. They show irregularly sintered particles with large interconnecting pores. The crystallite sizes are \sim

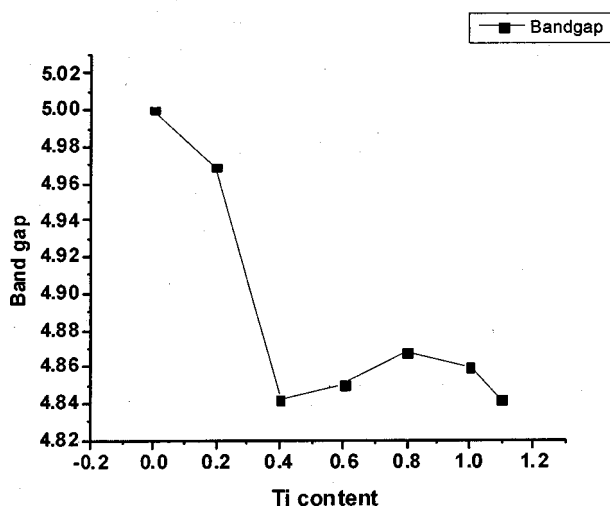
200 nm (Table A-5 in appendix). The SEM photographs of samples prepared by ceramic method are found to be similar to SEM pictures reported [20]. The SEM micrographs of the samples prepared by citrate gel method reveal that all grains are well connected in the pore free sintered body. This route of synthesis gives better morphology and packing of particles. This implies that the method of synthesis plays a major role in getting the desired morphology and homogeneity of particles. In various applications the requirement is not only the monophasic compound but also the microstructure of the sample.

2.4.2.2.4 Diffuse Reflectance and Absorbance spectra of oxides prepared by citrate gel method

Diffuse reflectance measurements were done to study the band gap of undoped $\text{Nd}_2\text{Zr}_2\text{O}_7$ and its modification upon doping with Ti. Band gap for the samples were calculated using the relation (2.8). Pure $\text{Nd}_2\text{Zr}_2\text{O}_7$ shows a band gap of 4.99 eV which decreases with increase in Ti content. The decrease is marginal (table 2.8). These values are in agreement with the reports that zirconates have large band gaps for electronic conduction i.e. they are insulators whereas titanates have band gap values sufficiently small for semiconducting behavior and exhibit mixed conduction [23]. Insulators show a band gap ~ 6 eV and Semiconductors show a band gap $\sim 0.5-3$ eV [182]. However in case of Ti doped samples, a second band gap is observed, which is due to presence of two conduction bands.

Table 2.8 Band gaps of $\text{Nd}_2\text{Zr}_x\text{Ti}_{2-x}\text{O}_7$ prepared by citrate gel method.

Compound	Band gap Eg1/Eg2 (eV)	Compound	Band gap Eg1/Eg2 (eV)
$\text{Nd}_2\text{Zr}_2\text{O}_7$	4.99	$\text{Nd}_2\text{Zr}_{1.4}\text{Ti}_{0.6}\text{O}_7$	4.85/3.37
$\text{Nd}_2\text{Zr}_{1.8}\text{Ti}_{0.2}\text{O}_7$	4.96/3.38	$\text{Nd}_2\text{Zr}_{1.2}\text{Ti}_{0.8}\text{O}_7$	4.88/3.37
$\text{Nd}_2\text{Zr}_{1.6}\text{Ti}_{0.4}\text{O}_7$	4.82/3.37	$\text{Nd}_2\text{Zr}_{1.0}\text{Ti}_{1.0}\text{O}_7$	4.85/3.35

**Figure 2.15 Variation of band gap with Ti concentration**

The diffuse reflectance spectra (figure 2.16) show variation in reflectance of $\text{Nd}_2\text{Zr}_2\text{O}_7$ and other compositions doped with Ti.

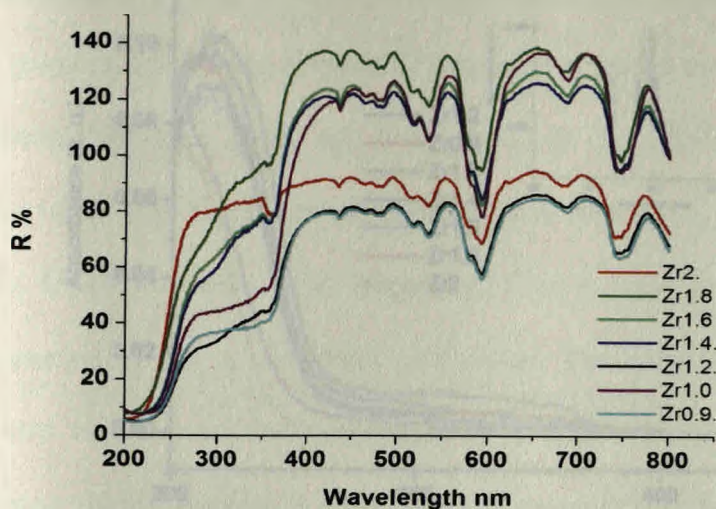


Figure 2.16 Diffuse reflectance spectra of $\text{Nd}_2\text{Zr}_x\text{Ti}_{2-x}\text{O}_7$ prepared by citrate gel method.

The absorbance spectra (figure 2.17) indicate a red shift in the absorbance of the solid solution on doping Zr with Ti. All samples show absorbance in the range 200-250 nm. There is also absorption at wavelength in the range of 300-400 nm in case of Ti doped samples which increases as Ti content increases. This may be attributed to titanium ion Ti^{+4} which do not show any absorption in the visible region. On introduction of Ti in the pyrochlore lattice, there is appearance of small peaks in the visible region of 540nm and 800nm. The absorbance peak at 540 nm may be due to Ti^{+3} . Recent studies on titanium glasses [191] have attributed this band to be due to ${}^2\text{B}_{2g} \rightarrow {}^2\text{B}_{1g}$ transitions of Ti^{+3} ion in distorted octahedral sites.

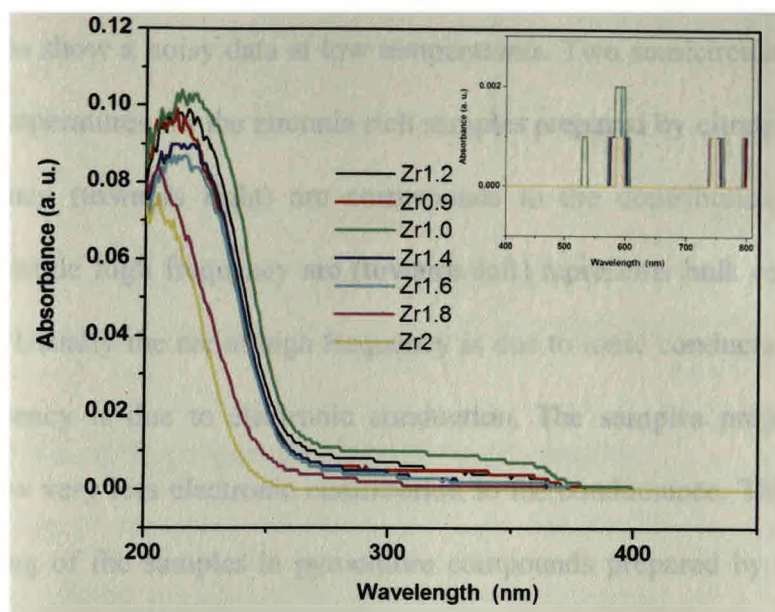


Figure 2.17 Absorbance spectra of $\text{Nd}_2\text{Zr}_x\text{Ti}_{2-x}\text{O}_7$ prepared by citrate gel method.

2.4.2.2.5 Conductivity studies

Zirconate pyrochlores are good oxide ion conductors but they also show a significant amount of electronic conduction on forming solid solutions with titanium [23]. The mechanism responsible for the underlying the ionic conductivity in pyrochlore oxides is the hopping of oxygen over oxygen ion vacancies in the 48f sites [32, 43, 55]. The vacancies are generated due to cation disorder in the structure. Oxygen diffusion occurs by hopping from 48f to 48f sites.

Pyrochlore oxides predominantly show ionic conductivity at low temperatures and electronic conductivity at very high temperatures. The alternating current impedance at different temperatures till 700°C was plotted in the complex plane for the samples $\text{Nd}_2\text{Zr}_x\text{Ti}_{2-x}\text{O}_7$ synthesized by ceramic route and citrate gel method. Figure 2.18 shows impedance plots for a) $\text{Nd}_2\text{Zr}_2\text{O}_7$, b) $\text{Nd}_2\text{Zr}_{1.8}\text{Ti}_{0.2}\text{O}_7$ prepared by citrate gel method. The plots for other compositions of both citrate gel and ceramic method are compiled in

figures A-4 in appendix.

The samples show a noisy data at low temperatures. Two semicircular arcs are visible at higher temperatures for the zirconia rich samples prepared by citrate gel method. The low frequency (towards right) arc corresponds to the contribution from the grain boundaries while high frequency arc (towards left) represents bulk contribution to the impedance. Usually the arc at high frequency is due to ionic conduction and the one at lower frequency is due to electronic conduction. The samples prepared by ceramic method show very less electronic contribution to the conductance. This may be due to poor sintering of the samples in pyrochlore compounds prepared by ceramic method. The samples prepared by citrate gel method due to proper sintering also show grain boundary contribution to the conductivity.

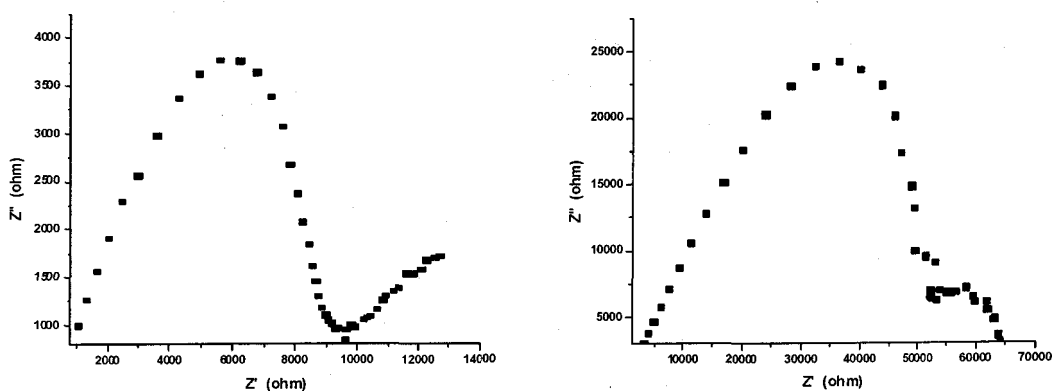


Figure 2.18 Impedance plots for a) $\text{Nd}_2\text{Zr}_2\text{O}_7$, b) $\text{Nd}_2\text{Zr}_{1.8}\text{Ti}_{0.2}\text{O}_7$ prepared by citrate gel method.

The direct current (dc) bulk resistance values from these plots were used to find direct current (dc) conductivity. The reported value of ionic conductivity for $\text{Nd}_2\text{Zr}_2\text{O}_7$ at 1000K is $2.7 \times 10^{-5} \text{ Scm}^{-1}$ [192], whereas $\text{Nd}_2\text{Zr}_2\text{O}_7$ prepared by citrate method in the present study shows a value of $2.2628 \times 10^{-5} \text{ Scm}^{-1}$ at 973 K. The highest value of σ_{dc} is found to be $1.8643 \times 10^{-4} \text{ Scm}^{-1}$ for $\text{Nd}_2\text{Zr}_{1.8}\text{Ti}_{0.2}\text{O}_7$ prepared by citrate gel method.

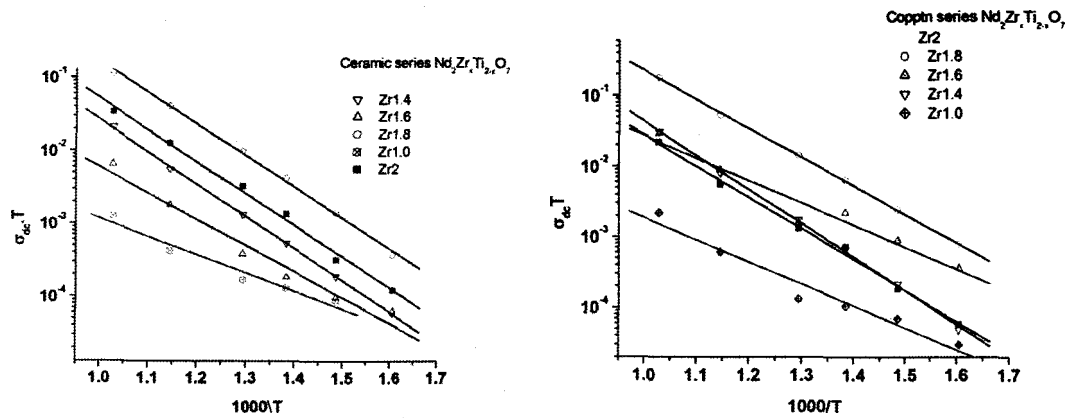


Figure 2.19 σ_{dc} of (i) ceramic and (ii) citrate gel samples.

If extrapolation of the graph (in figure 2.19) for $\text{Nd}_2\text{Zr}_{1.8}\text{Ti}_{0.2}\text{O}_7$ is done and σ_{dc} is calculated at 1000K citrate gel sample shows conductivity of $1.7 \times 10^{-3} \text{ Scm}^{-1}$ and ceramic sample shows conductivity of $8.1 \times 10^{-4} \text{ Scm}^{-1}$. These materials can be good candidates for use in fuel cells. Table 2.9 gives the values of σ_{dc} for the pyrochlore oxides prepared by both the methods. It is observed that the conductivity of the oxides prepared by citrate gel method is slightly higher than that of the oxides prepared by ceramic method. This may be explained on the basis of morphology of the sintered oxides. In oxides prepared by ceramic method, the particles are poorly sintered with large no of pores whereas the oxides prepared by citrate gel method have well connected grains in the pore free sintered body. The values of activation energy and pre-exponential factor determined from the linear fits to the σ_{dc} plots are included in the Table 2.9.

Table 2.9 variation of σ_{dc} , pre-exponential factor (σ_0) and activation energy (E) with decrease in concentration of Zr.

Citrate gel	σ_{dc} (Scm ⁻¹) at 973 K	E (eV)	σ_0	Ceramic	σ_{dc} (Scm ⁻¹) at 973 K	E (eV)	σ_0
Nd ₂ Zr ₂ O ₇	2.2628x10 ⁻⁵	0.87	6.9748x10 ²	Nd ₂ Zr ₂ O ₇	3.5158x10 ⁻⁵	0.86	1.118x10 ³
Nd ₂ Zr _{1.8} Ti _{0.2} O ₇	1.8643 x10 ⁻⁴	0.82	3.0200x10 ³	Nd ₂ Zr _{1.8} Ti _{0.2} O ₇	1.1981x10 ⁻⁴	0.90	6.607x10 ³
Nd ₂ Zr _{1.6} Ti _{0.4} O ₇	3.0349x10 ⁻⁵	0.62	3.7910x10 ¹	Nd ₂ Zr _{1.6} Ti _{0.4} O ₇	6.7241x10 ⁻⁶	0.70	2.229x10 ¹
Nd ₂ Zr _{1.4} Ti _{0.6} O ₇	3.1827x10 ⁻⁵	0.95	2.6146x10 ³	Nd ₂ Zr _{1.4} Ti _{0.6} O ₇	2.2082x10 ⁻⁵	0.87	6.543x10 ²
Nd ₂ Zr _{1.0} Ti _{1.0} O ₇	2.2512x10 ⁻⁶	0.62	2.3892	Nd ₂ Zr _{1.0} Ti _{1.0} O ₇	1.3237x10 ⁻⁶	0.49	2.7782

Neutron diffraction studies [55] have shown that a typical pyrochlore like Nd₂Zr₂O₇ has frenkel defects of about 5% in the oxide ion sub lattice of the compound at 673 K. It is because of these defects there is some conductivity in the almost perfect lattice of Nd₂Zr₂O₇. The conductivity is maximum at the composition of Zr, x = 1.8 for the samples prepared by both the methods as seen in Table 2.9 and Figure 2.19. It then decreases as the Zr content decreases. Thus doping pyrochlore oxide at B site with small amount of Ti ion helps in increasing the conductivity.

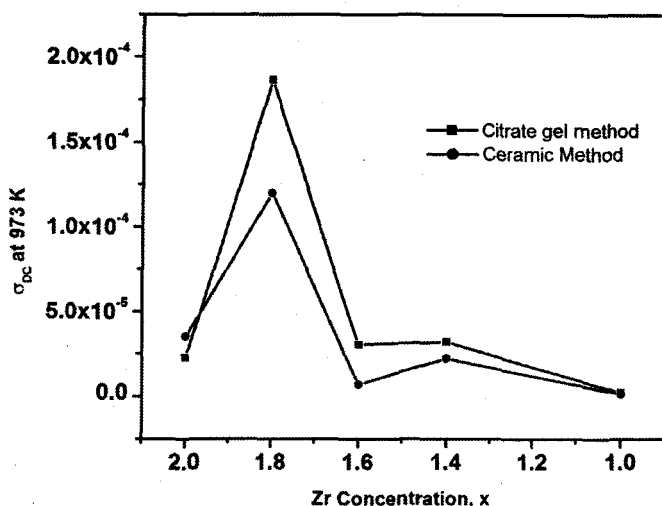


Figure 2.20 Variation of σ_{dc} with Zr content

The ordered pyrochlore structure provides low energy pathways for oxide ion migration. This results in decreased activation energy but the number of mobile oxide ions will be small due to order in the lattice. Cation disordering can cause an increase in frenkel defects at the oxide ion sites. This increases the pre-exponential factor, but also increases the activation energy [55]. Thus the increase in pre-exponential factor increases the conductivity but an increase in activation energy hinders the migration of oxide ions.

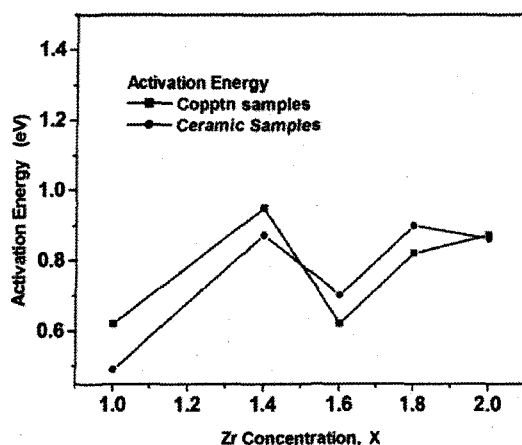


Figure 2.21 Variation of activation energy with Zr content.

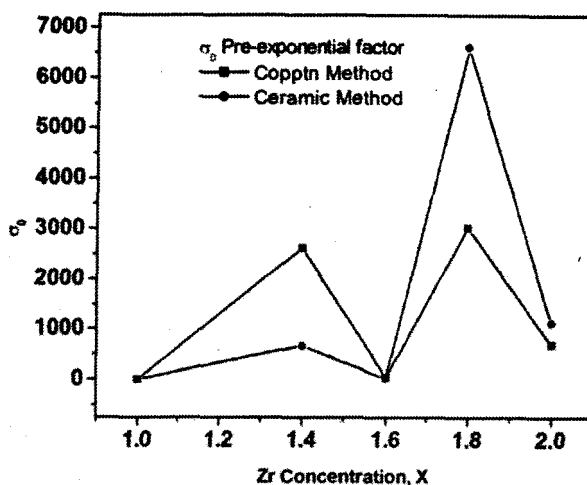
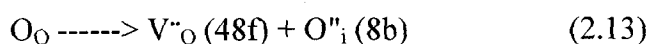


Figure 2.22 Variation of σ_0 with Zr content.

The increase in conductivity at composition of Zr, $x = 1.8$ ($\sigma_{dc} = 1.8643 \times 10^{-4} \text{ Scm}^{-1}$) at 973 K is due to increase in concentration of charge carriers as seen from pre-exponential factor. The decrease in the dc conductivity with further increase in Ti concentration is due to hindrance to the movement of charge carriers in the lattice, even though the activation energy for the conduction process remains low. This indicates that the order sets in the structure on further incorporation of Ti in the lattice. For the Ti content, $x = 1.0$ the conductivity is least which may be due to ordering of both cation and anion arrays on substitution of Zr ($Zr^{+4} = 0.72 \text{ \AA}$) by Ti ($Ti^{+4} = 0.605 \text{ \AA}$) when Ti:Zr is 1:1. Pyrochlore oxide series of the type $Gd_2Zr_xTi_{2-x}O_7$ is already investigated [193] and an increase in conductivity is reported on substitution of Ti by Zr. The XPS studies done by the researchers on the same system indicates that as Zr substitutes for Ti in $Gd_2Ti_2O_7$ to form $Gd_2(Ti_{1-x}Zr_x)_2O_7$, ($0.25 < x \leq 0.75$), cation antisite disorder occurs simultaneously with anion disorder which increases the conductivity [34].

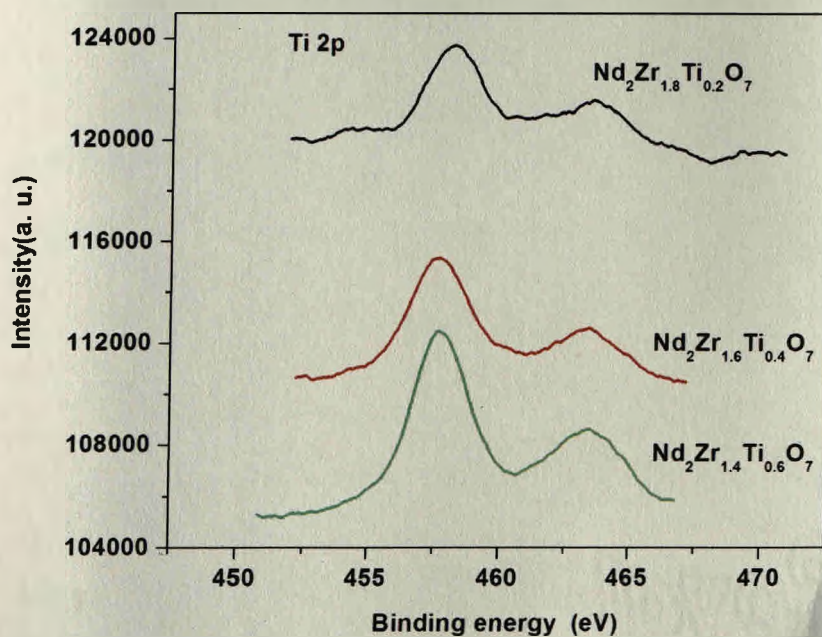
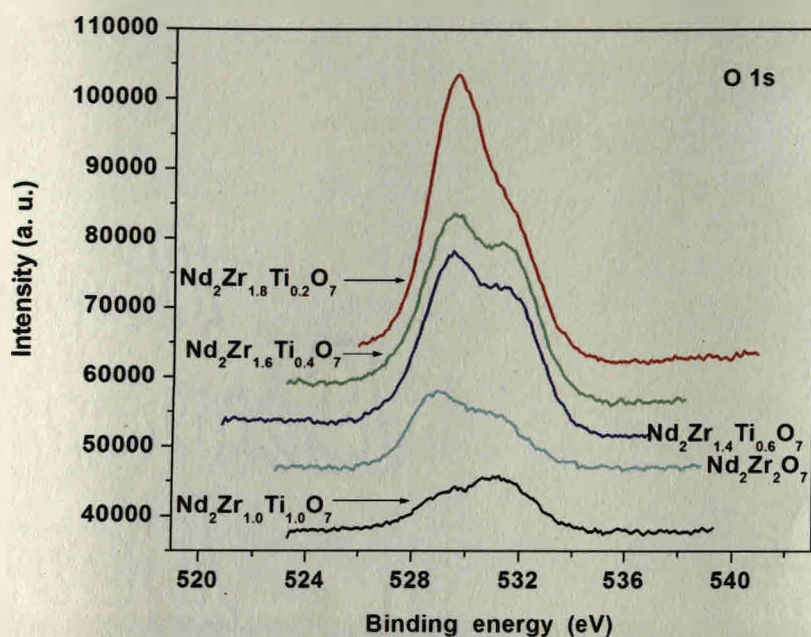
To understand the structure and the kind of defects in the lattice of $Nd_2Ti_xZr_{2-x}O_7$, XPS and ESR are used as tools. In pyrochlore oxide there are two types of oxygen sites (48f and 8a) occupied by oxide ions. The O 1s XPS shows two peaks, the one at lower BE is

for 8a oxygen and higher one for 48f oxygen. The difference in binding energy of oxygen is the consequence of the difference in the effective negative charge on oxygen. Lower the BE, higher the average electron density on the element. In $\text{Nd}_2\text{Zr}_2\text{O}_7$ six out of every seven oxygen ions occupy the 48f sites and each is coordinated by two Nd and two Zr/Ti ions. The other oxide ion occupies the 8a site and is surrounded by 4 Nd ions. Considering lower electronegativity of Nd^{+3} as compared with that of $\text{Zr}^{+4}/\text{Ti}^{+4}$ the ionic character of the Nd-O bond is greater than that of Zr-O/Ti-O bond. This means that the electron density on oxygen for Nd-O bond is higher than that of the Zr-O/Ti-O bond. Thus the peak in the O 1s spectra at lower BE is assigned to oxygen ions at 8a sites and the peak at higher BE is assigned to O at 48f sites. The XPS spectrum of O 1S electron (figure 2.23a) shows 2 peaks in case of $\text{Nd}_2\text{Zr}_2\text{O}_7$ which is also seen in case of $x = 0.4, 0.6$. The two peaks observed are corresponding to 48f and 8a oxygen ions. In case of $\text{Nd}_2\text{Ti}_2\text{O}_7$ also this difference in chemical environment of oxygen ions is reported by Atuchin et.al [194]. In $\text{Nd}_2\text{Ti}_2\text{O}_7$, the O 1s line is shown to have a main component at 529.4 eV and two weak intensity components at 527.1 and 531.8 eV. The small peak at the higher B.E. of 531.8 eV may be due to adsorbed OH groups and the other two components seem related to oxygen states in the crystal bulk. However in case of $\text{Nd}_2\text{Zr}_{1.8}\text{Ti}_{0.2}\text{O}_7$ there is merging of the peaks into one which means that the chemical environment of oxygen ions at 48f and 8a sites has become identical. This happens because of antisite cation disorder which leads to the environment of the 48f and 8b ions becoming more similar and giving rise to frenkel defect formation. These two are the two main disordering mechanisms in pyrochlore $\text{A}_2\text{B}_2\text{O}_7$



Thus the similarity between the two oxygen sites in pyrochlore oxides is a result of

disorder on cation antisites [34]. When the radii of the A and B cations are similar, there is cation swapping which leads to formation of cation antisites [20].



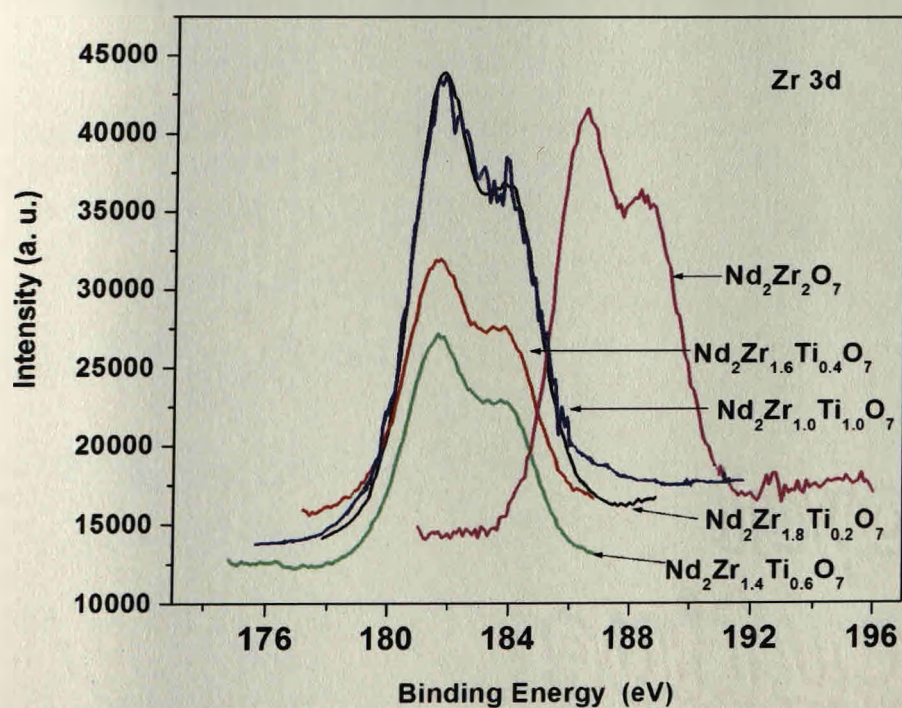
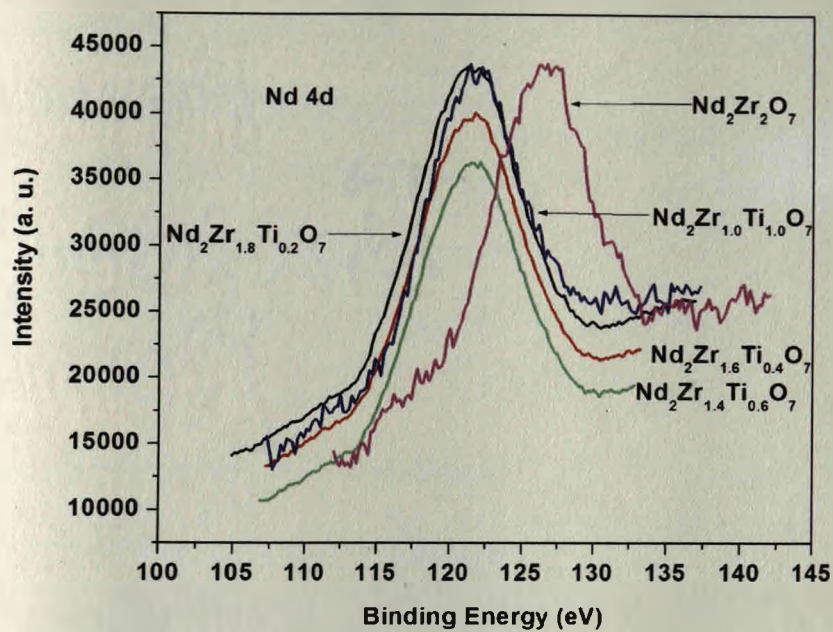


Figure 2.23 XPS spectrum of (a) O 1s electron, (b) Ti 2p electron, (c) Nd 4d electron, (d) Zr 3d electron

In the XPS spectrum of Ti 2p electron (figure 2.23 b), the recorded spectrum shows doublet with BE (Ti2p_{3/2}) at 457eV and BE (Ti2p_{1/2}) at 463 eV. The doublet is due to spin orbit interactions splitting of Ti2p into 2p_{3/2} and 2p_{1/2} states and spin orbit splitting $\Delta(\text{Ti}2p_{3/2}-\text{Ti}2p_{1/2}) = 6\text{eV}$. These are close to the values reported [195]. Presence of Ti⁺⁴ and Ti⁺³ is indicated by broadening of the Ti 2p lines in accordance with literature [196]. The peak for TiO is reported at lowest BE at 455.7 eV [197]. Ti⁺³ is reported at 457.8 eV [198]. A peak centred at 459.6 eV, is identified as Ti⁺⁴ in TiO₂ in literature [199].

The XPS spectrum of Nd 4d electron (figure 2.23 c), shows a peak at 126 eV in Nd₂Zr₂O₇ which gets shifted to lower binding energies of 122 eV on substitution of Zr by Ti. This lowering of the binding energy indicates higher average electron density on the element. In case of Zr 3d electron in Nd₂Zr₂O₇, (figure 2.23 d), a doublet is shown at 188 eV and 186.5 eV. The doublet is shifted to lower binding energy i.e. 184 eV and 182 eV with increase in Ti. The higher B.E. peak may be attributed to Zr 3d_{3/2} and lower one is due to Zr 3d_{5/2} and $\Delta(\text{Zr}3d_{5/2}-\text{Zr}3d_{3/2}) = 2\text{ eV}$ in accordance with reported [195]. In general it is observed that in the XPS spectra of Zr 3d and Nd 4d there is shift from higher BE of Nd₂Zr₂O₇ to lower BE on doping Zr with Ti indicating incorporation of Ti in the lattice.

ESR of the some representative compounds show a broad asymmetric line with $g = 1.905$ in all the compositions (figure 2.24). The presence of a signal at $g = 1.905$ is indicative of Ti⁺³ in the lattice [178]. The ESR signal also points out that Ti⁺³ is present in a distorted octahedral symmetry [191].

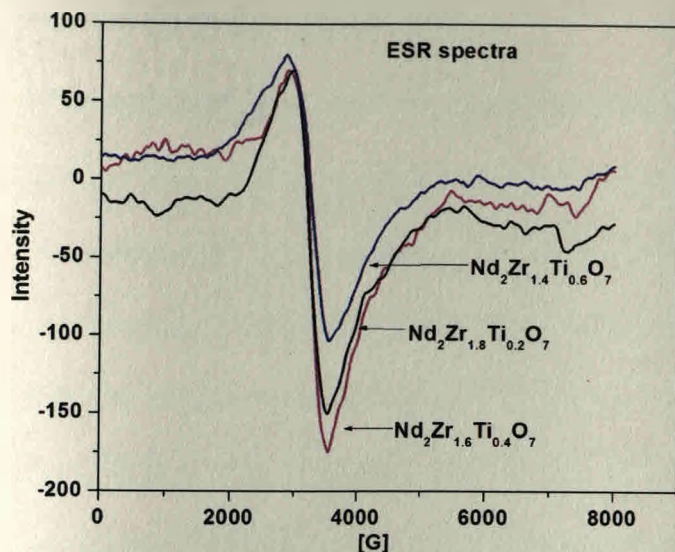


Figure 2.24 ESR spectra of some representative samples prepared by citrate gel method

Thus because of Ti^{+4} going to Ti^{+3} , there are vacancies created at the oxide ion site to maintain charge balance. This vacancy creation favours the diffusion of oxide ions and thus disorder in the lattice. An idea of disorder in the lattice is best reflected by an increase in ionic conductivity which is reported in table 2.9. The highest conductivity is exhibited by $Nd_2Zr_{1.8}Ti_{0.2}O_7$ [200].

Thus $Nd_2Zr_{1.8}Ti_{0.2}O_7$ pyrochlore compound can be used as a host for nuclear waste since already disordered it will be able to withstand high levels of radiation and morphologically the individual particles so closely packed that it will not let the radioactive material to leach out.

[200] R. Karmali, V.P. Borker, K.S. Rane, S.K. Deshpande, " Citrate gel route for synthesis of dense pyrochlores" *Materials chemistry and physics*, 129:3(2011) 1116-1120.

2.4.3 $\text{Nd}_{2-y}\text{Sr}_y\text{Zr}_2\text{O}_7$ ($x = 1.8, 1.0, 0.05$)

2.4.3.1 Phase identification of the thermal products of metal oxide precursors

Strontium Sr^{+2} (1.12 Å) being slightly larger than Nd^{+3} (1.01 Å) enters A site in the pyrochlore lattice [55]. The compositions prepared by doping with Sr in the pyrochlore lattice in the series $\text{Nd}_{2-y}\text{Sr}_y\text{Zr}_2\text{O}_7$ ($y = 1.8, 1.0$) led to the formation of perovskites SrZrO_3 and the resulting product becomes a pyrochlore-perovskite composite. However the composition with minimal amount of Sr gave pure pyrochlore oxide $\text{Nd}_{1.95}\text{Sr}_{0.05}\text{Zr}_2\text{O}_7$. XRD analysis reveals pure single phase compound which on sintering at 1400°C further increases the crystallites and refines the structure.

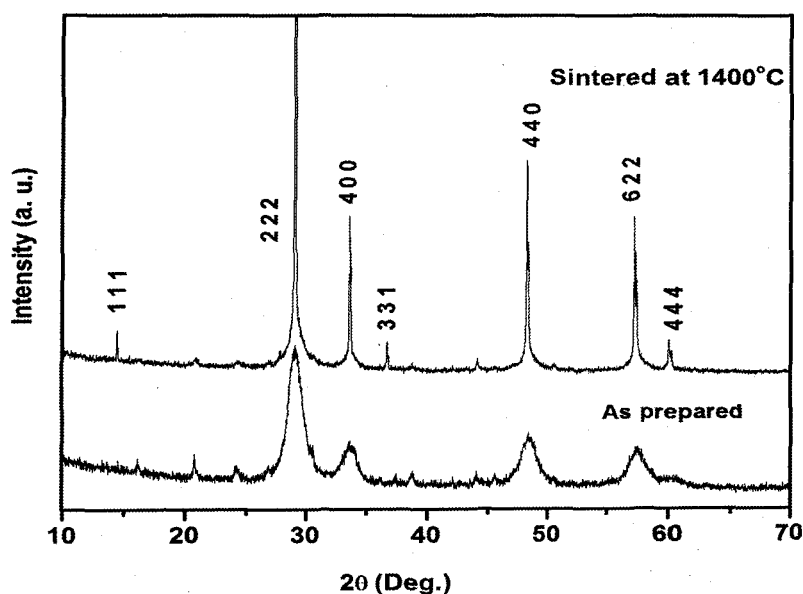


Figure 2.25 XRD patterns of $\text{Nd}_{1.95}\text{Sr}_{0.05}\text{Zr}_2\text{O}_7$ (i) powdered and (ii) Sintered at 1400°C .

2.4.3.2 Diffuse Reflectance and Absorbance spectra of pyrochlore oxides

Introduction of Sr in the crystal lattice of Neodymium zirconate causes a blue shift~200nm in the absorbance of the oxide. Calculated optical bandgap of the material is

4.85 eV.

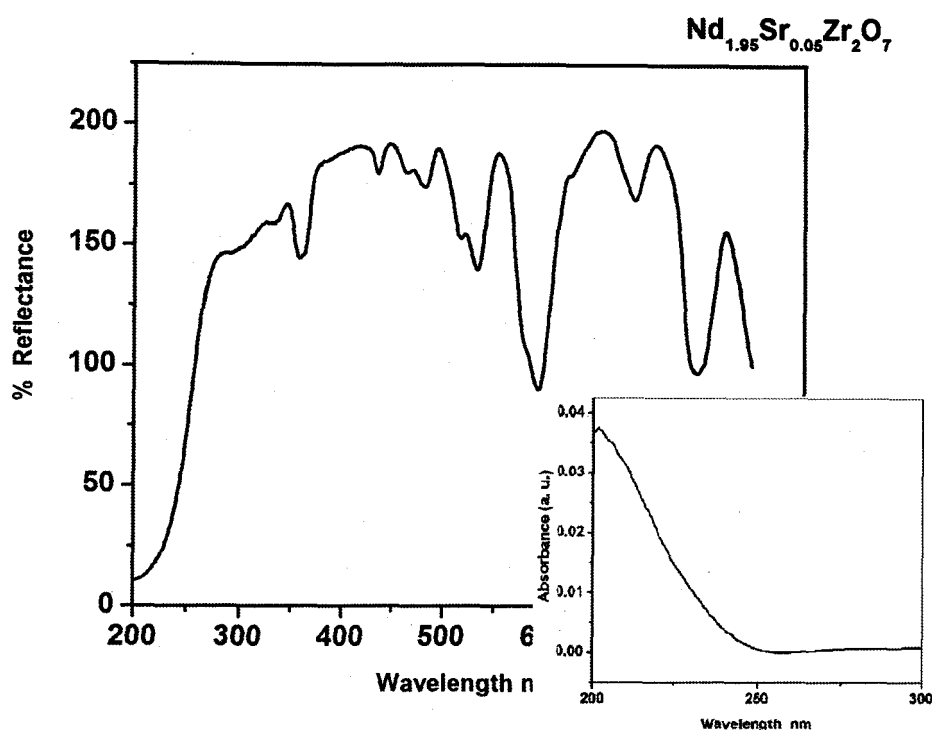


Figure 2.26 Diffuse Reflectance spectrum of $\text{Nd}_{2-y}\text{Sr}_y\text{Zr}_2\text{O}_7$ ($y = 0.05$) (Inset absorbance spectrum).

2.4.3.3 Leaching studies on $\text{Nd}_{2-y}\text{Sr}_y\text{Zr}_2\text{O}_7$ ($x = 0.05$)

The high level nuclear waste having long half life remains radioactive for a longer period. This high level waste is incorporated in the matrix of borosilicate glass or experimentally in pyrochlore lattice so as not to leach to the surrounding. The radioactivity is prevented by containment of the matrix in steel canister followed by concrete cover. But if radioactive element comes in contact with water, it leaches in the water body thereby contaminating the water. Thus the most important property of a nuclear waste form is its chemical durability when in contact with aqueous solutions. An ideal nuclear waste form should not allow the radionuclides to leach out in water on contact. For most safety analyses, the amount and type of radioactivity released into

solution by the solid waste form are the critical parameters, and a number of standard tests have been developed to provide this information [49]. Zirconate pyrochlore because of its high resistance to radiation damage is investigated here for its chemical durability. One of the pathways of nuclear fission of U-235 is fragmentation yields Sr hence nonradioactive isotope of strontium is incorporated in the lattice of zirconate pyrochlore. The performance assessment is done based on leachability of strontium from the oxide lattice. Deionized water is used for reference since it is simulant of fresh type groundwater [201].

The total amount of strontium in 1g pellet of pyrochlore is ~ 0.00748 grams as analysed by atomic absorption spectroscopy. Leaching studies were done on the powdered sample as well as pelletized samples sintered at 1000°C and 1400°C . Deionised water used for the purpose was free of strontium. Results of leaching studies are compiled in the table 2.10 below. Powdered sample on mixing with water analysing for Sr immediately indicates 22.21% release of total Sr present in the sample.

Table 2.10 Leaching studies of Sr carried out on $\text{Nd}_{1.95}\text{Zr}_2\text{Sr}_{0.05}\text{O}_7$

Days	Powdered sample % Leaching of Sr	Pellet sintered at 1000°C % Leaching of Sr		Pellet sintered at 1400°C % Leaching of Sr	
		RT	75°C	RT	75°C
30	80.82	67.20	73.26	2.56	8.68
60	90.11	68.93	86.81	5.22	11.70
90	90.11	77.67	86.81	10.50	23.30

Powdered sample kept at room temperature (stirred continuously) for 90 days show maximum amount of strontium upto 90 % in the water after 90 days. Pelletized sample (sintered at 1000°C) immersed in water at room temperature show 67% of the total strontium after 30 days which increases to 69% after another 30 days and to 78% after total of 90 days in water. Data obtained for the studies carried out at 75°C are comparable to the studies done at room temperature for over 3 years. This study indicates 73% of the total strontium after 30 days which increases to 87% after 60-90 days. The washing off of strontium from the pellets is supported by change in the morphology of the pellets immersed in water at RT and at high temperature of 75°C (figure 2.27). Pelletized sample (sintered at 1400°C) immersed in water at room temperature shows 2.56% of the total strontium after 30 days which increases to 5.22 % after 60 days and to 10.50 % after 90 days in water. Leaching studies carried out at 75°C indicates 8.68 % of the total strontium after 30 days which goes to 11.70 % after 60-days and 23.30 % after 90 days. The morphology of the pellets after carrying out leaching studies supports the observations (figure 2.28).

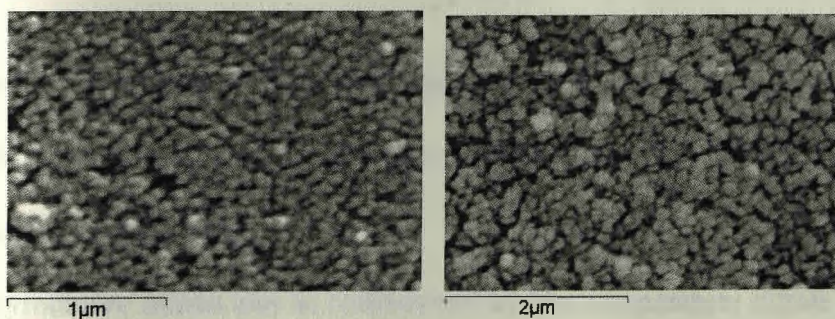


Figure 2.27 SEM of pelletized $\text{Nd}_{1.95}\text{Zr}_2\text{Sr}_{0.05}\text{O}_7$ sintered at 1000°C (x 50000), 1) before use for leaching, 2) after use for leaching (x 30000) of strontium at 75°C .

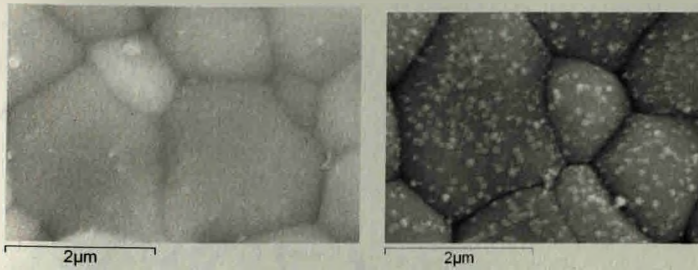


Figure 2.28 SEM of pelletized $\text{Nd}_{1.95}\text{Zr}_2\text{Sr}_{0.05}\text{O}_7$ sintered at 1400°C , 1) before use for leaching (x 30000), 2) after use for leaching (x 30000) of strontium at 75°C .

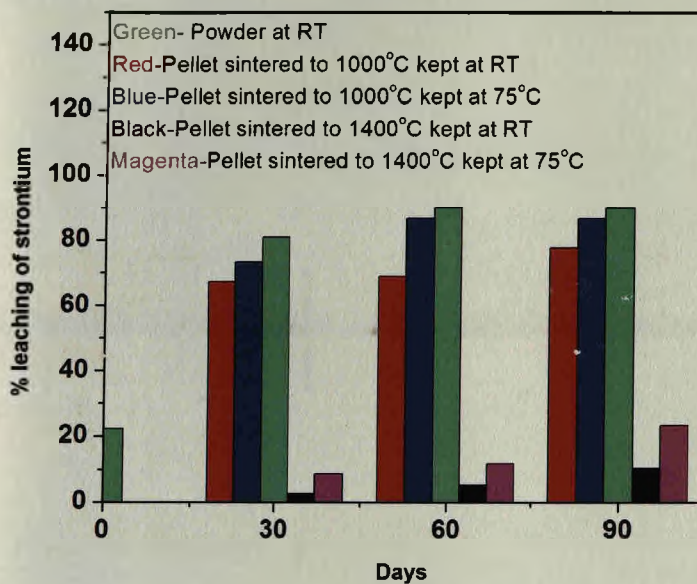


Figure 2.29 Leaching of strontium from the matrix of $\text{Nd}_{2-y}\text{Sr}_y\text{Zr}_2\text{O}_7$ ($y = 0.05$).

Thus it can be inferred that sintering the pyrochlore lattice at 1400°C is reasonably sufficient to hold Sr in it.

Thus pyrochlore oxides can be synthesized by low temperature citrate gel method. The oxides obtained sinter compactly and thus are very good materials for nuclear waste disposal. The pyrochlore oxides obtained on doping zirconates with titanium show cation antisite disorder in the lattice of $\text{Nd}_2\text{Zr}_{1.8}\text{Ti}_{0.2}\text{O}_7$. The material can thus serve as a host for nuclear waste. This oxide shows increased conductivity and can be thought of as a fuel cell material.

Chapter 3

ZnO System for

Photomineralization of organic compounds

Antibacterial Action and

Photodegradation of NO_x

3.1 Introduction

Zinc oxide photocatalyst finds applications in many fields like pollution control, degradation of environmental hazardous gases, removal of organic pollutants from water and inhibiting growth of undesirable microorganisms. It is a well-known semiconductor with an average bandgap of 3.37 eV. On exposure to ultraviolet radiations, electron-hole pairs are generated in it. UV radiation constitutes only few percents of the sunlight that reaches the earth's crust. Thus the scope of using solar light as a source of UV radiations is limited. Hence researchers are making efforts to exploit the visible light in photocatalysis by modifying the material properties through cation or anion doping and introducing oxygen deficiency.

The chapter deals with the experimental details and conclusions derived from the investigation done on zinc oxide/doped zinc oxide systems prepared with the aim to tap visible light from solar radiations. The synthesis of undoped and doped zinc oxide via oxalate and hydrazinated oxalate precursor methods and the various analytical techniques used for characterisation are described in the experimental section. The results and discussion section of this chapter deals with the analysis of oxalate and hydrazinated oxalate precursors of zinc oxide. The thermal decomposition of these complexes leading to formation of zinc oxide is studied by DTA-TG technique. The oxides are characterized by X-Ray diffraction (XRD), Scanning Electron Microscopy (SEM), X-Ray Photoelectron Spectroscopy (XPS), Energy Dispersive X-ray Spectroscopy (EDS) and Nitrogen analysis. The oxides of zinc prepared by three different methods are checked for their efficacy in photocatalytic degradation of Methylene Blue (MB), a model organic dye. Photodegradation of an industrial effluent is also tried using these oxides as a case study. It is reported that zinc oxide is good in abatement of NO_x, so studies have been carried out considering this aspect.

Antibacterial activity of undoped and doped ZnO is studied against *E. coli* cultures. *E. coli* is a gram negative bacterium responsible for food poisoning.

ZnO doped with small amounts of aluminium with valency +3 produces p-type ZnO. In the present study it has been synthesized and its dye degradation efficiency, antibacterial activity, NO_x abatement ability are checked. ZnO synthesis by spray pyrolysis method is also attempted.

3.2. Methods of preparation of Materials

Ultrafine metal oxides are produced by several modern methods like spray pyrolysis, pulsed laser ablation, ion sputtering and thermal decomposition. The use of these methods is limited due to high cost involved in the instrumentation or long time duration required for synthesis. To overcome these problems, an attempt is made to prepare fine oxides in our pot synthesis through precipitation as metal oxalate precursors followed by their thermal decomposition. Modification of the precursors is done by a novel hydrazine method. Hydrazine not only acts as a fuel but also takes part as a ligand in altering the precursor composition and modifies the thermal path. This results in a product at much lower temperatures as compared to the unhydrazinated precursors. In our spray pyrolysis method for the synthesis of oxides, the hydrazine assisted pyrolysis of metal nitrates is done in a home built apparatus. Hydrazine acts as a fuel during pyrolysis and also scavenges the nitrate ions to produce environment friendly by-products. Hence the methods are green and environment friendly. In the present investigation zinc oxide is prepared by pot synthesis as well as spray pyrolysis. The chemicals used for the synthesis are of analytical grade (AR). Distilled water is used throughout the synthesis.

3.2.1 Oxalate method

Stoichiometric amount of $\text{ZnCl}_2 \cdot \text{H}_2\text{O}$ solution (0.1 M) was taken in three necked flasks and stirred constantly on magnetic stirrer for few minutes. To this well stirred solution, required amount of warm oxalic acid solution (0.1 M) was added drop wise with constant stirring. The precipitate obtained was filtered and washed with distilled water. Washings were carried out until the precipitate was free from chloride. The precipitate was finally washed with alcohol. The oxalate precursor was dried at room temperature in a desiccator. The precursor obtained was labeled as OX.

3.2.2 Hydrazinated oxalate (Equilibration method)

a. ZnO System

Hydrazination of oxalate precursor was carried out by equilibration method. In this method, the dried oxalate precursor as prepared in section 3.2.1 was spread on a Petri dish and placed in a desiccator containing hydrazine hydrate (99% Merck). The hydrazine uptake was measured titrimetrically using standard KIO_3 [180]. The obtained precursor was labeled as OXE.

b. Aluminium doped ZnO

Aluminium (0.0005, 0.001, 0.002 and 0.003%) doped ZnO samples were prepared by hydrazinated oxalate (equilibration) method. Stoichiometric amount of metal salts (Zinc Chloride and Aluminium Chloride) solution was taken in three necked flask and stirred constantly on magnetic stirrer for few minutes. To this well stirred solution, required amount of oxalic acid solution was added drop wise with constant stirring. The precipitate obtained was filtered and washed with distilled water until the washings were free from chloride. The precipitate was finally washed with alcohol and air dried at room temperature. The dried oxalate precursor was spread in a desiccator containing

hydrazine hydrate (99% Merck). The hydrazine uptake was measured titrimetrically using KIO_3 [180]. The obtained precursors were labeled as E0.5, E1, E2 and E3.

3.2.3 Hydrazinated oxalate (Solution method)

a. ZnO System

The hydrazinated precursor was also obtained by adding stoichiometric amount of $\text{ZnCl}_2 \cdot \text{H}_2\text{O}$ solution (0.1 M) to a well stirred oxalic acid (0.1 M) and hydrazine hydrate solution (99% Merck) in three necked flask under inert (N_2 gas) atmosphere. The precipitate was filtered, washed with water and air dried. The precursor obtained was labeled as OXS.

b. Aluminium doped ZnO

Aluminium (0.0005, 0.001, 0.002 and 0.003%) doped ZnO samples were prepared by hydrazinated-oxalate (solution) method. The hydrazinated precursor was obtained by adding stoichiometric amount of metal ion solution (Zinc Chloride and Aluminium Chloride) to a well stirred oxalic acid and hydrazine hydrate solution in three necked flask under inert (N_2 gas) atmosphere. The precipitate was separated by filtration, washed with water and air dried.

3.2.4 Spray Pyrolysis of Zinc nitrate

In the pot synthesis modification of the oxalate precursor is done by a novel hydrazine method. During the thermal decomposition of the precursors, there may be agglomeration of particles of oxide leading to non-uniform particle size distributions. The applications in Nano technology demand uniform particle size in the range of nano, submicron and few microns. There are several improvised techniques for synthesizing nano materials, but for the large scale manufacturing, it is the spray pyrolysis method

which can still be used with some modification of the process parameters. The precursors used for the spray pyrolysis are metal chlorides, sulfates or nitrates. The synthesis by this method gives corrosive gaseous by-products along with the oxide. Hydrazine assisted pyrolysis of metal nitrates, [179] is an energy effective and environmentally friendly process for metal oxide synthesis. Hydrazine not only acts as a fuel to minimize the need of energy for pyrolysis, but it also scavenges the nitrate ions to produce environment friendly gaseous products such as nitrogen and water vapor. Spray pyrolysis of zinc nitrate to yield fine ZnO was done in a home built spray pyrolysis unit as shown in figure 3.1. Solutions of Hydrazine hydrate (99% Merck) and Zinc nitrate hexahydrate (1M) were bubbled in a glass reactor embedded in a muffle furnace at a temperature of 350- 400°C. The salt solution decomposes and the oxide formed gets collected in the collector tube.

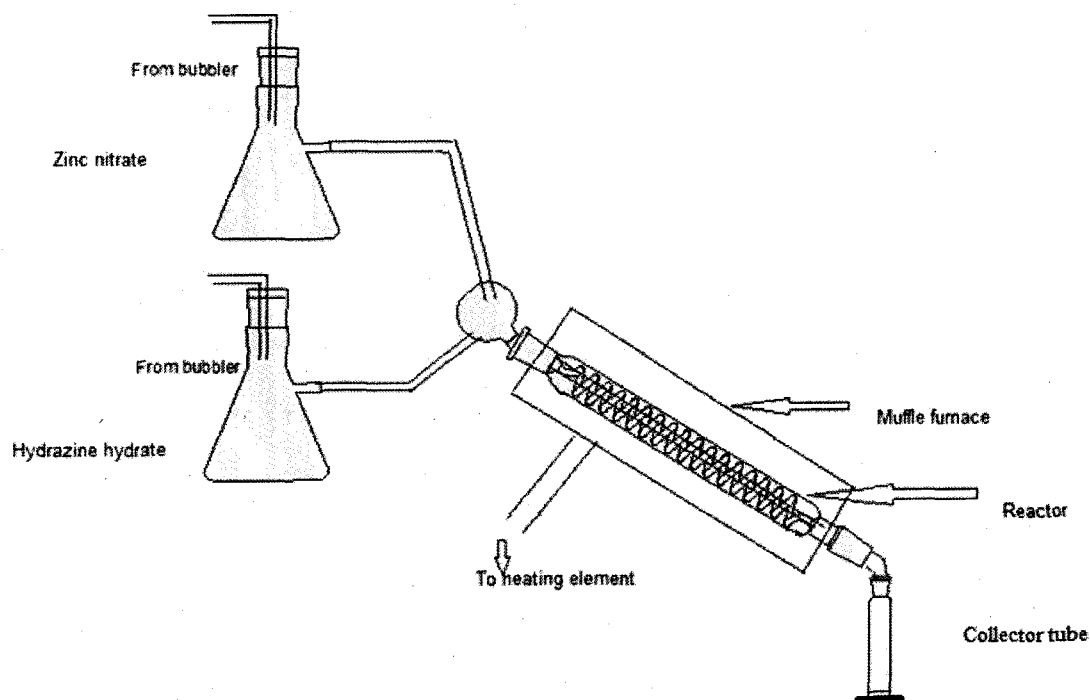


Figure 3.1 Set-up for spray pyrolysis

3.3 Characterization techniques

3.3.1. Chemical analysis:

The percentage of metal ions and hydrazine in the precursors were determined by standard chemical methods [180].

3.3.1.1 Estimation of Hydrazine: The details of the theory and procedure are described in chapter: 2, Section: 2.3.1.1

3.3.1.2 Estimation of Zinc

Zinc ions were estimated by complexometric titrations with EDTA solution. A known quantity of the precursor was dissolved in minimum amount of concentrated Hydrochloric acid and made the volume to 50 mL. 10 mL of this solution was taken in a conical flask, 2 mL buffer solution of pH=10 and a few drops of Eriochrome black –T indicator were added. The solution was titrated against standard 0.1 M EDTA till the colour changed from wine red to blue. Percentage of zinc in the sample was then calculated by using relation (3.1),

$$1 \text{ mL of } 0.1 \text{ M EDTA} = 6.538 \text{ mg Zinc} \quad (3.1)$$

3.3.2 Instrumental analysis

3.3.2.1 FTIR: The details of the theory, instrumentation and experiment are described in chapter: 2, Section: 2.3.2. 1.

3.3.2.2 Thermal analysis: The details of the theory, instrumentation and experiment are described in chapter: 2, Section: 2.3.2.2.

3.3.2.3 XRD: The details of the theory, instrumentation and experiment are described in chapter: 2, Section: 2.3.2.3.

3.3.2.4. Density Measurements: Densities of the powdered samples were found by liquid displacement method. Water was used as the liquid medium.

3.3.2.5 UV-Visible Diffuse reflectance spectrometry (DRS): The details of theory, instrumentation and experiment are described in chapter: 2, Section: 2.3.2.5.

3.3.2.6 Scanning electron microscopy: The details of the theory, instrumentation and experiment are described in chapter: 2, Section: 2.3.2.6.

3.3.2.7 BET Surface area measurements

Gas adsorption measurements are widely used for determining the surface area and pore size distribution of a variety of different solid materials, such as industrial adsorbents, catalysts, pigments, ceramics and building materials. Adsorption is the enrichment of one or more components in an interfacial layer. The term adsorption may also be used to denote the process in which adsorptive molecules are transferred to, and accumulate in, the interfacial layer. Its counterpart, desorption, denotes the converse process, in which the amount adsorbed decreases. The Brunauer-Emmett-Teller (BET) gas adsorption method is the most widely used standard procedure for the determination of the surface area of finely-divided and porous materials. The theory was proposed by Brunauer, Emmett and Teller in 1938. It is customary to apply the BET equation in the linear form

$$\frac{p}{n^a(p^\circ - p)} = \frac{1}{n_m^a C} + \frac{(C-1)p}{n_m^a C p^\circ} \quad (3.2)$$

where n^a is the amount adsorbed at the relative pressure p/p° and n_m^a is the monolayer capacity. BET surface area studies were carried out on the prepared oxides using Micromeritics Tristar 3000 surface area and porosity analyzer. Surface areas were determined according to Brunauer-Emmett-Teller (BET) method, after degassing the samples using nitrogen flow at 100°C for 5 hours.

3.3.2.8 Energy-dispersive X-ray spectroscopy (EDS)

Energy-dispersive X-ray spectroscopy (EDS or EDX) is an analytical technique used for the elemental analysis or chemical characterization of a sample. It is one of the variants of X-ray fluorescence spectroscopy which relies on the investigation of a sample through interactions between electromagnetic radiation and matter, analyzing the X-rays emitted by the matter in response to being hit with charged particles. Its characterization capabilities are due in large part to the fundamental principle that each element has a unique atomic structure allowing X-rays that are characteristic of an element's atomic structure to be identified uniquely from one another. A high-energy beam of charged particles such as electrons or protons, or a beam of X-rays, is focused into the sample being studied. At rest, an atom within the sample contains ground state (or unexcited) electrons in discrete energy levels or electron shells bound to the nucleus. The incident beam may excite an electron in an inner shell, ejecting it from the shell while creating an electron hole in its place. An electron from an outer, higher-energy shell then fills the hole, and the difference in energy between the higher-energy shell and the lower energy shell may be released in the form of an X-ray. The number of the X-rays emitted from a specimen and the energy associated can be measured by an energy-dispersive spectrometer. As the energy of the X-rays is characteristic of the difference in energy between the two shells of the atom from which they were emitted, this allows the determination of elemental composition of the specimen. EDS analysis was done on JEOL JSM – 5800. The samples were mounted on specimen stubs with double sided adhesive tapes and coated with thin layer of conducting material like gold by sputtering and then analyzed.

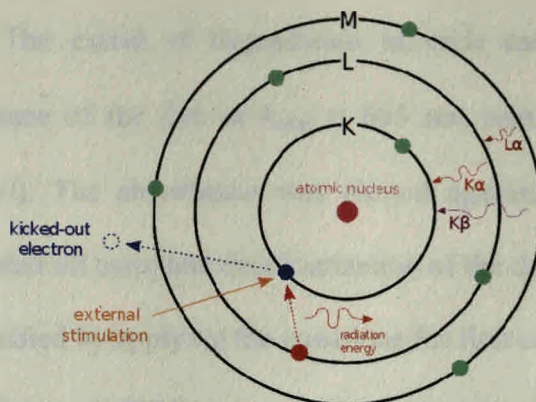


Figure 3.2 Diagram explaining principle of EDS

3.3.2.9 XPS: The details of the theory and instrumentation are described in chapter: 2, Section: 2.3.2.7. Experimental conditions are same as reported in section 2.3.2.7 except that Al K_{α} was used for nitrogen 1s level. All other core levels were recorded with Mg K_{α} .

3.4 Photocatalytic Applications

3.4.1 Dye degradations

3.4.1.1 Methylene blue (MB) dye degradation

a. UV-Visible absorbance

Photocatalytic activity of zinc oxide systems was studied by measuring their ability to degrade methylene blue dye in an aqueous solution in presence of sunlight. The intensity of insolation was measured by Luxmeter and power obtained from the solar light was measured by Solar Kit provided by Tata BP solar. Solar light intensity was measured for every 30 minutes and the average light intensity over the duration of each experiment was calculated. The sun light degradation studies were carried out in a conical flask containing a known concentration of methylene blue (0.5×10^{-4} M) and catalyst (200 milligram). A blank solution of MB of same concentration was also

exposed to sunlight. The extent of degradation in each case was determined by measuring the absorbance of the dye at $\lambda_{\max} = 665$ nm using a Shimadzu UV-Vis spectrometer (UV-2450). The absorbance was plotted against time and decrease in absorbance was calculated till complete decolourization of the dye solutions. Kinetics of dye degradation was studied by applying the equations for first order reactions.

b. Chemical Oxygen Demand (COD)

The COD of the dye solution was determined by titrimetry. Standard potassium dichromate was added to the test sample in acidic medium and refluxed. The amount of potassium dichromate remaining after refluxing was found by titration with standardized ferrous ammonium sulphate. COD (mg/L) was calculated by using standard relation. The chemical oxygen demand removal was calculated according to the equation, $\text{Removal (\%)} = 100(C_0 - C)/C_0$, (3.3)

where C_0 (mg/L) is the initial COD and C (mg/L) is the COD after degradation.

C. Electrospray ionization mass spectrometric analysis (ESI-MS)

Electrospray ionization mass spectrometric analysis (ESI-MS) is used as most efficient tool for the analysis of the products resulting from chemical transformations. Completely decolorized solutions of the dye were extracted with chloroform and the residues obtained were further dissolved in methanol to analyze the products of degradation. ESI-MS were carried out using an electrospray/quadrupole/time-of-flight (QqToF) mass spectrometer (QstarXL, MDS Sciex). The TOF experiment was performed to get the fingerprint of the reaction products followed by collision induced dissociation (CID) of major molecular ion in tandem mass spectrometry to give characteristic fragment ions resulting in the identification of transformed products.

d. Sulphate and nitrate estimation

The concentrations (mg/L) of nitrate ions, NO_3^- [202] and sulfate ions, SO_4^{2-} [203], were

tested on complete de-colorization of the dye solutions by standard chemical methods. Nitrate ions, NO_3^- were estimated by spectrophotometric method by developing colour using brucine - sulphanilic acid. A calibration curve was prepared using 0.5 to 2.5 mL of standard solution of potassium nitrate ($1\text{mL} = 0.01 \text{ mg nitrate}$). After proper dilution to 5 ml, 1 ml solution of brucine-sulphanilic acid was added followed by 10 mL of H_2SO_4 solution. The solutions were kept in dark for 10 minutes and then 10 mL of water added to it. Absorbance was recorded at 510 nm after cooling the solutions in dark for 20-30 minutes. The amount of nitrate in the unknown decolourized solution was estimated with the use of calibration curve prepared. The presence of sulphate was tested by turbidimetric method using barium salts. Sulphate ions were precipitated as BaSO_4 crystals of uniform size in acid medium. Light absorbed by the precipitate was measured by using a spectrophotometer. Calibration curve was prepared using 5-40 mL of standard sulphate solution ($1\text{mL}=100\mu\text{g}$ of SO_4^{2-}). The solutions were diluted to 100 mL followed by addition of conditioning agent and BaCl_2 crystals. The solutions were poured in absorption cell of photometer and O. D. was measured at wavelength of 420 nm.

3.4.1.2 Industrial effluent degradation

Zinc oxide system was used to degrade effluent of a crayon and marker manufacturing industry as a case study. The effluents were diluted (1:3) times before using for degradation. Catalyst concentration of 50 mg was added to the effluent (15mL) diluted with equal amount of distilled water. This was exposed to mid-day sunlight.

a. UV-Visible absorbance

The effluent is a mixture of different dyes, UV-Visible spectrum of the effluent showed many peaks. However the λ_{max} for the effluent was found to be 628.39 nm. Aliquots

were withdrawn after every 30 minutes and analyzed for absorbance at λ_{\max} .

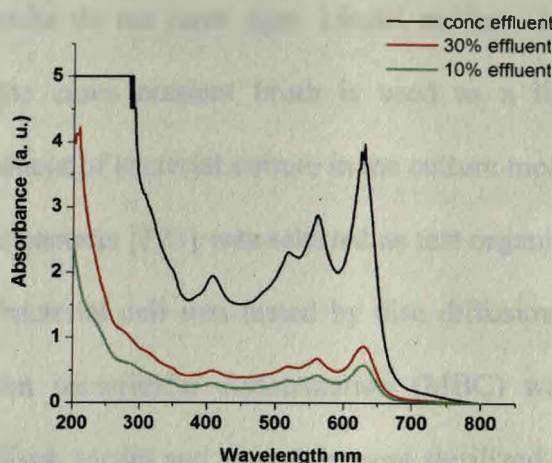


Figure 3.3 UV-Visible spectrum of industrial effluent

b. COD: The experimental details are described in section: 3.4.1.1.

3.4.2 Antibacterial Studies

Antibacterial studies are carried out by culturing the microbes in pure form on artificial media under laboratory conditions. A culture is defined as growth of microbes under contamination free condition in the laboratory on a suitable medium. Microbes are cultured to obtain populations of cells referred to as a colony. Culturing of microorganisms is done in the laboratory under aseptic conditions using sterilized glasswares and other appliances. Sterilization of glass wares and equipments is done using a giant pressure cooker called autoclave. Heating in an autoclave to above 121°C at 15psi for 15 minutes destroys nearly all living cells and spores. Incubator is an apparatus used for growing bacterial cultures under controlled environmental conditions, such as temperature and humidity. Nutrient substance prepared in a suitable manner so that microbes can grow on them is referred to as culture medium e.g. Nutrient broth with constituents peptone, beef extract, NaCl, and distilled water. Culture media can be solid

or liquid. Solid media are prepared by adding either agar or gelatin to the nutrients in liquid, while liquid media do not have agar. Liquid medium is also known as broth culture. In most of the cases nutrient broth is used as a liquid culture medium. Inoculation is the placement of bacterial culture in the culture medium.

E. coli a gram negative bacteria [123] was selected as test organisms. The ability of the oxides to rupture the bacterial cell was tested by disc diffusion method in solid agar medium. The Minimum bactericidal concentration (MBC) was found using liquid growth medium. The discs, media and materials were sterilized in an autoclave before the experiments. The experimental work was carried out under sterile conditions in a laminar air-flow chamber. The media and cultures were prepared as follows:

Nutrient agar plates- Agar media was prepared by mixing 1% agar with nutrient broth (28g/L). The dry components were heated to melt the agar and sterilize in a flask or bottle, then poured into the plates using aseptic technique in a sterile cabinet. MacConkey Agar is a differential medium recommended for the selective isolation and differentiation of lactose fermenting and lactose non-fermenting enteric bacilli. Its ingredients (g / L) are: Peptic digest of animal tissue 17.000, Proteose peptone 3.000, Lactose 10.000, Bile salts 1.500, Sodium chloride 5.000, Neutral red 0.030, Agar 15.000, Final pH (at 25°C) 7.1 ± 0.2 . The above components were dissolved in 1000ml of distilled water and boiled to dissolve the medium completely. It was sterilized by autoclaving at 121°C, 15psi for 15 minutes. Then it was allowed to cool and then poured into petri plates.

Nutrient Broth-To prepare broth the dry medium (28g/L) was layered onto the surface of a measured volume of water, mixed, and distributed into individual loosely capped tubes in racks. Heating was done to dissolve the components. Racks were sterilized and

then allowed to cool, and caps tightened to prevent evaporation.

E. coli culture was grown in nutrient broth for 18 hours at 37° C at 100 rpm on a rotary shaker. The number of bacterial cells was estimated by measuring the absorbance of the suspension at 600nm. A culture having Absorbance = 0.8-1.0 ($A_{\text{max}} = 600$) corresponding to 10^5 CFU per mL was used for all the antibacterial studies. The experiments were done in triplicate and the results were averaged.

3.4.2.1 Disc diffusion Assay

The disc diffusion study was done to find out antibacterial action of the oxides qualitatively. For disc diffusion study, a protocol applicable to inorganic metal oxides and composites was followed [123,204-205]. Nutrient agar medium was used as basal medium in the Petri plates used for the assay. 100 μ L of the bacterial suspension ($A_{600} = 0.8-1.0$) was added in 5mL of warm top nutrient agar, mixed well and poured evenly over the basal medium. The test *E. coli* culture was allowed to grow in the incubator at 37° C for 30 minutes. Slurry of the oxides (0.025g) was made in sterile water and was coated on sterile discs of filter paper of 6 mm diameter and placed on the nutrient media in the Petri plates. Filter paper disc without the oxide coatings was used as control. The petriplates were incubated for 18-24 hours and then the zones of inhibition around the sterile discs of filter paper were measured. Antibacterial action is indicated by the presence of an inhibition zone around the disc. More the zone of inhibition more is the antibacterial efficacy.

3.4.2.2 Minimum Bactericidal Concentration (MBC)

The MBC is the lowest concentration at which a compound will kill more than 99% of the added bacteria. Oxide powders ranging from 0.01 to 1.0 mMoles were added to

separate tubes containing 5 mL of L. B. (Luria Bertani) nutrient broth. The tubes were stirred continuously to facilitate homogenization. 100 μ L of *E. coli* culture ($A_{600} = 0.8-1.0$) was added to each tube and the resulting solutions were again stirred overnight (18-24 hours) on a rotary shaker at 37° C. Positive control was prepared using nutrient broth and *E. coli* culture. Negative control was prepared using nutrient broth and the oxide material without the culture. Aliquots of 100 μ L from all the tubes (including the positive and negative control tubes) were spread plated on MacConkey agar which is specific for coliforms. The plates were incubated at 37° C for 18-24 hours and checked for the growth.

3.4.3 Photodegradation of NO_x

3.4.3.1 Generation of NO_x

Generation of NO_x was done using concentrated nitric acid and copper foils. When concentrated nitric acid is added to copper fillings NO_x is liberated as per the following reaction:



3.4.3.2 Estimation of nitrite using Calibration curve

NO_x is a mixture of NO and NO₂. The amount of Nitrite formed during the generation of NO_x was found out as follows. Concentrated HNO₃ (10 drops) was added to Cu foils (0.02g) in an evacuated glass flask. The NO_x formed was immediately absorbed in sodium arsenite solution. A small amount of the absorbing solution was analysed by Jacob and Hochheiser method using sulphanilamide and N-(1- naphtha ethylene diamine) hydrochloride (NEDA) using calibration curve method.

3.4.3.3 Abatement of NO_x by photocatalysts

SETUP FOR NO_x DETERMINATION

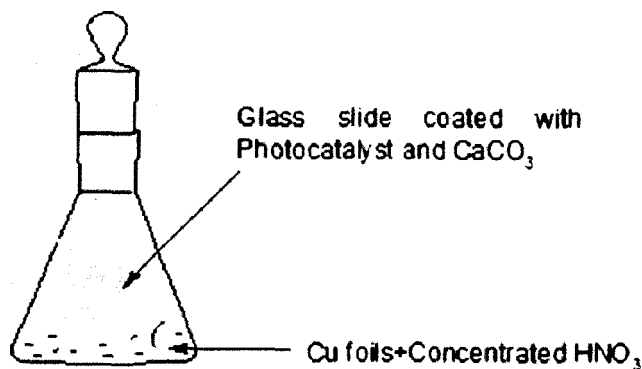


Figure 3.4 Set-up for abatement of NO_x

Glass slides were coated with slurry of the photocatalysts in water (0.05g) on both the sides and were inserted in the jar in which NO_x was generated by adding 10 drops of concentrated HNO₃ to 0.02g of Cu foils. The tightly closed jar was exposed to sunlight of intensity 550 lux units and time taken by the brown fumes of NO_x to disappear was noted. The procedure was also modified by adding equal amount (0.05g) of calcium carbonate with the photocatalyst. The nitric acid formed reacted with calcium carbonate and trapped nitrate releasing CO₂.

3.4.3.4 Qualitative estimation of nitrate

This method is based on the measurement of the yellow colour produced by the reaction between nitrate and brucine [202]. A 0.05g of the photocatalyst mixture was weighed accurately and mixed with 50 mL of distilled water. Around 2 ml of the solution was taken for analysis. The analysis was carried out as given in section 3.4.1.1d.

3.5 Results and discussions

3.5.1 ZnO and ZnO_{1-x}N_x system

3.5.1.1 Characterization of oxalate and hydrazinated oxalate precursors

3.5.1.1.1 Chemical analysis and formula fixation of oxalate and hydrazinated oxalate precursors

Chemical formulae of oxalate and hydrazinated oxalate precursors prepared were fixed by chemical analysis, FTIR and total weight loss studies (TG and Isothermal) before decomposition to the corresponding oxides. The proposed chemical formulae along with the analytical data of oxalate and hydrazinated oxalate precursors for zinc oxides have been summarized in Table 3.1. In general, the observed (Obsd) percentage (%) of total mass loss, oxalate ($C_2O_4^{2-}$) and hydrazine (N_2H_4) match well with the calculated (Calcd.) values based on the plausible formula in each case.

Table 3.1 Chemical analysis of oxalate and hydrazinated oxalate precursors and the proposed chemical formulae

Precursor	N ₂ H ₄ , %		C ₂ O ₄ , %		Zinc, %	
	Calcd.	Obsd.	Calcd.	Obsd.	Calcd.	Obsd.
ZnC ₂ O ₄ .2H ₂ O (OX)	-----	-----	46.4	46.2	34.5	33.5
ZnC ₂ O ₄ .N ₂ H ₄ .H ₂ O (OXE)	15.7	14.9	43.2	44.0	32.1	32.5
ZnC ₂ O ₄ .2N ₂ H ₄ (OXS)	29.4	28.9	40.5	41.1	30.0	30.6

3.5.1.1.2. FTIR analysis of oxalate and hydrazinated oxalate precursors

The infrared (IR) band positions of all the precursors have been compiled in the Table 3.2. The IR bands characteristic of the coordinated oxalate groups [184-185] observed at ~ 1650 and at ~ 1320 cm⁻¹ are due to ν_{as} (o-c-o) and ν_s (o-c-o), respectively attributed

to coordination of oxalate ion with zinc ion. A broad band in the region $3600-3000\text{ cm}^{-1}$ due to ν (O-H) stretching in the complexes is due to presence of water.

Hydrazine linkage to the metal in hydrazinated oxalate complexes is indicated by characteristic band positions due to ν (N-N) peak at $970-990\text{ cm}^{-1}$ and δ (NH_2) peaks at $1130-1200\text{ cm}^{-1}$ [186] along with the usual oxalate band positions. The broad peak due to ν (H_2O) in oxalate on hydrazination gets sharpened indicating appearance of ν (N-H) stretching bands. These observations and the chemical analysis in Table 3.1, further support the formation of hydrazinated complexes.

Table 3.2 IR absorptions of the oxalate and hydrazinated oxalate precursors.

Precursor	$\nu_s(\text{o-c-o}) /$ $\nu_{as}(\text{o-c-o})$ in cm^{-1}	$\delta(\text{o=c-o})$ in cm^{-1}	$\nu(\text{H}_2\text{O})/$ $\nu(\text{N-H})$ in cm^{-1}	$\nu(\text{N-N})$ in cm^{-1}	$\delta(\text{NH}_2)$ in cm^{-1}
$\text{ZnC}_2\text{O}_4 \cdot 2\text{H}_2\text{O}$ (OX)	1320/1625	820	3100-3500	-----	-----
$\text{ZnC}_2\text{O}_4 \cdot \text{N}_2\text{H}_4 \cdot \text{H}_2\text{O}$ (OXE)	1300/1654	779	3100-3400	972	1136
$\text{ZnC}_2\text{O}_4 \cdot 2\text{N}_2\text{H}_4$ (OXS)	1326/1654	806	3100-3500	992	1193

The IR spectral studies conducted on the residues obtained after thermal decomposition of oxalate and hydrazinated oxalate at 200, 300, 400 and 500°C , figure 3.5 clearly indicate the disappearance of the bands in the spectra specific to oxalate and hydrazine at $400-500^\circ\text{C}$, which is the decomposition temperature of the precursors.

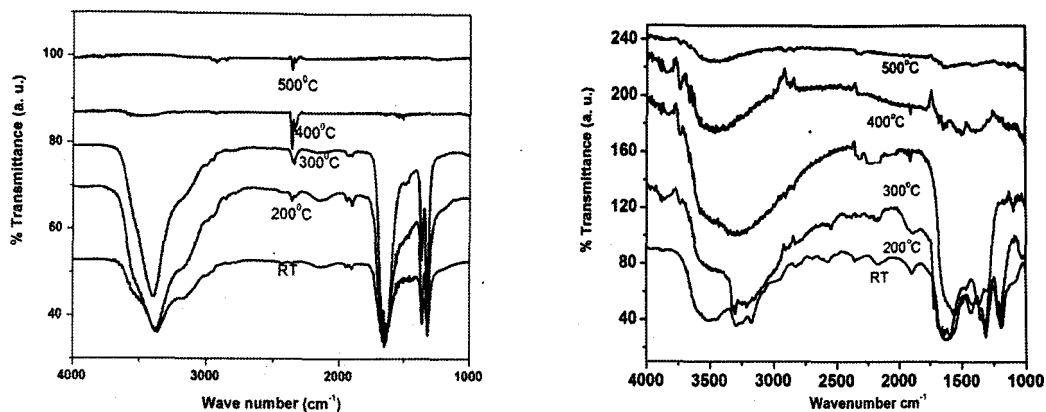


Figure 3.5 Stepwise IR spectra of the oxalate and hydrazinated oxalate precursors decomposed at different temperatures.

3.5.1.1.3 Thermal analysis of oxalate and hydrazinated oxalate precursors

The DTA-TG curves of the oxalate and hydrazinated oxalate precursors are as shown in figure 3.6 and the temperatures of various endothermic and exothermic processes are listed in table 3.3.

Table 3.3 Thermogravimetric data of the OX, OXE and OXS precursors

Precursor	Thermal process Endo-/Exo- in °C	Total Weight loss %		
		Theoretical	TG	Iso-thermal
ZnC ₂ O ₄ .2H ₂ O (OX)	Endo- 149.2/678, Exo -550°C	57.00	60.52	57.03
ZnC ₂ O ₄ .N ₂ H ₄ .H ₂ O (OXE)	Endo- 154.0/250/759.4 Exo - 98.2/572.9	59.90	61.33	59.60
ZnC ₂ O ₄ .2N ₂ H ₄ (OXS)	Endo-143.2/244.5/341.6/453.4/732.5 Exo-82.1/210/407.5/538.4	62.60	60.87	62.37

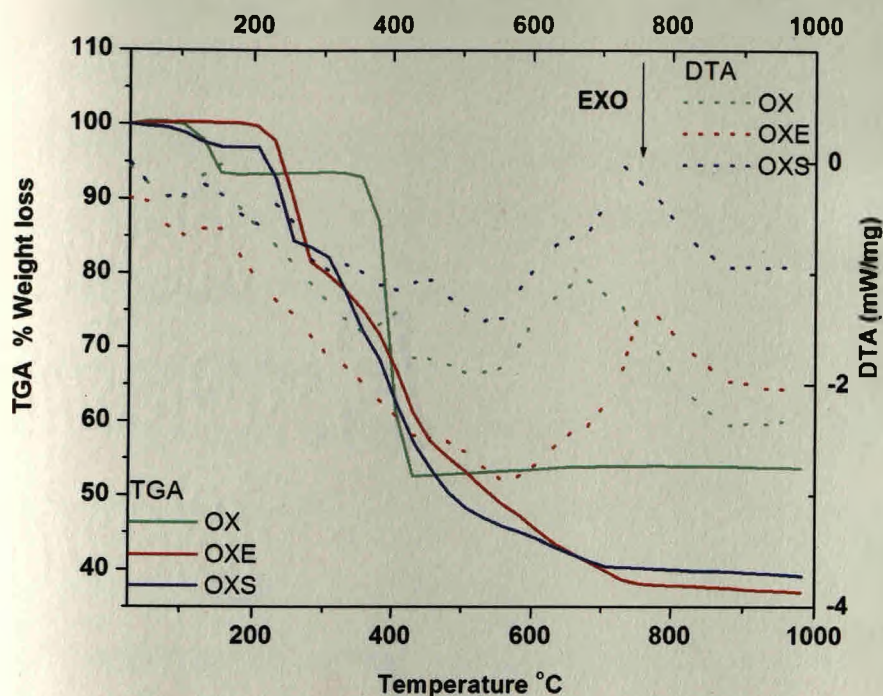
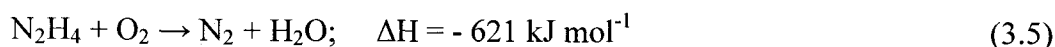


Figure 3.6 Thermogram of oxalate and hydrazinated oxalate precursors.

DTA-TG curve of oxalate precursor (OX) shows an endotherm at 149.2°C. There is an exotherm in the range 400-500 °C. Thus the oxalate dihydrate undergoes dehydration ~ 149.2°C. Decarboxylation and decomposition takes place at ~ 400- 600°C with the evolution of CO and CO₂. An endothermic peak is observed at 678°C. There is ~ 60.52% loss in weight which is in good agreement with the calculated and isothermal weight loss. The DTA-TG of hydrazinated oxalate precursor obtained by equilibration method (OXE) shows two small endotherms at 154.0 and 250 °C and a broad endotherm at 759.4 °C. The exotherms are observed at 98.2 °C and 572.9 °C. It is due to dehydration followed by dehydrazination and decarboxylation which are simultaneous. There is ~ 61.33% loss in weight which is in good agreement with the calculated and isothermal weight loss. The DTA-TG data of hydrazinated oxalate precursor obtained by solution method (OXS) shows small endotherms at 143.2, 244.5, 341.6, 453.4 and a

broad endotherm at 732.5°C. The exotherms observed are at 82.1, 210, 407.5 and 538.4 °C. The decomposition of the hydrazinated oxalate precursor completes at around 400°C. The dehydration is followed by dehydrazination and decarboxylation which are simultaneous. About 60.87% loss in weight obtained during thermal study is in good agreement with the calculated and isothermal weight loss. The decomposition of hydrazinated precursors releases hydrazine which reacts with the atmospheric oxygen and liberates enormous energy [188]



The hydrazine method of preparation introduces nitrogen in the lattice easily, formed during decomposition of N_2H_4 as per equation (3.5) [178]. Thus ZnO obtained from OXE and OXS precursors may have stoichiometry $\text{ZnO}_{1-x}\text{N}_x$

3.5.1.2 Characterization of oxides

The oxide obtained from oxalate is called as ZnO, from OXE is called as $\text{ZnO}_{1-x}\text{N}_x$ (E) and the one obtained from OXS is called as $\text{ZnO}_{1-x}\text{N}_x$ (S) in the further text.

3.5.1.2.1 Phase identification of ZnO and $\text{ZnO}_{1-x}\text{N}_x$ system by XRD

The phase identification of all the thermal products of the precursors has been done by x-ray diffraction studies and the interplanar spacing ‘d’ values have been compared with the JCPDS card no 5- 664, for hexagonal Wurtzite ZnO (Table A-6 in appendix). Figure 3.7 confirms the formation of single phase ZnO as the decomposition product of all the precursors. All diffraction features in $\text{ZnO}_{1-x}\text{N}_x$ materials are due to the ZnO lattice and no additional peaks have been observed due to nitrogen into the lattice. Various reports however make mention of a small shift in XRD to higher diffraction angles associated with $\text{ZnO}_{1-x}\text{N}_x$ materials, compared to ZnO, indicating an overall contraction of the lattice [102]. Broadening of peaks is observed in the XRD pattern of the oxide obtained

from OXS. This is due to fine particles of the oxide formed during the exothermic decomposition of the hydrazinated precursor [178].

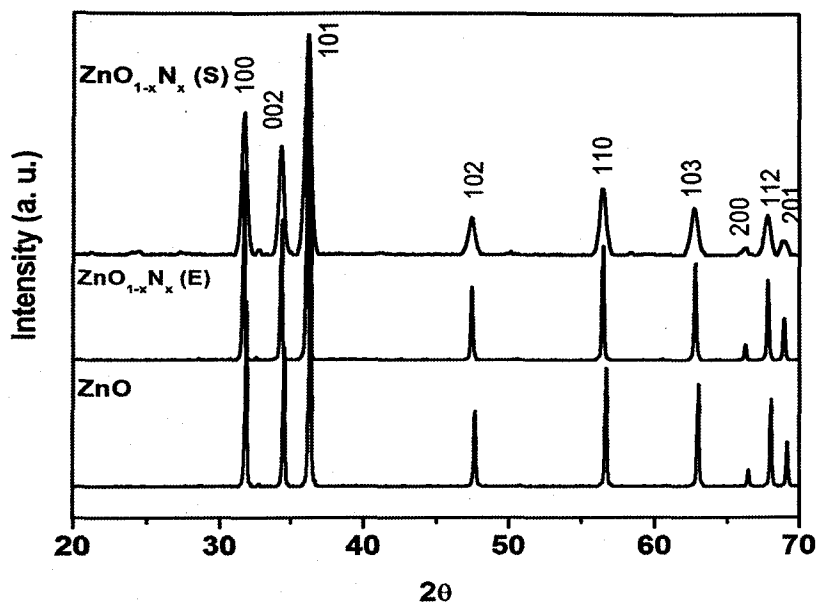


Figure 3.7 XRD of ZnO obtained from oxalate and hydrazinated oxalate precursors.

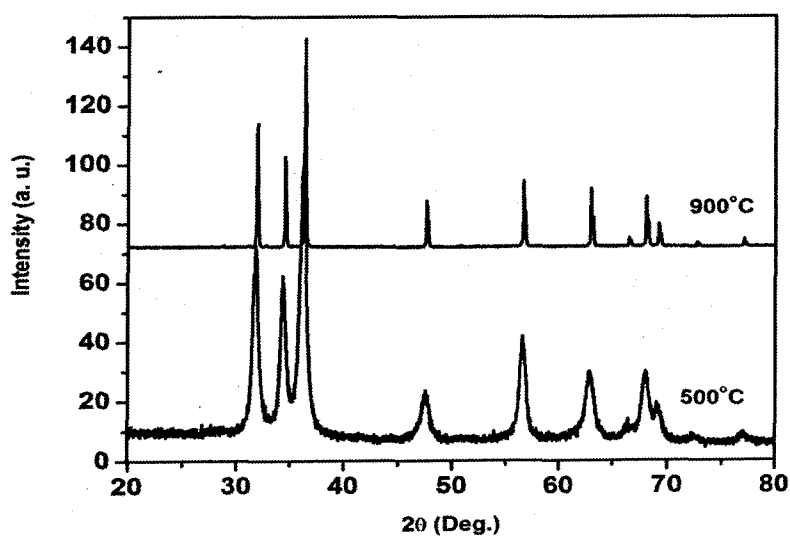


Figure 3.8 XRD of ZnO obtained from OXS precursor at decomposition temperature of i) 500°C and ii) 900°C.

Thermal analysis of the ZnO prepared from OXS precursor show no weight loss till the temperature of 600°C indicating high thermal stability. A small endotherm is observed at 143 °C which may be due to loss of any physisorbed water. A broad endotherm at 600°C is due to the growth and increase in crystallite size of ZnO as seen by the sharpening of the peaks in the XRD patterns recorded on heating the oxide at 900 °C (figure 3.8). Some researchers have reported this endotherm to be due to nitrogen desorption which occurs above 600°C [102]. The formation of oxides is also confirmed by IR analysis of the final decomposed product which shows absorption bands in the region of 500 cm⁻¹ corresponding to metal oxygen bonds (figure 3.5).

3.5.1.2.2 Density studies of ZnO and ZnO_{1-x}N_x system

Densities measured for ZnO obtained from OX, OXE and OXS precursors are compiled in table 3.4. Density of ZnO is 5.606 g/cm³[102]. ZnO prepared from OX shows density higher than the reported value suggesting that the material formed is compact. This is very well supported by low surface area of the material. In the case of ZnO_{1-x}N_x there is a large decrease in the density. This is supported by an increase in the surface area of the oxides suggesting the porous nature. A decrease in the density of the oxides indicates the fact that there exist vacancies in the lattice giving rise to defect type of structure on incorporation of N in the lattice. In a similar report however, a decrease in the density and increase in the surface area of these oxides is attributed to a decreasing interstitial N content in case of N doped ZnO [102].

3.5.1.2.3 Microstructure (SEM) Analysis of ZnO and ZnO_{1-x}N_x system

SEM photographs of the oxides are as shown in figure 3.9. The studies reveal rounded and spherical particles of the oxides.

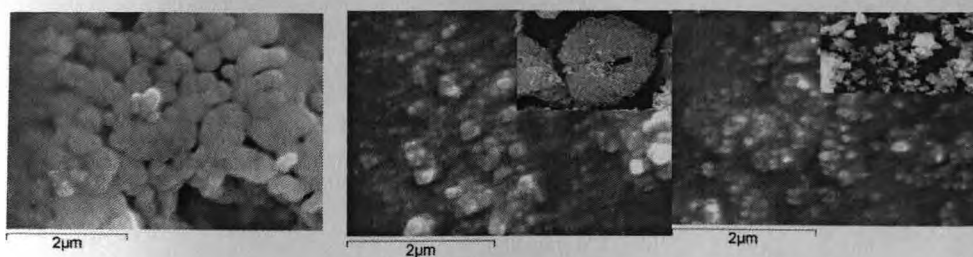


Figure 3.9 SEM pictures of 1) ZnO, 2) ZnO_{1-x}N_x (E) and 3) ZnO_{1-x}N_x (S) at x25000.

ZnO prepared by oxalate method show spherical particles of different sizes agglomerated to a large extent. Similar observation is also reported in case of TiO₂ prepared by oxalate method [178]. In case of hydrazinated oxalate precursors, the exothermicity of the decomposition reaction of hydrazine makes the final product fine and porous as seen in case of ZnO_{1-x}N_x prepared by equilibration method and solution method. Measured particle sizes are reported in table 3.4 which also suggests formation of fine particle oxides by hydrazinated oxalate route.

3.5.1.2.4 BET Surface area measurements on ZnO and ZnO_{1-x}N_x system

Table 3.4 gives the surface area of ZnO and ZnO_{1-x}N_x calculated by BET measurements. The ZnO prepared by the hydrazinated method are porous and with high surface area as compared to the ZnO prepared by the oxalate method. Low temperature-explosive decomposition of the hydrazine complexes, in general, found in studies [178] give rise to products with small particle size and large surface areas. The low surface area in case of ZnO prepared by the oxalate method is due to sintering effect.

Table 3.4 Physical properties of ZnO and ZnO_{1-x}N_x system

Sample	Particle size	Surface area in m ² /g	Density g/cm ³
ZnO	1-2 μm	8.137	6.58
ZnO _{1-x} N _x (E)	69 nm	11.806	4.53
ZnO _{1-x} N _x (S)	38 nm	37.566	3.66

3.5.1.2.5 Diffuse reflectance and Absorbance spectra of ZnO and ZnO_{1-x}N_x system

Figure 3.10 shows reflectance spectra of ZnO and ZnO_{1-x}N_x. ZnO with the wurzite structure is naturally n-type semiconductor due to its deviation from stoichiometry. It contains interstitial zinc atoms (Zn_i) due to presence of large voids and oxygen vacancies (V_o) in the crystal. Both these defects form donor levels [206].

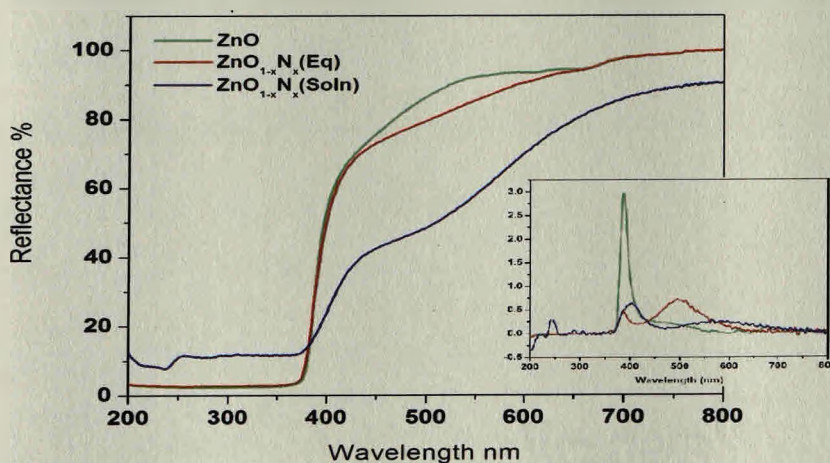


Figure 3.10 Diffuse reflectance spectra of ZnO and ZnO_{1-x}N_x (inset derivative of the diffuse reflectance spectra).

ZnO prepared by oxalate method shows an absorption cut off edge at ~375 nm similar to the reported [207]. In addition to the above, a new visible absorption band at ~600 nm is observed for ZnO_{1-x}N_x prepared by equilibration method and a new broad visible

absorption band with an absorption onset at ~ 600 nm and a band maximum at ~ 480 nm is observed for $\text{ZnO}_{1-x}\text{N}_x$ prepared by solution method (figures 3.10-3.11).

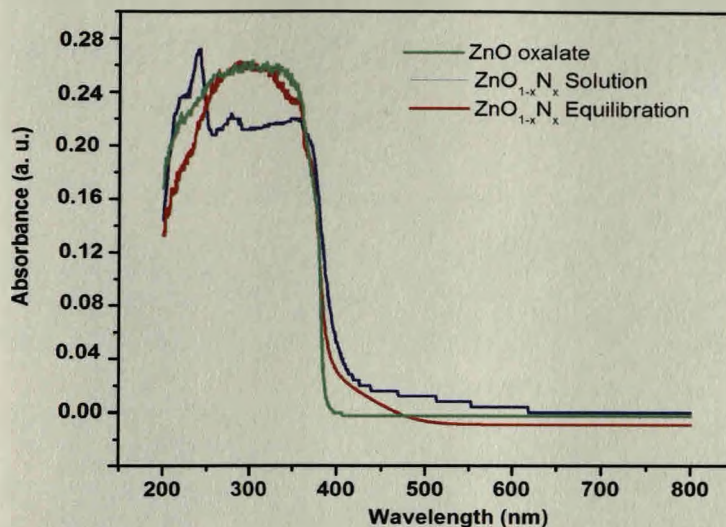


Figure 3.11 UV-Visible absorbance spectra of ZnO prepared by oxalate and hydrazinated oxalate methods.

These absorption edges may be due to changes in the band structure due to newly formed N 2p band located above the O 2p valence band. The absence of absorption in the visible region in case of ZnO prepared by oxalate method suggests that the visible light absorption in $\text{ZnO}_{1-x}\text{N}_x$ is due to introduction of N into the ZnO lattice and the creation of N2p state. ZnO is a semiconductor having absorbance in the UV region with a wide band gap of 3.37 eV [102]. The band gap values calculated from the derivative spectra displayed in the inset of DRS graph using the formula given below.

$$\text{Band gap (Eg) in eV} = 1239.8/\lambda_{\text{max}} \quad (3.6)$$

Where λ_{max} is the maximum wavelength of absorption obtained from differential plots of the UV-Vis reflectance spectra. The values are given in the table 3.5.

Table 3.5 Band gap values of the photocatalysts calculated from the derivative spectra.

Photocatalyst	Band gap (eV)
ZnO	3.19
ZnO _{1-x} N _x (E)	3.18
ZnO _{1-x} N _x (S)	3.09

N doped TiO₂ system is widely studied. When a semiconductor oxide like TiO₂ is doped with N, a decrease in its band gap is reported. This is due to mixing of nitrogen 2p states with oxygen 2p states on the top of the valence band or creation of N induced mid-gap level [178]. The mid gap level of N does not mix with O 2p level [208]. Based on the calculation by Asahi et al [209], bandgap narrowing occurs when a high-concentration of oxygen sites (6-12.5 at %) are substituted by nitrogen. Recently Okato et al. [210] claimed that the N doping induced optical bandgap narrowing does not occur with increase in the N concentration. It is also reported that incorporation of nitrogen introduces localized states in the bandgap of the material [211].

3.5.1.2.6 XPS studies on ZnO and ZnO_{1-x}N_x system

The XPS studies on the ZnO system also reveal the presence of nitrogen in the lattice of the oxides prepared by hydrazinated oxalate methods (figure 3.12). Nitrogen analysis carried out on the oxygen–nitrogen analyzer (HIROBA, EMGA, 2800) indicates ~ 13.75 at % N in case of ZnO prepared by hydrazinated oxalate (equilibration method). However no additional peaks are observed in the XRD patterns due to introduction of nitrogen in the lattice, in confirmation with the literature [102].

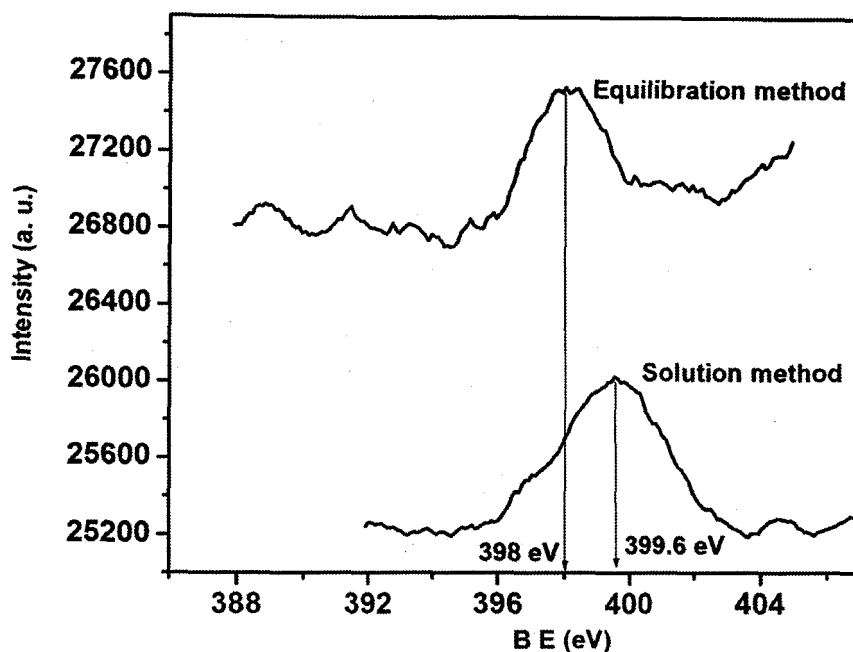


Figure 3.12 X-ray photoelectron spectrum of N in $\text{ZnO}_{1-x}\text{N}_x$.

The nature of nitrogen in the sample prepared by equilibration method is close to nitride type with binding energy (B.E.) ~ 398 eV, whereas in the sample prepared by solution method, nitrogen seems to resemble that of ammonia (charge density wise) and its binding energy is between 399-400 eV. Typical nitride nitrogen 1s electron shows B. E. of 397 eV [102]. This suggests that the electron density on nitrogen in $\text{ZnO}_{1-x}\text{N}_x$ is less than that of nitrides which is attributed to a more-covalent character of Zn-N bonds in $\text{ZnO}_{1-x}\text{N}_x$. The shift of B. E. of nitrogen 1s electron to higher values indicates covalent character of Zn-N bond.

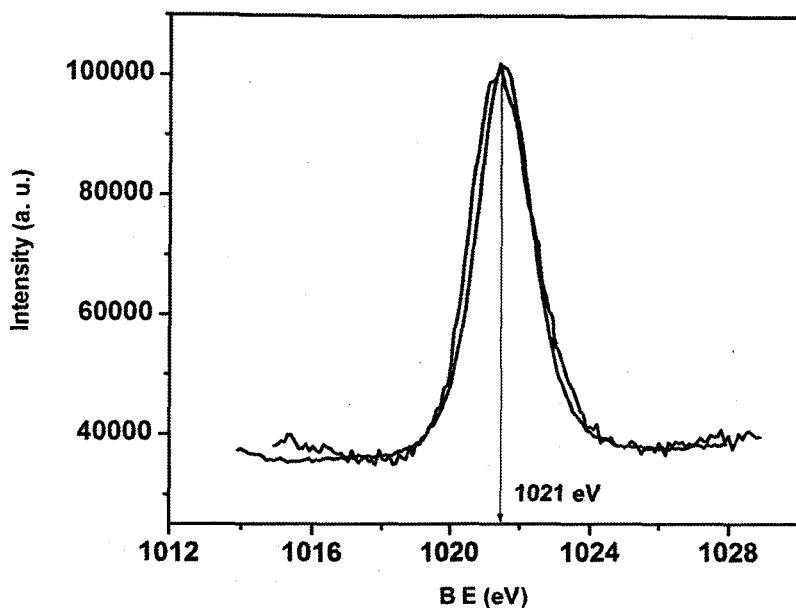


Figure 3.13 X-ray photoelectron spectrum of Zn 2p electron in $\text{ZnO}_{1-x}\text{N}_x$.

Zn 2p core level as reported in literature shows B. E. ~ 1022 eV [102]. In the present case, Zn 2p core level shows B. E. ~ 1021 eV (figure 3.13). The shifts of B. E. of Zn 2p core level to lower values also support covalent nature of Zn-N bond. Based on these, N-doped ZnO is considered to have a stoichiometry, $\text{ZnO}_{1-x}\text{N}_x$. Thus hydrazinate method helps in introduction of N in the zinc oxide lattice.

3.5.2 Aluminium doped ZnO system

Poor solubility of nitrogen in the lattice of ZnO limits efficient N doping in its lattice [102]. It is proposed that the solubility of nitrogen can be increased by introducing group III codopants such as Al, Ga, or In. The reactive codopants such as Al, Ga or In could form complexes with nitrogen, which enhance the incorporation of N-acceptors and thus produce p-type ZnO [212-213].

3.5.2.1 Characterization of precursors

3.5. 2.1.1 Chemical analysis and formula fixation of precursors

The proposed chemical formulae along with the analytical data of hydrazinated oxalate precursors prepared by solution method (S0.5-3) and equilibration method (E0.5-3) for the oxides have been summarized in table 3.6. The uptake of hydrazine by the precursors for Al doped ZnO is less as compared to precursors for Zinc oxide. In general, the observed (Obsd) percentage (%) of total mass loss, zinc and hydrazine (N_2H_4) match well with the calculated (Calcd.) values based on the plausible formula in each case.

Table 3.6 Proposed formulae for the hydrazinated oxalate precursors of Al doped ZnO.

Code	Precursor	N_2H_4 , %		Zinc, %		Total weight loss %		
		Calcd.	Obsd.	Calcd.	Obsd.	Theoretical	TG	Isothermal
S0.5	$ZnC_2O_4 \cdot \frac{1}{2}H_2O \cdot \frac{1}{2}N_2H_4$	8.9	8.9	36.6	37.1	54.4	51.8	53.1
S1	$ZnC_2O_4 \cdot \frac{1}{2}H_2O \cdot \frac{1}{2}N_2H_4$	8.9	8.3	36.6	36.6	54.4	54.2	52.5
S2	$ZnC_2O_4 \cdot \frac{1}{2}H_2O \cdot \frac{1}{2}N_2H_4$	8.9	8.4	36.6	36.9	54.4	53.6	54.0
S3	$ZnC_2O_4 \cdot \frac{1}{2}H_2O \cdot \frac{1}{2}N_2H_4$	8.9	8.3	36.6	37.1	54.4	55.4	53.6
E0.5	$ZnC_2O_4 \cdot \frac{1}{2}H_2O \cdot \frac{1}{2}N_2H_4$	8.9	9.0	36.6	36.2	54.4	52.5	53.5
E1	$ZnC_2O_4 \cdot H_2O \cdot N_2H_4$	14.9	14.2	32.5	33.0	59.6	58.7	59.2
E2	$ZnC_2O_4 \cdot H_2O \cdot \frac{1}{2}N_2H_4$	8.5	8.9	34.9	34.6	56.6	55.7	55.9
E3	$ZnC_2O_4 \cdot H_2O \cdot 2N_2H_4$	27.2	27	27.8	29.1	65.4	64.0	64.8

3.5.2.1.2 FTIR analysis of precursors

The infrared (IR) band positions of all the precursors have been compiled in the table 3.7. The IR bands characteristic of the coordinated oxalate groups [184-185] observed at ~ 1650 and at $\sim 1320 \text{ cm}^{-1}$ are due to ν_{as} (o-c-o) and ν_{s} (o-c-o), respectively attributed to coordination of oxalate ion with metal ions. A broad band in the region $3600\text{-}3000 \text{ cm}^{-1}$ due to ν (O-H) stretching in the complexes is due to presence of water. A band at 500 cm^{-1} is due to metal – oxygen linkage. Hydrazine linkage to the metal is indicated by characteristic band positions due to ν (N-N) peak at $990\text{-}1004 \text{ cm}^{-1}$ and δ (NH_2) peaks at $1150\text{-}1200 \text{ cm}^{-1}$ [186] along with the usual oxalate band positions. There is also a sharp peak in the range of $3100\text{-}3500 \text{ cm}^{-1}$ due to ν (N-H) stretching bands. These observations and the chemical analysis in Table 3.6, further support the formation of hydrazinated complexes.

Table 3.7 IR absorptions for the hydrazinated oxalate precursors of Al doped ZnO.

Precursor code	$\nu_{\text{s}}(\text{o-c-o}) / \nu_{\text{as}}(\text{o-c-o})$ in cm^{-1}	$\delta(\text{o=c-o})$ in cm^{-1}	ν (H_2O)/ $\nu(\text{N-H})$ in cm^{-1}	$\nu(\text{N-N})$ in cm^{-1}	$\delta(\text{NH}_2)$ in cm^{-1}
S0.5	1317/1651	759	3100-3500	997	1160
S1	1317/1577	797	3100-3500	990	1182
S2	1309/1614	797	3100-3500	997	1190
S3	1317/1614	819	3100-3500	990	1182
E0.5	1317/1644	796	3100-3500	990	1160
E1	1317/1651	797	3100-3500	990	1153
E2	1309/1629	804	3100-3500	997	1198
E3	1309/1659	797	3100-3500	1004	1153

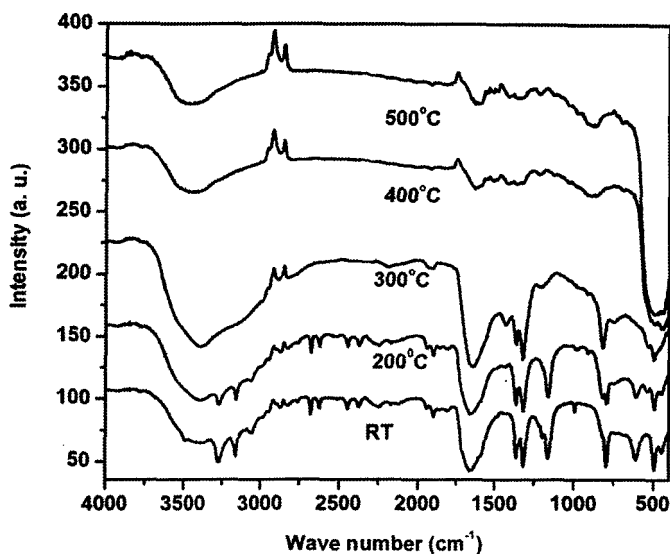


Figure 3.14 Stepwise IR spectra of the hydrazinated oxalate precursor E1 decomposed at different temperatures.

The IR spectral studies conducted on the residues obtained after thermal decomposition of hydrazinated oxalate precursors at 200, 300, 400 and 500°C, figure 3.14 indicate the disappearance of the bands in the spectra specific to oxalate and hydrazine at 400-500°C, which is the decomposition temperature. The metal-oxygen band around 500 cm^{-1} gets sharpened indicating formation of metal oxide.

3.5.2.1.3 Thermal analysis of precursors

Decomposition route of the hydrazinated oxalate precursors to the oxides was studied by DTA-TG. Thermogram of a representative sample 0.001% Al doped ZnO (solution method as well as equilibration method) is given in figure 3.15. The details of various thermal processes are compiled in table 3.8. The thermograms of other precursors are compiled in figure A-5 in appendix.

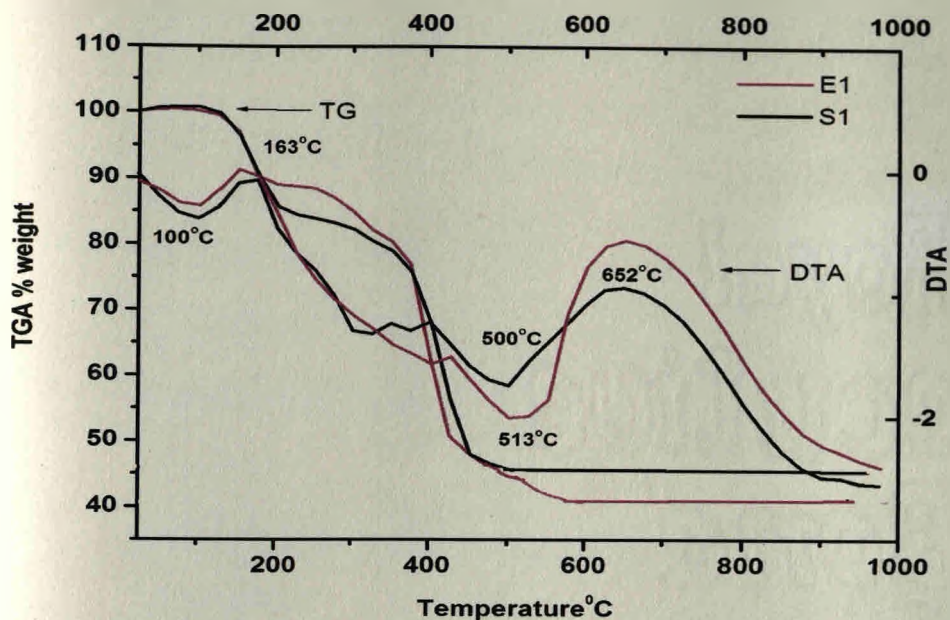


Figure 3.15 Thermograms of representative precursors i) E1, ii) S1.

The Thermogram of the precursors show two small endotherms at $\sim 160^\circ\text{C}$ and $390\text{--}450^\circ\text{C}$ and a broad endotherm at $600\text{--}650^\circ\text{C}$. Two exotherms are observed at $\sim 100^\circ\text{C}$ and $\sim 500^\circ\text{C}$. All these peaks are due to dehydration followed by dehydrazination and decarboxylation of the precursors. There is good agreement between the calculated and the isothermal weight loss. In general the precursor prepared by solution method shows rapid weight loss in the temperature range of $200\text{--}400^\circ\text{C}$. The decomposition of hydrazinated precursors release hydrazine which reacts with the atmospheric oxygen and liberates enormous energy [188] as given by equation (3.6). The hydrazine method of preparation introduces nitrogen in the lattice easily, formed during decomposition of hydrazine as per the equation which gets trapped in the lattice of the oxide [178]. Thus the oxides may be considered to have stoichiometry $\text{Zn}_{1-y}\text{Al}_y\text{O}_{1-x}\text{N}_x$.

Table 3.8 Thermogravimetric data of representative precursors E1 and S1

Precursor Code	Thermal process Endo-/Exo- in °C	Precursor Code	Thermal process Endo-/Exo- in °C
S0.5	Endo- 162.7/425/664.4 Exo-78/501.4	E0.5	Endo- 160.2/398/616.9/750 Exo-100/522.4
S1	Endo-163.2/431.9/651.9 Exo-100/500	E1	Endo- 166.4/345/391.5/638.9 Exo-100/513
S2	Endo- 169.5/405.6/652.9 Exo-100/510	E2	Endo- 151.9/647.4/840 Exo-100/535.9
S3	Endo-177.6/411/646.9/834 Exo-100/540	E3	Endo- 148.2/400/653.4 Exo-100/296.8/460.4

3.5.2.2 Characterization of the oxides

3.5.2.2.1 Phase identification of the oxides by XRD

The phase identification of all the final thermal products of the precursors is done by X-ray diffraction studies and the interplanar spacing, 'd' values have been compared with the JCPDS card no 5- 664, for hexagonal Wurtzite ZnO (Table A-7 in appendix). Figure 3.16 confirms the formation of single phase ZnO as the decomposition product of all the precursors. Our results in support with previous reports [214] show no new peaks corresponding to Al₂O₃ or any other impurities in the X-ray diffractogram on introduction of aluminium ion in the lattice of ZnO. However there is a small shift to higher diffraction angles as compared to ZnO_{1-x}N_x prepared by same methods indicating overall lattice contraction in Al doped samples.

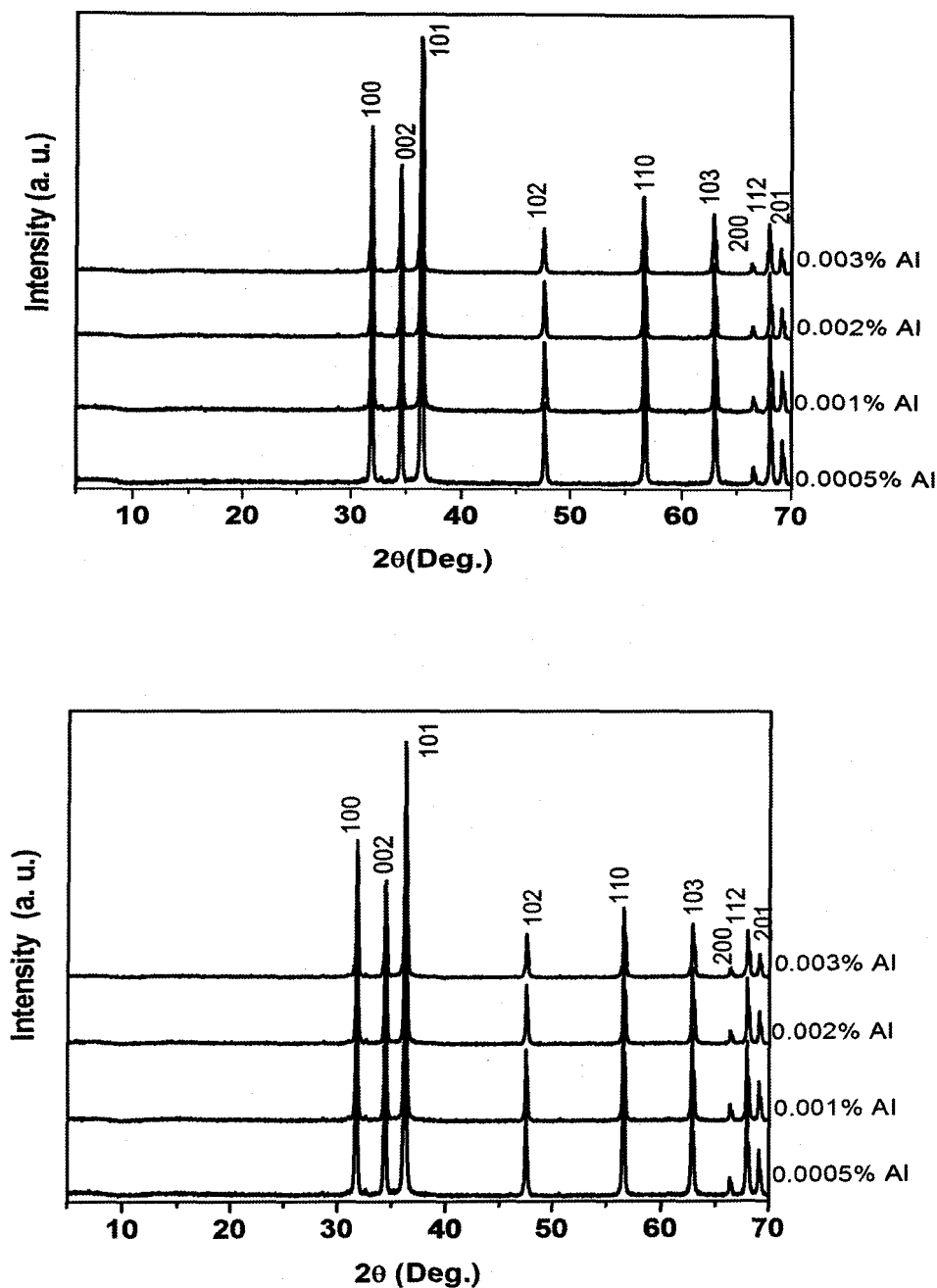


Figure 3.16 X-Ray diffraction patterns of Al doped ZnO samples prepared by i) Solution method, ii) Equilibration method.

3.5.2.2.2 Microstructure analysis of the oxides by SEM

SEM pictures of the representative oxides are as shown in figure 3.17. The particles are irregularly crystallized needles in case of oxide prepared by solution method whereas

the oxide prepared by equilibration method show cube shaped particles of uniform size. It is reported that the grains grow more easily when the aluminium dopant is incorporated in ZnO [214].

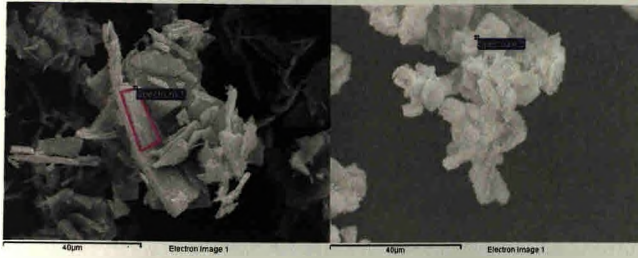


Figure 3.17 SEM of a) 0.001% Al doped ZnO (from S1) ,b) 0.001% Al doped ZnO (from E1)

3.5.2.2.3 Diffuse Reflectance and absorbance Spectra of the oxides

Figure 3.18 shows diffuse reflectance spectra of the oxides. All oxides are faint yellow in colour suggesting presence of N in the lattice. There is no change observed in the reflectance spectra on increase in aluminium content till the concentration is 0.001 %, however at 0.002% of aluminium doping there is an increase in the absorption. The bandgap values calculated from equation (3.6) are compiled in the table 3.9

Table 3.9 Bandgap values of Al doped ZnO calculated from the derivative spectra

Solution method	λ_{max} nm	Bandgap eV	Equilibration method	λ_{max} nm	Bandgap eV
0.0005% Al	386.5	3.21	0.0005% Al	389.9	3.17
0.001% Al	386.5	3.21	0.001% Al	388.7	3.19
0.002% Al	388.3	3.19	0.002% Al	388.1	3.19
0.003% Al	386.7	3.20	0.003% Al	388.5	3.19

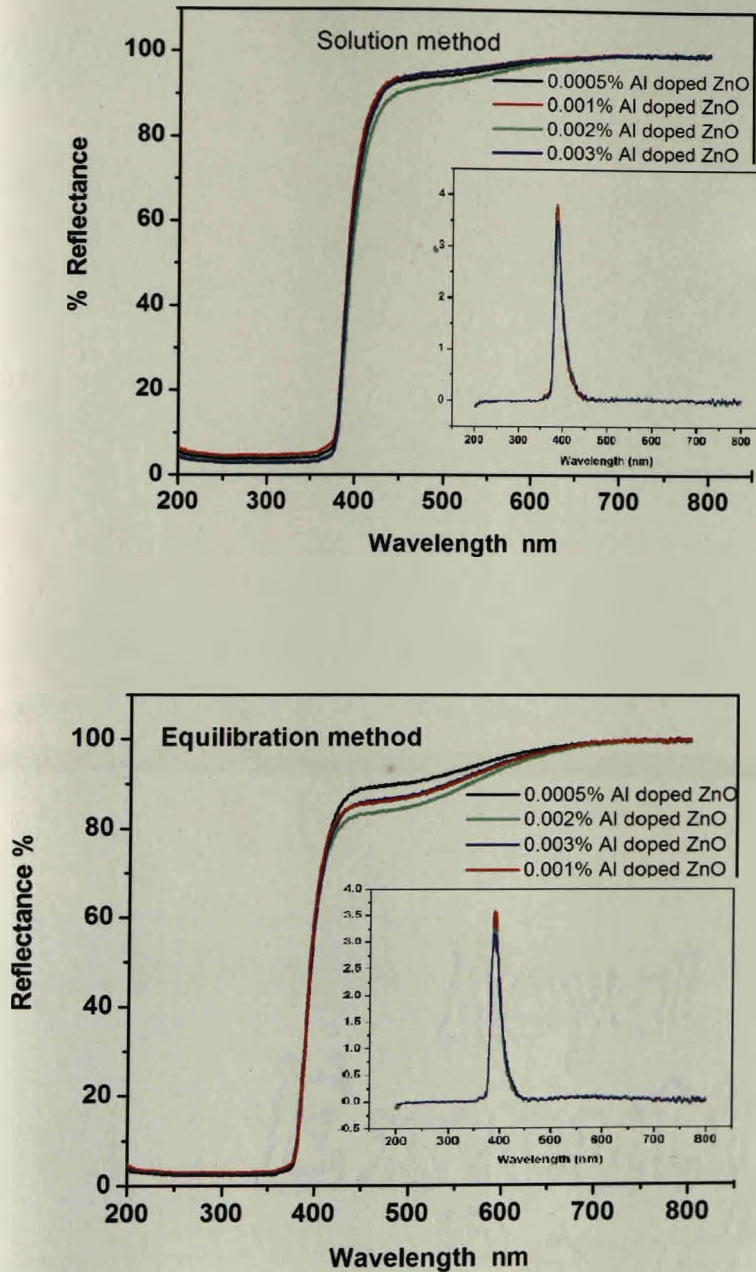


Figure 3.18 Diffuse reflectance spectra of Al doped samples, i) Equilibration method, ii) Solution method.

The absorbance spectra suggest absorbance in the range 200 to 400 nm for all the samples as shown in figure 3.19.

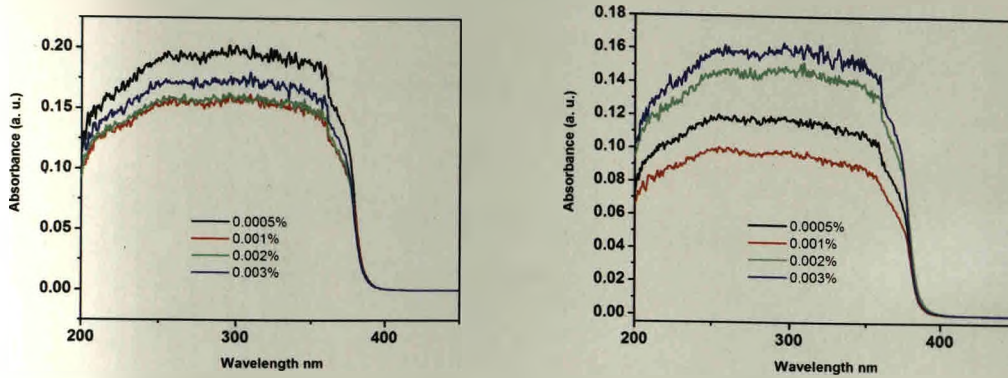


Figure 3.19 Absorbance spectra of Al doped samples, i) Equilibration method, ii) Solution method.

3.5.2.2.4 Elemental analysis of the representative oxides by EDS

The analyses of representative samples (S1 and E1) indicate presence of Al and N in the ZnO lattice suggesting the incorporation of Al and N in the lattice. Based on this the aluminium doped ZnO can be considered to have stoichiometry $Zn_{1-y}Al_yO_{1-x}N_x$

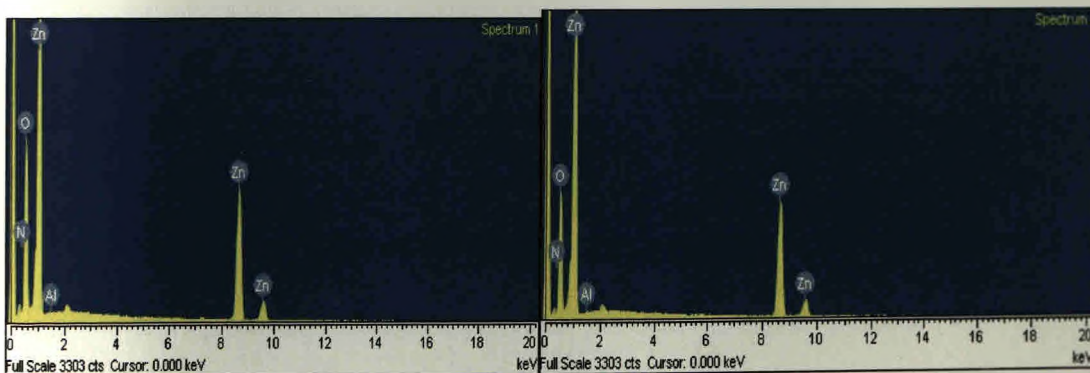


Figure 3.20 EDS of representative samples i) (S1) and ii) (E1)

Table 3.10 EDS data of the sample S1 and E1

Element	Weight%	Atomic%	Compd%
N K	1.43	3.81	5.52
Al K	0.04	0.06	0.08
Zn K	75.84	43.26	94.41
O	22.68	52.87	
Totals	100.00		

Element	Weight%	Atomic%	Compd%
N K	1.03	2.79	3.97
Al K	0.28	0.40	0.53
Zn K	76.72	44.62	95.50
O	21.97	52.19	
Totals	100.00		

3.5.3 Zinc Oxide prepared by Spray Pyrolysis

The oxide prepared by spray pyrolysis was analysed by SEM to study the morphology and EDS to check the presence of nitrogen. FTIR of the sample was also recorded.

3.5.3.1 SEM Analysis of ZnO prepared by spray pyrolysis

The SEM image of the ZnO prepared by spray pyrolysis is shown in figure 3.21. Microstructure studies show fine spherical particles with uniform size distribution. The particle sizes are in the range of 75-80 nm.

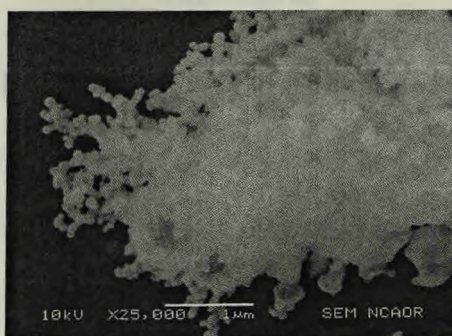


Figure 3.21 SEM image of ZnO prepared by spray pyrolysis.

3.5.3.2 Elemental analysis by EDS

Elemental analysis of ZnO prepared by spray pyrolysis reveals presence of Zn, O and N in the lattice (figure 3.22). This suggests that the method of spray pyrolysis effectively

incorporates nitrogen in the lattice of ZnO giving N doped ZnO.

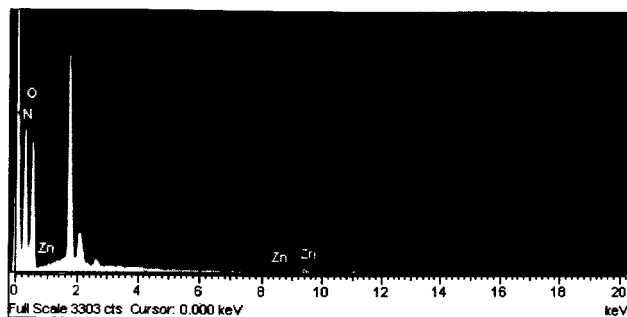


Figure 3.22 EDS of ZnO prepared by spray pyrolysis

3.5.3.3 IR analysis

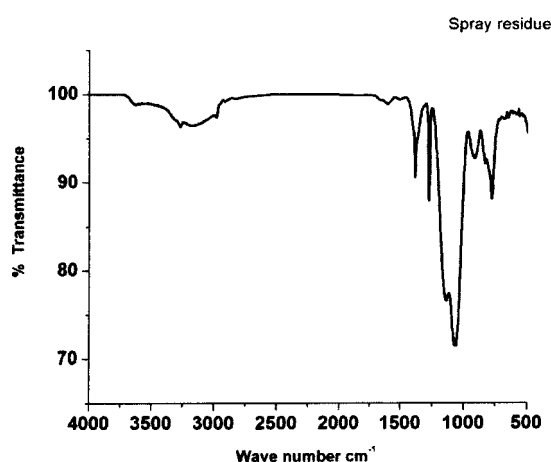


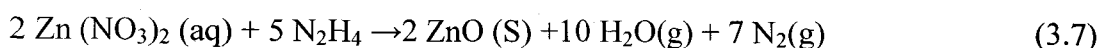
Figure 3.23 FTIR of ZnO prepared by spray pyrolysis.

IR spectroscopy indicates multiple bands in the region from 1500 to 500 cm^{-1} (figure 3.23). The presence of adsorbed OH is indicated by bands in the region of 3000-3500 cm^{-1} and metal-OH bending mode below 1200 cm^{-1} . Metal – oxygen bond is indicated by absorption near 500 cm^{-1} .

The process of spray pyrolysis is environment friendly as the hydrazine hydrate and the zinc nitrate react completely and no harmful products like NO_x or hydrazine are encountered as byproducts of the reaction. The benignity of the reaction has been confirmed by negative tests for nitrites, nitrates [202] and hydrazine [180] during the

course of spray pyrolysis.

The zinc nitrate undergoes pyrolysis in presence of hydrazine to give uniform sized oxide powders and by product N_2 and H_2O . It is found that there is formation of $N_2H_5NO_3$ [179] which has thermodynamic decomposition temperature of $120^\circ C$. The decomposition of $N_2H_5NO_3$ is exothermic with $\Delta H = -256.5 \text{ kJ mol}^{-1}$



The reaction is unlike that of simple pyrolysis of metal nitrates giving oxides and obnoxious gases.



The process of spray pyrolysis requires further exploration for optimizing the process conditions and yields of the resulting metal oxide.

3.5.4 Photocatalytic degradations

3.5.4.1 Photocatalytic studies of degradation of MB

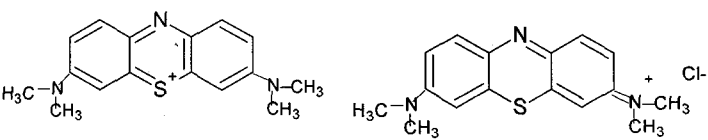
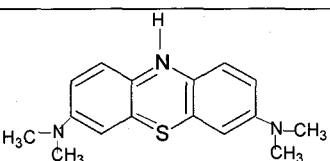
(i) ZnO and $\text{ZnO}_{1-x}\text{N}_x$ system

a. UV-Visible absorbance

Among the different dyes studied in literature, methylene blue is difficult to be decomposed under visible light and is usually regarded as a model dye to evaluate the activity of a photocatalyst. Methylene blue is a member of thiazine class of dyes and is used in optical oxygen sensing in food industry [215], oxidation- reduction indicator in chemistry and a biological stain [216]. It is used as a photosensitizer to produce singlet oxygen in photodynamic therapy for the treatment of cancer [217]. The reduced form of methylene blue in the absence of oxygen is colourless and is referred to as Leuco methylene blue (LMB). LMB is easily re-oxidized to MB by oxygen. Methylene blue degradation has been studied by various researchers, as the organic compound has

strong adsorption characteristics on many surfaces and a well-defined optical absorption maximum in the visible region. It is a cationic dye which exhibits two major absorption bands at ~ 293 ($\pi - \pi^*$) and ~ 665 ($n - \pi^*$) nm in dilute aqueous solutions, the latter having a shoulder at 610 nm [218].

Table 3.11 Structure and absorption wavelength of Methylene blue and Leuco methylene blue

Compound	Structure	λ_{\max}
Methylene blue	Cl^- 	665nm
Leuco Methylene blue		256nm

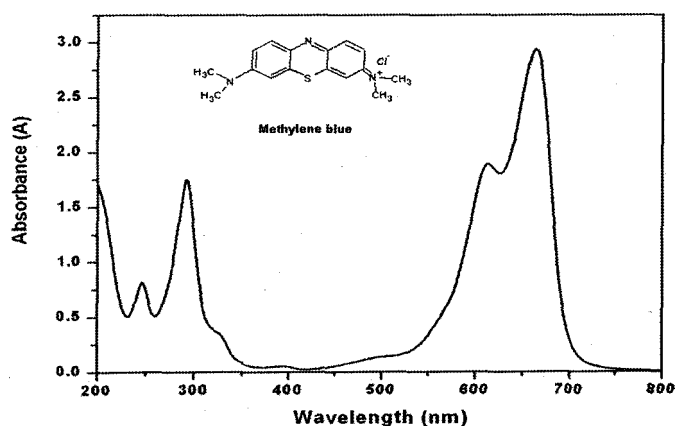


Figure 3.24 UV-Visible spectrum of Methylene Blue Dye

Prior to the photocatalytic studies, a solution of MB (0.5×10^{-4} M) and photocatalysts (200 mg) were mixed and kept in dark for 3-4 hours. There was only 6-7% removal of MB by adsorption. During BET adsorption studies on the photocatalysts, it was

observed that the plot of amount adsorbed against relative pressure show monolayer adsorption characteristics. This agrees with the adsorption of 6-7% MB on the photocatalysts surface. The average light intensity over the duration of each experiment carried out in sunlight (11:00 am to 3:00 pm) is 300 to 724 lux units and the power is 0.24 to 0.52 watt/cm on solar kit provided by TATA BP Solar Bangalore.

An absorbance scan between 200 and 800 nm as a function of time carried out for MB in the presence of photocatalysts ZnO and $ZnO_{1-x}N_x$ exposed to sunlight indicates a decrease in the intensity of the absorbance of MB at $\lambda_{max} = 665$ nm in both the cases. There is appearance of small peak at ~ 200 nm in the UV-Visible absorbance scans of MB. This is attributed to formation of H_2O_2 [219]. Formation of H_2O_2 is transient during the photocatalysis, it disappears as soon as it is formed. The UV-Visible absorbance scans of MB degradation by the photocatalysts are shown in figures 3.25(a, b, c). Blank MB is also exposed to the sunlight (photolysis) at the same time for comparison (figure 3.26). In Photolysis breaking of the bonds in the dye takes place due to direct attack of the light photons on dye molecule.

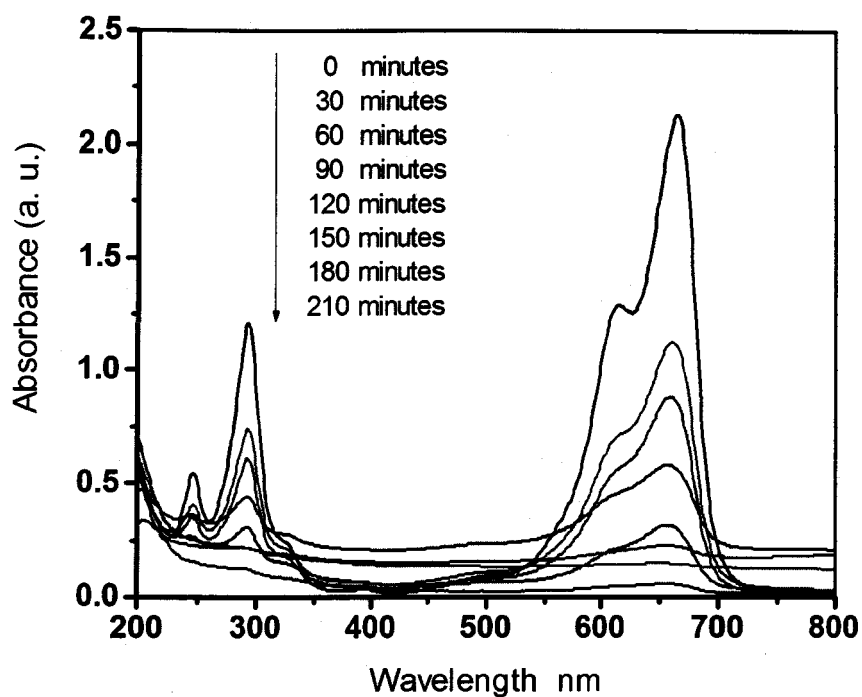


Figure 3.25a UV- Visible spectrum of MB on ZnO.

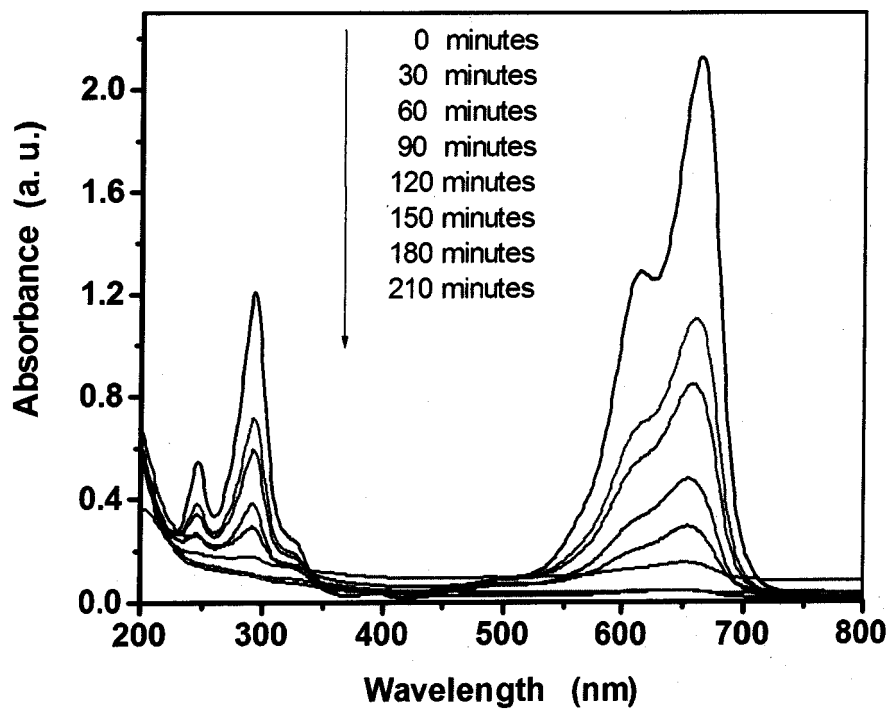


Figure 3.25b UV- Visible spectrum of MB on ZnO_{1-x}N_x (E)

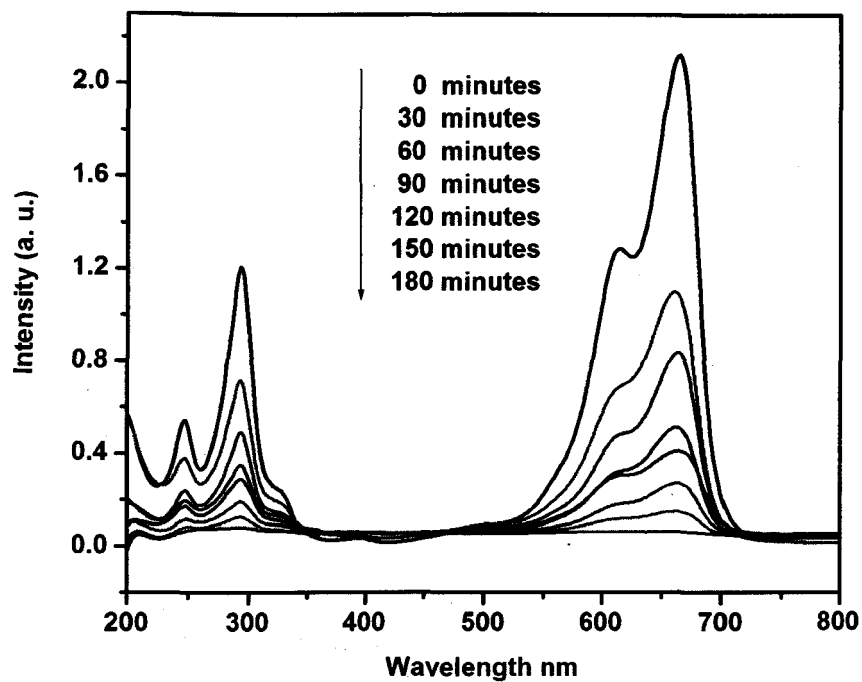


Figure 3.25c UV- Visible spectrum of MB on ZnO_{1-x}N_x(S).

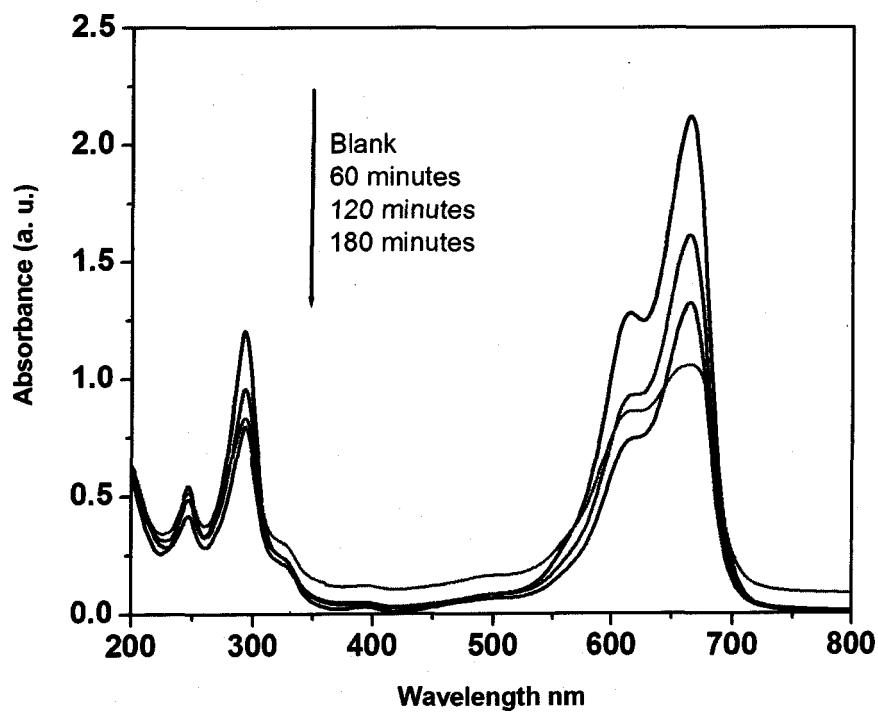


Figure 3.26 UV- Visible spectrum of MB on solar degradation (photolysis)

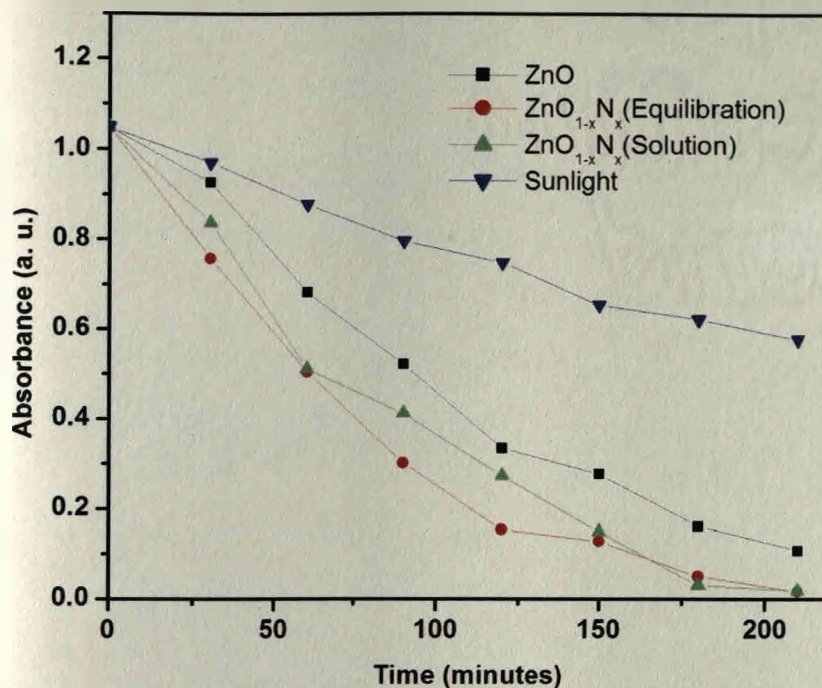


Figure 3.27 Absorbance against time plots for MB degradation.

Table 3.12 Time required for decolourization of MB by ZnO and ZnO_{1-x}N_x photocatalysts.

Photocatalyst	1.25x10 ⁻⁴ M of MB	0.5 x10 ⁻⁴ M of MB
ZnO (Oxalate)	210 min	180min
ZnO _{1-x} N _x (equilibration)	210min	150min
ZnO _{1-x} N _x (solution)	210min	150min

All photocatalysts show complete disappearance of blue colour of methylene blue within 2-3 hours of exposure to sunlight (figure 3.27). The time required for complete decolourization of MB increases with increase in its concentration as seen in table 3.12. As the concentration of the dye in solution increases, it prohibits the incident light from reaching the dye molecules and semiconductor oxide interface. Blank MB sample shows ~ 50% decolorization of MB without catalyst in almost the same time.

Several earlier studies report that the photocatalytic degradation of dyes follows the first order kinetics [74]. The present investigation also reveals that ZnO induced photocatalysis follows first order kinetics with respect to MB concentration. All the experimental results are based on first order plots ($\log C_0/C$ against time) as shown in figure 3.28 and the rate constants are derived from first order plots (table 3.13).

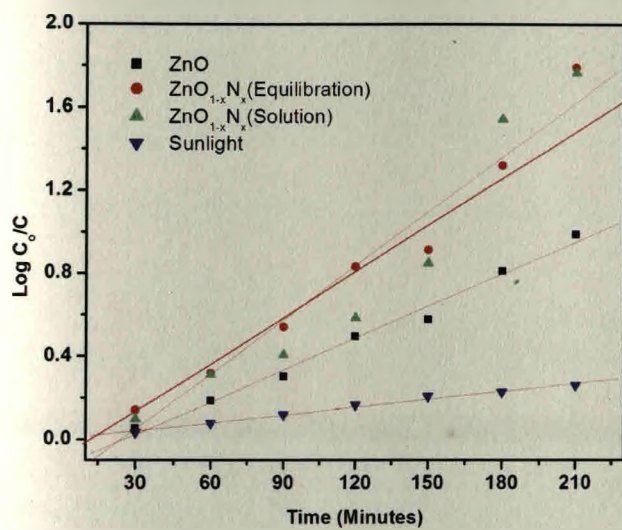


Figure 3.28 Plot of $\log C_0/C$ for MB degradation by the photocatalysts.

Table 3.13 Percent degradation of MB and the rate constants for the degradation reactions.

Photo-catalyst	% degradation for 0.5×10^{-4} M of MB	K (minute ⁻¹)
ZnO	90%	8.36×10^{-3}
ZnO _{1-x} N _x (equilibration)	98.4%	14.7×10^{-3}
ZnO _{1-x} N _x (solution)	98.3%	13.3×10^{-3}
Photolysis	45%	3.11×10^{-3}

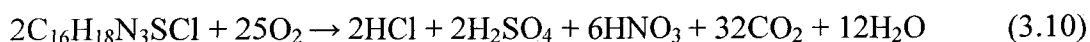
As seen from the rate constants, $\text{ZnO}_{1-x}\text{N}_x$ are more efficient in degrading the dye MB as compared to ZnO. The least rate constant of photolysis ($3.11 \times 10^{-3} \text{ min}^{-1}$) as compared to photocatalysis by ZnO and $\text{ZnO}_{1-x}\text{N}_x$ indicates that the rate of photolysis is negligible as compared to photocatalysis by ZnO and $\text{ZnO}_{1-x}\text{N}_x$.

b. COD removal capacity/Mineralization studies

Decolourization of MB does not amount to its degradation as disappearance of colour may also lead to formation of leuco MB which is colourless. Leuco-Methylene Blue readily oxidizes back to Methylene Blue by oxygen:



The reaction is sensitive to pH and takes place faster in alkaline medium [217]. However, in the case of photodegradation, decolorization results due to the irreversible aerobic degradation of the dye skeleton causing the permanent colour bleaching and hence oxidants or oxygen/air cannot regenerate the colour of the dye. The degradation of the dye proceeds according to the following reaction [112]:



The Chemical oxygen demand (C O D) test is widely used as an effective technique to measure the organic strength of waste water. The test allows measurement of waste in terms of the total quantity of oxygen required for the oxidation of organic matter to CO_2 and water.

The results of the chemical oxygen demand (COD) analysis done at zero time, after 30 minutes of the degradation and at the end of the complete de-colorization of MB under sunlight are tabulated in the table 3.14 for all the catalysts. The reduction in the COD values of the treated dye solution indicates the mineralization of the dye molecules

along with the colour removal. Among the catalysts, ZnO obtained from the oxalate showed 67% COD removal capacity and this ability is enhanced to ~ 85% when the oxide prepared from the hydrazine derivative of the oxalate precursor is used. Though all showed ~100% de-colorization of MB in two hours of exposure to sunlight, COD removal capacity indicates ZnO obtained from the oxalate precursor is poor in mineralization of the dye as compared to that obtained from hydrazinated oxalate precursor, suggesting that the decolorization is not the indication of removal of the organic moiety. Direct photolysis shows an increase in the COD to 572.4 mg/L (85%) on complete decolourization indicating the presence of enormous amount of organic moiety generated. Complete mineralization of MB (equation 3.10) leads to acid ions, Cl^{-1} , SO_4^{-2} , NO_3^{-1} and gaseous CO_2 . Our measurements (except chloride ion), table 3.14, indicate the formation of these ions suggesting mineralization of the dye. From table 3.14 it can be seen that the ZnO obtained from the hydrazinated oxalate precursor showed higher COD removal capacity, increased CO_2 and SO_4^{2-} concentration compared to that prepared from oxalate precursor. Nitrate was not detected in the early stages of degradation which may be because of formation of ammonium ions first and their subsequent oxidation to nitrates. Quantity of sulphate ions released is lower than the stoichiometry. This may be either due to loss of S containing volatile compounds such as H_2S / SO_2 or partially irreversible adsorption of some SO_4^{2-} ions on the surface of the catalyst as observed in case of degradation of MB on titania [111]. The stoichiometric ratio of N to S is 3 according to the formula of MB. The ratio of the nitrates to the sulphates formed is found to be less than the stoichiometric ratio 3. The reason for this may be the escape of these ions from solution as gases. According to degradation reaction of MB equation (3.10), the acid ions produced should decrease the pH of the solution and increase the conductivity due to formation of ions. The degraded

dye solution tested for pH by pH-metry shows pH close to neutral. The conductivity as recorded using conductometer indicates that it remains almost constant. This supports the fact that organic acids formed are converted to CO₂. Similarly nitrates and sulphates are removed as gases as soon as they are formed [220].

Table 3.14 Products of mineralization of MB on photocatalysts.

Photo-catalyst	COD mg/L			% COD Removal	Free CO ₂ final mg/L	Nitrate final mg/L	Sulphate mg/L	
	initial	30min	final				30min	final
ZnO	84	44	28	67	10.69	0.80	0.16	0.88
ZnO _{1-x} N _x (E)	84	36	08	90	14.25	0.80	0.11	0.99
ZnO _{1-x} N _x (S)	84	-----	12	86	-----	2.4	-----	10.6
Photolysis	84	294	572.4	-85(added)	-----	2.6	0.75	32.5

c. Electro Spray Ionization-Mass Spectrometry studies (ESI-MS): Identification of the degraded products of MB

In the present investigation of the de-colorization of MB in combination with the measurements of COD removal capacity, estimation of NO₃¹⁻, SO₄²⁻ ions and free CO₂ it is difficult to ascertain that complete mineralization of the dye has occurred. There might be some organic degradation products still remaining due to their difficulty in further photo-degradation. In order to check such possibility we carried out ESI-MS studies. ESI-MS study is a soft ionization technique wherein ions are separated on the basis of their mass/charge, m/z ratio by the application of small potential. The results of such study have been compiled in the Table 3.15(a, b, c). The spectra are compiled in appendix (A-6 to A-8). ESI-MS of methylene blue molecular ion (MB⁺) gives major

peak at 284 corresponding to methylene blue molecular ion $C_{16}H_{18}N_3S$ and a small peak at $m/z = 270$, $C_{15}H_{16}N_3S$ (Azure B). High energy application fragments methylene blue molecular ion. There is formation of well-known homologues of MB, Azure A ($C_{14}H_{14}N_3S$, $m/z = 256$), Azure B ($C_{15}H_{16}N_3S$, $m/z = 270$), and Azure C ($C_{13}H_{12}N_3S$, $m/z = 241$) [110]. The oxidative photo degradation of MB involves several intermediates and identification of all of them becomes difficult due to very low concentrations of these and many of them cannot be detected because of their poor extractability in the organic medium. However the ones reported in the present study of decolourized solutions extracted with chloroform are different from the ones reported [110] as obtained by ion bombardment. This indicates that the photodegradation of MB has occurred and the fragments detected are the photodegradation products of MB and not produced by the ionization technique in the instrument. The following fragments have been identified in the study (compiled in table 3.15): The presence of a peak at $m/z = 284$ in case of sunlight photolysis (without catalyst) corresponds to methylene blue molecular ion $C_{16}H_{18}N_3S$. The peak at $m/z = 270$ ($C_{15}H_{16}N_3S$), and 198 ($C_{12}H_8NS$) seen in case of sunlight photolysis only, correspond to loss of methyl groups, and dimethyl amino groups from aromatic rings on both sides of MB respectively. This points out to the fact that MB degradation by photolysis proceeds through formation of azure B ($C_{15}H_{16}N_3S$, $m/z = 270$) and then removal of dimethyl amino groups from the aromatic ring. The fragmentation in case of sunlight photolysis is due to direct attack of the light photons on MB molecule or due to attack of hydroxide radicals generated from water by light photons.

The peaks at $m/z = 306$ ($C_{14}H_{16}N_3O_3S$), 279 ($C_{13}H_{15}N_2O_3S$) seem to be due to successive addition of hydroxyl in the MB molecule. Similar degradation products at $m/z = 300$ ($C_{16}H_{18}ON_3S$), 316 ($C_{16}H_{18}O_2N_3S$) and 332 ($C_{16}H_{18}O_3N_3S$) due to successive

addition of hydroxyl in the methylene blue molecule are observed by Batista et al. [75]. The breaking of MB molecule is suggested by the presence of peaks at $m/z = 205$ ($C_6H_9O_4 N_2S$), 200 ($C_8H_{10}O_3NS$), 192 ($C_6H_{10}O_4NS$), 183 ($C_8H_{11}O_3 N_2$), 176 ($C_6H_{10}O_3NS$), 168 ($C_8H_{10}O_3N$), 158 ($C_6H_8NO_2S$) and 149 ($C_4H_5O_6$).

Table 3.15a. Products of MB degradation on ZnO photocatalyst analyzed by ESI-MS.

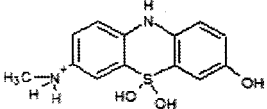
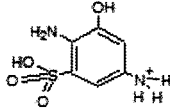
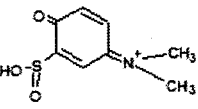
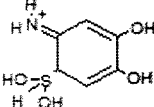
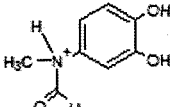
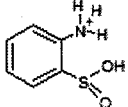
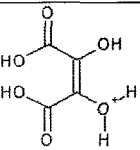
ZnO		
 <p>$C_{13}H_{15}O_3N_2S$, (M^+)=279.1189</p>	 <p>$C_6H_9O_4N_2S$, (M^+)=205.0545</p>	 <p>$C_8H_{10}O_3NS$, (M^+)=200.0814</p>
 <p>$C_6H_{10}O_4NS$, (M^+)=192.0265</p>	 <p>$C_8H_{10}O_3N$, (M^+)=167.9653</p>	 <p>$C_6H_8O_2NS$, (M^+)=158.0668</p>
 <p>$C_4H_5O_6$, (M^+)=148.9934</p>		

Table 3.15b. Products of MB degradation on ZnO_{1-x}N_x photocatalysts analyzed by ESI-MS.

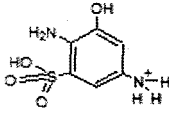
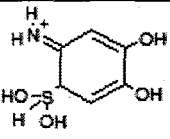
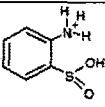
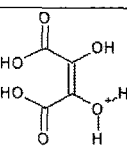
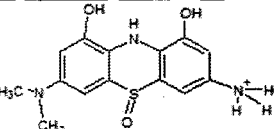
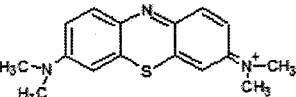
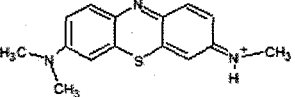
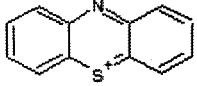
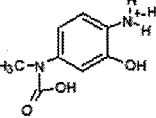
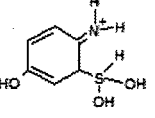
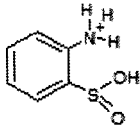
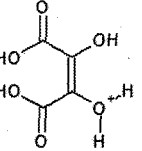
ZnO _{1-x} N _x (S)/(E)		
 <p>C₆H₉O₄N₂S, (M⁺)=205.0523</p>	 <p>C₆H₁₀O₄NS, (M⁺)=192.0268</p>	 <p>C₆H₈O₂NS, (M⁺)=158.0668</p>
 <p>C₄H₅O₆, (M⁺)=148.9939</p>		

Table 3.15c. Products of MB degradation during photolysis analyzed by ESI-MS.

Sunlight (Blank) photolysis		
 <p>C₁₄H₁₆O₃N₃S, (M⁺)=306.1127</p>	 <p>C₁₆H₁₈N₃S, (M⁺)=284.07774</p>	 <p>C₁₅H₁₆N₃S, (M⁺)=270.0679</p>
 <p>C₁₂H₈NS, (M⁺)=198.0964</p>	 <p>C₈H₁₁O₃N₂, (M⁺)=183.0843</p>	 <p>C₆H₁₀O₃NS, (M⁺)=176.1126</p>
 <p>C₆H₈O₂NS, (M⁺)=158.0690</p>	 <p>C₄H₅O₆, (M⁺)=148.9956</p>	

d. Identification and separation of degradation products of MB:**Thin Layer Chromatography (TLC)**

The solutions of MB dye (0.5×10^{-4} M), original solution and completely decolourized (by photocatalysis and photolysis) are extracted in chloroform and TLC is run with ethyl acetate: Petroleum ether (50%) to carry out separation and identification of degradation products of MB. The separation depends on the relative affinity of compounds towards stationary and mobile phase. The compounds under the influence of mobile phase travel over the surface of stationary phase. During this movement the compounds with higher affinity to stationary phase travel slowly while the others travel faster thus aiding the separation of components. The R_f value for each component is then worked out using the formula:

$$R_f = \frac{\text{distance travelled by component}}{\text{distance travelled by solvent}} \quad (3.11)$$

Upon development of TLC only blue coloured spot corresponding to MB dye is seen. On increasing the solvent polarity from 50% ethyl acetate to 70% ethyl acetate single spot corresponding to each sample is observed. These sample spots are unclear and run close to the solvent front. It is reported in literature that TLC of reaction mixture of MB with reducing sugars, run in Butanol: Water: Acetic acid, B:W:A (12:3:5) isolates the product spots [221]. Hence the TLC was run in BWA. Only one spot is visible for each of the samples. The R_f values are same as that of the original MB dye even on repeating the experiment several times.

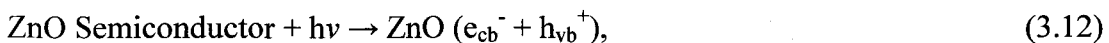


Figure 3.29 TLC of the degraded MB solution.

e. MB degradation mechanism

Photocatalytic degradation of organic materials on semiconductors is a hydroxyl radical mechanism. Hydroxyl radicals are highly oxidizing and nonselective agents and are generated according to following reactions:

The light photon generates electron hole pair on shining on the semiconductor,



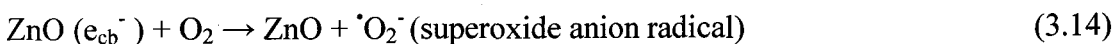
where e_{cb}^- = electrons in the conduction band (cb)

h_{vb}^+ = holes in the valence band (vb)

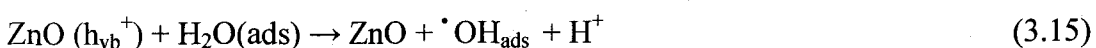
The $e^- h^+$ pair quickly diffuses to the surface. Their recombination occurs usually in several nanoseconds.



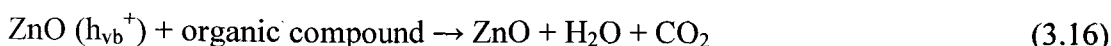
Therefore the electrons and holes should be captured by any of the chemical species which exist on the surface of the semiconductor. The electron thus formed reacts with dissolved or adsorbed oxygen.



The holes formed in the valence band oxidize water and/or adsorbed hydroxyl ions from the photocatalyst surface.



Direct oxidation by surface holes is also possible when the organic molecule is strongly adsorbed on the photocatalyst surface [77].



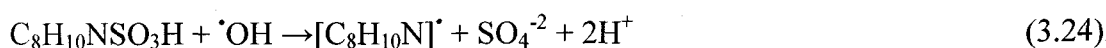
Using ESR spectroscopy data it is reported that the formation of active $\cdot\text{OH}$ and $\cdot\text{O}_2^-$ species takes place during photodegradation of organic compounds [222]. It is also reported that the superoxide radical anion is unstable in aqueous media and is readily converted to $\cdot\text{OH}$ radicals via formation of H_2O_2 [223].



The mechanism of photodegradation of MB is studied by various researchers [75,110-111] using ESI-MS. The photodegradation proceeds through hydroxyl radical mechanism and it is very well supported by detection of hydroxylated products by ESI-MS investigation in our study. It is reported that the $\cdot\text{OH}$ radicals formed attack the $\text{C}=\text{S}^+$ functional group in MB forming sulfoxide ($\text{RS}=\text{OR}'$). The attack of the second OH radical on the sulfoxide produces sulfone ($\text{RSO}_2\text{R}'$) and causes the dissociation of two benzenic rings. Sulfone then gives rise to sulfinic acid (RSO_3H) which further gets oxidised to sulphate (reactions 3.20-3.24).



And/or



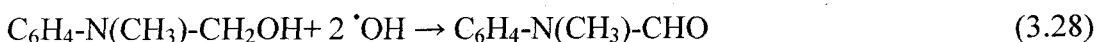
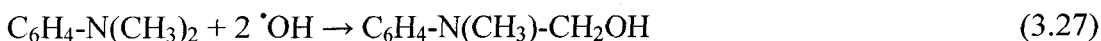
In our studies, the formation of sulphate in the initial 30 minutes of photodegradation

(table 3.15), detection of sulphonated products support this route of photodegradation of MB. The amino group in MB can be substituted by $\cdot\text{OH}$ radical, forming the corresponding phenol and releasing $\cdot\text{NH}_2$ radical which generates ammonia and ammonium ions, estimated to be primary products. These are then slowly oxidised into nitrates.



In our studies, nitrate was not detected in the early stages of degradation, thus supporting the mechanism of formation of ammonia and its subsequent oxidation to nitrates.

The other two symmetrical dimethyl-phenyl-amino groups in MB undergo a progressive degrading oxidation of one methyl group by an attack from $\cdot\text{OH}$ radical, producing an alcohol, then an aldehyde and an acid.



The amino group forms ammonium ions, the aromatic ring undergoes hydroxylations producing phenolic metabolites which decarboxylates into CO_2 by photo-Kolbe reaction.



The degradation of blank MB is due to photolysis by solar radiation or by OH radicals generated in photolysis of water by solar light. Direct photolysis initiates some degradation of MB. The rate of the reaction is however very small as indicated by kinetic studies and C O D values. Thus photolysis can be neglected in comparison to photocatalysis.

Liu et al. report photosensitization by dyes as a means of degradation of dyes like MB. Dyes like MB absorb photons in the visible region of light to generate electrons which are directly injected in the conduction band of the semiconductor oxide. This transfer of electrons by the dye initiates the photodegradation of the formed dye cation radical in visible light. The photoefficiencies for the dye sensitized photocatalytic degradation are smaller than those for the direct photocatalytic degradation [224] and hence can be neglected.

ZnO however dissolves in the aqueous solution under UV illumination, due to the reaction shown below [225].



The concentration of Zn^{+2} undergoing dissolution is very small as compared to initial concentration of ZnO. Dissolution is less at neutral pH and in dark. This dissolution can be prevented by presence of species which can react more efficiently with the photogenerated holes of the semiconductor particle. The presence of surface hydroxyl groups on ZnO act as hole scavenger and prevents the photo oxidation of the photocatalyst.



f. Reuse of ZnO and $\text{ZnO}_{1-x}\text{N}_x$ photocatalysts

ESI-MS indicates presence of some organic moieties in the decolorized solution of MB. The lifetime as well as efficiency of the catalysts can negatively affect the adsorption of the degradation process. Thus reusability is another measure of the efficiency of a photocatalyst. The ability of the catalysts to be reused is checked by repeating the degradation of fresh solutions of MB on the already used catalysts for 3 runs. All show

decolourization of MB in almost the same time during reuse (table 3.16). There is increased formation of sulphates and nitrates. $ZnO_{1-x}N_x$ decolourizes MB in nearly the same time in all 3 runs but shows a decrease in COD removal in 2nd run and an increase in the 3rd run. On the other hand undoped ZnO takes more time to degrade MB for the 3rd run, however efficiently removes COD upto 80.95%. There is increase in formation of sulphate in the 3rd run. The reason for decreased efficiency of the photocatalysts in degradation of the dye during 2nd run may be due to blocking of the active sites of the photocatalyst surface by some of the degradation products.

Table 3.16 Products of mineralization of MB during reuse of photocatalysts.

	ZnO			$ZnO_{1-x}N_x$ (E)			$ZnO_{1-x}N_x$ (S)		
	COD %	Sulphate mg/L	nitrate mg/L	COD %	Sulphate mg/L	nitrate mg/L	COD %	Sulphate mg/L	nitrate mg/L
1 cycle	67.00	0.88	0.8	90.47	0.8	0.99	85.71	1.06	2.4
2 cycle	69.05	3.0	1.8	69.05	2.4	1.32	42.86	6.15	2.4
3 cycle	80.95	2.2	1.8	78.5	7.9	2.6	90.48	1.8	3.1

Diffuse reflectance spectra of the photocatalysts recorded after each reuse indicates no change in the bandgaps of ZnO and $ZnO_{1-x}N_x$ suggesting that the absorption characteristics of the catalysts do not change and they can be reused after proper activation i.e. vigorous washing with water and drying. However a slight change is observed in the absorbance profile of the photocatalysts (figures A-9 in appendix).

(ii) Aluminium doped ZnO System

Table 3.17 gives MB degradation results on aluminium doped ZnO. All the photocatalysts show complete disappearance of blue colour of MB within an hour of exposure to sunlight. Thus the photodegradation efficiency of Al, N co-doped samples is more than that of ZnO and $\text{ZnO}_{1-x}\text{N}_x$. Doping ZnO with aluminium in small amounts thus increases dye degradation ability of ZnO. Similar reports of increase in dye degradation ability of ZnO upon doping with aluminium are found in literature [226].

Table 3.17 Degradation of MB by aluminium doped ZnO samples.

Photocatalyst (Solution method)	% Degradation	Photocatalyst (Equilibration method)	% Degradation	Photo-catalyst	% Degradation
0.0005% Al doped ZnO	96.6	0.0005% Al doped ZnO	95.2	ZnO	90%
0.001% Al doped ZnO	97	0.001% Al doped ZnO	95	$\text{ZnO}_{1-x}\text{N}_x$ (E)	98.4%
0.002% Al doped ZnO	97.4	0.002% Al doped ZnO	96	$\text{ZnO}_{1-x}\text{N}_x$ (s)	98.3%
0.003% Al doped ZnO	96.8	0.003% Al doped ZnO	95.6		

3.5.4.2 Photocatalytic degradation of effluents

Dyes are used to impart attractive colours to textiles, paints, water colours, crayons etc.

The dyeing processes carried out in the industrial houses release large amount of waste waters with high concentration of persistent dyes and chemicals. An effluent with such diverse composition is used for photocatalytic degradation in the present study. Since the effluent is a mixture of different dyes, UV-Visible spectrum of the effluent shows many peaks corresponding to different chromophores. A chromophore is a chemical

group capable of selective light absorption resulting in the coloration of certain organic compounds. The λ_{\max} for the effluent is found to be 628.39 nm (figure 3.30).

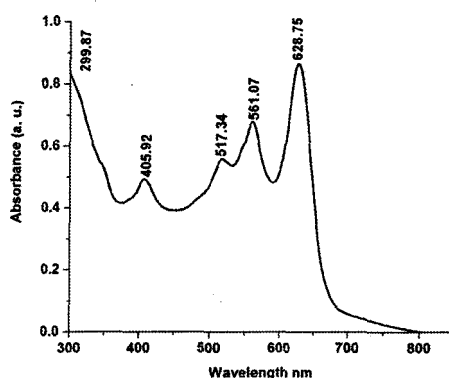


Figure 3.30 UV-Visible spectrum of Industrial effluent

The effluent was subjected to degradation after dilution with three parts of water. Effluent degradation carried out on ZnO, ZnO_{1-x}N_x (equilibration), ZnO_{1-x}N_x (solution) showed that individually they can remove only some of the chromophores from the effluents but are unsuccessful in breaking down other chromophores showing absorbance at 561, 513, 490, 261, 224 nm etc (figure A-10 in appendix). A blank solution of effluent in sunlight does not get degraded on account of photolysis. When ZnO and ZnO_{1-x}N_x (E) were used together for degradation of dye effluent, the mixture could degrade most of the chromophores present in the effluent. It is observed that decolourization takes place in 150 minutes of exposure to sunlight (figure 3.31). The initial COD of the effluent is 96 mg/L indicating high organic content. Upon decolourization, the COD decreases to 48 mg/L indicating 50% COD removal capacity. The pH of the effluent is 6-7 which changes to acidic upon complete decolourization of the solution suggesting formation of acid ions. The chromophore with absorbance at λ_{\max} 628 nm however requires a long time to degrade. Thus the organic residue remaining may be contributed by the chromophore at 628 nm. It is observed that at the

end of the degradation a pink residue is left in the solution (figure 3.32).

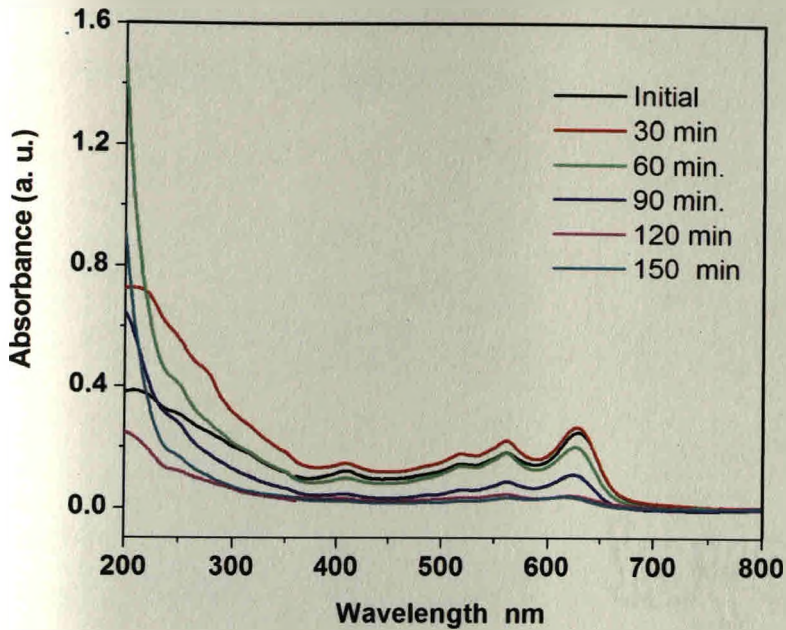


Figure 3.31 UV-Visible spectrum of Industrial effluent during degradation by photocatalysts.



Figure 3.32 Degradation of effluent using ZnO and ZnO_{1-x}N_x with time (left to right)

pH of a solution affects the degradation of dye in solution, surface properties of the photocatalysts and formation of hydroxyl radicals. Thus pH of a solution is an important parameter while studying degradation of the effluents. The pH of the effluent is 6-7. The effect of pH on the degradation process is studied by exposing the effluent

solution in presence of mixture of photocatalysts ZnO and $\text{ZnO}_{1-x}\text{N}_x$ at different pH to the sunlight till decolourization. The degradation of all other chromophores is observed at all pH except the one at 628 nm which decreases in intensity but does not vanish completely at all pH values ranging from acidic to alkaline as shown in figure 3.33.

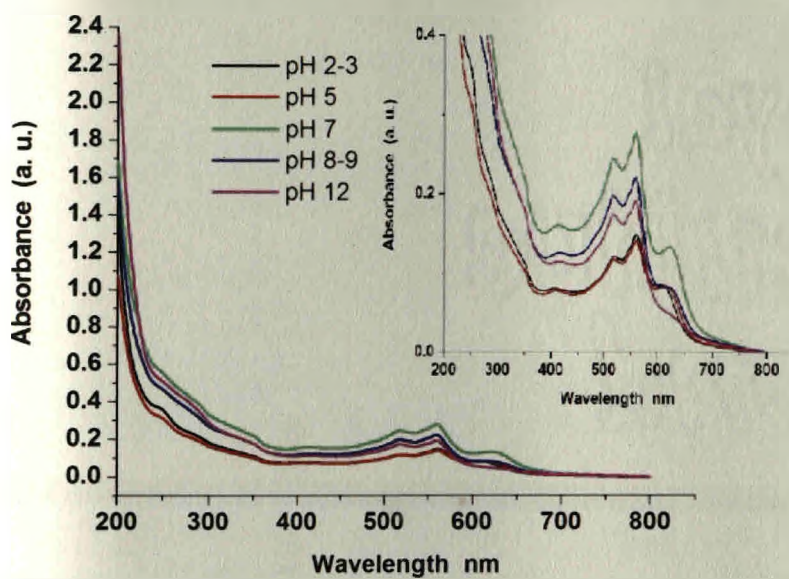


Figure 3.33 Degradation of industrial effluent at different pH values.

Industrial effluents may contain various salts used to impart and fix attractive colours to the objects. Salts like NaCl , Na_2CO_3 are often present in the dye effluents. Thus it is important to know the efficiency of photocatalysts in degrading the effluents in their presence.

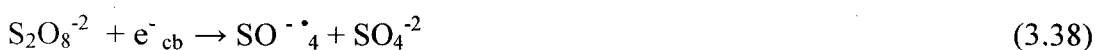
The degradation slows down on addition of NaCl and Na_2CO_3 . The decrease in the degradation of the dye in the presence of chloride ions is due to hole scavenging properties of chloride ions.



The decrease in the degradation of the dye in presence of carbonate ions is due to hydroxyl ion scavenging property of carbonate ions.



Reports on photodegradation of dyes [227] refer use of $\text{K}_2\text{S}_2\text{O}_8$ and H_2O_2 in increasing the rate of photodegradation of the effluents. On addition of $\text{K}_2\text{S}_2\text{O}_8$ and H_2O_2 , there is increased degradation of the effluent. Potassium persulphate is a beneficial oxidizing agent because sulphate anion radical is formed by reactions of potassium persulphate with semiconductor generated electrons.



Sulphate anion radical that is formed in the reactions 3.37 and 3.38 is a strong oxidant ($E^0=2.6$ eV) [227] and degrades the dye. On addition of hydrogen peroxide, the degradation process is fastened. This is due to photolysis of hydrogen peroxide to generate hydroxyl radicals [227].



Thus industrial effluents can be treated using a mixture of ZnO and $\text{ZnO}_{1-x}\text{N}_x$ (E) as both photocatalysts together can break down most of the chromophores in the effluent. However for complete destruction of all organic matter to CO_2 and water, further exposure to sunlight (even after complete decolourization) is required.

3.5.5 Antibacterial Activity of ZnO

3.5.5.1 Disc diffusion method

ZnO is found to strongly resist micro-organisms [113-117]. The disc diffusion study is carried out to find out effectiveness of an antibacterial material against *E. coli* bacteria. The presence of an inhibition zone indicates antibacterial action. The results of the disc diffusion studies on ZnO suspensions with different particle sizes against *E. coli* are

given in Table 3.18. More the zone of inhibition more is the antibacterial efficacy. It is found that ZnO and N doped ZnO ($\text{ZnO}_{1-x}\text{N}_x$) are effective against the tested bacterial strain. The $\text{ZnO}_{1-x}\text{N}_x$ prepared by equilibration as well as solution method show a larger inhibition zone (9 mm) as compared to commercial zinc oxide (7 mm) (Figure 3.39).

The order of inhibition is $\text{ZnO}_{1-x}\text{N}_x$ (E) = $\text{ZnO}_{1-x}\text{N}_x$ (S) > ZnO > commercial ZnO.

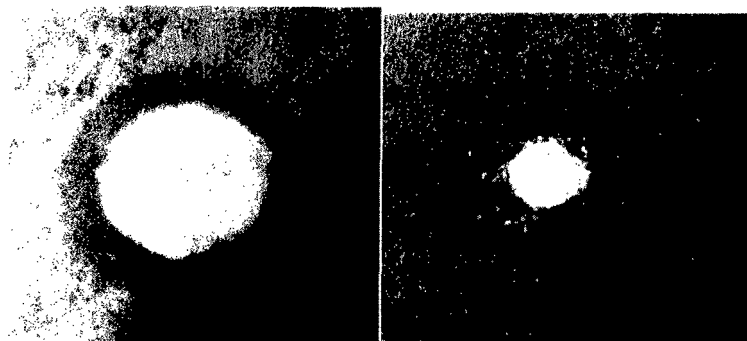


Figure 3.34 Disc diffusion assay of i) $\text{ZnO}_{1-x}\text{N}_x$ ii) ZnO (spray pyrolysis)

Table 3.18 Zone of inhibitions of *E. Coli* on ZnO and $\text{ZnO}_{1-x}\text{N}_x$

Compound	Particle size in nm	Zone of inhibition
ZnO	100-200	8 mm
$\text{ZnO}_{1-x}\text{N}_x$ (equilibration)	69	9 mm
$\text{ZnO}_{1-x}\text{N}_x$ (solution)	38	9 mm
ZnO commercial	> 1 μm	7 mm
ZnO (spray pyrolysis)	75-80	15mm
Control	-----	6 mm

ZnO is activated by UV light to create electron-hole pairs (e^-h^+). The holes split H_2O molecules (from the suspension of ZnO) into OH^- and H^+ . Dissolved oxygen molecules are converted to superoxide radical anions ($^{\cdot}\text{O}_2^-$), which react with H^+ to generate (HO_2^{\cdot}) radicals. These hydroxyl radicals upon collision with electrons produce hydrogen peroxide anions (HO_2^-), which react with hydrogen ions to produce molecules of H_2O_2 [125]. The generated H_2O_2 can penetrate the cell membrane and kill the bacteria [120]. Since, the hydroxyl radicals and superoxide radical anions are negatively charged

particles; they cannot penetrate into the cell membrane and must remain in direct contact with the outer surface of the bacteria.



A normal laboratory environment has fluorescent lighting which emits 4% UV light. So ZnO is 'activated' by this small amount of UV component of the visible light prevalent in the laboratory. In the case of $\text{ZnO}_{1-x}\text{N}_x$ the absorbance is in the visible region of the light which increases the formation of electron – hole pair and thus facilitates the formation of more hydrogen peroxide and increases the antibacterial action. This explains the increase in the zone of inhibition [228].

It is observed that the small particle size and large surface area also tends to increase the area exposed to light and enhances the absorption in the visible region of the electromagnetic spectrum. All these are responsible for more absorbance in the visible light and an increased zone of inhibition. While the dependence of zone of inhibition on the size of the particles is well explained by Yamamoto et al., some reports however indicate that particle size and toxicity of ZnO are unrelated [126].

[228] R. S. Karmali, A. Bartakke, V. P. Borker, K. S. Rane, "Bactericidal action of N doped ZnO in sunlight" *Biointerface Research in Applied Chemistry*, 1 (2011) 057-063.

Disc diffusion studies on the N doped ZnO prepared by spray pyrolysis shows 1.5 cm broader zone of inhibition proving to be a very good inhibitor of *E. coli*. The presence of nitrogen in the ZnO powder obtained from spray pyrolysis is verified by EDS analysis. Thus the nitrogen may be present in some form in the compound which may be making it more effective in its antibacterial action. Aluminium doped ZnO does not show any zone of inhibition against *E. coli*. Our studies are also supported by many literature reports which indicate mild toxicity of Al_2O_3 against the bacteria [229]. Although Al_2O_3 is believed to be toxic to most living organisms [115], aluminium doped ZnO does not show any toxicity towards *E. coli*.

Thus in this case it may be concluded that antibacterial efficiency of ZnO is completely lost on doping with aluminium. It is suggested that the free-radical scavenging properties of the particles might have prevented cell wall disruption and thus no antimicrobial action [229] in Al doped ZnO.

3.5.5.2 Minimum Bactericidal Concentration (MBC)

The Zinc oxide samples prepared by oxalate and hydrazinated oxalate methods are tested for bactericidal efficiency in terms of minimum bactericidal concentration (MBC) by the standard microbial methods. If the material being tested does not kill but instead inhibits the growth of bacteria (bacteriostatic agent), the bacteria will grow when it is removed from the solution containing the material and colonies will be formed on plating an aliquot. If the material being tested is bactericidal, the absence of bacterial colonies will be observed upon plating. The MBC is the lowest concentration at which a compound will kill more than 99% of the added bacteria (Bactericidal). A lower MBC corresponds to higher antibacterial effectiveness. The results of the MBC tests carried out at different concentrations of ZnO and $\text{ZnO}_{1-x}\text{N}_x$ (equilibration and solution method)

and commercial ZnO by plating on Mackonkey agar are compiled in table 3.19.

Table 3.19 Colonies of E Coli on various concentrations of ZnO and ZnO_{1-x}N_x

Milimoles of ZnO	ZnO	ZnO _{1-x} N _x (e)	ZnO _{1-x} N _x (s)	Commercial ZnO
0.01	+++	+++	+++	+++
0.05	+++	+++	+++	+++
0.1	++	++	+	+++
0.5	+	+	-	++
1.0	14*	56*	-	++

Legend: * no of colonies, + Matt growth, - No growth

The growths of colonies are indicated by '+' sign. A '-' sign indicates no growth and colonies which could be counted are indicated by number. In case of ZnO, ZnO_{1-x}N_x prepared by equilibration method, thick growth of colonies is observed at lower concentration of the oxides. Few countable colonies grow at the concentration of 1 mM of the oxide and beyond this concentration no growth is observed (figure 3.35). Thus the Minimum Bactericidal Concentration is above 1 mM. As perceived from the table 3.19, commercial ZnO shows lower antibacterial property as it shows thick growth of colonies in the concentration range under study. ZnO_{1-x}N_x prepared by solution method shows growth of bacterial colonies upto concentration of 0.1 mM. Thus it has MBC of 0.5 mM (figure 3.35). It is reported that the Minimum Inhibitory Concentration of an antibacterial agent decreases with decrease in particle size of the compound [115]. Thus the lower inhibitory concentration in case of ZnO_{1-x}N_x prepared by solution method may be attributed to its smaller particle size and also large surface area and absorbance in the visible region of the electromagnetic spectrum.



Figure 3.35 Bacteriocidal action in MacConkey broth by 1.0 mM $ZnO_{1-x}N_x$ prepared by i) solution method and ii) equilibration method.

From the above studies it can be concluded that Zn^{+2} in minute concentration does not inhibit bacterial growth. It is reported in literature [123], it is known that Zn^{+2} ions act as a nutrient at very low concentration hence ZnO may not be active against *E. coli* in a low concentration range. Zinc traces are an essential cofactor in a variety of cellular processes, but at higher concentrations it is toxic. Hence $ZnO_{1-x}N_x$ (S) prepared by hydrazinated oxalate shows lower MBC and is a biocidal agent effective against *E. coli*.

3.5.6 NO_x studies

NO_x is a major air pollutant emitted by industrial boilers and power plants. It is a precursor of acid rain if it persists in the atmosphere. NO_x is a mixture of NO and NO₂. The amount of NO₂ in the NO_x generated by the reaction of Cu foils on concentrated sulphuric acid estimated by Jacob and Hochheiser method using sulphanilamide and N-(1-naphtha ethylene diamine) dihydrochloride (NEDA) is ~ 5 ppm. The NO_x generated is not removed from the tightly closed jar on exposure to sunlight (intensity 550 lux units). Introduction of photocatalysts coated slide in the tightly closed jar containing NO_x on exposure to light there is removal of gas in 2 minutes. However if the same assembly is kept in dark there is no clearing of NO_x.

It is observed that when ZnO and $ZnO_{1-x}N_x$ coated slides are placed in NO_x atmosphere

in sunlight, the NO_x is absorbed and nitric acid is formed. It causes dissolution of the photocatalysts. To avoid this ZnO was mixed with equal amount of CaCO₃ and coated on glass slides. The nitric acid formed reacts with CaCO₃ and releases CO₂ as per the reaction (3.45), thereby not allowing ZnO to dissolve.



All photocatalysts absorb NO_x within 2 minutes of exposure to sunlight (intensity 500-550 lux). Commercial ZnO does not show any removal of NO_x during the experiment. The aluminium doped ZnO samples also remove NO_x within 1-3 minutes on exposure to sunlight of same intensity. Results obtained are compiled in table 3.20 below.

Table 3.20 Time taken by prepared ZnO and doped ZnO for removal of NO_x.

Photocatalyst	Time minutes	Photocatalyst (Solution method)	Time minutes	Photocatalyst (Equilibration method)	Time minutes
ZnO	2	0.0005% Al doped ZnO	1	0.0005% Al doped ZnO	1
ZnO _{1-x} N _x (E)	2	0.001% Al doped ZnO	3	0.001% Al doped ZnO	2
ZnO _{1-x} N _x (S)	2	0.002% Al doped ZnO	2	0.002% Al doped ZnO	1
		0.003% Al doped ZnO	1	0.003% Al doped ZnO	3

The photocatalyst mixture scraped off from the slide after its use in the removal of NO_x gives positive test for nitrate by brucine method [202]. This indicates that the NO_x is converted to nitrate by the photocatalysts.

The probable mechanism of NO_x removal may be as follows: The electron-hole pairs are produced during the photo excitation of ZnO and ZnO_{1-x}N_x. The electrons in the

conduction band react with molecular oxygen to form reactive hydroxide and superoxide radicals [133, 230-231]. The nitrogen monoxide reacts with these reactive radicals to produce HNO_2 or HNO_3 . It is also reported that about 20% of nitrogen monoxide is decomposed to nitrogen and oxygen directly [232].

NO_x removal by ZnO is studied qualitatively in the above experiments. ZnO powders are unstable in acidic and basic media and as observed in our studies and undergo dissolution in the acidic medium of nitric acid produced. This limits the use of ZnO for NO_x removal. Coupling it with CaCO_3 helps in trapping nitrogen in nitrate form and releasing CO_2 gas without dissolving itself. The CO_2 formed can be utilized for some other purpose. Hence there is no fear of the products HNO_2 and HNO_3 decreasing the photocatalytic ability and the life of the catalysts.

There are reports of NO_x removal by N doped TiO_2 . N doping is believed to have increased the photocatalytic activity. It is also reported that photocatalytic activity of the N doped TiO_2 increased with increasing nitrogen content and specific surface area of the photocatalysts [133]. Present work requires further exploration for understanding the effect of N doping, particle size and surface area in NO_x degradation.

Thus synthesis of Zinc oxide photocatalyst by hydrazination method introduces nitrogen in the lattice. The oxide so formed is efficient in degrading the dye as well as industrial effluent. It is found to be a good bactericidal agent against *E. coli*. The environmental pollutants like NO_x can also be removed efficiently using it with calcium carbonate. The use of hydrazine lowers the energy requirement in synthesis and also scavenges unwanted gases evolved during preparation.

Chapter 4

Iron oxide system

For

Photomineralization of organic compounds

4.1 Introduction

The iron ore rejects/tailings are generated after removal of high grade ore. These are usually stored in the pits at the mining site. During rains they flow into fields and during summer, the fine material flies as dust in the surrounding, thus polluting the nearby environment. The content of iron in the rejects is reported to be ~ 40%. In the present era of deteriorating resources rejects with ~ 40% iron loading cannot be wasted. It must be used as a technologically important material. Iron salts have been used in degradation of organics like phenols, dyes, coking wastewaters, industrial effluents [153-157]. Ores like limonite (Iron rich), Pelagite (Manganese rich) are investigated for their use in oxidation of dyes [149-150]. In view of this, one of the ore reject samples is used to degrade organic dyes. Thus the oxides in the ore rejects are investigated to find whether they can be utilized for abating environmental pollutants thereby making them value added materials. Methylene Blue (MB) is taken as a representative dye. MB degradation or for that matter organic materials degradation in aqueous solution is normally attempted through photo Fenton mechanism by the use of advanced oxidation process (AOP) which combines a strong oxidizing agent (e.g. H_2O_2 , O_3) and catalyst (Ferrous material). Since in the ore rejects a small amount of Fe^{+2} is present it is thought to be used for MB degradation possibly through Fenton or (Photo Fenton) mechanism.

In 1890's Henry John Horstman Fenton developed [233] a solution of hydrogen peroxide and an iron catalyst to oxidize contaminants or waste waters. The solution known as Fenton reagent was used to destroy organic compounds such as trichloroethylene (TCE) and tetrachloroethylene (PCE). The ferrous Iron (II) of the iron catalyst gets oxidized by hydrogen peroxide to ferric iron (III), a hydroxyl radical and a hydroxyl anion.

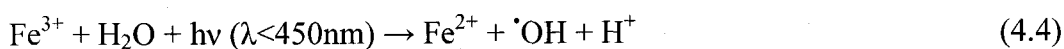


Iron (III) is then reduced back to iron (II), a peroxide radical and a proton by the same hydrogen peroxide (disproportionation reaction).



Reaction (4.1) was suggested by Haber and Weiss in the 1930s, [234]. In the net reaction the presence of iron is truly catalytic and two molecules of hydrogen peroxide are converted into two hydroxyl radicals and water. The generated radicals then engage in secondary reactions. The hydroxyl radicals ($\cdot\text{OH}$) are effective in destroying organic chemicals because they are reactive electrophiles (electron preferring) that react rapidly and non-selectively with nearly all electron rich organic compounds. They have an oxidation potential of 2.33V and exhibit faster rate of oxidation reactions as compared to conventional oxidants such as H_2O_2 and KMnO_4 .

Iron (II) sulfate is a typical iron compound in Fenton's reagent. Fenton's reagent is also used in organic synthesis for the hydroxylation of arenes in a radical substitution reaction. Use of such advanced oxidation process (AOP) by the combination of strong oxidizing agents (e.g. H_2O_2 , O_3) with the catalysts (e.g. transition metal ions) and even irradiation (Photo Fenton) are now finding wide applicability in abating water borne environmental problems. Beneficial role of coupling Fenton oxidation with irradiation is closely related to iron being generated in the following redox cycle producing two hydroxyl radicals per molecule of H_2O_2 decomposed,



The formation of hydroxyl radicals in Fenton or photo-Fenton reaction is attributed to the decomposition of the photo-active $\text{Fe}(\text{OH})^{2+}$ [153].



Iron ore reject (total Fe ~ 54%) from a particular region (of Goa) consisting of ~1.1% FeO corresponding to ~3.25% Fe₃O₄ mainly consisted of FeOOH with hardly any organic admixture as ~7.5 % weight loss (FeOOH forms Fe₂O₃ by losing 10.13% weight) was observed at ~ 700°C. We envisaged that it may be a suitable candidate for the mineralization of organic materials in water body through Fenton like mechanism.

4.2 Characterization

The iron ore rejects sample was collected from one of the Goan mines. The muddy red colored sample was finely crushed and pulverized. Following analyses were carried out on it.

4.2.1 Chemical Analysis of the ore reject sample: Presence of Fe

The sample was treated with concentrated hydrochloric acid to dissolve iron content of the ore. Insoluble components like silica remained as residue which was then filtered. Chemical analysis of Fe was done by titrations with standard Potassium dichromate solution using diphenylamine indicator. Potassium dichromate is a strong oxidizing agent which oxidizes all Fe⁺² to Fe⁺³. The ferric ions present in the solution were converted to ferrous ions using stannous chloride. Excess of stannous chloride was neutralized by adding mercuric chloride. The solution was titrated against standard Potassium dichromate solution to get total Fe.

4.2.2 Instrumental analysis

4.2.2.1. X-ray diffraction (XRD): Phase identification

Phase identification of the ore rejects was done by XRD. The details of the theory and instrumentation are described in chapter: 2, section: 2.3.2.3. XRD of the iron ore reject

was recorded on the instrument Rigaku Powder X-ray diffractometer using Cu K α ($\lambda = 1.5418 \text{ \AA}$) radiation filtered through Nickel filter in the instrument operating at V= 30 kV and I = 15 mA.

4.2.2.2 Energy Dispersive X-ray Spectroscopy (EDS)

The elemental analysis of the ore rejects was done by EDS. The details of the theory, instrumentation and experimental conditions are described in chapter: 3, section: 3.3.2.8.

4.2.2.3 Magnetization measurements

The saturation magnetization measurement was done by using Satmagan (Saturation Magnetization Analyzer). It is a magnetic balance in which a sample is weighed in gravitational and magnetic fields. If the field is strong enough to saturate the magnetic material in the sample, the ratio of the two weights is linearly proportional to the amount of magnetic material in the sample. A finely powdered dry sample was filled in the sample cell compactly and closed with the plug. It was then analyzed by SATMAGAN Model 135 of Corrigan Make. The instrument was calibrated by using a series of standard compounds.

4.2.2.4 Scanning Electron Microscopy (SEM)

The morphology of the ore reject sample was studied by SEM. The details of the theory, instrumentation and experimental conditions are described in chapter: 2, section: 2.3.2.6.

4.2.2.5 UV-Visible Diffuse reflectance spectrometry (DRS)

The absorbance and reflectance characteristics of the ore reject was studied by UV-Visible spectroscopy. The details of the theory, instrumentation and experimental conditions are described in chapter: 2, section: 2.3.2.5.

4.2.2.6 Fourier Transform Infrared (FTIR) Spectroscopy

The ore rejects sample was subjected to IR analysis to understand the chemical structure of the rejects. The details of the theory, instrumentation and experimental conditions are described in chapter: 2, section: 2.3.2.1.

4.3 Degradation of Methylene blue (MB) Dye

4.3.1 Photocatalytic Degradation of MB

The iron content present in the iron ore reject may be able to photodegrade the organic substrates in presence of H_2O_2 or hydroxide ions by mechanism similar to Fenton reaction. With this aim in mind, iron oxide was prepared from the ore rejects. The iron from the ore reject was extracted with concentrated hydrochloric acid leaving behind the insoluble residue of the rest. Fe_2O_3 was prepared from the extract using standard procedure [180] wherein iron was precipitated as hydroxide maintaining a controlled pH of 3-4. The precipitate of hydroxide was then filtered, washed, dried and decomposed to give Fe_2O_3 . This Fe_2O_3 was used for photocatalytic degradation of organic dye MB in sunlight at alkaline pH.

In another attempt, γ - Fe_2O_3 prepared from the ore rejects was used for photodegradation of MB. The γ - Fe_2O_3 was prepared from ore rejects [148] by precipitation as hydroxide at a controlled pH of 3-4. The precipitate of hydroxide was then filtered, washed, dried and equilibrated with hydrazine by keeping it in a petri dish

over hydrazine hydrate, $N_2H_4.H_2O$ (99%), in a desiccator for 4–5 days. On exposure to ordinary atmosphere it decomposed autocatalytically to $\gamma-Fe_2O_3$. This $\gamma-Fe_2O_3$ was used for photocatalytic degradation of organic dye MB in sunlight at alkaline pH.

The iron in the crude form as ore reject was also used for degradation of a test solution of MB at alkaline pH.

4.3.1.1 Photocatalytic Degradation of MB on iron ore rejects

It was observed that iron ore rejects effectively decolourize test solution of MB in presence of sunlight. Photodegradation process of any organic substrate on a photocatalyst surface depends upon various parameters like nature and concentration of the substrate, concentration of the photocatalyst, light source and intensity, pH, temperature etc. Hence, it is important to study the effect of these parameters on degradation of MB using ore rejects. In all the investigations, intensity of incident sunlight was 300 to 724 lux units. Although it was envisaged that degradation of organic substrate on a photocatalyst surface will take place at alkaline pH, it was necessary to study the effect of acidic as well as neutral range of pH on degradation. Hence photodegradation of MB (50 ml of 5×10^{-5} M (16 ppm) diluted to 150 mL) in presence of 200 mg iron ore reject was studied at pH values from 1 to 11. Effect of initial concentration of the dye on its photodegradation (pH = 11, iron ore reject = 200mg) at concentrations of 10, 16, 20, 30 and 40 ppm was studied. Ore concentrations ranging from 10 mg to 2g were used to study the effectiveness in photodegradation of MB (pH = 11, MB concentration = 16 ppm). Effect of Temperature ($8^\circ C$ to $48^\circ C$) on photodegradation of MB (pH = 11, MB concentration = 16 ppm, iron ore reject = 200mg) was also studied.

4.3.1.2 Degradation of MB on iron ore rejects at alkaline and neutral pH in sunlight

As obtained ore reject (200 mg) in the fine mesh size of 200 was added to 50 ml of 5×10^{-5} M (16 ppm) methylene blue (MB) in a clean conical flask (500 mL) and volume was made up to 150 mL with distilled water. The pH of the solution was maintained at 11 (optimum pH) and 7 (neutral pH). The solutions were exposed to sunlight (11 am to 3 pm) with continuous stirring. The average intensity of sunlight during 4 hours of the mid day was in the range of 300 to 724 lux (Lux meter LX-101) and the power was between 0.24 and 0.52 watt/cm (Solar kit, TATA BP Solar Bangalore, India). Small aliquots of the experimental solution were withdrawn after every 30 minutes and the extent of de-colorization of MB was monitored spectrophotometrically at $\lambda_{\max} = 665$ nm (Shimadzu UV-2401-Rev A 6700) in the range 200-800 nm. The decolourization studies were also done on MB without the addition of the ore rejects (Blank solution).

The decolourized solutions were analyzed by ESI-MS for detection of organic residues. The COD, nitrate and sulphate estimation were done to study the mineralization of MB in the decolourized dye solution. The experimental details are as described in chapter: 3, section: 3.4.1.1 b-d.

4.3.1.3 Effect of dyeing chemicals and additives on MB degradation by ore rejects

The industrial effluents contain various other chemicals used to impart attractive colours to the textiles along with the dye [74]. The degradation should occur in presence of the chemicals like NaCl, Na_2CO_3 used in dyeing process [227]. The effect of these chemicals on the efficacy of iron ore rejects in the degradation of dye is studied.

Certain chemicals like $K_2S_2O_8$, H_2O_2 [227] are reported to enhance the degradation of dyes. Hence, an attempt is also made to study the degradation of the dye in presence of these additives. For studying the effect of these additives ($NaCl$, Na_2CO_3 and $K_2S_2O_8$) on MB degradation in sun, five conical flasks with concentrations 0, 25, 50, 100 and 200 mg of the additives (separately) in 100 ml of distilled water were added to 50 ml solution of MB and solutions were made alkaline. In case of H_2O_2 concentrations 0.01, 0.02, 0.03 and 0.04 M prepared in 100ml distilled water were added to 50 ml solution of MB. The solutions were made alkaline.

4.3.2 Thermal degradation of MB

Thermal degradation of MB ($5 \times 10^{-5}M$, 16 ppm, 10 ml) in the presence of ore rejects (10 mg) was carried out at neutral pH at different temperatures viz. 40, 60, 80 and $100^\circ C$. Small aliquots of these solutions were withdrawn and the extent of decolorization of MB was monitored spectrophotometrically at $\lambda_{max} = 665$ nm (Shimadzu UV-2401-Rev A 6700) in the range 200-800 nm. A blank solution of MB, without addition of ore rejects was also subjected to heat at different temperatures viz. 40, 60, 80 and $100^\circ C$ simultaneously and checked for degradation.

4.4 Results and discussion

4.4.1 Characterization of Ore rejects

4.4.1.1 Chemical Analysis of the ore reject sample: Presence of Fe

Chemical analysis reveals the presence of about 54% of total Fe (Fe^{+2} and Fe^{+3}) in the iron ore reject. Iron in Fe^{+2} form as FeO of $\sim 1.01\%$ corresponds to 3.25% Fe_3O_4 (table 4.2). Most of the iron is present in FeOOH form. This is supported by presence of

diagnostic bands for FeOOH in the FTIR spectra. Isothermal weight loss studies of ore rejects indicate 7.5% loss at 700°C indicating very little or negligible amount of moisture/ organic matter in the rejects.

4.4.1.2 Analysis of ore rejects by XRD: Phase identification

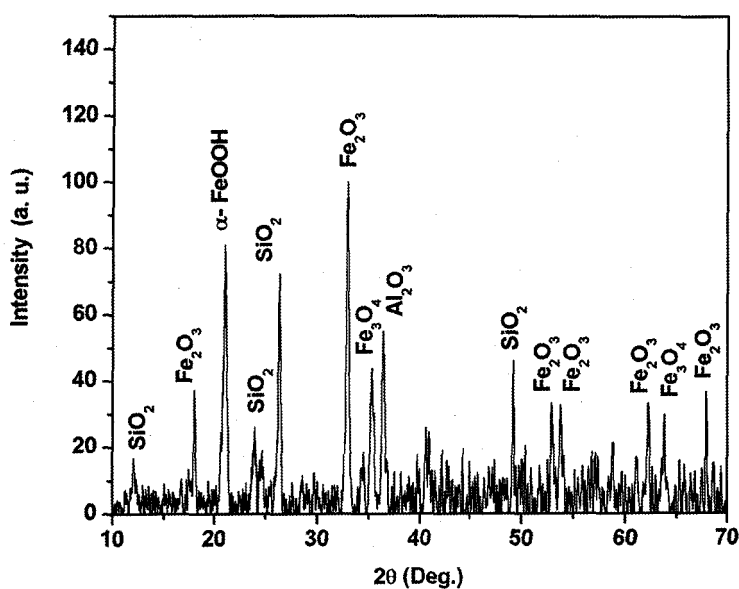


Figure 4.1 XRD pattern of iron ore rejects.

XRD analysis of iron ore rejects (figure 4.1) show the presence of Fe_2O_3 (α , γ , ϵ), Fe_3O_4 , α -FeOOH, SiO_2 , Al_2O_3 etc. The peak positions are matched with the JCPDS cards number 13- 534, 16-394, 16- 653, 16-895, 18- 1169, 19-629, 25-1402, 28-491, 31-1233. This confirms the data of chemical analysis as regards the presence of FeO, Fe_2O_3 , Fe_3O_4 and α -FeOOH.

4.4.1.3 Elemental analysis of ore rejects by Energy Dispersive X-ray Spectroscopy

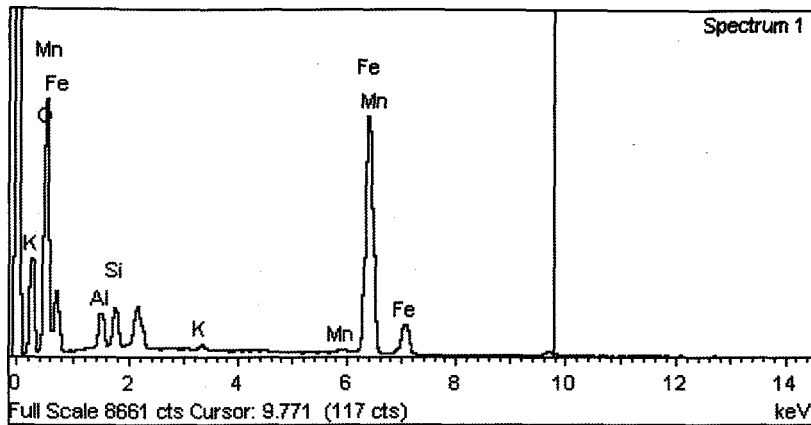


Figure 4.2 Elemental analysis of iron ore rejects

EDS analysis (figure 4.2) shows that the iron ore rejects contain Fe, Al, Si and traces of metals like K and Mn. Table 4.1 gives weight% of the elements present in the iron ore rejects. The iron content of 50% matches well with chemical analysis results.

Table 4.1 EDS results of analysis on iron ore rejects.

Element	Weight%	Atomic%
O K	43.64	71.07
Al K	2.74	2.64
Si K	2.60	2.42
K K	0.32	0.21
Mn K	0.70	0.33
Fe K	50.00	23.33
Totals	100.00	

4.4.1.4 Saturation magnetization studies of Ore rejects

Results of analysis on the instrument SATMAGAN are compiled in the table 4.2.

Table 4.2 Chemical analysis of iron ore rejects

Ore reject sample	Total Fe(%)	FeO (%)	Fe ₃ O ₄ (%)	Fe ₃ O ₄ (%) SATMAGAN
Before use for degradation of MB dye	53.94	1.01	3.25	5.02
After use for degradation of MB dye	53.70	1.44	4.64	5.55

The content of Fe₃O₄ (Magnetite) in the ore rejects is 5.02 % according to the analysis carried out on the instrument SATMAGAN. This value is however higher than that calculated by chemical analysis (3.25%). This may be due to presence of magnetic component like magnetic gamma ferric oxide, γ -Fe₂O₃, present along with Fe₃O₄.

4.4.1.5 Scanning Electron Microscopy of ore rejects

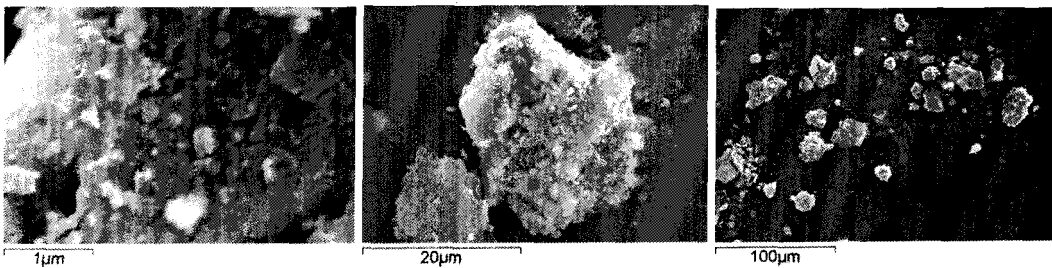


Figure 4.3 Scanning electron micrographs of iron ore reject at different magnifications.

SEM pictures show particles of varied sizes and shapes in the ore rejects.

4.4.1.6 Diffuse Reflectance and Absorbance spectra of the ore rejects

Diffuse reflectance spectroscopy show absorbance of ore rejects in the visible region of the electromagnetic spectrum. Iron ore rejects contain oxides of iron (ferrous and ferric) along with hydroxide. A variety of colours are exhibited by oxides of iron. The variation of colours exhibited by the iron oxides is because of different types of

electronic transitions within the $3d^5$ shell of the Fe^{+3} ion [235]. The band-gap of iron ore reject calculated from equation 2.8 is 2.19 eV.

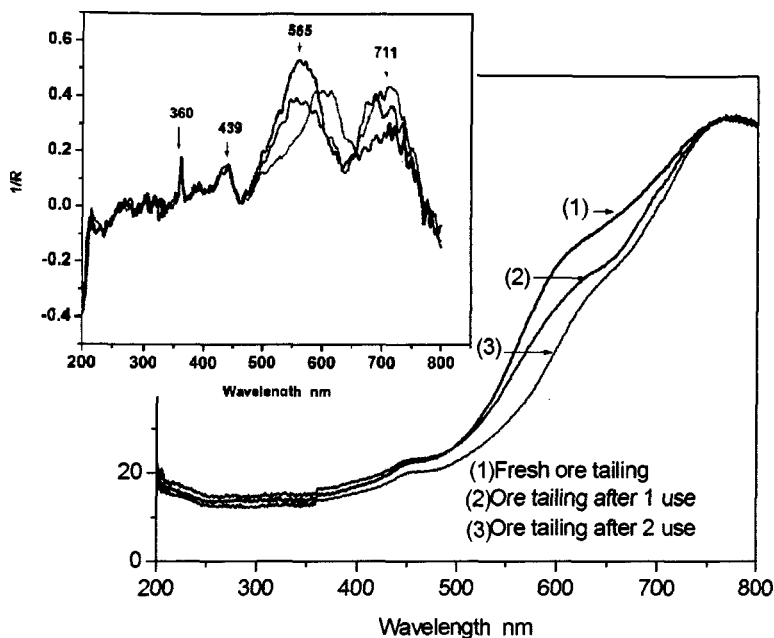


Figure 4.4 Diffuse reflectance spectra of iron ore rejects(inset derivative)

Table 4.3 Derivative peaks obtained from diffuse reflectance spectra of iron ore rejects.

Fresh sample (nm)	After 1 use in degradation (nm)	After 2 use in degradation (nm)
360	360	360
439	439	439
565	560	604
714	687	711

Derivative spectra of the rejects show 4 distinct peaks as tabulated in table 4.3. The peaks may be assigned to the phases Goethite (α -FeOOH), Maghemite (γ -Fe₂O₃), Hematite (α -Fe₂O₃) and Magnetite (Fe₃O₄) in accordance with the literature. Literature

reports of hematite and goethite, having distinct first derivative peaks, centred at 565 and at 435 nm, respectively [236]. An intense band due to electron pair transition (EPT) in haematite (α - Fe_2O_3) between 521-565 nm differentiates it from EPTs of the other Fe oxides (479 to 499 nm) [237]. The ferrihydrite ($\text{Fe}_5\text{HO}_8.4\text{H}_2\text{O}$) and feroxyhite (δ - FeOOH) samples show ${}^4\text{T}_2 \rightarrow {}^6\text{A}_1$ transition at 698 to 734 nm. The presence of maghemite is also confirmed by a peak at 360 nm. The spectrum of magnetite is similar to that of haematite and FeOOH [238]. The absorbance spectra of the ore rejects indicate its absorbance is in the range of 200-400 nm. It also shows an absorption peak in the visible region of the spectrum i. e. 450-600 nm (figure 4.5).

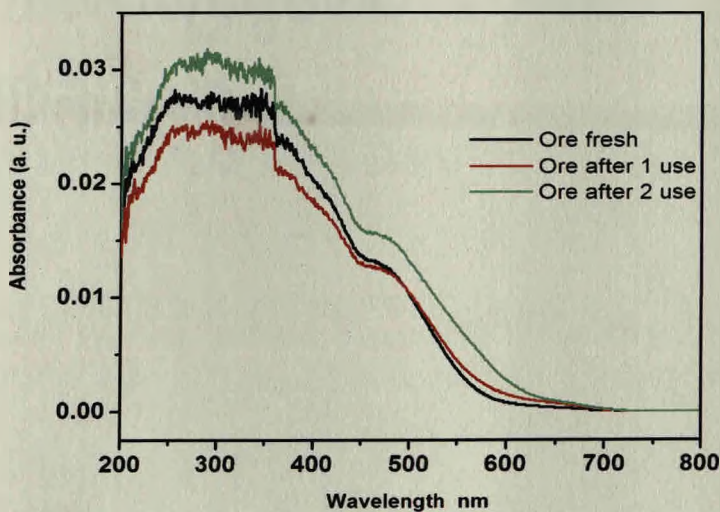


Figure 4.5 Absorbance spectra of iron ore rejects.

4.4.1.7 IR analysis of ore rejects

FTIR analysis of the ore rejects show absorptions corresponding to the bonds given in the table 4.4.

Table 4.4 IR absorption bands of iron ore rejects

Frequency cm^{-1}	Bond
545	Fe-O bond in Fe_3O_4
913	O-H bending
795	O-H bending
1650	H-O-H bending
3146(broad)	OH stretch in FeOOH
3694	Surface hydroxyl groups

FTIR shows absorption corresponding to Fe-O in Fe_3O_4 . The presence of broad and intense absorption band at $3100\text{-}3200\text{ cm}^{-1}$ is due to FeOOH . Absorptions at 795 and 913 cm^{-1} are due to O-H bending and serve as diagnostic bands for FeOOH [149]. Absorption at 3694 cm^{-1} represents surface hydroxyl groups. These results agree well with results of chemical analysis.

4.4.2 Photocatalytic degradations

4.4.2.1 Degradation of MB on Fe_2O_3 and $\gamma\text{-Fe}_2\text{O}_3$ from iron ore rejects in sunlight

The iron ore rejects contain Fe, Al, Si and traces of metals like K and Mn in the form of oxides, carbonates and hydroxides. Fe_2O_3 prepared from the ore rejects did not degrade MB when placed in sunlight (figure A-11 in appendix). The inefficiency of Fe_2O_3 to degrade the dye may be due to recombination of electron and hole on oxide surface as soon as they are formed as explained in the literature [239]. The $\gamma\text{-Fe}_2\text{O}_3$ also was not able to photodegrade the dye (figure A-11 in appendix). It reveals that pure Fe_2O_3 does not contribute to the degradation of dye due to electron- hole recombination. Hence in the further study a known amount of the ore reject was directly used for photodegradation without converting it to Fe_2O_3 .

4.4.2.2 Degradation of MB on iron ore rejects in sunlight

Since iron ore rejects effectively degraded test solution of MB dye in presence of

sunlight, it could be very well used in the photodegradation of MB. The process of photodegradation was studied by varying several parameters like nature and concentration of the substrate, concentration of ore reject, pH and temperature.

4.4.2.2.1 Effect of pH on degradation of MB on iron ore rejects in sunlight

The pH of a solution not only affects the surface properties of the semiconductor but also the dissociation of dye molecules and the formation of hydroxyl radicals [78] which in turn affects the dye degradation. Thus it is necessary to understand the effect of pH on the degradation of dye by the ore rejects.

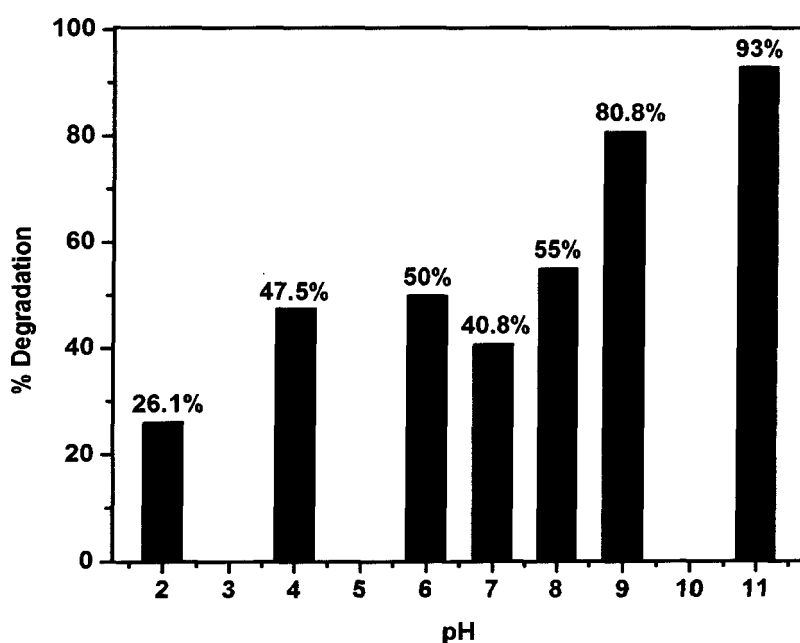


Figure 4.6 Degradation of MB at different pH in sunlight.

The graph in figure 4.6 represents degradation of MB at different pH values in 150 minutes. Experiments conducted at pH ranging from 1 to 11 indicate that in acidic solution, the degradation is slow and it increases as the pH increases to 11. At pH 11 the

degradation is complete within 150 minutes. The main reaction in photodegradation is hydroxyl radical attack on the dye molecule. There is more hydroxyl radical formation at high concentration of the hydroxyl ions. Under basic conditions of pH ~ 11 there are more hydroxyl ions in solution which induces more $\cdot\text{OH}$ radical formation facilitating the degradation.

4.4.2.3.2 Effect of initial concentration of dye on degradation of MB on iron ore rejects in sunlight

During dyeing process in an industry, the concentration of dye varies depending on the need. The concentration of the dye which can be degraded easily with a certain amount of ore reject is therefore important. Figure 4.7 illustrates the degradation of MB dye with different initial dye concentration of 10, 16, 20, 30, 40 ppm for sunlight exposure of 180 minutes for the fixed amount of ore reject (200 mg). The solution was maintained at alkaline pH of 11. It is observed that for 10 and 16 ppm concentration of MB, the degradation is complete within 2-3 hours. Dye concentration of 20-40 ppm takes more time for degradation.

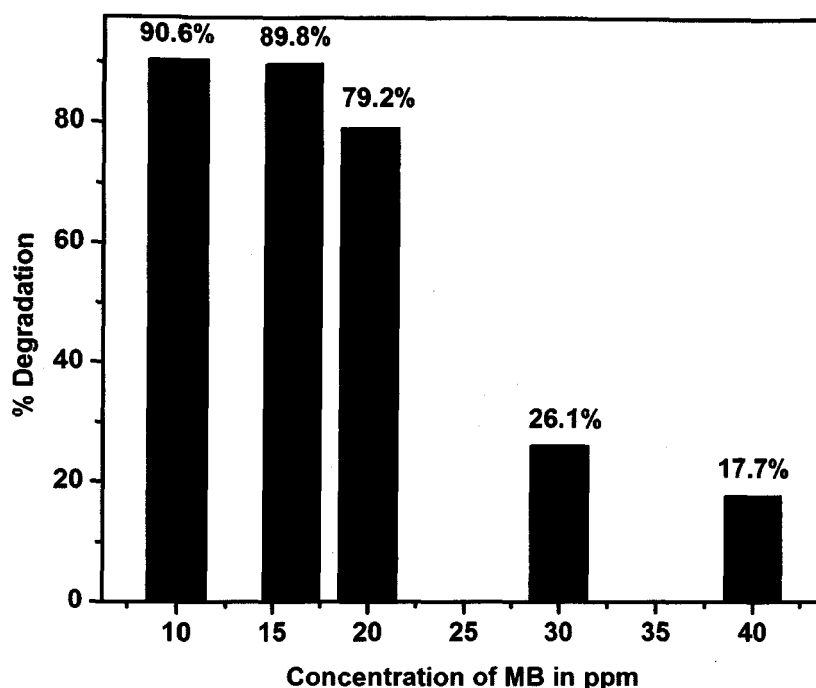


Figure 4.7 Degradation of MB at different dye concentrations in sunlight with fixed amount (200 mg) of iron ore rejects

The rate of degradation decreases with increase in MB concentration. This may be because of fewer active sites available for the reaction. Also with increased dye concentration, sunlight cannot penetrate inside the solution and generation of hydroxyl radicals is hindered [240].

4.4.2.3.3 Effect of concentration of ore rejects on degradation of MB on iron ore rejects in sunlight

Ore rejects concentration from 10 mg to 2g was added to the dye solution (5×10^{-5} M, 16 ppm) in different conical flasks maintained at pH 11.

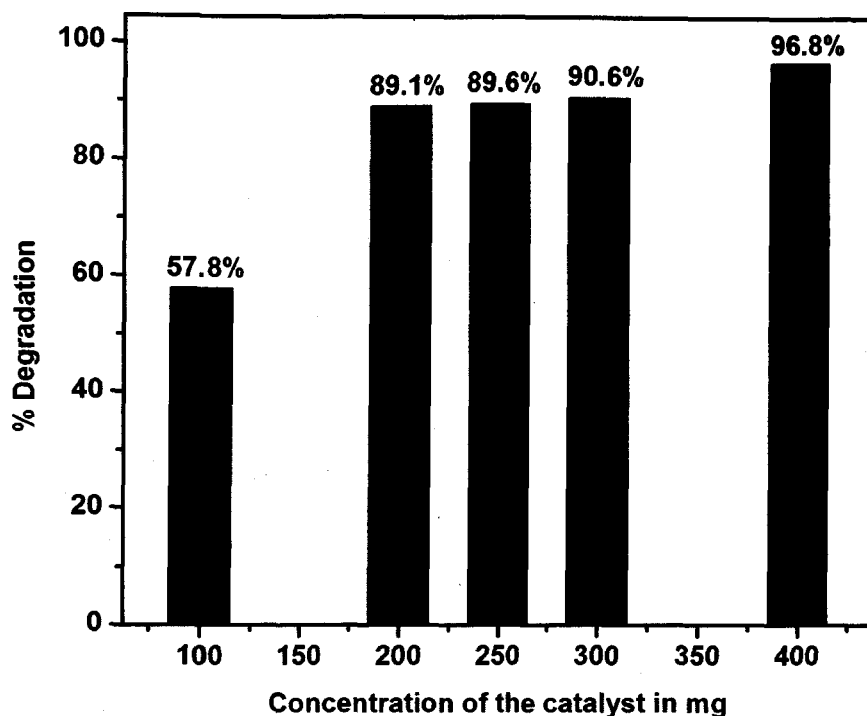
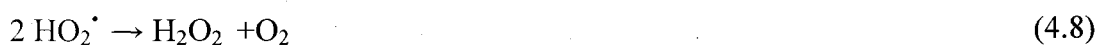
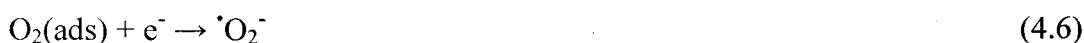


Figure 4.8 Degradation of MB at different concentrations of ore rejects in sunlight at $5 \times 10^{-5} \text{M}$ (16 ppm) of MB and alkaline pH.

Figure 4.8 shows the effect of ore concentration on photo catalytic degradation of MB. It is observed that as the concentration of ore rejects is increased, the degradation of the dye also increases. For concentration of 400 mg of ore rejects, the solution decolorizes after 90 minutes. Further it is observed that for the ore rejects concentration of 2g the solution gets decolorized immediately after mixing without even exposure to sun. Thus the higher concentration of ore rejects helps in faster removal of colour. Literature reports that during degradation of the dye, an increase in the concentration of the oxide increases the rate of degradation due to increase in the concentration of the active sites on the oxide surface. With further increase in the loading of the oxide, the rate of dye degradation is expected to decrease due to screening effect of light by semiconductor oxide itself.

From the above two studies, it is revealed that more the concentration of ore rejects better is the degradation of the dye. Higher the concentration of dye more is the requirement of ore reject.

On addition of more quantity of ore reject (> 2 grams for 150 ml of 0.5×10^{-5} M solution of MB) there is instantaneous colour disappearance. To check whether the colour disappearance is due to degradation or adsorption of MB, the used ore reject was filtered and then stirred with water and some organic solvent. It did not impart bluish colour to the washing indicating degradation and not adsorption. The reason for decolourization of MB on addition of an excess of ore rejects may be explained as due to formation of H_2O_2 by Fe^{+2}/Fe^{+3} .



4.4.2.3.4 Effect of Temperature on degradation of MB on iron ore rejects in sunlight

The degradation of MB in sunlight and presence of ore was studied at various temperatures in the range 8°C to 48°C . With increase in temperature, there is an increase in the degradation of Methylene Blue. The decolourization is over within 20-25 minutes. Rate of a reaction is directly proportional to the temperature of the reaction. The process of dye degradation proceeds through formation of hydroxyl radicals. The hydroxyl radicals are generated by reaction of hydroxide ions with the hole of the

electron-hole pair created in the semiconductor oxide. The hole if allowed to recombine with the electron, there will be delay in the dye degradation.

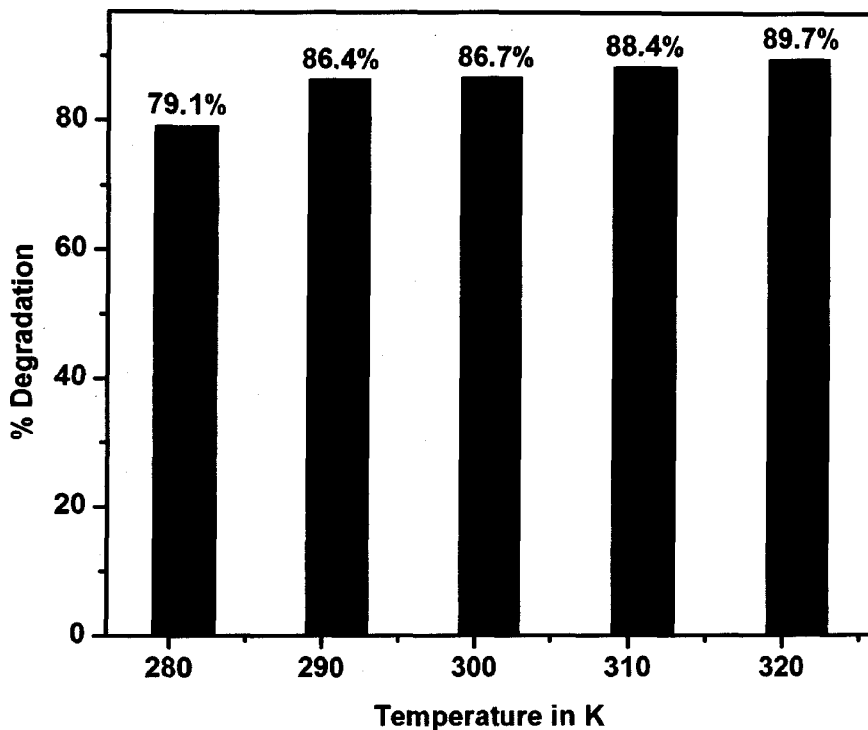


Figure 4.9 Degradation of MB at different temperatures in sunlight and 200 mg of ore rejects, 5×10^{-5} M (16 ppm) of MB and alkaline pH.

The photodegradation of MB can be thought to be similar to photo Fenton mechanism and thus an increased rate of reaction with increase in temperature indicating additional effect of supply of energy in terms of heat helping in formation of hydroxyl radicals. This is in agreement with the literature reports [241].

4.4.2.4 Degradation of MB on iron ore rejects at alkaline and neutral pH in sunlight

a. UV-Visible absorbance

MB degradation in presence of sunlight was carried out in alkaline and neutral pH at room temperature. The absorbance of the solution was recorded after definite intervals of time. Alkaline pH was chosen because maximum degradation was observed at pH 11. A second study was carried out at neutral pH because of minimum degradation occurring when pH is 7 (UV-Visible spectrum not shown). MB absorbs in the UV as well as visible region of the electromagnetic spectrum as seen in figure 4.10. The absorption spectrum of MB in alkaline solution shows two maxima of absorbance at 665 nm and 610 nm which are assigned to the absorption bands of monomeric and dimeric forms of MB. Under strongly alkaline conditions methylene blue is slowly converted to methylene violet by hydrolysis of a dimethyl amino group. Due to this its absorbance shifts to 580 nm [242]. It is observed that the absorbance corresponding to the chromophores at 665 nm and 610 nm at alkaline pH diminishes with time in presence of sunlight (Figure 4.10). There is no formation of methylene violet and ~90% de-colorization occurred in 150 minutes. At neutral pH the degradation is only 45% in 150 minutes.

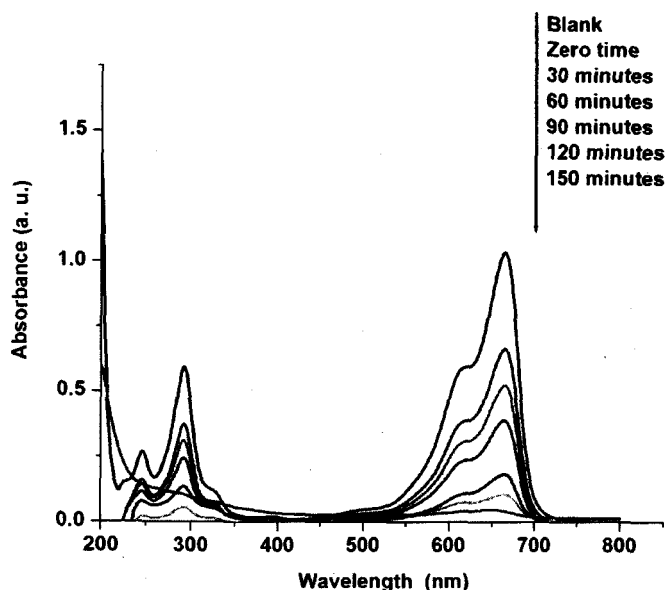
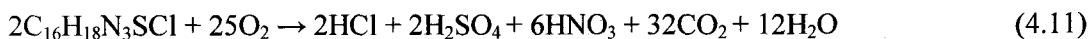


Figure 4.10 Degradation of MB in sunlight at alkaline pH using iron ore rejects.

b. Mineralization products of MB

Decolourization of MB was observed on exposure to sunlight in presence of ore rejects. It is also important to understand whether there is only decolourization of MB or decolourization followed by mineralization to CO_2 , water and acid ions. The colourless solution obtained after the degradation was analyzed for COD to see the extent of degradation of MB. This test is widely used as an effective technique to measure the organic strength of wastewater. The test allows the measurement of waste in terms of the total quantity of oxygen required for the oxidation of organic material to CO_2 and water. The COD of the dye solution before and after the treatment shows a decrease in COD. The reduction in COD values indicates the mineralization of the dye molecules along with the colour removal. Thus MB degrades according to the reaction [112]:



And hence there should be mineralization products like CO_2 , nitrate and sulphate

formed. The analysis of these products confirms the mineralization of the dye. It is observed that in alkaline as well as neutral pH, there occurs decolourization as well as degradation. There is partial mineralization in case of MB degradation at neutral pH as indicated by COD, nitrate, sulphate and CO₂ analysis. Hence the degradation at neutral pH was not studied further. However thermal degradation of MB at neutral pH is reported in the later section.

Table 4.5 Products of mineralization of MB at alkaline and neutral pH.

	%COD removal (after 30 minutes)	% COD removal (after 150 minutes)	Free CO ₂ mg/l	Nitrate after 150 minutes mg/l	Sulphate after 30 minutes mg/l	Sulphate after 150 minutes mg/l
Iron ore rejects at Neutral pH	38.1%	66.7%	3.56	0.77	0.139	0.394
Iron ore rejects at Alkaline pH	47.6%	85.7%	49.89	0.77	2.55	3.101
Sunlight (Blank)	- (added)	-85(added)	-----	2.6	0.75	32.5

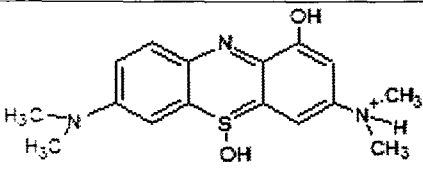
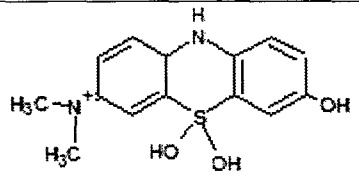
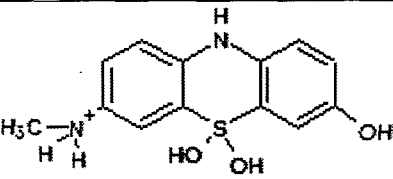
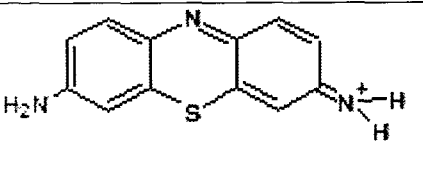
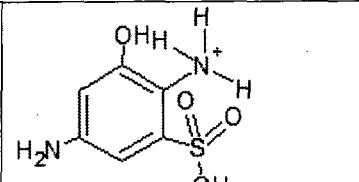
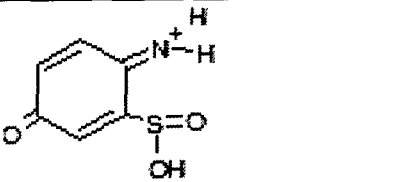
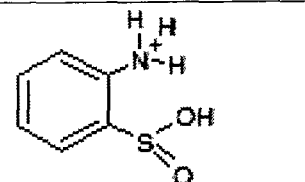
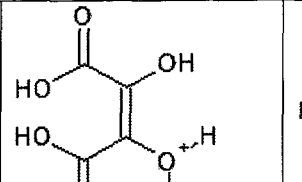
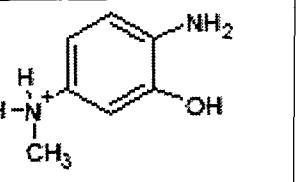
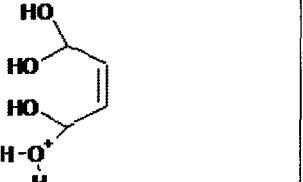
In case of solar degradation of MB at alkaline pH, 86% COD removal is observed after complete decolourization of MB. Nitrate is not detected in the early stages of solar degradation which may be because of formation of ammonium ions first and their subsequent oxidation to nitrates. The results are in agreement with those reported [111]. Quantity of sulphate ions released by iron ore rejects is lower as compared to sulphate produced during photolysis which may be due to loss of sulphur containing volatile compounds like H₂S/SO₂ in photocatalysis [111]. The pH of the solution remained alkaline throughout the degradation and on completion of degradation, the pH comes to neutral range. This may be due to formation of acids during degradation which neutralize the alkaline solution. The conductivity of the solution also shows a gradual increase and later decrease towards complete decolourization indicating the formation of ions and then escape of ions as gases. The conductivity becomes negligible on

complete decolourization.

c. ESI-MS studies

Since decolourization does not give clear idea about the extent of degradation, ESI-MS studies were carried out for the degraded solutions to know if there are any organic moieties still remaining in the solution. Following are the fragments obtained on analyzing the decolourized solution of MB after 150 minutes.

Table 4.6 Products of solar degradation of MB on iron ore rejects analyzed by ESI-MS.

Iron Ore catalysed degradation of MB in sunlight			
 <p>$C_{16}H_{20}N_3O_2S$ (M^+)=318.0305</p>	 <p>$C_{14}H_{17}N_2O_3S$ (M^+)=293.0952</p>	 <p>$C_{13}H_{15}N_2O_3S$ (M^+)=279.0897</p>	
 <p>$C_{12}H_{10}N_3S$ (M^+)=228.1013</p>	 <p>$C_6H_9N_2O_4S$ (M^+)=205.0275</p>	 <p>$C_6H_6NO_3S$ (M^+)=172.0599</p>	
 <p>$C_6H_8NO_2S$ (M^+)=158.0504</p>	 <p>$C_4H_5O_6$ (M^+)=148.9778</p>	 <p>$C_7H_{11}N_2O$ (M^+)=139.0138</p>	 <p>$C_4H_6O_4$ (M^+)=121.0012</p>

The results indicate that the degradation occurs via the hydroxyl radical mechanism. The oxidative photo degradation of MB involves several intermediates and identification of all of them becomes difficult due to very low concentration and many of them cannot be detected because of their poor extractability in the organic medium. All the products formed during solar degradation of MB are listed in table 4.6. The spectra are compiled in appendix, figure 12. The peak at $m/z = 228$ ($C_{12}H_{10}N_3S$) correspond to loss of methyl groups from aromatic rings on both sides of MB respectively. The peaks at $m/z = 318$ ($C_{16}H_{20}N_3O_2S$), 293 ($C_{14}H_{17}N_2O_3S$) and 279 ($C_{13}H_{15}N_2O_3S$) seem to be due to successive addition of hydroxyl to the MB molecule. The OH radicals are supplied by the continuous generation of Fe^{+2} which give rise to hydroxyl radicals by the reaction given below:



The breaking of MB molecule is suggested by the presence of peaks at $m/z = 205$ ($C_6H_9N_2O_4S$), 172 ($C_6H_6NO_3S$), 158 ($C_6H_8NO_2S$), 149 ($C_4H_5O_6$), 139 ($C_7H_{11}N_2O$) and 121 ($C_4H_6O_4$). Thus though COD indicates liberation of organic moiety as gases, some fragments are found to be present after degradation.

d. Kinetics of photo degradation of MB:-

The photocatalytic degradation obeys apparently pseudo first order kinetics at low initial MB concentration and the rate expression is given by

$$\ln \frac{A_0}{A} = \ln \frac{C_0}{C} = Kt \quad (4.12)$$

Plots of $\log C_0/C$ against time for photocatalytic degradation upon linear regression equals the apparent first order rate constant K and the value of rate constant K is equal to $0.00862 \text{ minute}^{-1}$.

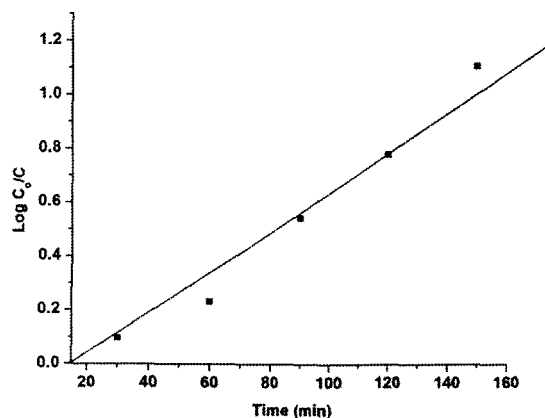


Figure 4.11 Plot of $\ln C_0/C$ against time during solar degradation of MB by iron ore rejects.

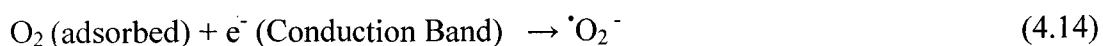
The linear behaviour of $\ln C_0/C$ as a function of time suggests a first order kinetic reaction with respect to MB concentration.

d. Photocatalytic degradation Mechanism

The iron ore reject has semiconducting properties [243]. The semiconductor materials when irradiated generate electron-hole pairs.



Oxygen molecules (O_2) adsorbed on the surface of the semiconductor oxide form superoxide radical anion.



The surface hydroxyl groups of the semiconductor oxide get converted to hydroxyl radicals.



Using ESR spectroscopy data it is reported that the formation of active $\cdot OH$ and $\cdot O_2$ species takes place during photodegradation of organic compounds [219]. It is also

reported that the superoxide radical anion is unstable in aqueous media and is readily converted to $\cdot\text{OH}$ radicals via formation of H_2O_2 [220]. The photo degradation reaction of organic compound, R proceeds through the reaction with hydroxyl radicals. The hydroxyl radicals can oxidize simple organic pollutants directly, while refractory ones can only be degraded through complex pathway [244].



In the present study, iron ore reject in excess added directly to a solution of MB is found to decolorize MB. FeO content of iron ore reject increases from 1.01 % to 1.44%, Table 4.1, after its use for degradation. The increase in Fe^{+2} content after mineralization of MB by ore rejects in sunlight suggest that the electrons formed on the semiconducting ore reject reduce Fe^{+3} to Fe^{+2} .



There by Fe^{+2} content increases. The holes created due to irradiation are involved in the hydroxyl radical formation.



The hydroxyl radicals are powerful oxidants which degrade the dye molecules at a faster rate. Reactions (4.17) and (4.18) inhibit the electron hole recombination and hence enhance the photo-degradation of MB.

Thus it can be concluded that MB degradation by iron ore at alkaline pH proceeds through formation of hydroxide radicals from Fe^{+2} , the mechanism of which is similar to photo Fenton reaction. Fe^{+3} get reduced to Fe^{+2} by taking up the electron of the electron-hole pair. The $\cdot\text{OH}$ radical formed reacts with the organic compound to form radical of organic compound. Some $\cdot\text{OH}$ radicals combine to form H_2O_2 . Fe^{+2} produced reacts with H_2O_2 to form Fe^{+3} and $\cdot\text{OH}$ radicals back. There by the chain continues [217].



So there is continuous generation of Fe^{+2} which give rise to hydroxyl radicals and degradation of the organic compound takes place. The increase in Fe^{+2} has been confirmed by chemical analysis, increase in Fe_3O_4 content after the first use of reject for degradation (table 4.1).

4.4.2.5 Effect of dyeing chemicals on MB degradation by iron ore rejects

4.4.2.5.1 Presence of NaCl along with MB dye

Sodium chloride usually comes out in the effluent along with sectional waste in textile mills.

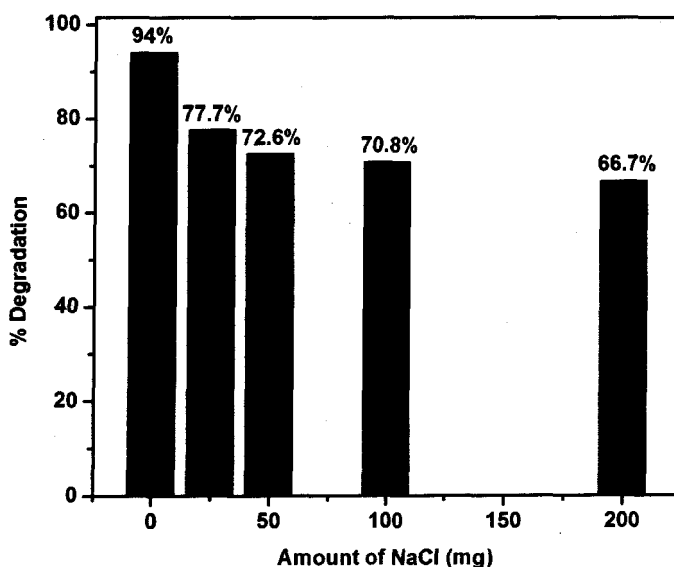


Figure 4.12 Degradation of MB at different concentrations of NaCl.

Figure 4.12 reflects effect of NaCl on the photocatalytic activity of iron ore rejects (200mg), MB concentration of 16 ppm at alkaline pH. It is observed that as the concentration of NaCl increases, the efficiency of photodegradation decreases. The decrease in the degradation of the dye in the presence of chloride ions is due to hole

scavenging properties of chloride ions.



They are instantaneously converted into chloride radical anions which block the surface sites normally available at the semiconductor oxide /dye interface. Thus there is decrease in degradation of dye with increase in NaCl concentration. Figure 4.13 shows UV-Visible spectrum of MB during degradation on iron ore rejects in presence of 200 mg of NaCl.

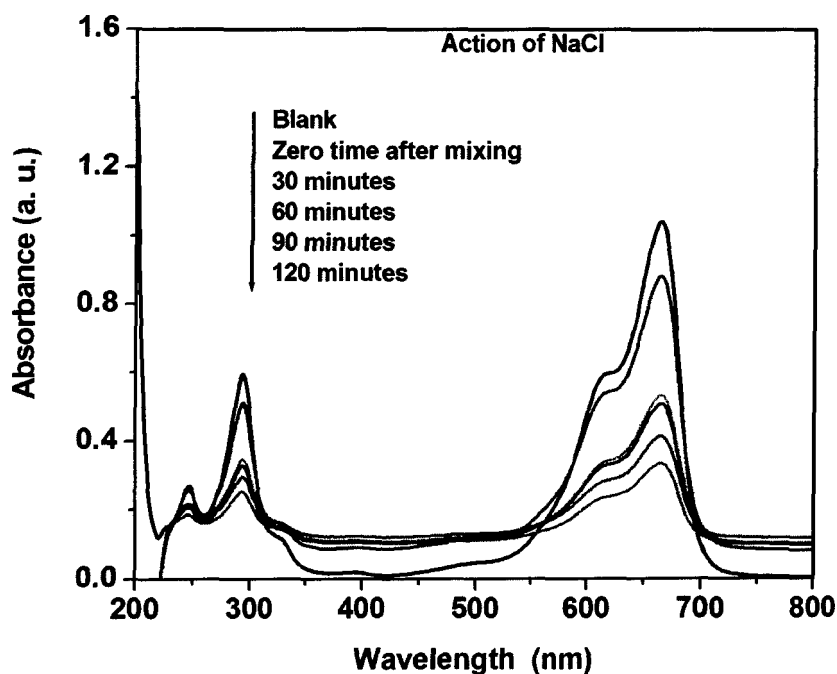


Figure 4.13 Degradation of MB (16 ppm) by iron ore rejects (200 mg) in presence of 200 mg of NaCl.

It is observed that during degradation of MB, the peak in the UV- Visible spectrum of MB at 200 nm due to H_2O_2 is absent. This may be attributed to the hole scavenging property of chloride ions which does not let formation of $\cdot\text{OH}$ radicals and hence the formation of H_2O_2 . The decrease in the rate of photodegradation in presence of NaCl is

because of deficiency of H_2O_2 and $\cdot\text{OH}$. This supports the fact that the degradation proceeds through formation of electrons and holes followed by formation of H_2O_2 .

4.4.2.5.2 Presence of Na_2CO_3 along with MB dye

Sodium carbonate is one of the common auxiliary chemical employed in textile processing operations. Sodium carbonate is mainly used in the dyeing bath in order to adjust the pH of the bath. It plays an important role in fixing of the dye on the fabric and in the fastness of the colour.

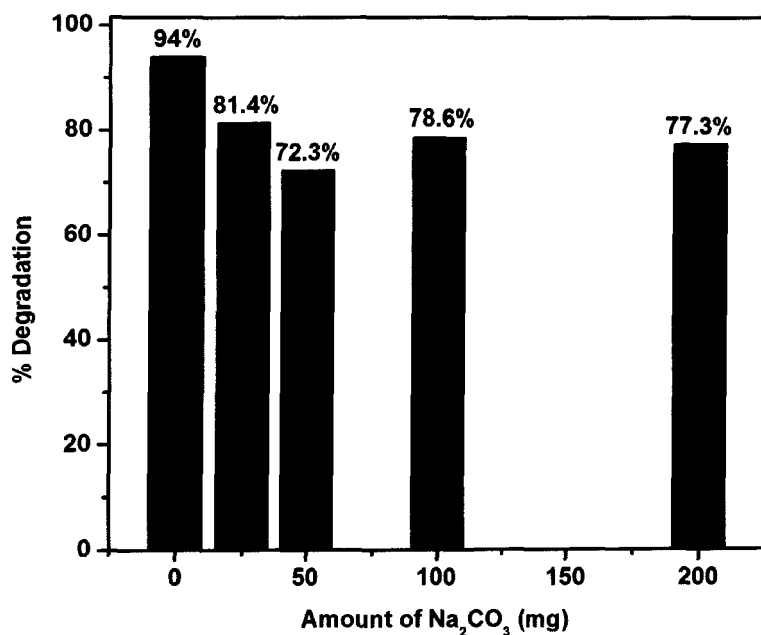


Figure 4.14 Degradation of MB (16 ppm) by iron ore rejects (200mg) at different concentrations of Na_2CO_3 .

Figure 4.14 reflects effect of Na_2CO_3 on the ore catalysis using iron ore rejects (200mg), MB concentration of 16 ppm at alkaline pH. The degradation decreases on the increased addition of Na_2CO_3 upto 50 mg and further increases for 100 and 200 mg of Na_2CO_3 . Figure 4.15 shows UV-Visible absorption spectrum of MB during degradation

on iron ore rejects in presence of 200 mg of Na_2CO_3 .

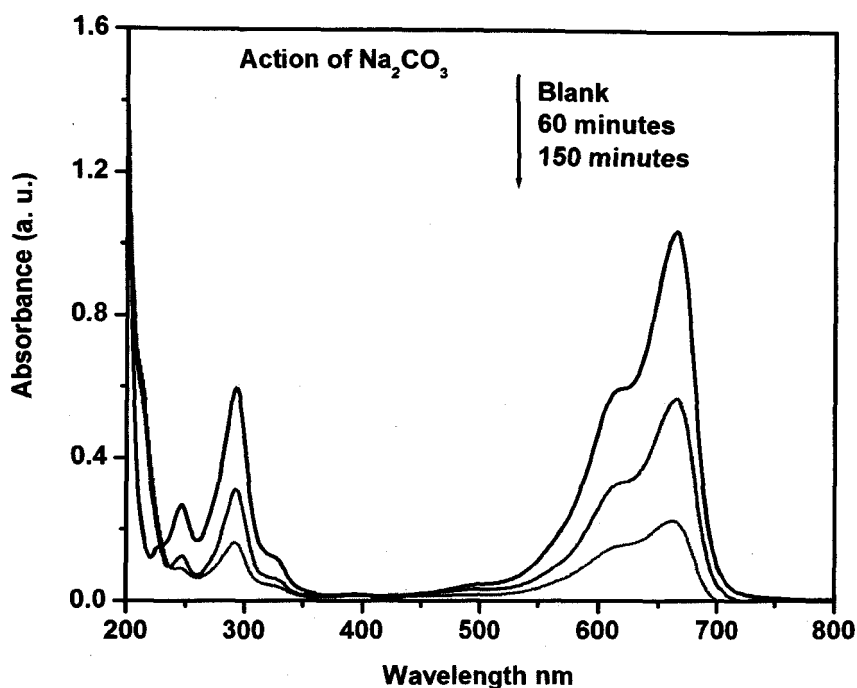


Figure 4.15 Degradation of MB (16 ppm) by iron ore rejects (200 mg) in presence of 200 mg of Na_2CO_3 .

The decrease in the degradation of the dye in presence of carbonate ions may be due to hydroxyl ion scavenging property of carbonate ions thus suggesting hydroxyl radical mechanism of dye degradation.



These radical ions i.e. $\text{CO}_3^{\cdot-}$ may also block the active sites on the oxide surface thus deactivating the oxide towards MB. These generated radical anions are oxidants itself, but the oxidation potential is less than that of the hydroxyl radical. Thus the increase in the rate of degradation in presence of more carbonate ions is because of carbonate

radical anions attacking the dye molecules.

4.4.2.6 Effect of additives on MB degradation by iron ore rejects

4.4.2.6.1 Effect of addition of $K_2S_2O_8$ to MB dye

$K_2S_2O_8$ is known to enhance degradation of dyes [227] so this study is carried out to check its effect on dye degradation in presence of iron ore reject sample.

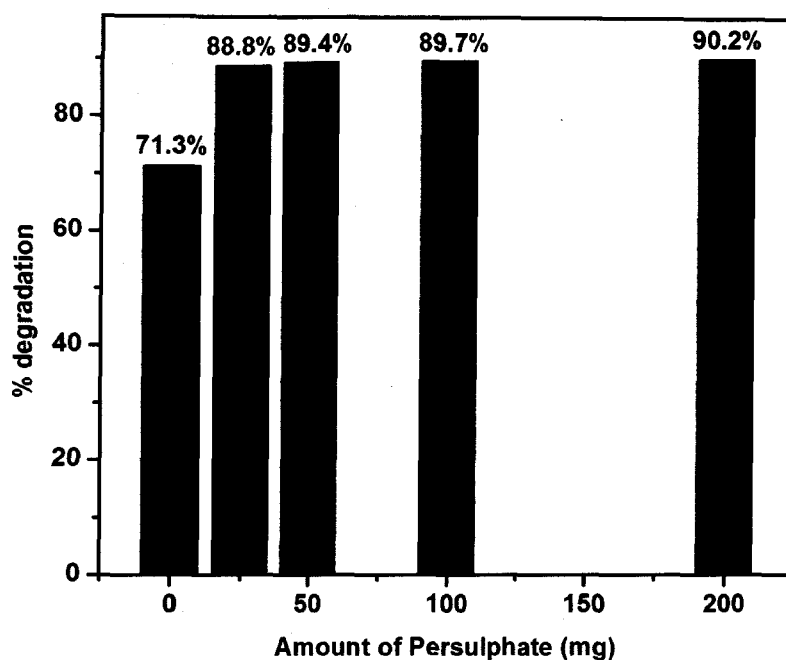


Figure 4.16 Degradation of MB (16 ppm) by iron ore rejects (200 mg) at different concentrations of $K_2S_2O_8$

Figure 4.16 reflects effect of $K_2S_2O_8$ on the ore catalysis. The degradation of the dye increases with increasing amount of persulphate ion concentration. There is marginal increase in degradation of MB when $K_2S_2O_8$ added is increased from 25mg to 200mg. Thus 25 mg can be taken as optimum quantity required enhancing degradation. The solution with highest concentration of $K_2S_2O_8$ with 200mg degrades to 90% within 60 minutes of exposure to sun. Figure 4.17 shows UV-Visible absorption spectrum of MB during degradation of MB on iron ore rejects in presence of 200mg of $K_2S_2O_8$.

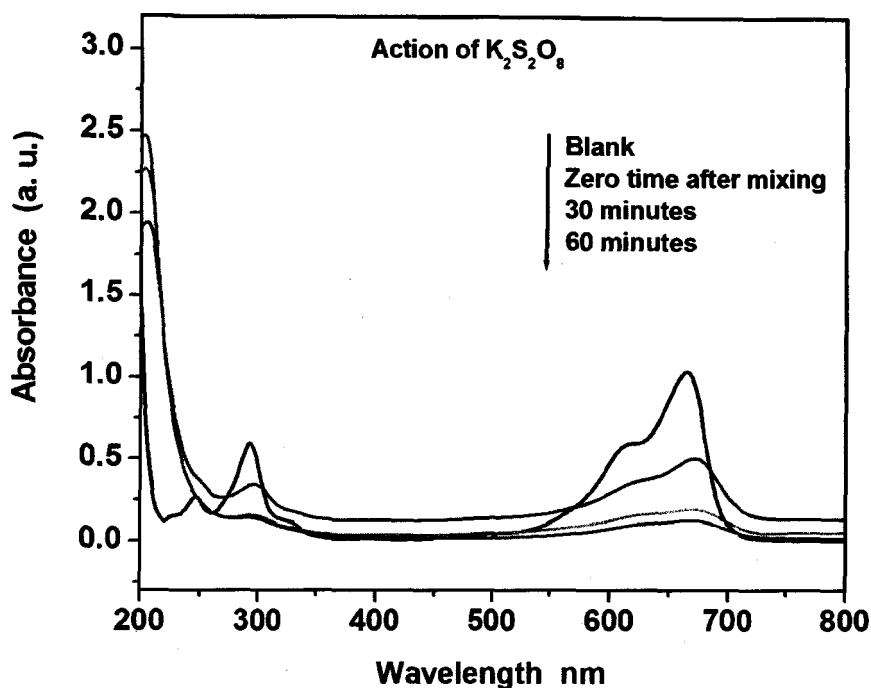
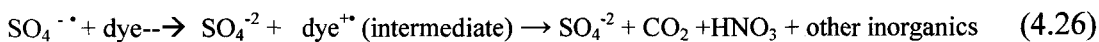


Figure 4.17 Degradation of MB (16 ppm) by iron ore rejects (200 mg) in presence of 200 mg of $K_2S_2O_8$

$K_2S_2O_8$ forms sulphate by reactions with semiconductor generated electrons.



The sulphate anion radical is a strong oxidant ($E^0 = 2.6V$). It has the unique nature of attacking dye molecules at various positions and hence fragmentation of the dye molecules is rapid.



4.4.2.6.2 Effect of addition of H_2O_2 to MB dye

H_2O_2 is another chemical compound known to enhance degradation of dyes [227] so this study is carried out to check its effect on dye degradation in presence of ore reject

sample.

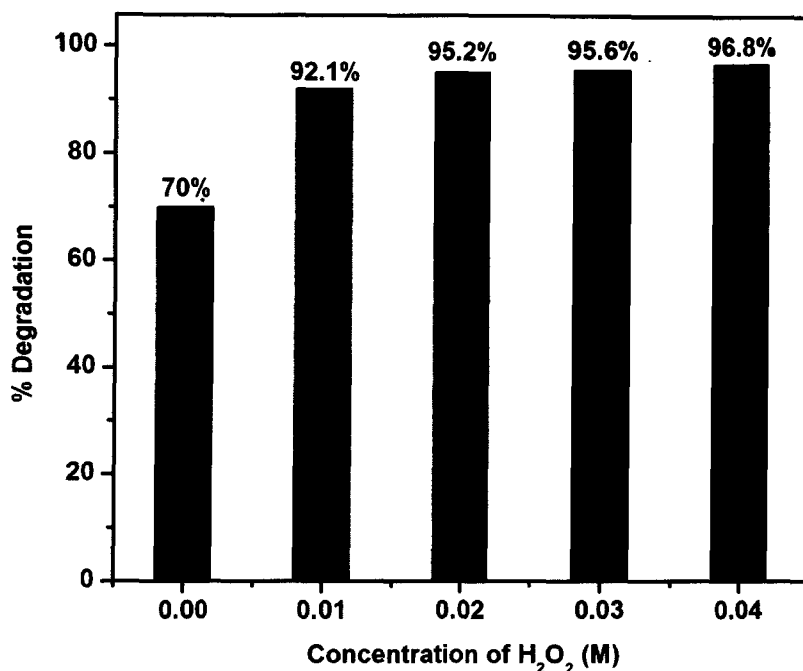


Figure 4.18 Degradation of MB (16 ppm) by iron ore rejects (200 mg) at different concentrations of H₂O₂

Figure 4.18 shows the influence of H₂O₂ dosage on the degradation efficiency of the dye. The increase of H₂O₂ concentration results in a faster degradation of the dye. At 0.01M concentration, it degrades 92 % MB. The dye solution with highest concentration of H₂O₂ with 0.04M degrades MB solution to ~ 97% within 60 minutes of exposure to sun. The photolysis of H₂O₂ generates hydroxyl radicals [227] and H₂O₂ is suitable for trapping electrons [231] thus preventing their recombination. Thus presence of H₂O₂ fastens the degradation process. Figure 4.19 shows UV-Visible absorption spectrum of MB during degradation on iron ore rejects at H₂O₂ concentration of 0.04 M.

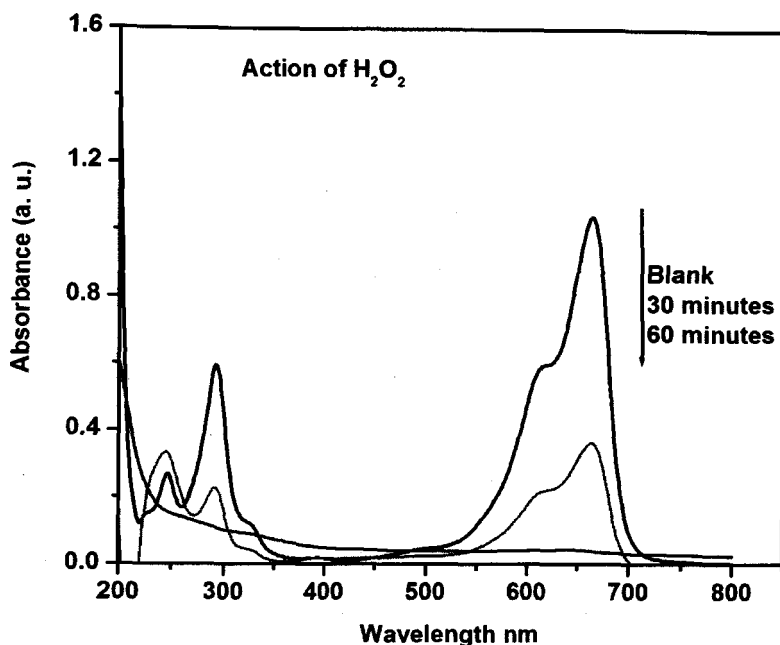


Figure 4.19 Degradation of MB (16 ppm) by iron ore rejects (200 mg) in presence of 0.04M H₂O₂

An excess of H₂O₂ decreases the reaction rate due to quenching of $\cdot\text{OH}$ radicals and formation of perhydroxide radical which is less reactive.

4.4.2.7 Reuse of ore rejects for MB degradation

Iron ore rejects can be effectively reused for degradation of MB after proper washing and drying. It is observed that during the first run of its use degradation of MB is complete in 150 minutes, second run of degradation, the decolourization is over by 120 minutes and in the third run decolourization is complete by 90 minutes. The decolourization is followed by mineralization of MB and the mineralization ability of the iron ore rejects is slightly altered. Hence iron ore rejects show excellent reusability.

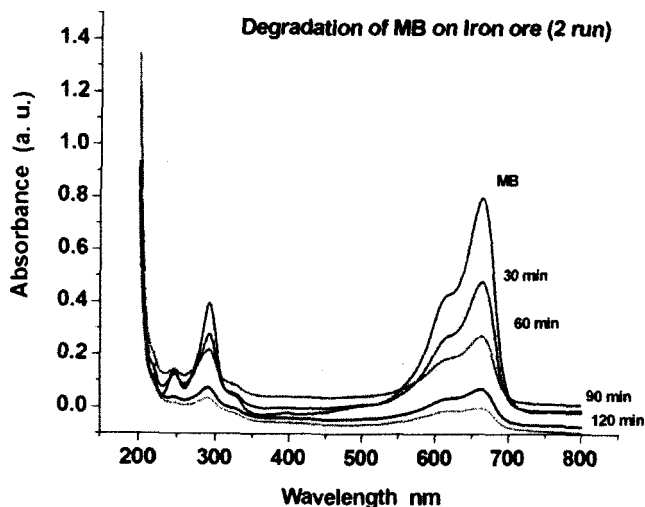


Figure 4.20 Degradation of MB (16 ppm) on iron ore rejects (200 mg) in second run

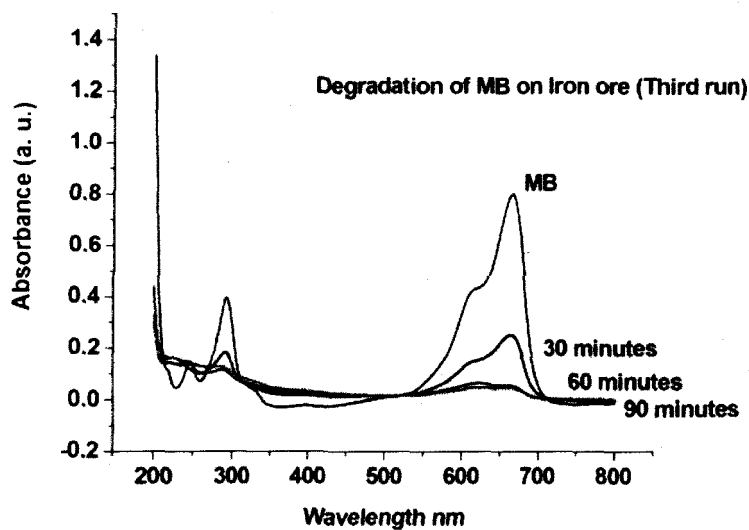


Figure 4.21 Degradation of MB(16 ppm) on iron ore rejects (200 mg) in third run

Table 4.7 COD removal and mineralization products of degradation of MB on reuse.

Iron ore rejects	% COD Removal	Nitrate mg/L	Sulphate mg/L
1 run	85.7	0.77	3.101
2 run	90	3.0	1.92
3 run	73.8	5.99	4.6

The increased efficiency of iron ore rejects during its reuse may be due to photo Fenton type mechanism operating in the degradation process. There is formation of Fe^{+2} from

Fe^{+3} as shown in equation (4.17). This generation of Fe^{+2} gives rise to more hydroxyl radicals. Formation of more hydroxyl radicals increases the photocatalytic activity of the rejects. The formation of Fe^{+2} is supported by increased Fe_3O_4 content by chemical analysis after reuse, table 4.2. Thus as Fe_3O_4 content (Fe^{+2}) increases there is increase in photodegradation.

It is observed that the degree of crystallinity of ore rejects is reduced considerably after one use as specified by the XRD patterns (figure 4.22). The agglomeration of the ore reject is also supported by SEM (figure 4.23).

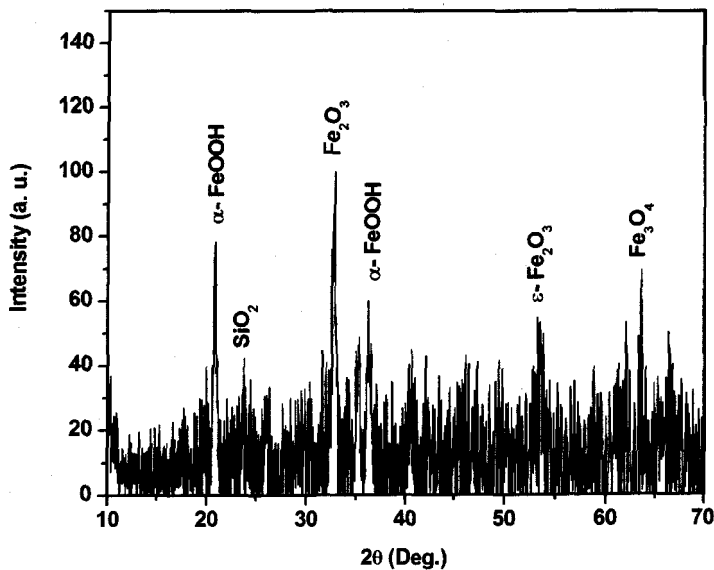


Figure 4.22 XRD of iron ore rejects after use for degradation of MB.

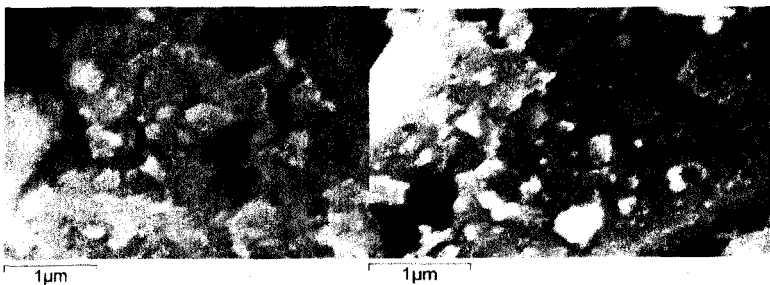


Figure 4.23 SEM images of iron ore rejects after use for photodegradation of MB (x33000).

Diffuse Reflectance Spectra recorded after use (figure 4.4) show blue shift of absorption maximum of the ore rejects. There is even increase in absorbance of ore rejects after use. The bandgaps calculated from derivative plots show a slight decrease. This decrease in the band gap along with increased concentration of Fe^{+2} may be enhancing the degradation capacity of ore reject on reuse.

Table 4.8 Calculated bandgaps of iron ore rejects

Iron ore rejects	Band-gap (eV)
Fresh	2.19
After 1 use in degradation of MB	1.95
After 2 use in degradation of MB	1.75

4.4.2.8 Thermal degradation of methylene blue by iron ore rejects

It was observed earlier that temperature has an additional effect of enhancing the degradation during solar degradation of MB. Hence it is important to understand the effect of temperature on degradation of MB. The thermal degradation study of MB in the presence and absence of iron ore rejects was undertaken at different temperatures viz. 40, 60, 80 and 100°C. At 100°C the decolorization of 74% of MB is achieved. Iron ore rejects loading in MB followed by thermal treatment shows 82 % degradation at 60°C. This suggests a gainful effect of temperature in the degradation of MB with iron ore.

Thermal degradation of MB in absence of sunlight and at neutral pH may be due to formation of H_2O_2 by $\text{Fe}^{+2}/\text{Fe}^{+3}$. When energy is supplied to the MB degradation process in the form of heat, there is an increase in the rate of reactions (4.6) to (4.10).

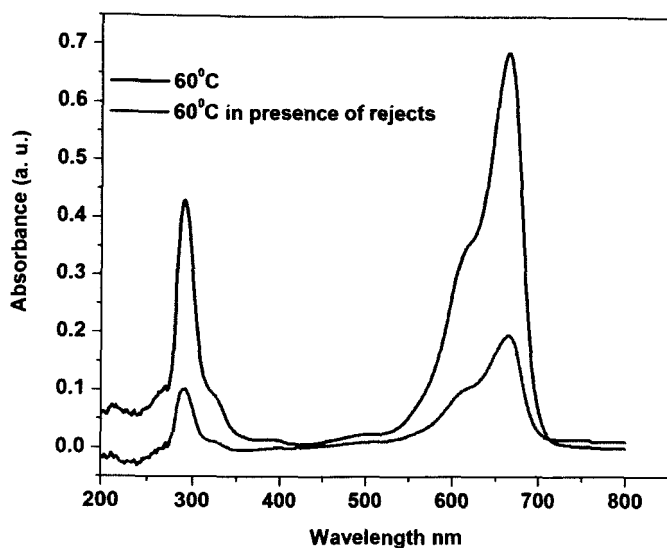
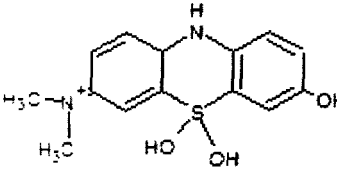
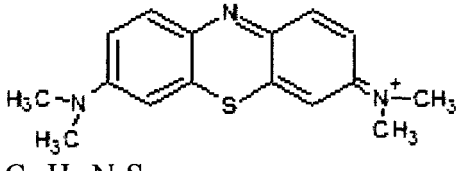
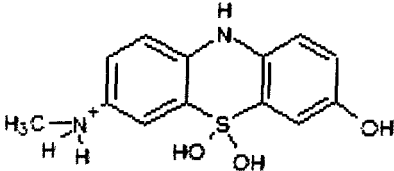
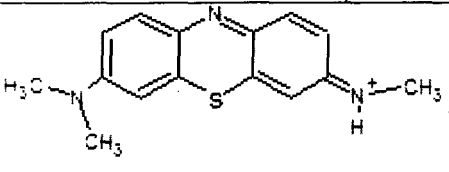
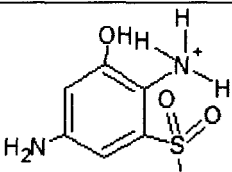
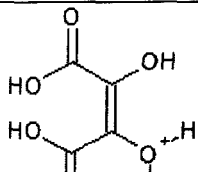


Figure 4.24 Thermal degradation of MB by iron ore rejects at 60°C.

Thermal degradation of MB also shows formation of colourless degradation products all of which cannot be identified and studied due to low concentration and poor extractability in organic medium. Some of the generated products are similar to the ones seen during solar degradation of MB. All the products formed during these degradations are listed in Table 4.9. The spectra are compiled in figure A-12 in appendix.

Table 4.9 Products of thermal degradation of MB by iron ore rejects analyzed by ESI-MS.

Iron Ore Catalysed (Thermal)		
 <p>$C_{14}H_{17}N_2O_3S$ (M^+)=293.0506</p>	 <p>$C_{16}H_{18}N_3S$ (M^+)=283.9956</p>	 <p>$C_{13}H_{15}N_2O_3S$ (M^+)=279.0404</p>
 <p>$C_{15}H_{16}N_3S$ (M^+)=269.9910</p>	 <p>$C_6H_9N_2O_4S$ (M^+)=204.9981</p>	 <p>$C_4H_5O_6$ (M^+)=148.9575</p>

The presence of a peak at $m/z = 284$ ($C_{16}H_{18}N_3S$) in case of thermal degradation corresponds to methylene blue molecular ion indicating that there is no complete decolourization of MB during thermal treatment. The peak at $m/z = 270$ ($C_{15}H_{16}N_3S$) is due to Azure B, the product formed with loss of a methyl group attached to the aromatic rings of MB. The peaks at $m/z = 293$ ($C_{14}H_{17}N_2O_3S$) and 279 ($C_{13}H_{15}N_2O_3S$) are due to formation of hydroxylated product. The breaking of MB molecule forming the products is revealed by the presence of peaks at $m/z = 205$ ($C_6H_9N_2O_4S$) and 149 ($C_4H_5O_6$).

The study shows that iron ore rejects rather than dumping in pits as a waste material and creating pollution can be used as dye degrade of industrial effluent. It has reusability. Presence of sunlight, higher temperature and alkaline medium helps in faster degradation. Although other chemicals present in effluent of dye industry lower the degradation, additives like H_2O_2 can be added to increase efficacy of the process.

Chapter 5

Summary, Conclusions and Future Scope

Summary and Conclusions

The pollution menace has crossed all its limits in the 21st century. The very basic cause of environmental degradation is growing population. Because of the rise in population at alarming rate there is high demand of food, goods and energy. This has necessitated need of industrialisation. Industrialisation has led to the problem of pollution of air, water and soil. The waste materials are thrown in the surroundings without processing. Thus it is high time to think of 'waste management', a comprehensive, integrated and rational approach towards maintenance of environmental quality. The processes are to be developed that convert the wastes to form environmental friendly products before passing them to surroundings. The need of the hour is that researchers should design methods of treating sewage and industrial effluents and find measures to abate them. The methods used should involve minimum utilization of energy.

Energy is the key ingredient for the economic growth of the country. Power generation and availability of energy decide growth of industry and agriculture. Energy is also required for domestic purpose and so there is geometric increase in its need. Fossil fuels at present are the main sources of energy and cannot meet the growing demands. The energy crisis has necessitated setting up of nuclear power plants. Enormous amount of energy is released from a small amount of Fuel. Breeding of fuel is also done and it is supposed to be clean source of energy if utmost care is taken at every stage. Nuclear fission creates radioactive waste which has to be managed in proper way. It should not create problem for present as well as the future generations. Thus the need is to confine the radioactive waste in certain materials that would not leach them to the surroundings after geological disposal.

In the present research work, we have tried to seek some routes to tackle a few

environmental pollutants. Metal oxides are used in the abatement of environmental pollutants. The preparation of the oxides being a chemical process puts burden on the energy resources. Hence, we have opted for green processes consuming less energy in their synthesis. The oxalate and hydrazinated oxalate precursor methods of oxide formation yield materials with better morphology and better properties at much lower temperatures. Hydrazine also acts as scavenger of obnoxious gases given out during synthesis of oxides. Citrate gel route is another method of preparation of metal oxides which gives product oxides at much lower temperatures. The citrate gel route amongst the various types of preparation methods, gives better morphology of sintered samples. The compactly packed material can serve as a good material for nuclear waste disposal restricting the release of radionuclides by the process of leaching.

Chapter 2 contains study of pyrochlore materials for nuclear waste management. Studies done on various host lattices to retain nuclear wastes suggest use of the materials which are more resistant to amorphisation. At present borosilicate glass is used as host matrix for radioactive wastes which are then packed in stainless steel canisters buried in deep underground trenches. It can retain the material without leaching for about 100 years. Pyrochlore oxides are suggested as leading candidates that can hold the radioactive materials for millions of years and so synthesis of pyrochlore oxides is attempted successfully by oxalate, hydrazinated oxalate, citrate gel and ceramic route in the present studies. Pyrochlore oxide, $\text{Nd}_2\text{Zr}_2\text{O}_7$ prepared by citrate gel method has a uniform morphology. When $\text{Nd}_2\text{Zr}_2\text{O}_7$ is doped with Strontium (a common byproduct of nuclear fission), it tends to hold Sr in its lattice strongly on sintering at 1400°C . Thus the ceramic material $\text{Nd}_2\text{Zr}_2\text{O}_7$ prepared by citrate gel method and sintered show better retention of strontium in its lattice and can be thought as a

potential material for nuclear waste disposal.

Besides, a series of pyrochlore oxides $\text{Nd}_2\text{Zr}_x\text{Ti}_{2-x}\text{O}_7$ was synthesised by citrate gel method. In this series replacement of Zr by Ti is expected to bring a disorder in the lattice. The ionic conductivity study shows higher values of conductivity for $\text{Nd}_2\text{Zr}_{1.8}\text{Ti}_{0.2}\text{O}_7$. This is due to disorder in the lattice and presence of Ti^{+3} which creates vacancies at oxide sites favouring diffusion of ions thereby increasing conductivity. Since a disordered lattice can withstand the amorphisation more readily than the ordered one, this material can be of use in the nuclear waste disposal. It can also be used in applications like fuel cells.

Chapter 3 deals with the synthesis of ZnO photocatalysts, active in the visible region of the electromagnetic radiation so that when they are used in the degradation of pollutants, no additional source of energy is required during degradation. Solar energy that is bountiful and available naturally can be used for the process. The hydrazinated oxalate method of synthesis is used in the synthesis of ZnO. It incorporates nitrogen in the lattice of ZnO facilitating its absorption in the visible region of the electromagnetic spectrum. The formation of fine sized particles and large surface area also facilitates the absorption process. This N-doped ZnO obtained from the hydrazinated precursor shows more efficient degradation of methylene blue, a model dye as compared to undoped ZnO. Formation of SO_4^{2-} , NO_3^- and CO_2 from the degraded MB solution indicates the mineralization of the dye. ESI-MS results indicate presence of small amount of some organic moieties even on complete decolourization. No loss in the efficiency of ZnO and $\text{ZnO}_{1-x}\text{N}_x$ after use in degradation makes them suitable for reuse. The Zinc oxide and $\text{ZnO}_{1-x}\text{N}_x$ prepared are also effective in degrading industrial effluents. $\text{ZnO}_{1-x}\text{N}_x$ obtained from the hydrazinated precursor also shows an increased antibacterial property

against bacteria *E. coli*. The prepared ZnO and N doped ZnO photocatalysts are active in degradation of NO_x. Thus ZnO synthesized from hydrazinated oxalate can be used in degradation of dye effluents, NO_x. Its antibacterial property can also be harnessed.

On doping ZnO with small amount of aluminium, the photodegradation ability increases. The NO_x degradation ability remains the same, however the antibacterial activity is lost on doping with aluminium.

Spray pyrolysis of zinc nitrate in presence of hydrazine hydrate is also attempted. The method gives N doped ZnO with uniform particle size distribution. The set up requires more sophistication. The N doped ZnO obtained by the method is very effective inhibitor of bacteria *E. coli*.

In chapter 4, study of one more pollutant in the local scenario is reported. The iron ore rejects stored in the pits create pollution in agricultural areas. The oxides present in ore are used as technologically important material in dye degradation which gives value addition to these rejects. The iron ore rejects usually thrown away during mining are used directly to oxidize organic dyes. Addition of iron ore shows immediate fading of the colour of methylene blue. It also effectively degrades MB in sunlight and even thermally. MB degradation by iron ore rejects at alkaline pH in sunlight is similar to photo Fenton reaction. Formation of SO₄²⁻, NO₃⁻ and CO₂ from the degraded MB solution indicates the mineralization of the dye. ESI-MS results indicate presence of some organic moieties even on complete decolourization. No loss in the efficiency of iron ore reject is observed after three runs, rather the efficiency increases due to formation of Fe⁺². Thus iron ore tailings may be recommended to be used as a bed to treat dye effluents in industry before passing it to the surrounding.

Future Scope

Citrate gel method of synthesis yields oxides at much lower temperature of 900°C compared to conventional ceramic method of obtaining oxides at 1400°C. Use of Hydrazine hydrate lowers the temperature of decomposition of precursors and also reduces the particle size in case of synthesis of $\text{ZnO}_{1-x}\text{N}_x$. These methods can be used for the synthesis of other strategic materials.

Leaching studies of Strontium from neodymium zirconate lattice can be performed by sintering the matrix at still higher temperatures (1600°C) to further minimize the leaching of Sr from the lattice of neodymium zirconate.

Photodegradation of dyes and other organics on ZnO, $\text{ZnO}_{1-x}\text{N}_x$ and iron ore rejects can be optimized so as to carry out complete mineralization of organic moiety to carbon dioxide and water.

The antibacterial properties of ZnO and $\text{ZnO}_{1-x}\text{N}_x$ can be made use of in textiles, medicated bandages, sterile dressings etc. The antibacterial studies can be carried out on other strains of bacteria.

NO_x determination can be carried out quantitatively to estimate and enhance the photocatalytic activity of the photocatalysts.

The oxidation property of iron ore rejects can be utilised for environment friendly applications. The iron ore tailings may be used as a bed to treat dye effluents coming out from industries before sending it to the surroundings. The work carried out and results obtained for the representative organic dye is relevant to degradation of pesticides and other organic effluents also. A bed of iron ore tailings may be formed around the fields so that excess pesticides and fertilizers which get washed away in the water bodies present around fields get degraded and do not leach in the water bodies.

References

- [1] D. G. Campbell, Nuclear chemical disasters (part-4):- The most polluted area on Earth, U K Progressive Magazine.
- [2] Managing low radioactivity material from the decommissioning of nuclear facilities technical reports series no. 462 International atomic energy agency Vienna, 2008.
- [3] U.S. EPA Handbook, Ground water vol.1: Ground water and contamination, Office of research and development Washington DC (1990).
- [4] K. Govindarajalu, Industrial Effluent and Health Status - A Case Study of Noyyal River Basin, Proceedings of the Third International Conference on Environment and Health, Chennai, India, (2003) 150 – 157.
- [5] S. Mukherjee, P. Nellyyat, Ground water pollution and emerging environmental challenges of Industrial Effluent Irrigation: A case study of Mettupalayam Taluka, Tamilnadu, IWMI-TATA Water Policy Program's 5th Annual Partners' Research Meet (2006).
- [6] S. Dan'azumi, M. H. Bichi, Industrial Pollution and Implication on Source of Water Supply in Kano, Nigeria, International Journal of Engineering & Technology IJET-IJENS, 10: 01.
- [7] Vegetables being watered with industrial effluents, Karachi Digest, The News.
- [8] Kudremukh concerns, Frontline environment, 18(2001) Sep. 01 - 14.
- [9] M. H. Wong, Environmental Impacts of Iron Ore Tailings Tolo Harbour, Hong Kong, Environmental Management, 5, 135-145.
- [10] B. T. Marques, J. F. Vetelino, A semiconducting metal oxide sensor array for the detection of NO_x and NH₃, Sensors and actuators B, 77 (2001) 100-110.
- [11] T. Taku, Y. Takeshi, O. Akinori, Atmospheric environmental problems caused by aircraft exhaust gases, Journal title- Nippon Koku Gakkai Nenkai Koenkai Koenshu (Japanese language) 30(1999)79-82.
- [12] Acid rain and Japan: Passing the buck, The Economist, 328 (1993) 68-69.
- [13] A. E. Ringwood, S. E. Kesson, N. G. Ware, W. Hibberson, A. Major, Nature (London) 278 (1979) 219.
- [14] A. E. Ringwood, P. M. Kelly, Philos. Trans. R. Soc. London 319 (1986) 63.
- [15] A. E. Ringwood, Safe disposal of high level nuclear reactor wastes: a new strategy, Australian National University Press, Canberra, 1978.

- [16] B.B. Ebbinghaus, R.A. Van Konynenburg, E.R. Vance, M.W. Stewart, A. Jostsons, J.S. Allender, D.T. Rankin, Ceramic Composition for Immobilization of Actinides, US Patent 6,137,025(1999).
- [17] I. T. Todorov, J. A. Purton, N. L. Allan, M. T. Dove, Simulation of radiation damage in gadolinium pyrochlores, *J. Phys.: Condens. Matter* 18(2006)2217-2234.
- [18] B. J. Kennedy, Structural trends in pyrochlore type oxides, *Physica B* 241-243(1998) 303-310.
- [19] Y. D. Kolekar, S. B. Kulkarni, K. Chakraborty, A. Das, S. K. Paranjpe, P. B. Joshi, Structural study and electrical properties of Zr-doped $\text{Nd}_2\text{Sn}_2\text{O}_7$ pyrochlore compounds, *Pramana-Journal of physics*, 63(2004)189-197.
- [20] J. M. Longo, P.M. Racciah, J.B. Goodenough, $\text{Pb}_2\text{M}_2\text{O}_{7-x}$ (M = Ru, Ir, Re) — Preparation and properties of oxygen deficient pyrochlores, *Mater. Res. Bull.*, 4 (1969) 191-202.
- [21] T. Yu, Electrical properties and structural disorder in stannate pyrochlores, Massachusetts Institute of technology (1996).
- [22] M. T. Weller, R. W. Hughes, J. Rooke, C. S. Knee, J. Reading, The pyrochlore family- a potential panacea for the frustrated perovskite chemist, *Dalton Trans.*, 19 (2004) 3032-3041.
- [23] P. J. Wilde, C. R. Catlow, Defects and diffusion in pyrochlore structured oxides, *Solid State Ionics*, 112(1998)173-183.
- [24] C. Chiu, Y. Lee, H. Sheu, H. I. Kao, Phase Transition and the Thermal Activated Ordering of the Ions with Pyrochlore Phase in $\text{Ln}_2\text{Zr}_2\text{O}_7$ (Ln = Sm, Eu), *Journal of the Chinese Chemical Society*, 57(2010) 925-931.
- [25] N. Kolpakova, P. Charnetzki, W. Nawrochik, P. Syrnikov, A. Lebedev, Dielectric relaxation and ferroelectricity in $\text{Cd}_2\text{Nb}_2\text{O}_7$ pyrochlore, *Journal experimental and theoretical physics*, 94 (2002) 395-402.
- [26] H. Sakai, K. Yoshimura, H. Ohno, T. D. Matsuda, H. Kato, S. Kambe, R. Walstedt, Y. Haga, Y. Onuki, *J. Phys.: Condens. Matter*, 13(2001) L 785.
- [27] N. Taira, M. Wakeshima, Y. Hinatsu, Magnetic properties of iridium pyrochlores $\text{R}_2\text{Ir}_2\text{O}_7$ (R = Y, Sm, Eu and Lu), *J. Phys.: Condens. Matter*, 13 (2001) 5527-5533.
- [28] J. G. Park, Y. Jo, J. Park, H.C. Kim, H. C. Ri, Sh. Xu, Y. Moritomo, S.W. Cheong, Electrical and Magnetic properties of $\text{R}_2\text{Mo}_2\text{O}_7$ (R =Nd, Sm, Gd and Dy), *Physica B*, 328 (2003) 90-94.
- [29] J. Christopher, C. S. Swamy, Surface characterization and catalytic activity of $\text{Ln}_2\text{Ti}_2\text{O}_7$ (Ln=Y, Sm, Gd and Tb), *J. Mater. Sc.*, 26 (1991)4966-4970.

- [30] Y. Xie, J. Wang, R. Liu, X. Su, Z. Sun, Z. Li, Preparation of $\text{La}_{1.9}\text{Ca}_{0.1}\text{Zr}_2\text{O}_{6.95}$ with pyrochlore structure and its application in synthesis of ammonia at atmospheric pressure *Solid State Ionics*, 168 (2004) 117-121.
- [31] J. Wu, X. Wei, N. P. Padture, P. G. Klemens, M. Gell, E. Garcia, P. Miranzo, M. I. Osendi, *J. Am. Ceram. Soc.*, 85(2002) 3031-35.
- [32] K. J. Moreno, G. Mendoza-Suarez, A. F. Fuentes, J. Garcia-Barriocanal, C. Leon, J. Santamaria, Cooperative oxygen ion dynamics in $\text{Gd}_2\text{Ti}_{2-x}\text{Zr}_x\text{O}_7$, *Phys. Rev. B* 71(2005) 132301.
- [33] S. X. Wang, B. D. Begg, L. M. Wang, R. C. Ewing, W. J. Weber, K.V. Govindan kuttty, *J. Mater. Res.*, 14 (1999) 4470.
- [34] J. Chen, J. Lian, L. M. Wang, R. C. Ewing, R. G. Wang, W. Pan, X-Ray photoelectron spectroscopy study of disordering in $\text{Gd}_2(\text{Ti}_{1-x}\text{Zr}_x)_2\text{O}_7$ pyrochlores, *Phys. Rev. Lett.* 88 (2002) 105901- 1 to 4.
- [35] S. J. Patwe, A. K. Tyagi, Solubility of Ce^{+4} and Sr^{+2} in the pyrochlore lattice of $\text{Gd}_2\text{Zr}_2\text{O}_7$ for simulation of Pu and alkaline earth metal, *Ceramics Intern.* 32(2006) 545-548.
- [36] S. X. Wang, L. M. Wang, R. C. Ewing, K. V. Govindan Kuttty, Ion irradiation of rare earth- and Yttrium-titanate pyrochlores, *Nucl. Inst. and Methods in Phys. Res. B*, 169 (2000) 135-140.
- [37] Y. F. Volkov, S. V. Tomilin, A. N. Lukinykh, A. A. Lizin, A. A. Elesin, A.G. Yakovenko, *Radiochem.* 46 (2004) 351.
- [38] R. C. Ewing, Safe management of actinides in the nuclear fuel cycle: Role of mineralogy, *Comptes Rendus Geoscience* 343 (2011) 219-229.
- [39] A. V. Shlyakhtina, L. G. Shcherbakova, A. V. Knotko, A. V. Steblevskii, Study of the fluorite–pyrochlore–fluorite phase transitions in $\text{Ln}_2\text{Ti}_2\text{O}_7$ ($\text{Ln}=\text{Lu}, \text{Yb}, \text{Tm}$), *J. Solid State Electrochem.*, 8 (2004) 661-667.
- [40] X. L. Xia, Z. G. Liu, J. H. Ouyang, Order-disorder transformation and enhanced oxide-ionic conductivity of $(\text{Sm}_{1-x}\text{Dy}_x)_2\text{Zr}_2\text{O}_7$ ceramics, *J. Power Sources*, 196 (2011)1840-1846.
- [41] J. Lian, L. Wang, J. Chen, K. Sun, R. C. Ewing, J. Matt Farmer, L. A. Boatner, The order–disorder transition in ion-irradiated pyrochlore, *Acta Materialia*, 51(2003)1493-1502.
- [42] P. Nachimuthu, S. Thevuthasan, M. H. Engelhard, W. J. Weber, D. K. Shuh, N. M. Hamdan, B. S. Mun, E. M. Adams, D. E. McCready, V. Shutthanandan, D. W. Lindle, G. Balakrishnan, D. M. Paul, E. M. Gullikson, R. C. C. Perera, J. Lian, L. M. Wang, R. C. Ewing, Probing cation antisite disorder in $\text{Gd}_2\text{Ti}_2\text{O}_7$ pyrochlore by site-specific near-

- edge x-ray absorption fine structure and x-ray photoelectron spectroscopy, *Phys. Rev. B* 70, 100101(R) (2004).
- [43] M. Pirzada, R. W. Grimes, L. Minervini, J. F. Maguire, K. E. Sickafus, Oxygen migration in $A_2B_2O_7$ pyrochlores, *Solid State Ionics*, 140 (2001) 201–208.
- [44] J. Lian, W. J. Weber, W. Jiang, L. M. Wang, L. A. Boatner, R. C. Ewing, Radiation-induced effects in pyrochlores and nanoscale materials engineering, *Nucl. Inst. and Methods in Phys. Res. B*, 250 (2006) 128-136.
- [45] G. R. Lumpkin, K. R. Whittle, S. Rios, K. Trachenko, M. Pruneda, E. J. Harvey, S. A. T. Redfern, K. L. Smith, N. J. Zaluzec, Radiation damage in pyrochlore and related compounds, *Materials Research Society Symposium Proceedings*, 932(2006) 549-558.
- [46] F. X. Zhang J. Lian, U. Becker, R. C. Ewing, J. Hu, S. K. Saxena, High-pressure structural changes in the $Gd_2Zr_2O_7$ pyrochlore, *Phys. Rev. B*, 76 (2007) 214104-214108.
- [47] P. M. Martin, R.C. Belin, P. J. Valenza, A. C. Scheirost, EXAFS study of the structural phase transition in the americium zirconate pyrochlore, *J. Nucl. Mater.*, 385 (2009) 126-130.
- [48] B. D. Begg, N. J. Hess, D. E. MacCready, S. Thevuthasan, W. J. Weber, Heavy ion irradiation effects in $Gd_2Ti_{2-x}Zr_xO_7$, *J. Nucl. Mater.*, 289 (2001) 188-193.
- [49] R. Ewing, W. Weber, J. Lian, Nuclear waste disposal—pyrochlore ($A_2B_2O_7$): Nuclear waste form for the immobilization of plutonium and “minor” actinides, *J. Appl. Phys.*, 95 (2004)5949-5971.
- [50] J. Lian, X. T. Zu, K. V. G. Kutty, J. Chen, L. M. Wang, R. C. Ewing, Ion-irradiation-induced amorphization of $La_2Zr_2O_7$ pyrochlore, *Phys. Rev. B* 66 (2002) 054108
- [51] C. Heremans, B. J. Wuensch, J. K. Slatick, E. Prince, *Mater Res. Soc. Symp. Proc.* 293, 349 (1990).
- [52] Y. Liu, R. L. Withers, L. Norén, The pyrochlore to ‘defect fluorite’ transition in the $Y_2(Zr_yTi_{1-y})_2O_7$ system and its underlying crystal chemistry, *J. Solid State Chem.* 179 (2006) 928-934.
- [53] K. J. Moreno, A. F. Fuentes, U. Amador, J. Santamaría, C. León, Influence of structural disorder on the dynamics of mobile oxygen ions in $Dy_2(Ti_{1-y}Zr_y)_2O_7$, *J. Non-Cryst. Solids*, 353(2007) 3947-3955.
- [54] B. P. Mandal S. K. Deshpande, A. K. Tyagi, ionic conductivity enhancement in $Gd_2Zr_2O_7$ pyrochlore by Nd doping, *J. Mater. Res.*, 23 (2008)911-916.

- [55] K. V. G. Kutty, C. K. Mathews, T. N. Rao, U. V. Varadaraju, Oxide Ion Conductivity in some substituted Rare Earth Pyrochlores, *Solid state ionics*, 80 (1995) 99-110.
- [56] M. P. Van Dijk, K. J. De Vries, A. J. Burggraaf, Oxygen ion and mixed conductivity in compounds with the fluorite and pyrochlore structure, *Solid State Ionics* 9&10(1983) 913-920.
- [57] M. A. Spears, S. Kramer, H. L. Tuller, P. K. Moon, Ionic and mixed conducting ceramics, in: T. A. Ramanarayanan, H. L. Tuller (Eds), 91(12) *Electrochem. Soc.*, Pennington NJ (1991) 32.
- [58] E. J. Harvey, K. R. Whittle, G. R. Lumpkin, R. I. Smith, S. Redfern, Solid solubilities of $(La, Nd)_2(Zr, Ti)_2O_7$ phases deduced by neutron diffraction, *J. Solid State Chem.*, 178 (2005) 800-810.
- [59] B. P. Mandal, A. K. Tyagi, Pyrochlores: Potential multifunctional materials, *BARC Newsletter*, 313, Mar-Apr 2010.
- [60] S. Lutique, R. J. M. Konings, V. V. Rondinella, J. Somers, T. Wiss, The thermal conductivity of $Nd_2Zr_2O_7$ pyrochlore and the thermal behavior of pyrochlore based inert matrix fuel, *J. Alloys compd.*, 352 (2003) 1-5.
- [61] S. Lutique, P. Javorský, R. J. M. Konings, A. C. G. van Genderen, J. C. van Miltenburg, F. Wastin, Low temperature heat capacity of $Nd_2Zr_2O_7$ pyrochlore, *J. Chem. Thermodyn.*, 35 (2003) 955-965.
- [62] W. Carmack, R. Fielding, P. Medvedev, M. Meyer, M. Todosow, H. B. Hamilton, J. Nino, S. Phillpot, J. Tulenko, AECL/US INERI –Development of inert matrix fuels for plutonium and minor actinide management in power reactors-fuel requirements and down-select report, U.S. Department of Energy (2005) 1-40.
- [63] C. Tracy, Phase Composition-Microstructure-Thermal Conductivity Relationships in $MgO-Nd_2Zr_2O_7$ Composite Inert Matrix Materials, MDI Final Report, LA-UR 09-06689.
- [64] P. Shukla, T. Watanabe, J. C. Nino, J. S. Tulenko, S. R. Phillpot, Thermal Transport Properties of MgO and $Nd_2Zr_2O_7$ Pyrochlore by Molecular Dynamics Simulation, *J. Nucl. Mater.*, 380 (2008) 1-7.
- [65] S. J. Yates, K. J. McClellan, J. C. Nino, The effect of processing on the thermal diffusivity of $MgO-Nd_2Zr_2O_7$ composites for inert matrix materials, *J. Nucl. Mater.*, 393(2009) 203-211.
- [66] S. J. Yates, P. Xu, J. Wang, J. S. Tulenko, J. C. Nino, Processing of magnesia-pyrochlore composites for inert matrix materials, *J. Nucl. Mater.*, 362 (2007) 336-342.
- [67] P. Xu, K. Holliday, K. R. Czerwinski, J. C. Nino, Dissolution behavior of MgO -

- pyrochlore composites in acidic solutions, *J. Nucl. Mater.*, 394 (2009) 39–45.
- [68] T. Feng, D. R. Clarke, D. Jiang, J. Xia, J. Shi, Neodymium zirconate ($\text{Nd}_2\text{Zr}_2\text{O}_7$) transparent ceramics as a solid state laser material, *Appl. Phys. Lett.* 98 (2011) 151105.
- [69] A. Bakin, A. El-Shaer, A. C. Mofor, M. Al-Suleiman, E. Schlenker, A. Waag, ZnMgO-ZnO Quantum Wells Embedded in ZnO Nanopillars: Towards Realisation of Nano-LEDs, *Physica Status Solidi (c)* 4 (2007) 158–161.
- [70] Y. B. Li, Y. Bando, D. Golberg, ZnO nanoneedles with tip surface perturbations: Excellent field emitters, *Appl. Phys. Lett.* 84 (2004) 3603-3605.
- [71] Y. W. Heo, L. C. Tien, Y. Kwon, D. P. Norton, S. J. Pearton, B. S. Kang, F. Ren, Depletion-mode ZnO nanowire field-effect transistor, *Appl. Phys. Lett.* 85 (2004) 2274.
- [72] H. T. Wang, B. S. Kang, F. Ren, L. C. Tien, P. W. Sadik, D. P. Norton, S. J. Pearton, J. Lin, Hydrogen-selective sensing at room temperature with ZnO nanorods, *Appl. Phys. Lett.* 86 (2005) 243503.
- [73] L. C. Tien, P.W. Sadik, D. P. Norton, L. F. Voss, S. J. Pearton, H. T. Wang, B. S. Kang, F. Ren, Hydrogen sensing at room temperature with Pt-coated ZnO thin films and nanorods *Appl. Phys. Lett.* 87 (2005) 222106.
- [74] K. Byrappa, A. K. Subramani, S. Ananda, K. M. Lokanatha Rai, R. Dinesh, M. Yoshimura, Photocatalytic degradation of rhodamine B dye using hydrothermally synthesized ZnO, *Bull. Mater. Sci.*, 29 (2003) 433-438.
- [75] A. P. L. Batista, H. W. Pereira carvalho, G. H. P. Luz, P. F. Q. Martins, M. Goncalves, L. C. A. Oliveira, Preparation of CuO/SiO₂ and photocatalytic activity by degradation of methylene blue, *Environ. Chem. Lett.*, 8 (2010) 63-67.
- [76] A. Fujishima, K. Honda, Electrochemical photolysis of water at a semiconductor electrode, *Nature*, 238 (1972) 37–38.
- [77] A. Sobczynski, A. Dobosz, Water purification by photocatalysis on semiconductors, *Polish journal of environmental studies*, 10 (2001) 195-205.
- [78] N. Daneshwar, S. Aber, M. S. Seyed Dorraji, A. R. Khataee, M. H. Rasoulifard, Preparation and investigation of photocatalytic properties of ZnO nanocrystals: Effect of operational parameters and kinetic study, *International journal of chemical and biomolecular engineering*, 1(2008)23-28.
- [79] S. Chakrabarti, B. K. Dutta, Photocatalytic degradation of model textile dyes in wastewater using ZnO as semiconductor catalyst, *J. Hazard. Mater.*, 112 (2004)269-278.
- [80] C. A. K. Gouvêa, F. Wypych, S. G. Moraes, N. Durán, N. Nagata, P. Peralta-

- Zamora Semiconductor-assisted photocatalytic degradation of reactive dyes in aqueous solution, *Chemosphere* 40 (2000) 433-440.
- [81] N. Daneshvar, D. Salari, A. R. Khataee, Photocatalytic degradation of azo dye acid red 14 in water on ZnO as an alternative catalyst to TiO₂, *J. Photochem. Photobiol., A*: 162 (2004) 317-322.
- [82] M. A. Behnajady, N. Modirshahla, R. Hamzavi, Kinetic study on photocatalytic degradation of C.I. Acid Yellow 23 by ZnO photocatalyst, *J. Hazard. Mater.*, 133 (2006) 226-232.
- [83] A. Akyol, M. Bayramoğlu, Photocatalytic degradation of Remazol Red F3B using ZnO catalyst, *J. Hazard. Mater.*, 124 (2005) 241-246.
- [84] K. Hayat, M. A. Gondal, M. M. Khaled, S. Ahmed, Kinetic study of laser-induced photocatalytic degradation of dye (alizarin yellow) from wastewater using nanostructured ZnO, *J. Environ Sci Health A: Tox Hazard Subst Environ Eng.* 45(2010) 1413-20.
- [85] K. Yogendra, K. M. Mahadevan, S. Naik, N. Madhusudhana, Photocatalytic activity of synthetic ZnO composite against Coralene red F3BS dye in presence of solar light, *International Journal of Environmental Sciences* 1:5(2011)839-846.
- [86] S. Sakthivel, B. Neppolian, M. Palanichamy, B. Arabindoo, V. Murugesan, Photocatalytic degradation of leather dye over ZnO catalyst supported on alumina and glass surfaces, *Water Sci. Technol.*, 44 (2001) 211-8.
- [87] L. A. Ghule, A. A. Patil, K. B. Sapnar, S. D. Dhole, K. M. Garadkar, Photocatalytic degradation of methyl orange using ZnO nanorods, *Toxicol. Environ. Chem.*, 93 (2011) 623-634.
- [88] S. Baruah, M. A. Mahmood, M. T. Zar Myint, T. Bora, J. Dutta, Enhanced visible light photocatalysis through fast crystallization of zinc oxide nanorods, *Beilstein J. Nanotechnol.* 1(2010) 14-20.
- [89] N. Daneshvar, S. Aber, M.S. Seyed Dorraji, A.R. Khataee, M.H. Rasoulifard, Photocatalytic degradation of the insecticide diazinon in the presence of prepared nanocrystalline ZnO powders under irradiation of UV-C light, *Sep. Purif. Technol.*, 58 (2007) 91-98.
- [90] M. A. Gondal, M. N. Sayeed, Laser-enhanced photocatalytic degradation of organic pollutants from water using ZnO semiconductor catalyst, *J. Environ. Sci. Health., Part A*, 43 (2008)70-77.
- [91] M. Muruganadham, N. Sobana, M. Swaminathan, Solar assisted photocatalytic and photochemical degradation of reactive black 5, *J. Hazard. Mater.*, 137 (2006)1371-6.
- [92] G. A. Epling, C. Lin, Photoassisted bleaching of dyes utilizing TiO₂ and visible

- light, *Chemosphere* 46(2002)561-570.
- [93] S. Colis, H. Bieber, S. Begin-Colin, G. Schmerber, C. Leuvrey, A. Dinia, *Chem. Phys. Lett.* 422(2006)529–533.
- [94] R. Ullah, J. Dutta, Photocatalytic degradation of organic dyes with manganese-doped ZnO nanoparticles, *J. Hazard. Mater.*, 156 (2008)194–200.
- [95] R. Wang, J. H. Xin, Y. Yang, H. Liu, L. Xu, J. Hu, The characteristics and photocatalytic activities of silver doped ZnO nanocrystallites, *Appl. Surf. Sci.* 227 (2004) 312–317.
- [96] R. Slama, F. Ghribi, A. Houas, C. Barthou, L. El Mir, Photocatalytic and optical properties vanadium doped zinc oxide nanoparticles, *Int. J. Nanoelectronics and Materials* 3(2010)133-142.
- [97] X. Lu, Z. Liu, Y. Zhu, L. Jiang, Sonochemical synthesis and photocatalytic property of zinc oxide nanoparticles doped with magnesium(II), *Mater. Res. Bull* 46 (2011) 1638-1641.
- [98] K. Hsiao, S. Liao, Y. Chen, Synthesis, characterization and photocatalytic property of nanostructured Al-doped ZnO powders prepared by spray pyrolysis, *Mater. Sci. Eng., A*, 447 (2007)71-76.
- [99] S. Anandan, A. Vinu, T. Mori, N. Gokulakrishnan, P. Srinivasu, V. Murugesan, K. Ariga, Photocatalytic degradation of 2,4,6-trichlorophenol using lanthanum doped ZnO in aqueous suspension, *Catal. Commun.*, 8 (2007)1377-1382.
- [100] P. Zhou, X. Yu, L. Yang, Z. Tao, Simple air oxidation synthesis and optical properties of S-doped ZnO microspheres, *Mater. Lett.*, 61 (2007) 3870-3872.
- [101] A. B. Patil, K. R. Patil, S. K. Pardeshi, Ecofriendly synthesis and solar photocatalytic activity of S-doped ZnO, *J. Hazard. Mater.*, 183(2010) 315-323.
- [102] M. Mapa, C. S. Gopinath, Combustion Synthesis of Triangular and Multifunctional ZnO_{1-x}N_x ($x \leq 0.15$) Materials, *Chem. Mater.* 21(2009)351–359.
- [103] H. Hu, C. Deng, Q. Feng, Y. Gao, M. Song, Preparation and characterization of skin coloured N doped ZnO nanocrystals, *Mater. Sci. forum* 663-665 (2011) 243-246.
- [104] S. Cho, J. Jang, J. S. Lee, K. Lee, Carbon-doped ZnO nanostructures synthesized using vitamin C for visible light photocatalysis, *Cryst. Eng. Comm.*, 12(2010) 3929-3935.
- [105] F. Barka-Bouaifel, B. Sieber, N. Bezzi, J. Benner, P. Roussel, L. Boussekey, S. Szunerits, R. Boukherroub, Synthesis and photocatalytic activity of iodine-doped ZnO nanoflowers, *J. Mater. Chem.* 21(2011) 10982-10989.

- [106] J. Luan, S. Zheng, X. Hao, G. Luan, X. Wu, Z. Zou, Photophysical and photocatalytic properties of novel M_2BiNbO_7 ($M=$ In and Ga), *J. Braz. Chem. Soc.* 17 (2006)1368-1376.
- [107] X. Feng, S. Zhu, H. Hou, Investigation of 207 nm UV radiation for degradation of organic dye in water, *Water SA*, 32 (2006) 43-48.
- [108] Z. Yu, S. S. C. Chuang, Probing Methylene Blue Photocatalytic Degradation by Adsorbed Ethanol with In Situ IR, *J. Phys. Chem. C*, 111 (2007) 13813-13820.
- [109] M. Noorjahan, M. Pratap Reddy, V. Durga Kumari, B. Lavedrine, P. Boule, M. Subrahmanyam, Photocatalytic degradation of H- acid over a novel TiO_2 thin film fixed bed reactor and in aqueous suspensions, *J. Photochem. Photobiol. A*, 156 (2003) 179-187.
- [110] H. Gnaser, M. R. Savina, W. F. Calaway, C. E. Tripa, I. V. Veryovkin, M. J. Pellin, Photocatalytic degradation of methylene blue on nanocrystalline TiO_2 : Surface mass spectrometry of reaction intermediates, *Int. J. Mass Spectrom.*, 245 (2005) 61-67.
- [111] A. Houas, H. Lachheb, M. Ksibi, E. Elaloui, C. Guillard, J. Herrmann, Photocatalytic degradation pathway of methylene blue in water, *Appl. Catal. B*, 31(2001)145-157.
- [112] S. Nath, S. K. Ghosh, S. Panigahi, T. Thundat, T. Pal, Synthesis of selenium nanoparticle and its photocatalytic application for decolourization of Methylene blue under UV irradiation, *Langmuir*, 20 (2004) 7880-7883.
- [113] J. Sawai, Quantitative evaluation of antibacterial activities of metallic oxide powders (ZnO , MgO and CaO) by conductimetric assay, *J. Microbiol. Methods*, 54 (2003) 177-182.
- [114] K. H. Tam, A. B. Djurišić, C. M. N. Chan, Y. Y. Xi, C. W. Tse, Y. H. Leung, W. K. Chan, F. C. C. Leung, D. W. T. Au, Antibacterial activity of ZnO nanorods prepared by a hydrothermal method, *Thin Solid Films* 516 (2008) 6167-6174.
- [115] N. Jones, B. Ray, K. T. Ranjit, A. C. Manna, Antibacterial activity of ZnO nanoparticle suspensions on a broad spectrum of microorganisms, *FEMS Microbiol. Lett.* 279 (2008) 71-76.
- [116] J.H. Li, R.Y. Hong , M.Y. Li, H.Z. Li, Y. Zheng, J. Ding, Effects of ZnO nanoparticles on the mechanical and antibacterial properties of polyurethane coatings, *Progress in Organic Coatings*, 64 (2009)504-509.
- [117] X. Li, Y. Xing, Y. Jiang, Y. Ding ,W. Li, Antimicrobial activities of ZnO powder-coated PVC film to inactivate food pathogens, *International Journal of Food Science & Technology*, 44 (2009)2161-2168.
- [118] R. Rajendran, C. Balakumar, H. A. Mohammed Ahammed, S. Jayakumar, K.

- Vaideki, E.M. Rajesh, Use of zinc oxide nano particles for production of antimicrobial textiles, *International Journal of Engineering, Science and Technology*, 2 (2010) 202-208.
- [119] J. C. Yu, W. Ho, J. Lin, H. Yip, P. K. Wong, Photocatalytic activity, antibacterial effect, and photoinduced hydrophilicity of TiO₂ films coated on a stainless steel substrate, *Environ. Sci. Technol.* 37(2003) 2296-2301.
- [120] M. Fang, J. H. Chen, X. L. Xu, P. H. Yang, H. F. Hildebrand, Antibacterial activities of inorganic agents on six bacteria associated with oral infections by two susceptibility tests, *Int. J. Antimicrob. Agents*, 27 (2006) 513-7.
- [121] D. Blake, P. Maness, Z. Huang, E. J. Wolfrum, J. Huang, W. A. Jacoby, Application of the Photocatalytic Chemistry of Titanium dioxide to disinfection and the killing of cancer cells, *Sep. Purif. Methods* 28 (1999)1-50.
- [122] P. K. Stoimenov, R. L. Klinger, G. L. Marchin, K. J. Klabunde, Metal oxide nanoparticles as bactericidal agents, *Langmuir*, 18 (2002) 6679–6686.
- [123] N. Padmavathy, R. Vijayaraghavan, Enhanced bioactivity of ZnO nanoparticles—an antimicrobial study, *Sci. Technol. Adv. Mater.*, 9 (2008) 035004.
- [124] R. Brayner, R. Ferrari-Iliou, N. Brivois, S. Djediat, M. F. Benedetti, F. Fievet, Toxicological impact studies based on *Escherichia coli* bacteria in ultrafine ZnO nanoparticles colloidal medium, *Nano Lett.* 6 (2006) 866-70.
- [125] O. Yamamoto, M. Komatsu, J. Sawai, Z. Nakagawa, Effect of lattice constant of Zinc oxide on antibacterial characteristics, *J. Mater. Sci.- Mater. Med.*, 15 (2004) 847-851.
- [126] L. Adams, D. Lyon, P. Alvarez, Comparative eco-toxicity of nanoscale TiO₂, SiO₂ and ZnO water suspensions, *Water Research*, 40(2006) 3527 – 3532.
- [127] O. Akhavan, M. Mehrabian, K. Mirabbaszadeh, R. Azimirad, Hydrothermal synthesis of ZnO nanorod arrays for photocatalytic inactivation of bacteria, *J. Phys. D: Appl. Phys.* 42 (2009)1-10.
- [128] Y. Liu, L. He, A. Mustapha, H. Li, Z. Q. Hu, M. Lin, Antibacterial activities of zinc oxide nanoparticles against *Escherichia Coli* O157:H7, *Journal of applied microbiology* 107:4(2009)1193-1201.
- [129] P. Gajjar, B. Pettee, D. W. Britt, W. Huang, W. P. Johnson, A. J. Anderson, Antimicrobial activities of commercial nanoparticles against an environmental soil microbe, *Pseudomonas putida* KT2440, *Journal of Biological Engineering*, 3 (2009).
- [130] J. Zhang, Y. Hu, M. Matsuoka, H. Yamashita, M. Minagawa, H. Hidaka, M. Anpo, Relationship between the Local Structures of Titanium Oxide photocatalysts and

- their reactivities in the decomposition of NO, *J. Phys. Chem. B*, 105 (2001) 8395–8398.
- [131] S. Devahasdin, C. Fan, Jr., K. Li, D. H. Chen, TiO₂ photocatalytic oxidation of nitric oxide: transient behaviour and reaction kinetics, *J. photochem. Photobiol. A*, 156 (2003) 161–170.
- [132] F. L. Toma, G. Bertrand, D. Klein, C. Coddet, Photocatalytic removal of nitrogen oxides via titanium dioxide, *Environ. Chem. Lett.*, 2 (2004) 117–121.
- [133] S. Yin, Y. Aita, M. Komatsu, J. Wang, Q. Tang, T. Sato, Synthesis of excellent visible-light responsive TiO_{2-x}N_y photocatalyst by a homogeneous precipitation-solvothermal process, *J. Mater. Chem.*, 15 (2005) 674–682.
- [134] M. M. Ballari, M. Hunger, G. Husken, H. J. H. Brouwers, NO_x photocatalytic degradation employing concrete pavement containing titanium dioxide, *Appl. Catal. B: Environmental* 95 (2010) 245–254.
- [135] D. H. Chen, K-Y. Li, R. Yuan, Photo catalytic Coating on Road Pavements/Structures for NO_x Abatement, Annual Project Report Submitted to Houston Advanced Research Center and Office of Air Quality Planning and Standards U.S. Environmental Protection Agency (2007) 1–18.
- [136] K. S. Rane, V. M. S. Verenkar, P. Y. Sawant, Dielectric behavior of MgFe₂O₄ prepared from chemically beneficiated iron ore rejects, *Bull. Mater. Sci.*, 24 (200) 323–330.
- [137] S. N. de Souza, Effect of mining rejects on the nutrient chemistry of Mandovi estuary, Goa, *Indian Journal of Marine Sciences*, 28 (1999) 355–359.
- [138] M. K. Ghose, P. K. Sen, Recovery of usable ore fines from iron ore tailings and their environmental management – A case study, *Land Contamination & Reclamation*. 7(1999) 143–149.
- [139] P. Kamat, Goa Iron Ore exports recovering as demand from china picks up, *The Hindu business line*, (2009).
- [140] T. I. Balandina, A. A. Zaliznyak, G. G. Zelinskaya, E. P. Rashina, V. N. Shapakidze, I. V. Gedzhadze, The use of tailings from the enrichment of copper pyrites ore for making dark-green glass hollow-ware, *Glass and Ceramics*, 32 (1975) 658–659.
- [141] Z. Yi, H. Sun, X. Wei, C. Li, Iron ore tailings used for the preparation of cementitious materials by compound thermal activation, *International Journal of Minerals, Metallurgy and Materials* 16 (2009) 355–358.
- [142] C. Li, H. Sun, Z. Yi, L. Li, Innovative methodology for comprehensive utilization of iron ore tailings: Part 2: The residues after iron recovery from iron ore tailings to prepare cementitious material, *J. Hazard. Mater* 174(2010)78–83.

- [143] M. Yellishetty, V. Karpe, E.H. Reddy, K.N. Subhash, P.G. Ranjith, Reuse of iron ore mineral wastes in civil engineering constructions: A case study, *Resources, Conservation and Recycling* 52 (2008)1283-1289.
- [144] V. M. S. Verenkar, Beneficiation of Goan ore rejects to get pure iron oxide and utilization of the iron oxide to synthesize ferrites, high-tech magnetic materials, Ph.D. Thesis, Goa University, Goa, India (1997).
- [145] P. Y. Sawant, Physico-chemical methods to determine the trace rare elements in Goan ore rejects and beneficiate the ore to get pure iron oxides useful for high-tech ferrite manufacture, Ph. D Thesis, Goa University, Goa, India (1998).
- [146] K. S. Rane, V. M. S. Verenkar, P. Y. Sawant, Hydrazine method of synthesis of γ -Fe₂O₃ useful in ferrites preparation. Part IV – preparation and characterization of magnesium ferrite, MgFe₂O₄ from γ -Fe₂O₃ obtained from hydrazinated iron oxyhydroxides and iron (II) carboxylato-hydrazinates, *J. Mater. Sci. Mater. Electr.* 10 (1999)133-140.
- [147] K. S. Rane, V. M. S. Verenkar and P. Y. Sawant, Digest of the 8th international conference on ferrites (ICF 8), Kyoto, Japan, (Tokyo: The Japan Society of Powder and Powder Metallurgy), Paper No.19 Pp. I-2 page 158, (2000).
- [148] K S Rane, V M S Verenkar, P Y Sawant, Ferrite grade iron oxides from ore rejects, *Bull. Mater. Sci.* 24 (2001)331–338.
- [149] W. F. De Souza, I. R. Guimarães, L. C.A. Oliveira, M. C. Guerreiro, A.L. N. Guarieiro, K. T. G. Carvalho, Natural and H₂ reduced limonite for organic oxidation by a fenton like system: Mechanism study via ESI-MS and theoretical calculations, *J. Mol. Catal. A: Chem.* 278 (2007)145-151.
- [150] J. Q. Chen, D. Wang, M. Zhu, C. Gao, Study on degradation of methyl orange using pelagite as photocatalyst, *J. Hazard. Mater.* 138 (2006)182-186.
- [151] Z. Hong, T. Hongxiao, Adsorption and degradation of phenol on natural manganese ore surfaces, *Acta Scientiae Circumstantiae*, 6 (1999).
- [152] Z. Hui, R. Xin-chao, Z. Qing-fu, Photocatalytic Oxidation of Dispersed Blue-2bln Dyestuff in Modified Manganese Ore Suspension, *Journal of Wuhan Textile S.n.T. Institute*, 01(2003).
- [153] H. Feng, L. Le-cheng, J. Zhejiang, Degradation kinetics and mechanisms of phenol in photo-Fenton process, *Univ SCI* 5 (2004)198-205.
- [154] A. Kumar, M. Paliwal, R. Ameta, S. Ameta, Photochemical treatment of rhodamine B waste water by photofenton reagent, *Indian Journal of chemical technology*, 15(2008)7-11.
- [155] L. WenXiu, L. Qing, L. XiuFang, S. YunTing, C. WenBin, Photocatalytic

- degradation of coking wastewater by nanocrystalline (Fe, N) co-doped TiO₂ powders Science China, Technological sciences, 53 (2010)1477–1482.
- [156] D. Trujillo, X. Font, A. Sánchez, Use of Fenton reaction for the treatment of leachate from composting of different wastes, *J. Hazard. Mater.*, 138 (2006) 201-204.
- [157] K. Barbusiński, Toxicity of Industrial Wastewater Treated by Fenton's Reagent, *Polish Journal of Environmental Studies*, 14 (2005)11-16.
- [158] N. Kulkarni, S. Sampath, V.Venugopal, Preparation and characterization of Purochlore:[La_{1-x}Pu_x]₂Zr₂O₇ (x = 0-1), *J. Nucl. Mater.*, 281(2000) 248-250.
- [159] Y. Mao, G. Li, W. Xu, S. Feng, Hydrothermal Synthesis and characterization of nanocrystalline Pyrochlore oxides M₂Sn₂O₇ (M= La, Bi, Gd, Y), *J. Mater. Chem.* 10 (2000) 479-482.
- [160] J. Wu, X. Wei, N. Padture, P. Klemens, M. Gell, E. Garcia, P. Miranzo and M. Osendi, Low thermal conductivity rare earth zirconates for potential thermal barrier coating applications, *J. Am Ceram. Soc.*, 85 (2002) 3031-35.
- [161] K. Li, H. Wang, H. Yan, Hydrothermal preparation and photocatalytic properties of Y₂Sn₂O₇ nanocrystals, *J. Mol. Catal. A: Chem.*, 249 (2006) 65–70.
- [162] L. Torres-Martinez, I. Juarez-Ramirez, J. S. Ramos-Garza, F. Vazquez-Acosta, S. W. Lee, Photocatalytic performance of pyrochlore-type structure compounds, Bi₂MTaO₇ (M = Al, Ga, Fe or In), on Alizarin Red S degradation, *Advanced Research in Physics and Engineering*.
- [163] M. Sansernnivet, P. Limthongkul, Preparation and characterization of bismuth ruthenate pyrochlore via solid state reaction and sol-gel methods, *Songklanakarin J. Sci. Technol.* 31 (2009) 669-673.
- [164] Z. Chen, W. Gong, T. Chen, G. Xiong, G. Huang, Preparation of Y₂Ti₂O₇ nanocrystal by Sol-Gel method and its characterization, *Advanced Materials Research* 97 – 101(2010) 2175-2179.
- [165] K. S. Rane, H. Uskaikar, R. Pednekar, R. Mhalsikar, The low temperature synthesis of metal oxides by novel hydrazine method, *Journal of Thermal Analysis and Calorimetry*, 90 (2007) 627-638.
- [166] A. Alemi, R. E. Kalan, Preparation and characterization of neodymium tin oxide pyrochlore nanocrystals by the hydrothermal method, *Radiation Effects & Defects in Solids*, 163 (2008) 229–236.
- [167] Y. Zhang, Z. Yan, F. Liao, C. Liao, C. Yan, Citrate gel synthesis and characterization of (ZrO₂)_{0.85}(REO_{1.5})_{0.15} (RE = Y, Sc) solid solutions, *Mater. Res. Bull.* 39 (2004)1763-1777.

- [168] M. M. Patil, V. V. Deshpande, V. Ravi, Synthesis of nanocrystalline $\text{Sn}_{0.2}\text{Zr}_{0.8}\text{TiO}_4$ by the citrate gel method, *Ceramics International*, 32 (2006) 345-347.
- [169] V. Ravi, S. D. Kulkarni, V. Samuel, S.N. Kale, J. Mona, R. Rajgopal, A. Daundkar, P. S. Lahoti, R. S. Joshee, Synthesis of $\text{La}_{0.7}\text{Sr}_{0.3}\text{MnO}_3$ at 800°C using citrate gel method, *ceramics international*, 33(2007)1129-1132.
- [170] S. P. Devi, H.S. Maiti, A modified citrate gel route for the synthesis of phase pure $\text{Bi}_2\text{Sr}_2\text{CaCu}_2\text{O}_8$ superconductor, *J. Mater. Res.*, 9 (1994)1357-1362.
- [171] A. Kahoul, P. Nkeng, A. Hammouche, F. Naamoune, G. Poillerat, A Sol-Gel Route for the Synthesis of $\text{Bi}_2\text{Ru}_2\text{O}_7$ Pyrochlore Oxide for Oxygen Reaction in Alkaline Medium, *J. Solid State Chem.*, 161 (2001) 379-384.
- [172] Y. Xie, J. Wang, R. Liu, X. Su, Z. Sun, Z. Li, Preparation of $\text{La}_{1.9}\text{Ca}_{0.1}\text{Zr}_2\text{O}_{6.95}$ with pyrochlore structure and its application in synthesis of ammonia at atmospheric pressure, *Solid state ionics*, 168 (2004) 117-121.
- [173] S. M. Zanetti, S. A. Da Silva, Synthesis and characterization of bismuth zinc niobate pyrochlore nanopowders, *Mat. Res.*, 10 (2007) 261-266.
- [174] C. Chiua, Y. Leea, H. Sheub, H. I. Koa, Phase Transition and the Thermal Activated Ordering of the Ions with Pyrochlore Phase in $\text{Ln}_2\text{Zr}_2\text{O}_7$ ($\text{Ln} = \text{Sm}, \text{Eu}$), *Journal of the Chinese Chemical Society*, 57(2010)925-931.
- [175] K. D. Bhatte, P. Tambade, S. Fujita, M. Arai, B. M. Bhanage, Microwave-assisted additive free synthesis of nanocrystalline zinc oxide, *Powder Technology*, 203 (2010) 415-418.
- [176] P. R. Chang, J. Yu, X. Ma, Preparation of porous starch and its use as a structure-directing agent for production of porous zinc oxide, *Carbohydrate Polymers*, 83 (2011)1016-1019.
- [177] K. C. Patil, M. M. A. Sekar, *International journal of self propagating high temperature synthesis*, 3 (1994)181-186.
- [178] K.S. Rane, R. Mhalsiker, S. Yin, T. Sato, Kuk Cho, E. Dunbar, P. Biswas, Visible light-sensitive yellow $\text{TiO}_{2-x}\text{N}_x$ and Fe-N co-doped $\text{Ti}_{1-y}\text{Fe}_y\text{O}_{2-x}\text{N}_x$ anatase photocatalysts *J. Solid State Chem.*, 179 (2006) 3033-3044.
- [179] S. Basak, K. S. Rane, P. Biswas, Hydrazine-Assisted, Low-Temperature Aerosol Pyrolysis Method to Synthesize $\gamma\text{-Fe}_2\text{O}_3$, *Chem. Mater.*, 20 (2008) 4906-4914.
- [180] I. A. Vogel, *A Textbook of Quantitative Inorganic analysis* (Longman U K) 1978.
- [181] B. S. Furniss, A. J. Hannaford, P. Smith, A. Tatchell, *Vogel's Textbook of practical organic chemistry*, 5th edition Longman group UK Ltd 1989.

- [182] A. R. West, Solid state chemistry and its applications, John Wiley & Sons, 1984.
- [183] S. Ray, Electron microscopy making invisible visible, Science Reporter March (2003) 18-21.
- [184] J. Fujita, A.E. Martell, K. Nakamoto, J.Chem, Phys. 36 (1962) 324.
- [185] J. Fujita, A. E. Martell, K. Nakamoto, J. Chem, Phys. 36 (1962) 331.
- [186] A. Braibanti, F. Dallavalle, M. A. Pellinghelli, E. Leporati, The Nitrogen-Nitrogen Stretching Band in Hydrazine Derivatives and Complexes, Inorganic chemistry, 7 (1968) 1430-1433.
- [187] R. Mhalsikar, Syntheses and characterization of catalytic & sensor materials, Ph. D. Thesis, Goa University, Goa, India, (2008).
- [188] E. W. Schmidt, Hydrazine and its Derivatives, Wiley, New York, 1984.
- [189] N. Arul Dhas, K. C. Patil, J. Mater. Chem., 3 (1993) 1289-1294.
- [190] JCPDS- International centre for diffraction data, 17- 0458.
- [191] F. H. El-Batal, UV Visible, infra-red, raman and ESR spectra of gamma irradiated TiO₂ doped sodalime phosphate glasses, Indian J. pure appl. Phys. 47(2009) 631-642.
- [192] Burgaaf, Van Dijk, Verkerk, Solid state ionics, 5(1981)519.
- [193] P. K. Moon, H. L. Tuller, Solid state ionics, 28-30(1988) 470.
- [194] V. V. Atuchin, T. A. Gavrilova, J.-C. Grivel, V. G. Kesler, Electronic structure of layered titanate Nd₂Ti₂O₇, Surface Science, 602 (2008) 3095.
- [195] J. Wang, Z.G. Wu, X.M. Yuan, S.R. Jiang, P.X. Yan, The effect of heat treatment on the structure and chemical homogeneity of ferroelectrics PLZT thin films deposited by R. F. sputtering, Mater. Chem. Phys. 88 (2004) 77.
- [196] J. Guillot, F. Fabreguette, L. Imhoff, O. Heintz, M. C. Marco de Lucas, M. Sacilotti, B. Domenichini, S. Bourgeois, Amorphous TiO₂ in LP-OMCVD TiN_xO_y thin films revealed by XPS, Applied Surface Science, 177 (2001) 268-272.
- [197] H.F. Franzen, M.X. Umana, J.R. McCreary, R.J. Thorn, J. Solid State Chem. 18 (1976) 363.
- [198] C. H. Hwang, K. Cho, Y. Takagi, K. Kawamura, An XPS study of amorphous and crystalline Cu₅₀Ti₅₀ alloy, Journal of Physics C: Solid State Physics, 18 (1985)2575.

- [199] S. O. Saied, J.L. Sullivan, T. Choudhury, C. G. Pearce, *Vacuum* 38 (1988) 917.
- [200] R. Karmali, V.P. Borker, K.S. Rane, S.K. Deshpande, Citrate gel route for synthesis of dense pyrochlores, *Materials chemistry and physics*, 129 (2011) 1116-1120.
- [201] S. Nakayama, Y. Iida, T. Nagano, T. Akimoto, Leaching Behavior of a Simulated Bituminized Radioactive Waste Form under Deep Geological Conditions, *J. Nucl. Sci. Technol.*, 40 (2003) 227–237.
- [202] N. Manivasakam, *Physicochemical examination of water sewage and industrial effluents*, (Pragati Prakashan, Meerut) 1980, p. 91.
- [203] N. Manivasakam, *Physicochemical examination of water sewage and industrial effluents*, (Pragati Prakashan, Meerut) 1980, p. 83.
- [204] V. Sambhy, M. M. MacBride, B. R. Peterson, A. Sen, Silver Bromide Nanoparticle Composites: Dual Action Tunable Antimicrobial Material, *J. Am. Chem. Soc.*, 128 (2006) 9798-9808.
- [205] J. X. Wang, L. X. Wen, Z. H. Wang, J. F. Chen, Immobilization of silver on hollow silica nanospheres and nanotubes and their antibacterial effects, *Mater. Chem. Phys.*, 96 (2006) 90-97.
- [206] M. Joseph, H. Tabata, T. Kawai, p- type electrical conduction in ZnO thin films by Ga and N codoping, *Jpn. J. Appl. Phys.*, 38 (1999), L 1205-L1207.
- [207] J. Lu, Q. Zhang, J. Wang, F. Saito, M. Uchida, *Powder Technol.*, 162 (2006) 33.
- [208] H. Irie, S. Washizuka, N. Yoshino, K. Hashimoto, Visible-light induced hydrophilicity on nitrogen-substituted titanium dioxide films, *CHEM. COMMUN.*, 11(2003)1298–1299.
- [209] R. Asahi, T. Morikawa, T. Ohwaki, K. Aoki, Y. Taga, Visible-Light Photocatalysis in Nitrogen-Doped Titanium Oxides, *Science*, 293 (2001) 269-271.
- [210] T. Okato, T. Sakano, M. Obara, Suppression of photocatalytic efficiency in highly N-doped anatase films, *Phys. Rev. B*, 72 (2005)115124.
- [211] D. N. Tafen, J. Wang, N. Wu, J. P. Lewis, Visible light photocatalytic activity in nitrogen-doped TiO₂ nanobelts, *Appl. Phys. Lett.*, 94 (2009) 093101.
- [212] T. Yamamoto, H. Katayama-Yoshida, Solution Using a Codoping Method to Unipolarity for the Fabrication of p-Type ZnO, *Japanese Journal of Applied Physics*, 38 (1999) L166-L169.
- [213] Sonny Xiao-zhe Li, Nitrogen Doped Zinc Oxide Thin Film, A thesis for Master

- of Science, UNIVERSITY of CALIFORNIA, BERKELEY, 2003.
- [214] K.J. Chen, T.H. Fang, F.Y. Hung, L.W. Ji, S.J. Chang, S.J. Young, Y.J. Hsiao, The crystallization and physical properties of Al-doped ZnO nanoparticles, *Appl. Surf. Sci.*, 254 (2008) 5791–5795.
- [215] O. Impert, A. Katafias, P. Kita, A. Mills, A. Pietkiewicz-Graczyk, G. Wrzeszcz, Kinetics and mechanism of a fast leuco-methylene blue oxidation by copper(II)-halide species in acidic aqueous media, *Dalton Trans*, (2003) 348-353.
- [216] M. John Plater, A degradation product of methylene blue, *ARKIVOC*, 2003 (i) 37-42.
- [217] S. Lee, A. Mills, Novel photochemistry of *leuco*-Methylene Blue, *CHEM. COMMUN.*, 18 (2003) 2366–2367.
- [218] D. Heger, J. Jirkovsky, P. Klán, Aggregation of Methylene Blue in Frozen Aqueous Solutions Studied by Absorption Spectroscopy, *J. Phys. Chem. A*, 109 (2005) 6702-6709.
- [219] S. Yang, H. He, D. Wu, D. Chen, Y. Ma, X. Li, J. Zhu, P. Yuan, Degradation of methylene blue by heterogeneous fenton reaction using titanomagnetite at neutral pH values: Process and affecting factors, *Ind. Eng. Chem. Res.* 48(2009) 9915-9921.
- [220] J. Donlagica, J. Levec, Comparison of Catalyzed and Noncatalyzed Oxidation of Azo Dye and Effect on Biodegradability, *Environ. Sci. Technol.*, 32(1998) 1294-1302
- [221] R. Azmat, Kinetics of methylene blue with organic reductants, University of Karachi, Pakistan, 2004.
- [222] H. Fu, L. Zhang, S. Zhang, Y. Zhu, J. Zhao, Electron Spin Resonance Spin-Trapping Detection of Radical Intermediates in N-Doped TiO₂-Assisted Photodegradation of 4-Chlorophenol. *J. Phys. Chem. B.*, 110 (2006) 3061–3065.
- [223] T. Wu, T. Lin, J. Zhao, H. Hidaka, N. Serpone, TiO₂-Assisted Photodegradation of Dyes. 9. Photooxidation of a Squarylium Cyanine Dye in Aqueous Dispersions under visible light irradiation, *Environ. Sci. Technol.*, 33 (1999)1379-1387.
- [224] G. Liu, J. Zhao, Photocatalytic degradation of dye sulforhodamine B: a comparative study of photocatalysis with photosensitization, *New J. Chem.*, 24 (2000) 411-417.
- [225] X. G. Zhang, Corrosion and electrochemistry of Zinc, Plenum Press, New York, 1996.
- [226] M. Bizarro, High photocatalytic activity of ZnO and ZnO:Al nanostructured films deposited by spray pyrolysis, *Applied Catalysis B: Environmental* 97 (2010)198-203.
- [227] B. Neppolian, S. R. Kanel, H. C. Choi, M. V. Shankar, B. Arabindo, V.

- Murugesan, Photocatalytic degradation of reactive yellow 17 dye in aqueous solution in the presence of TiO₂ with cement binder, *International Journal of photoenergy*, 5(2003).
- [228] R. S. Karmali, A. Bartakke, V. P. Borker, K. S. Rane, Bactericidal action of N doped ZnO in sunlight, *Biointerface Research in Applied Chemistry*, 1 (2011) 057-063.
- [229] I. M. Sadiq, B. Chowdhury, N. Chandrasekaran, A. Mukherjee, Antimicrobial sensitivity of *Escherichia coli* to alumina nanoparticles, *Nanomedicine*, 5(2009)282-6.
- [230] S. Yin and T. Sato, Synthesis and photocatalytic properties of fibrous Titania prepared from protonic layered Tetratitanate precursor in supercritical alcohols, *Ind. Eng. Chem. Res.*, 39(2000) 4526–4530.
- [231] H. Gerischer, A. Heller, The role of oxygen in photooxidation of organic molecules on semiconductor particles, *J. Phys. Chem.*, 95(1991) 5261–5267.
- [232] M. Anpo, in *Recent Developments on Visible Light Response Type Photocatalysts* (ISBN 4-86043-009-03), (2002) NTS, Tokyo, p. 9.
- [233] H. J. H. Fenton, Oxidation of tartaric acid in presence of iron, *J. Chem. Soc., Trans.* 65 (1894) 899–911.
- [234] F. Haber, J. Weiss, Über die Katalyse des Hydroperoxydes, *Naturwissenschaften* (1932).
- [235] J. Torrent, V. Barro'n, Diffuse reflectance spectroscopy of iron oxides, *Encyclopedia of Surface and Colloid Science*, Copyright D 2002 by Marcel Dekker, Inc. All rights reserved.
- [236] A. C. Scheinost, A. Chavernas, V. Barron, J. Torrent, Use and limitations of second derivative diffuse reflectance spectroscopy in the visible to near-infrared range to identify and quantify Fe oxide minerals in soils, *Clays and Clay Minerals*, 46 (1998)528-536.
- [237] Z.X. Shen, J.J. Cao, X.Y. Zhang, R. Arimoto, J.F. Ji, W.L. Balsam, Y.Q. Wang, R.J. Zhang, X.X. Li, Spectroscopic analysis of iron-oxide minerals in aerosol particles from northern China, *Science of the Total Environment* 367 (2006) 899-907.
- [238] R. M. Cornell, U. Schwertmann, *The iron oxides: structure, properties, reactions, occurrences and uses*, 2nd Completely Revised and Extended Edition (2003) Wiley-VCH.
- [239] R. A. Mansoori, S. Kothari, R. Ameta, Use of ZnO as a photocatalyst in photocatalytic bleaching of rhodamine B, *J. Indian chemical Soc.* 81(2004)335-337.

[240] L. Adamcikova, K. Pavlikova, P. Sevcik, The decay of methylene blue in alkaline solution, *React. Kinet. Catal. Lett.*, 69 (2000) 91-94.

[241] J. K. Leland, A. J. Bard, Photochemistry of colloidal semiconducting iron oxide polymorphs, *J. Phys. Chem.*, 91 (1987) 5076-5083.

[242] J. Jiang, J. F. Bank, C. Scholes, Sub second time resolved spin trapping followed by stopped-flow EPR of Fenton reaction products. *J. Am. Chem. Soc.*, 115 (1993) 4742-4746.

APPENDIX - I

Table A-1 : d values calculated by XRD for zirconates prepared by oxalate and hydrazinated oxalate

Gd ₂ Zr ₂ O ₇ (oxalate)		Gd ₂ Zr ₂ O ₇ (OxH)		Gd ₂ ZrCeO ₇ (ox)		Gd ₂ ZrCeO ₇ (OxH)	
2θ	d	2θ	d	2θ	d	2θ	d
28.71	3.1074	28.63	3.1159	29.0	3.080	28.50	3.1332
30.17	2.9598	30.18	2.9583	29.60	3.019	29.00	3.080
33.37	2.6829	34.99	2.5623	34.00	2.638	33.7	2.6608
47.96	1.8951	47.87	1.8986	49.20	1.8526	48.40	1.8793
50.35	1.8110	50.35	1.8110	56.50	1.6295	56.90	1.6189
56.68	1.6225	56.63	1.6240	58.00	1.5908	59.21	1.5593
60.07	1.5389	59.59	1.5501				
Nd ₂ Zr ₂ O ₇ (ox)				Nd ₂ Zr ₂ O ₇ (OxH)			
2θ	d	2θ	d	2θ	d	2θ	d
14.40	6.1461	14.48	6.1111				
28.99	3.0771	29.07	3.0639				
30.81	2.8997	30.87	2.8941				
33.61	2.6639	33.59	2.6655				
48.23	1.8852	48.27	1.8838				
50.65	1.8007	49.39	1.8437				
57.15	1.6103	57.24	1.6081				
60.08	1.5388	60.06	1.5390				

Table A-2: Crystallite sizes of zirconates prepared by oxalate and hydrazinated oxalate methods (calculated by Scherer's formula)

Compound	Particle size in nm
Gd ₂ Zr ₂ O ₇ (oxalate)	16.11
Gd ₂ Zr ₂ O ₇ (Hydrazinated oxalate)	20.63
Gd ₂ ZrCeO ₇ (oxalate)	13.92
Gd ₂ ZrCeO ₇ (Hydrazinated oxalate)	11.46
Nd ₂ Zr ₂ O ₇ (oxalate)	28.70
Nd ₂ Zr ₂ O ₇ (Hydrazinated oxalate)	28.70

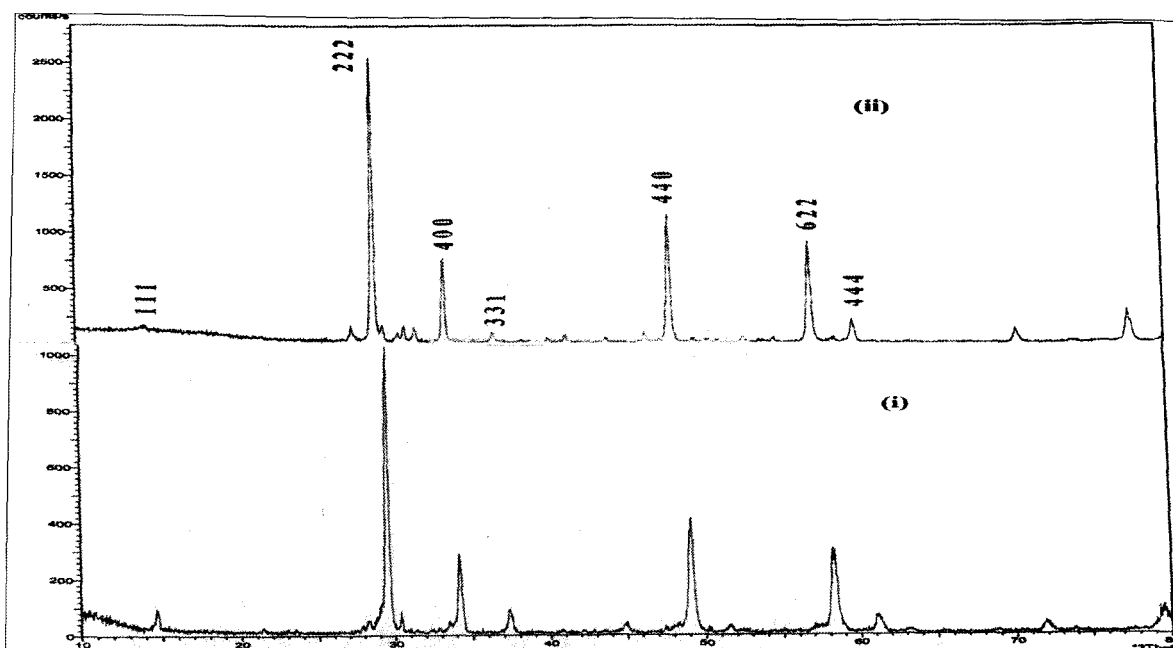


Figure A-1: XRD patterns of as prepared (i) $\text{Nd}_2\text{Zr}_{1.8}\text{Ti}_{0.2}\text{O}_7$ and (ii) $\text{Nd}_2\text{Zr}_{1.0}\text{Ti}_{1.0}\text{O}_7$ (citrate gel method)

Table A-3: Calculated d values for $\text{Nd}_2\text{Zr}_x\text{Ti}_{2-x}\text{O}_7$ prepared by Ceramic method

$\text{Nd}_2\text{Zr}_{1.8}\text{Ti}_{0.2}\text{O}_7$		$\text{Nd}_2\text{Zr}_{1.6}\text{Ti}_{0.4}\text{O}_7$		$\text{Nd}_2\text{Zr}_{1.4}\text{Ti}_{0.6}\text{O}_7$		$\text{Nd}_2\text{Zr}_{1.2}\text{Ti}_{0.8}\text{O}_7$		$\text{Nd}_2\text{Zr}_{1.0}\text{Ti}_{1.0}\text{O}_7$	
2θ	d								
14.38	6.1544	14.52	6.0953	14.50	6.1037	-----	-----	14.62	6.0538
27.82	3.2042	28.08	3.1751	28.04	3.1795	28.22	3.1597	28.20	3.1618
29.06	3.0702	29.36	3.0395	29.30	3.0456	29.18	3.0579	29.48	3.0274
33.70	2.6574	34.04	2.6316	33.94	2.6391	33.82	2.6482	34.16	2.6226
36.82	2.4390	37.08	2.4225	37.08	2.4225	37.08	2.4225	37.34	2.4062
41.54	2.1721	41.80	2.1592	41.98	2.1503	41.44	2.1772	41.12	2.1933
44.32	2.0421	44.74	2.0239	44.70	2.0256	44.40	2.0386	44.82	2.0205
48.40	1.8791	48.86	1.8625	48.76	1.8660	48.60	1.8718	48.82	1.8639
50.76	1.7971	51.38	1.7769	50.40	1.8091	50.96	1.7905	50.40	1.8091
57.48	1.6020	58.10	1.5863	57.94	1.5903	57.70	1.5964	58.32	1.5809
60.30	1.5336	60.42	1.5308	60.26	1.5345	60.54	1.5821	60.12	1.5378

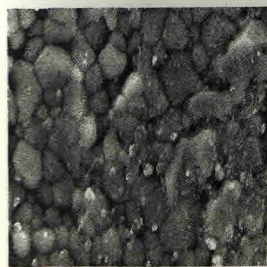
Table A-4: Calculated d values for $\text{Nd}_2\text{Zr}_x\text{Ti}_{2-x}\text{O}_7$ prepared by citrate gel method.

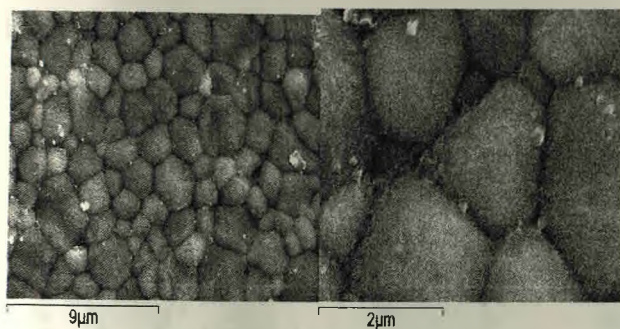
$\text{Nd}_2\text{Zr}_{1.8}\text{Ti}_{0.2}\text{O}_7$		$\text{Nd}_2\text{Zr}_{1.6}\text{Ti}_{0.4}\text{O}_7$		$\text{Nd}_2\text{Zr}_{1.4}\text{Ti}_{0.6}\text{O}_7$		$\text{Nd}_2\text{Zr}_{1.2}\text{Ti}_{0.8}\text{O}_7$		$\text{Nd}_2\text{Zr}_{1.0}\text{Ti}_{1.0}\text{O}_7$	
2 θ	d								
14.46	6.1205	14.42	6.1374	14.50	6.1037	14.58	6.0704	14.54	6.0870
27.84	3.2019	27.86	3.1997	27.92	3.1929	28.14	3.1684	28.12	3.1707
29.02	3.0744	29.14	3.0620	29.18	3.0578	29.38	3.0375	29.46	3.0294
33.64	2.6619	33.78	2.6512	33.84	2.6467	34.06	2.6301	34.12	2.6256
36.78	2.4416	36.92	2.4326	36.98	2.4288	37.20	2.4150	37.40	2.4025
41.60	2.1691	41.64	2.1672	41.66	2.1662	41.74	2.1622	41.52	2.1735
44.18	2.0483	-----	-----	44.44	2.0369	-----	-----	44.96	2.0145
48.38	1.8812	48.54	1.8740	48.62	1.8711	48.94	1.8596	49.10	1.8539
50.72	1.7984	50.90	1.7925	50.92	1.7918	51.32	1.7788	50.52	1.8051
57.40	1.6040	57.66	1.5974	57.72	1.5959	58.10	1.5863	58.28	1.5819
60.22	1.5354	60.48	1.5295	60.56	1.5276	60.68	1.5249	61.28	1.5114

A-5 Crystallite size calculated by Scherer's method for the $\text{Nd}_2\text{Zr}_x\text{Ti}_{2-x}\text{O}_7$ series

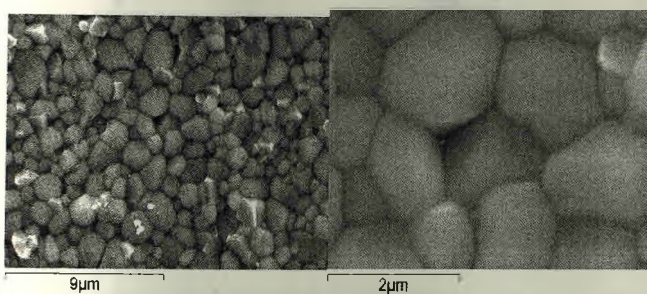
Compound	Citrate gel method (nm)		Ceramic method (nm)
	As prepared	Sintered	
$\text{Nd}_2\text{Zr}_2\text{O}_7$	40	188.2	132.9
$\text{Nd}_2\text{Zr}_{1.8}\text{Ti}_{0.2}\text{O}_7$	39	188.2	188.3
$\text{Nd}_2\text{Zr}_{1.6}\text{Ti}_{0.4}\text{O}_7$	34	158.4	188.4
$\text{Nd}_2\text{Zr}_{1.4}\text{Ti}_{0.6}\text{O}_7$	39	188.3	188.4
$\text{Nd}_2\text{Zr}_{1.2}\text{Ti}_{0.8}\text{O}_7$	39	188.4	188.3
$\text{Nd}_2\text{Zr}_{1.0}\text{Ti}_{1.0}\text{O}_7$	33	188.5	188.4

A-2 SEM images of pyrochlore samples prepared by citrate gel method.

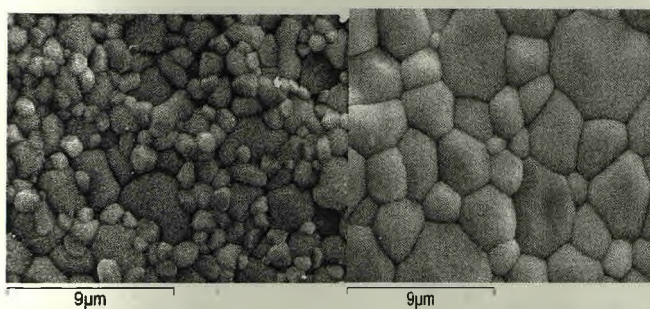
 $\text{Nd}_2\text{Zr}_2\text{O}_7$ (x700 and x2700)



B) $\text{Nd}_2\text{Zr}_{1.6}\text{Ti}_{0.4}\text{O}_7$ (x700 and x2700)



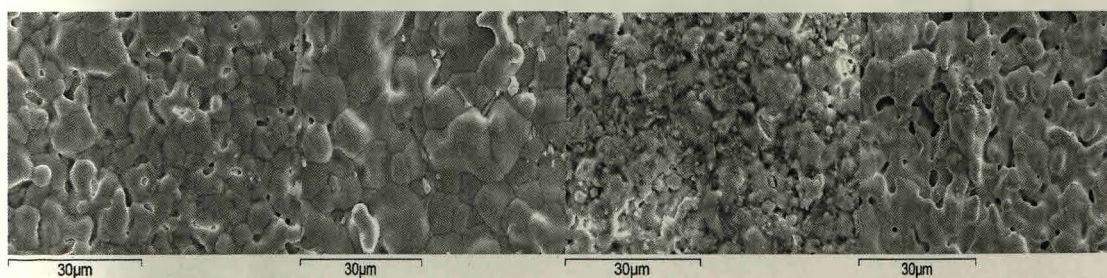
C) $\text{Nd}_2\text{Zr}_{1.4}\text{Ti}_{0.6}\text{O}_7$ (x700 and x2700)



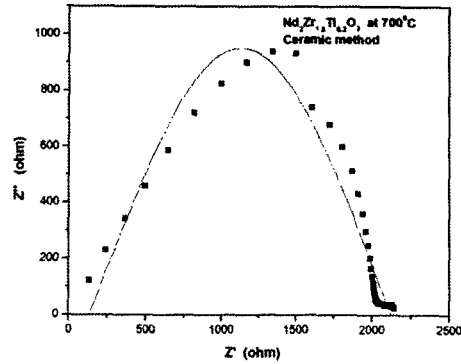
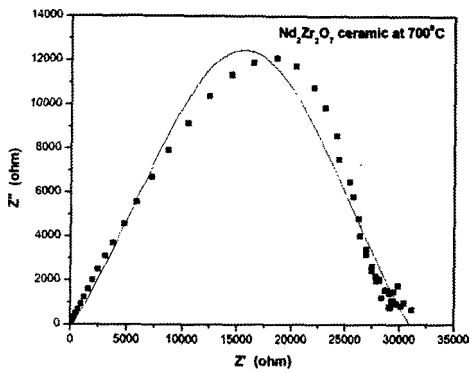
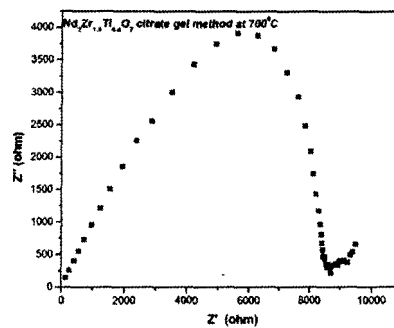
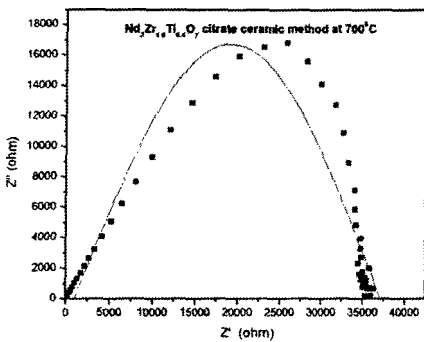
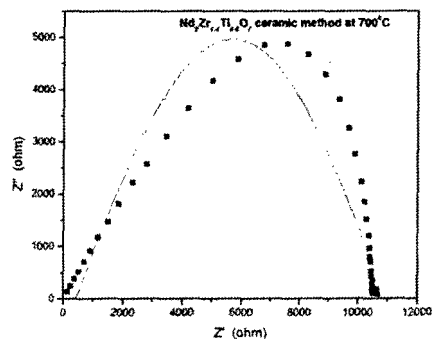
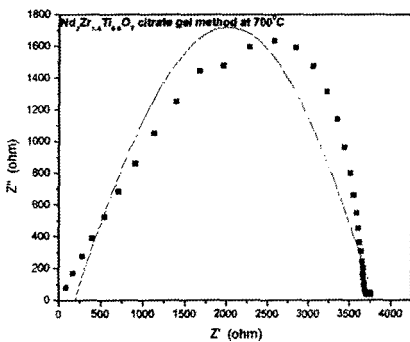
d) $\text{Nd}_2\text{Zr}_{1.2}\text{Ti}_{0.8}\text{O}_7$ (x700 and x2700)

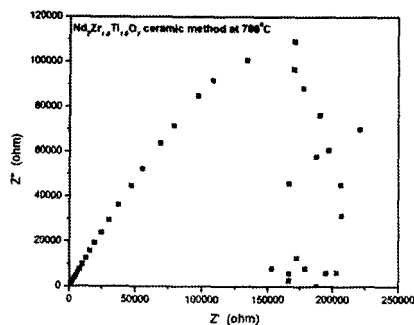
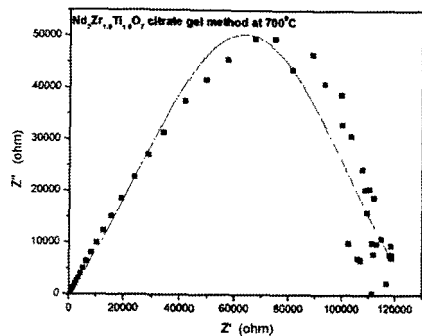
Figure A-3: SEM images of pyrochlore samples prepared by ceramic method (x 700).

A) $\text{Nd}_2\text{Zr}_2\text{O}_7$ B) $\text{Nd}_2\text{Zr}_{1.6}\text{Ti}_{0.4}\text{O}_7$ C) $\text{Nd}_2\text{Zr}_{1.4}\text{Ti}_{0.6}\text{O}_7$ d) $\text{Nd}_2\text{Zr}_{1.2}\text{Ti}_{0.8}\text{O}_7$



Figures A-4: Impedance plots at 700°C (973K) for

a) $\text{Nd}_2\text{Zr}_2\text{O}_7$, b) $\text{Nd}_2\text{Zr}_{1.8}\text{Ti}_{0.2}\text{O}_7$ prepared by ceramic method,c) $\text{Nd}_2\text{Zr}_{1.6}\text{Ti}_{0.4}\text{O}_7$ (citrate gel method), d) $\text{Nd}_2\text{Zr}_{1.6}\text{Ti}_{0.4}\text{O}_7$ (ceramic method),e) $\text{Nd}_2\text{Zr}_{1.4}\text{Ti}_{0.6}\text{O}_7$ (citrate gel method), f) $\text{Nd}_2\text{Zr}_{1.4}\text{Ti}_{0.6}\text{O}_7$ (ceramic method),

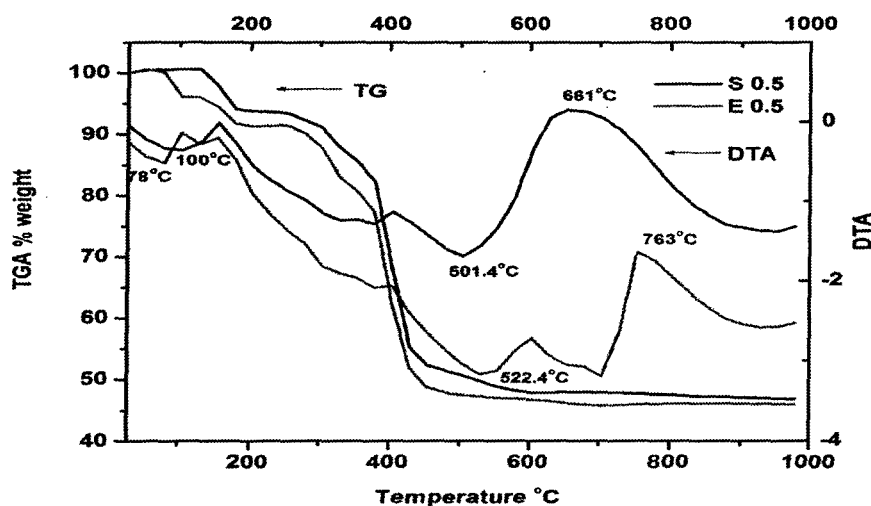


g) $\text{Nd}_2\text{Zr}_{1.0}\text{Ti}_{1.0}\text{O}_7$ (citrate gel method), h) $\text{Nd}_2\text{Zr}_{1.0}\text{Ti}_{1.0}\text{O}_7$ (ceramic method)

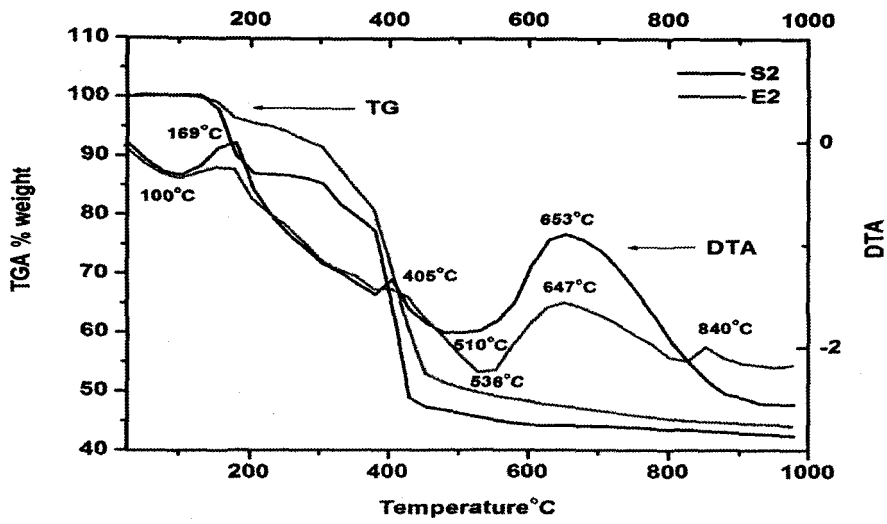
Table A-6: Calculated d values for ZnO and $\text{ZnO}_{1-x}\text{N}_x$ prepared by oxalate and hydrazinated oxalate method.

ZnO (Zincite) 5-664			ZnO (Oxalate)		ZnO(OXH Equilibration)		ZnO(OXH Solution)	
2θ	d	I/I ₀	2θ	'd'	2θ	'd'	2θ	'd'
31.74	2.816	71	31.95	2.7981	31.59	2.8290	31.59	2.8290
34.42	2.602	56	34.56	2.5919	34.19	2.6198	34.34	2.6083
36.24	2.476	100	36.42	2.4637	36.21	2.4781	36.21	2.4781
47.52	1.911	29	47.56	1.9096	47.49	1.9121	47.34	1.9180
56.52	1.626	40	56.67	1.6222	56.45	1.6281	56.45	1.6281
62.84	1.477	35	62.99	1.4738	62.81	1.4777	62.67	1.4806
66.36	1.407	06	66.51	1.4042	66.28	1.4085	66.28	1.4085
67.89	1.379	28	68.01	1.3768	67.86	1.3794	67.86	1.3794
69.04	1.359	14	69.13	1.3572	69.03	1.3589	68.87	1.3616

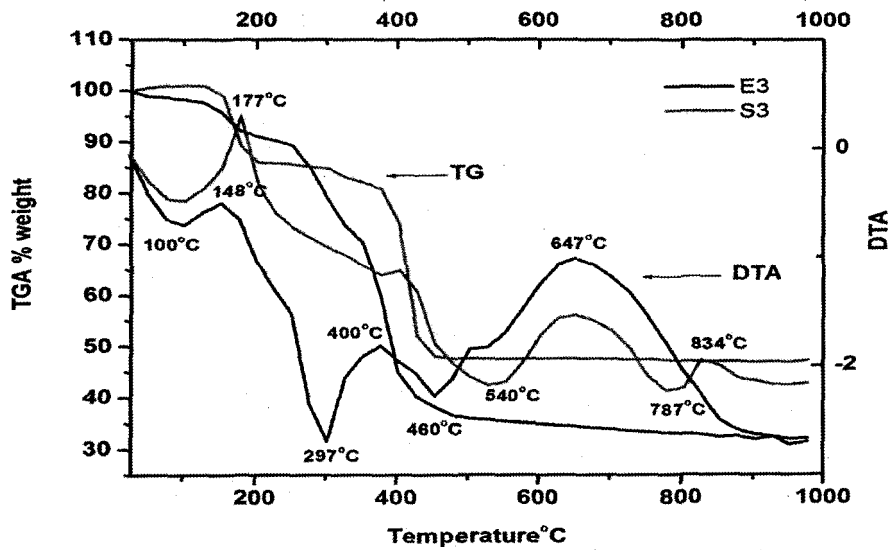
Figures A-5: Thermograms of hydrazinated oxalate precursors



i) for 0.0005% Al doped ZnO (S= solution method) (E=equilibration method)



ii) for 0.002 % Al doped ZnO (S= solution method) (E=equilibration method)



iii) for 0.003% Al doped ZnO (S= solution method) (E=equilibration method)

Table A-7: Calculated d values for aluminium doped ZnO prepared by hydrazinated oxalate (i) Equilibration and (ii) Solution method.

ZnO(Zincite) 5-664			5E		1E		2E		3E	
2θ	d	I/I ₀	2θ	'd'	2θ	'd'	2θ	'd'	2θ	'd'
31.74	2.816	71	31.85	2.8059	31.85	2.8059	31.86	2.8057	31.66	2.8222
34.42	2.602	56	34.48	2.5981	34.48	2.5981	34.48	2.5981	34.48	2.5981
36.24	2.476	100	36.24	2.4761	36.24	2.4761	36.24	2.4761	36.24	2.4761
47.52	1.911	29	47.47	1.9130	47.47	1.9130	47.47	1.9130	47.47	1.9130
56.52	1.626	40	56.59	1.6245	56.59	1.6245	56.59	1.6245	56.59	1.6245
62.84	1.477	35	62.91	1.4755	62.91	1.4755	62.91	1.4755	62.91	1.4755
66.36	1.407	06	66.42	1.4058	66.43	1.4058	66.43	1.4058	66.43	1.4058
67.89	1.379	28	68.01	1.3768	68.01	1.3768	68.01	1.3768	67.82	1.3802
69.04	1.359	14	69.05	1.3586	69.05	1.3586	69.05	1.3586	69.05	1.3586

ZnO(Zincite) 5-664			5S		1S		2S		3S	
2θ	d	I/I ₀	2θ	'd'	2θ	'd'	2θ	'd'	2θ	'd'
31.74	2.816	71	31.85	2.8059	31.85	2.8059	31.86	2.8057	31.86	2.8059
34.42	2.602	56	34.48	2.5981	34.48	2.5981	34.48	2.5981	34.48	2.5981
36.24	2.476	100	36.41	2.4650	36.41	2.4649	36.24	2.4761	36.24	2.4761
47.52	1.911	29	47.64	1.9066	47.64	1.9066	47.64	1.9066	47.64	1.9066
56.52	1.626	40	56.78	1.6195	56.78	1.6195	56.59	1.6245	56.59	1.6245
62.84	1.477	35	62.91	1.4755	62.91	1.4755	62.91	1.4755	62.74	1.4791
66.36	1.407	06	66.42	1.4058	66.43	1.4058	66.60	1.4026	66.43	1.4058
67.89	1.379	28	68.01	1.3768	68.18	1.3738	68.01	1.3768	67.82	1.3802
69.04	1.359	14	69.24	1.3554	69.24	1.3554	69.24	1.3554	69.05	1.3586

Figure A-6 :ESI-MS spectra of i)MB and ii) its major ion on application of high energy

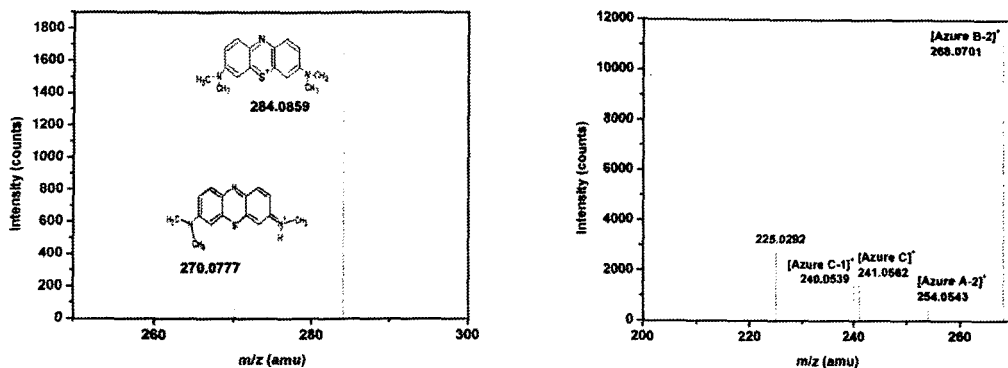
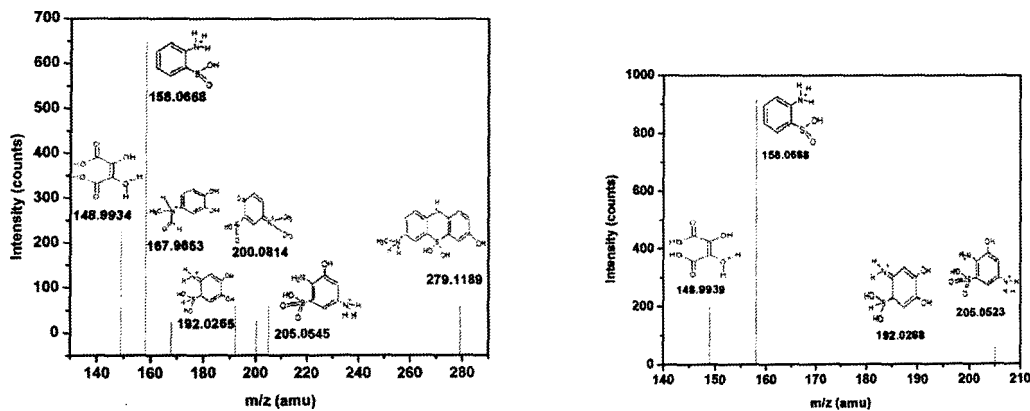
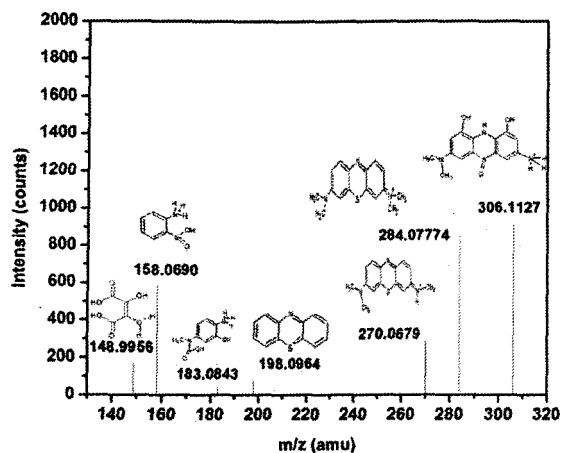
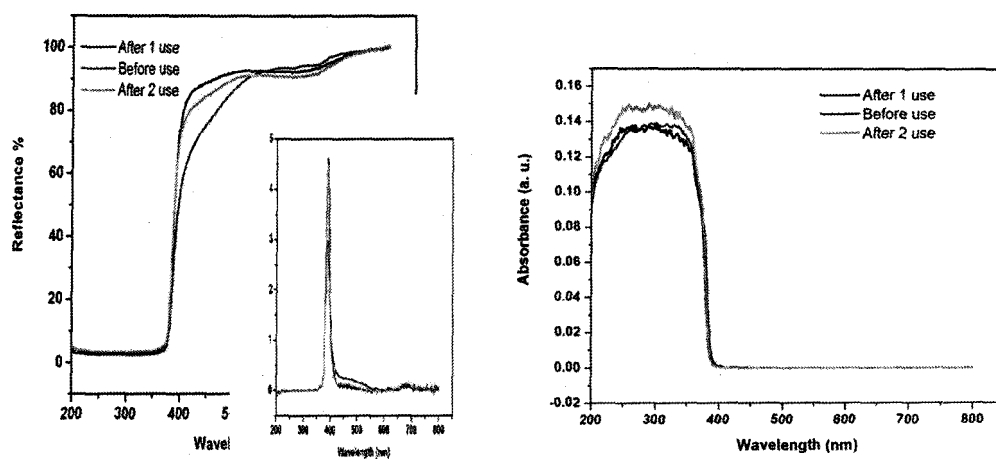
Figure A-7:ESIMS of MB on photodegradation by i)ZnO and ii) ZnO_{1-x}N_x

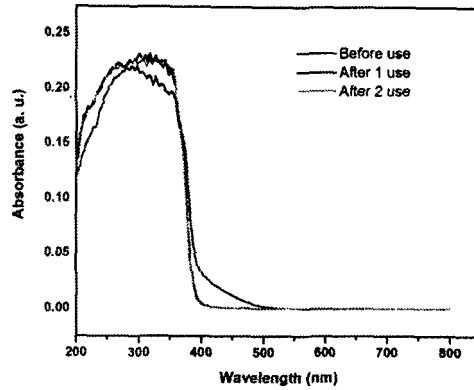
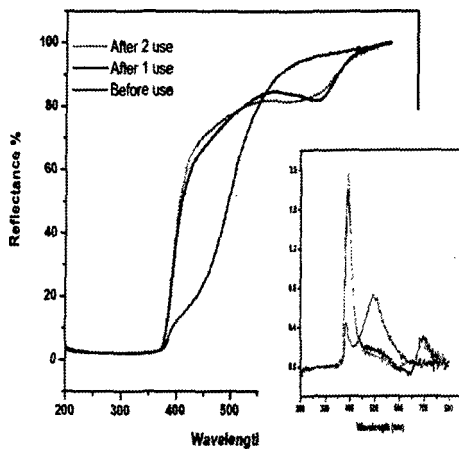
Figure A-8:ESIMS of MB on degradation by photolysis in sunlight



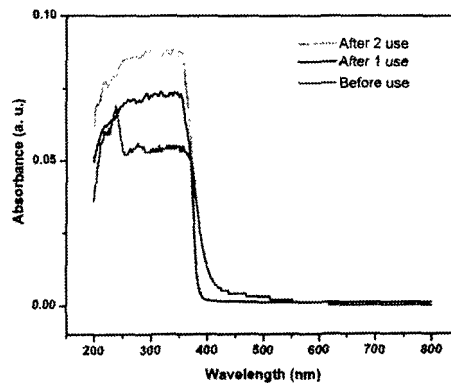
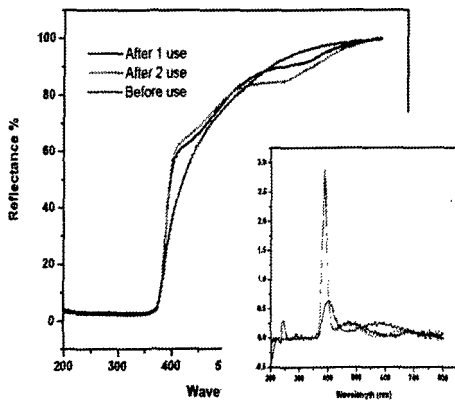
Figures A-9 diffuse reflectance and absorbance spectra of



i) ZnO prepared by oxalate method.



ii) ZnO_{1-x}N_x prepared by hydrazinated oxalate (equilibration) method.



iii) ZnO_{1-x}N_x prepared by hydrazinated oxalate (solution) method.

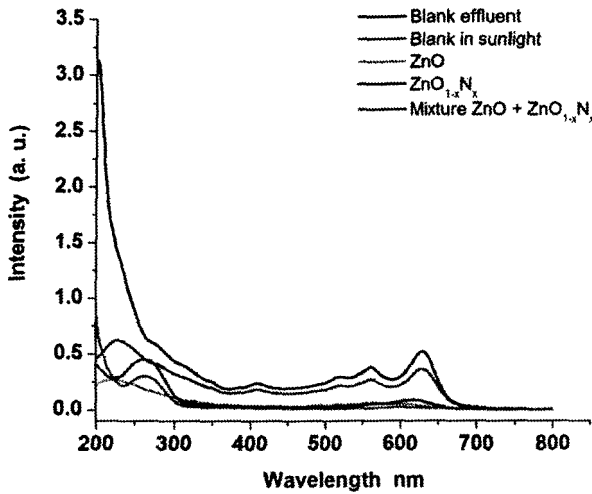


Figure A-10 : Degradation of industrial effluents on ZnO and ZnO_{1-x}N_x photocatalysts.

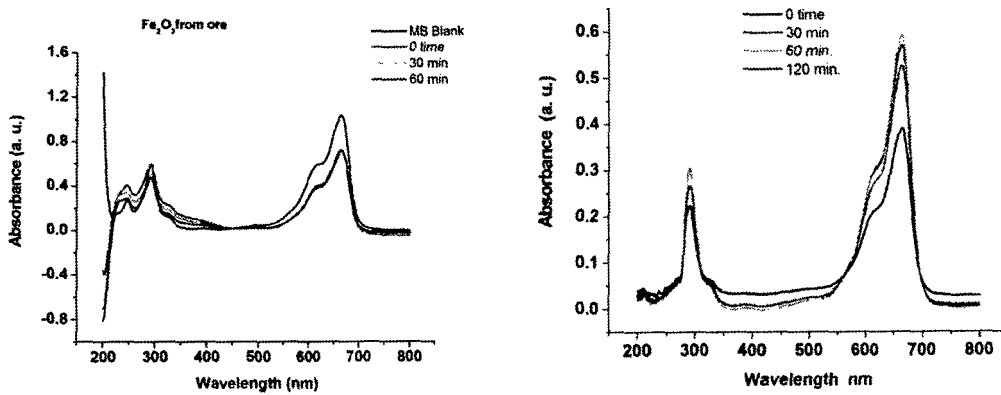
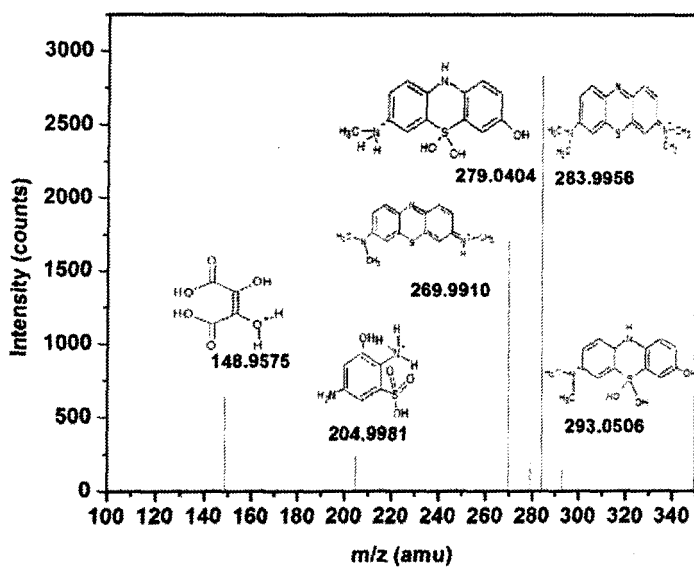
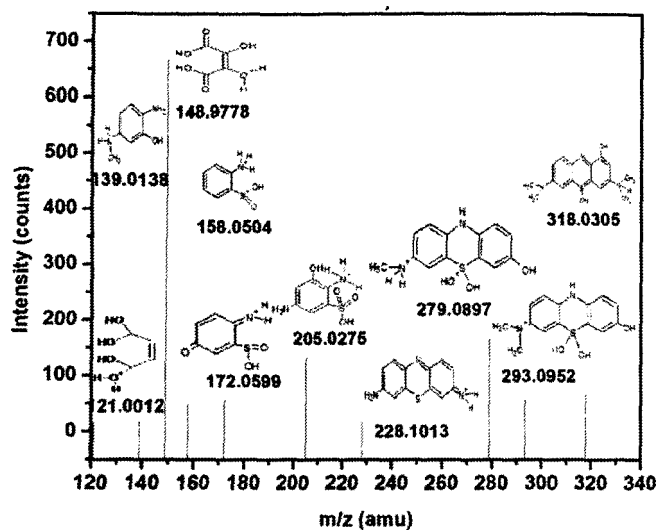


Figure A-11 : Degradation of MB on i) Fe₂O₃ and ii) γ -Fe₂O₃ prepared from ore rejects

Figure A-12:ESI-MS spectra of MB on degradation by iron ore rejects, i)Solar and ii) Thermal.



APPENDIX – II**LIST OF PUBLICATIONS****A. International Journals**

1. Rajashri S. Karmali, Amruta Bartakke, Vrinda P. Borker, Koyar S. Rane, Bactericidal action of N doped ZnO in sunlight, *Biointerface research in applied chemistry* 1:2(2011).
2. R. Karmali, V. P. Borker, K. S. Rane, S. K. Deshpande, Citrate gel route for synthesis of dense pyrochlores, *Materials chemistry and physics*, 129:3(2011) 1116-1120.
3. Rajashri Karmali, Vrinda Borker, Koyar Rane & Chandrakant G. Naik, Value addition to the low grade iron ore rejects, accepted for publication in *The journal of solid waste technology and management*.

LIST OF PAPERS PRESENTED**A. International Conference**

1. Rajashree Karmali, Vrinda Borker, K.S.Rane, A.K.Tyagi, Low Temperature Synthesis of Pyrochlore Oxides, $\text{Nd}_2\text{Zr}_x\text{Ti}_{2-x}\text{O}_7$, presented at Crystal growth and Crystal Technology, sendai, Japan 2008.
2. Rajashree Karmali, Vrinda Borker, Koyar Rane, Zirconate pyrochlores as matrix for nuclear waste disposal, at International Conference on synthetic and structural chemistry at Mangalore University, Mangalore, India, December 8-10, 2011.

B. National Conference

1. Rajashree S. Karmali, Vrinda P. Borker, A. K. Tyagi, Low Temperature Synthesis of Neodymium Zirconate, in the Fourth National Symposium and Conference on Solid State Chemistry and Allied Areas (ISCAS-2005) at Goa University on Dec 1-3, 2005.
2. Rajashree karmali, V. P. Borker, K S Rane, A. K. Tyagi, Ionic conductivity of Neodymium Zirconate prepared by precursor method, in two day national seminar on the role of Material science in Electronic Industry & Information Technology sponsored by UGC at DM's college on 9-10th March 2006.
3. R. Karmali, V. P. Borker, C. G. Naik, K.S.Rane, Advanced oxidation of organic wastes using semiconductor oxides” at Dr. A. V. Baliga college of Arts and Science, Kumta in one day National Seminar on “Water Chemistry for society, industry and its present scenario for domestic use” on 6th December 2010.

4. R. Karmali, V. Borker, K.S.Rane, Leaching of Strontium from strontium doped pyrochlore for Nuclear waste disposal studies, in the National Conference on Science, Technology and applications of Rare Earths 2011, Munnar, Kerala state, India August 19- 20, 2011.

5. Rajashri Karmali, Vrinda Borker, K. S. Rane, Significance of morphology, particle sizes, structure and material properties of ZnO in tackling the environmental problems, in the 7th Biennial National symposium and conference on solid state chemistry and allied areas (ISCAS-2011) November 24-26, 2011.

6. Rajashree Karmali, Vrinda Borker and K.S.Rane , Synthesis and Characterisation of N doped ZnO and its use as photocatalyst in dye degradation in National Seminar on Nanomaterials: Synthesis, Characterisation and applications organized by Smt. Parvatibai Chowgule college of Arts and Science Margao-Goa on 2nd and 3rd February, 2012.